BORON-DOPED DIAMOND AS A RESILIENT ELECTRODE MATERIAL IN MOLTEN SALTS

By

Hannah Katherine Patenaude

Bachelor of Science – Chemistry
Bachelor of Arts – Communication Studies
University of Nevada, Las Vegas
2020

A dissertation submitted in partial fulfillment
of the requirements for the

Doctor of Philosophy – Radiochemistry

Department of Chemistry and Biochemistry
College of Sciences
The Graduate College

University of Nevada, Las Vegas
May 2024

UNLV | GRADUATE COLLEGE

Dissertation Approval

The Graduate College
The University of Nevada, Las Vegas

March 22, 2024

This dissertation prepared by

Hannah Katherine Patenaude

entitled

Boron-Doped Diamond as a Resilent Electrode Material in Molten Salts

is approved in partial fulfillment of the requirements for the degree of

Doctor of Philosophy – Radiochemistry
Department of Chemistry and Biochemistry

Kenneth Czerwinski, Ph.D.
Examination Committee Chair

Artem Gelis, Ph.D.
Examination Committee Member

Daniel Koury, Ph.D.
Examination Committee Member

Marisa Monreal, Ph.D.
Examination Committee Member

Cory Rusinek, Ph.D.
Graduate College Faculty Representative

Matthew Sheridan, Ph.D.
Graduate College Faculty Representative

Alyssa Crittenden, Ph.D.
Vice Provost for Graduate Education & Dean of the Graduate College

Emma Bloomfield, Ph.D.
Graduate College Faculty Representative

Abstract

Boron-Doped Diamond as a Resilient Electrode Material in Molten Salts

By

Hannah Katherine Patenaude

Dr. Kenneth R. Czerwinski, Committee Chair
Professor of Chemistry
University of Nevada, Las Vegas

Molten salt chemistry has a range of applications within nuclear technology, including for the Molten Salt Reactors (MSRs) and pyroprocessing to recover valuable actinides for energy and national security needs. However, the high-temperature, corrosive nature of molten salts makes them particularly challenging to deploy on an industrial scale and study in benchtop measurements. Material accountability and corrosion monitoring of MSR fuels are essential components to the successful deployment of MSRs, and electroanalytical techniques like cyclic voltammetry (CV) and spectroelectrochemistry (SEC) can provide a wealth of information to describe salt systems *in situ*. To perform such measurements, it is imperative to have materials that can withstand the harsh environment of molten chloride and fluoride salts. It is hypothesized that boron-doped diamond (BDD), a well-studied, 'designer' electrode material, can serve as a resilient working electrode in molten salt systems given its previous applications to other harsh environments.

To better understand the use of BDD in molten salts, it was first studied in aqueous systems using CV to determine the impact of crystal structure, morphology, and carbon hybridization (e.g., sp^2 or sp^3) on the electrochemical response. Potassium ferricyanide, hexaammineruthenium(III) chloride, europium trichloride, and uranyl nitrate were all

evaluated using CV on the two distinct sides of free-standing BDD to find that there is, in fact, an difference between large and small-grain structures of polycrystalline diamond. Values for formal potential (E^o), peak separation (ΔE_p), diffusion coefficients (D), and heterogeneous electron transfer rate constants (k) were compared for each side of the BDD to quantify the quality of each response. Then, a novel optically transparent electrode (OTE) design from free-standing BDD was applied to SEC measurements of aqueous potassium ferricyanide to determine E^o and D. Following successful measurements, this OTE could be a resilient design applicable for actinide species in molten salt systems to help characterize MSR fuels.

Then, BDD was exposed to chloride (NaCl-KC) and fluoride (FLiNaK) molten salts under various conditions for extended periods to determine if it would survive under the most extreme environments (i.e., exposed to air, in inert atmosphere, using non-purified salts, using thermally dried salts, etc.). The material was then evaluated using scanning electron microscopy (SEM), profilometry, Raman spectroscopy, X-ray photoelectron spectroscopy (XPS), and Time-of-Flight Secondary Ion Mass Spectroscopy (ToF-SIMS) to determine changes to the surface structure and chemistry after exposure. There was virtually no change to the material after exposure except in the case of chloride salt that was not dried and was exposed to air where etching was seen in some regions of the crystal structures. However, when aqueous CV was performed on the samples to determine changes to the electrochemical performance, there was very little change, including for the corroded sample.

Finally, BDD was used to perform CV on $Eu^{3+/2+}$ and $U^{4+/3+}$ redox couples in chloride salts using various BDD electrode geometries. Successful measurements of Eu were performed using free-standing BDD and thin-film BDD in LiCl-KCl, and U was evaluated with thin-film BDD in LiCl-KCl and $MgCl_2$-NaCl electrolytes. The impact of BDD crystal structure with the differing electrode geometries for Eu and changing electrolyte cation side for U were significant and produced an interesting set of results that opened doors for a wide range of future studies. Ultimately, BDD successfully performed measurements of f-block species relevant to MSR fuels and should be further explored under various conditions and optimized electrode designs.

Acknowledgments

Many thanks to the following sponsors for providing funding in support of this work:

1) This material is based upon work supported under the Department of Energy, Office of Nuclear Energy, Nuclear Energy University Program Project #: 20-19188 and the University Nuclear Leadership Program Fellowship. Any opinions, findings, conclusions, or recommendations expressed in this publication are those of the author(s) and do not necessarily reflect the views of the Department of Energy Office of Nuclear Energy.
2) A portion of the work represented in this publication was conducted at the Los Alamos National Laboratory. The author(s) would like to acknowledge the Laboratory Directed Research and Development Program support for Project #20210113DR for Advanced Characterization to Enable Prediction of Actinide-Molten Salt Behavior and Project #20210527CR and #20240478CR-GTS for the Seaborg Institute – Center for Advancing Actinide Science and 1090 Technology at Los Alamos National Laboratory. Los Alamos National Laboratory, an affirmative action/equal opportunity employer, is operated by Triad National Security, LLC, for the National Nuclear Security Administration of the U.S. Department of Energy under contract 89233218CNA000001. This document has been approved by the LANL Classification Office: LA-UR-24-22170.
3) A portion of the work represented in this publication was supported by the Molten Salt Reactor Program through the U.S. Department of Energy, Office of Nuclear Energy's Gateway for Accelerated Innovation in Nuclear.

This work is representative of much more than the last four years of my research as a graduate student. My journey to this point began in 2015 when my rejection from Harvard became motivation to hit the ground running at the University of Nevada, Las Vegas. It was one of the best things to ever happen to me, and UNLV will always have a special place in my heart thanks to the opportunities and people it brought during my time as a Rebel.

First and foremost, I must thank those who kickstarted my career in Radiochemistry at UNLV: Dr. Frederic Poineau for providing four years of support as my undergraduate research advisor; Dr. Cory Rusinek who gave me the opportunity to jump into molten salts (figuratively, of course) as my advisor for the first three years of my graduate career and showed me that electrochemistry isn't so bad; Dr. Ken Czerwinski for providing invaluable guidance over many years, and taking on the challenge of being my advisor for the final segment of my Ph.D. work; Drs. Artem Gelis, Dan Koury, and Matthew Sheridan for serving on my dissertation committee; and Dr. Emma Frances Bloomfield for helping me move the nuclear industry forward through communication studies and rhetoric research while serving as an invaluable mentor for the last seven years.

Next, it is imperative to recognize the life-changing opportunities I have been afforded at the Los Alamos National Laboratory thanks to many generous scientists and engineers: Dr. Franz Freibert, who saw something in me that was worth bringing to the Land of Enchantment and for his continued support through the Seaborg Institute; Dr. Marisa Monreal for taking me under her wing as a full-time graduate research assistant

for the last 18 months, sharing the secrets to success at LANL, and serving as an example of the scientist I can only aspire to become some day; Dr. Vedant Mehta who tested my patience while I pretended to be an engineer for a summer, and has become a great friend in the process; Dr. Charles Lhermitte who trusted me with his beloved molten salt electrochemistry infrastructure in order to complete my dissertation research; Drs. Scott Parker, Rami Batrice, Karla Erickson, and Nicolas Capra for helping me troubleshoot various laboratory challenges, like rebuilding the Dirty Mike glovebox after I forgot to run the chiller last summer; Dr. Emma Gordon, who helped me become an SEM aficionado; Drs. Clare Hatfield, Sarah Hickam, and Sarah Hernandez for taking my characterization to the next level with Raman, profilometry, and ToF-SIMS; Dr. Jarom Chamberlain for not turning off my furnaces, providing emotional support, and bringing me a new bestie and Target run partner, Jenna; and, of course, my darling Clementine.

The number of fellow students who have supported my career is longer than I can list here. Significant highlights include Drs. Rosendo Borjas, James Louis-Jean, and AJ Swift, who taught me valuable life and laboratory lessons as mentors during my undergraduate years; Nastasija Damjanovic, Renee Olney, and Jason Rakos, who helped me run various experiments described in the following manuscript all while they completed their undergraduate journeys; and Josie Libero, Jonathan George, Kelly Seeley, Liuba Williams, Nick Ciccetti, and the rest of the UNLV Radiochemistry family for the lasting memories.

Last and most importantly, I must thank those who have unconditionally supported my ambitious life plans: Mom and Dad, whose hard work allowed me to pursue my dreams

without hesitation; Ani and Caleb for listening to me say ‘molten salt’ too many times when I got home every day; Butterbean, Jack, Tex, Winston, and Koda for being my furry companions through the good and bad times; my dear friends and biggest cheerleaders, Ashleigh Bivins, Emalee Schuler, Nicole Thomas, Alexia Mercier, Kaylee Cunningham, and Stinky Pete; and Christopher for being the best life partner I could wish for, along with the rest of the Roys-Basile family who gave me a home away from home for so many years.

Table of Contents

List of Tables

List of Figures

List of Equations

1 Introduction

1.1 Motivation

The research presented in this dissertation aims to expand the limited repository of robust materials suitable for applications in molten alkali and alkaline earth halide salts (i.e., NaCl,). Boron-doped diamond (BDD) is expected to be a resilient, conductive material in the extreme environment of high-temperature, corrosive, and potentially radioactive molten salts. With the potential to help characterize fuel salts or provide online monitoring, BDD may be able to support the deployment of multiple Generation IV reactor designs and enhance pyroprocessing technology. The initial steps to determine BDD's applicability in these systems included using various aqueous analytes ($K_3Fe(CN)_6$, $Ru(NH_3)_6Cl_3$, $EuCl_3$, and $UO_2(NO_3)_2$) to explore the impacts of varied surface morphology due to the 'grown' (top) and 'nucleation' (bottom) sides of free-standing polycrystalline diamond on the electrochemical response when used as a working electrode. Additionally, aqueous matrices were used to test a novel BDD optically transparent electrode (OTE) design for spectroelectrochemistry (SEC) measurements with the hope of translating the concept for molten salt systems.

The resilience of BDD was tested in chloride and fluoride molten salts by exposing coupons to NaCl-KCl (50-50 mol%) and FLiNaK (46.5-11.5-42 mol% LiF-NaF-KF), two common eutectics,[1-4] and performing subsequent analysis. Scanning electron microscopy (SEM), profilometry, Raman spectroscopy, X-ray photoelectron spectroscopy (XPS), and time-of-flight secondary ion mass spectroscopy (ToF-SIMS) were used to determine changes to the topography and surface chemistry of the BDD after exposure. Aqueous

electrochemistry with well-studied analytes ($K_3Fe(CN)_6$ and $Ru(NH_3)_6Cl_3$) was then repeated on the exposed BDD to determine changes in electrochemical response. Finally, BDD was used as a working electrode in molten chloride salts to study Eu and U redox reactions. The goal of this work is to perform a preliminary evaluation of how BDD can be used to explore fundamental chemistry on f-block elements in molten salts while studying its survivability in harsh environments to support the development of molten salt technology for advanced reactors and the nuclear fuel cycle.

1.2 Actinide Molten Salts

Given their high-temperature, corrosive nature, molten salt environments are particularly challenging at both the benchtop and industrial scales. Regardless of the environment, f-block chemistry constitutes a unique set of challenges related to the complex electron structures and radioactivity, particularly concerning actinides. While molten (or 'fused') salt chemistry began in the early 20th century, there is still a need to improve the reliability and standardization of measurements performed on these systems.[5] There are multiple applications for alkali and alkaline earth halide salts, including as thermal storage for Concentrated Solar Plants (CSPs),[6] as fuel carriers or coolants for Molten Salt Reactors (MSRs),[7] and in pyroprocessing techniques for used nuclear fuel and stockpile stewardship in the weapons complex.[8-12] Therefore, actinide molten salt systems must be well-understood, and the list of robust materials for their various applications needs to be expanded.

1.2.1 Molten Salt Reactors

While MSRs are a part of the Generation IV (or 'Advanced') reactor fleet, the concept is not new. In 1992, the Director of the Oak Ridge National Laboratory, Alvin Weinberg, described the Molten Salt Reactor Experiment (MSRE, operated 1965-1969) as a "Dark Horse Breeder" that was lost in the shuffle of rapidly advancing nuclear energy technology. In his words, the MSR concept was overlooked because "our main problem is not that our idea is a poor one—rather it is different from the main line, and has too chemical a flavor to be fully appreciated by non-chemists" (p. 153).[13] The modern advanced MSR includes high-temperature, corrosive, and often radioactive matrices that are challenging to study in the laboratory and typically require unconventional infrastructure. Fortunately, countless researchers have still embarked on the challenge of studying molten salts, and the field has become increasingly robust over the last decade.

The MSRE is the only MSR that has been brought to full operation and, therefore, still provides invaluable information as modern designs are developed. It used ^{235}U and ^{233}U fuel systems in a solution of LiF-BeF_2-ZrF_4-UF_4 (65-29.1-5-0.9 mol%) at 650 °C with a FLiBe (66-34 mol% LiF-BeF_2) coolant.[14] Although funding for the MSRE ended, efforts to develop a commercial-scale MSR continued in national laboratory and university research settings. For example, **Figure 1.1** outlines early calculations of the oxidation states of various actinides in the salt for future molten salt breeder reactor fuels soon following the termination of the MSRE, accompanied by a list of redox reaction potentials measured for various electrode materials in FLiBe in **Table 1.1**, all of which were determined in 1974.[15] However, research efforts as recent as 2020 have relied on this original data as the only

point of reference for benchmarking reactor operations while the industry prepares to deploy modern MSRs.[16]

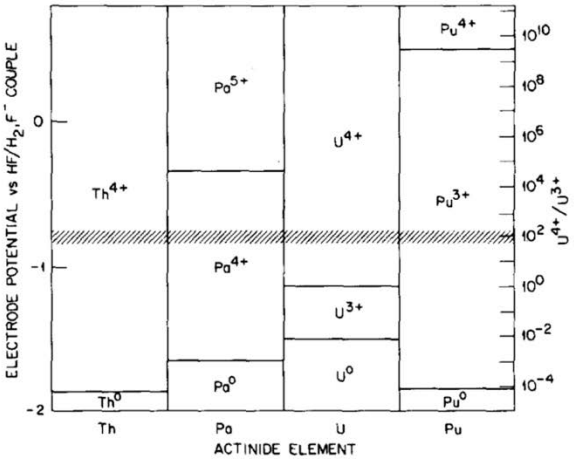

Figure 1.1 Actinide oxidation states vs. $HF/H_2,F^-$ as a function of U^{4+}/U^{3+} ratios in FLiBe calculated after the MSRE. The shaded region was determined to be the optimum redox potential range.[15,i]

Table 1.1 Redox potentials determined for FLiBe electrolyte at 600 °C vs. $HF(g)/H_2,F^-$ after the MSRE.[15,ii]

Li^+/Li	-2.66 V	Cr^{2+}/Cr	-0.45 V
La^{3+}/La	-2.29 V	Fe^{2+}/Fe	-0.08 V
Th^{4+}/Th	-1.87 V	$HF(g)/H_2,F^-$	0 V
Be^+/Be	-1.85 V	Ni^{2+}/Ni	+0.38 V
U^{4+}/U^{3+}	-1.15 V	$F_2(g)/F^-$	+2.87 V

Contemporary MSR designs range from chloride fuel salt systems, fluoride fuel salt systems, and non-salt fuels paired with molten salt coolants. Therefore, to support the deployment of these designs, thermodynamic characteristics, redox behaviors, and resilient structural materials must be well understood for the wide range of matrices that may exist within each of these designs. Nevertheless, there are still many gaps in the

[i] Reprinted from the Journal of Nuclear Materials, 51/1, C.F. Baes, Jr., The chemistry and thermodynamics of molten salt reactor fuels, 157, Copyright (1974), with permission from Elsevier.

[ii] Reprinted from the Journal of Nuclear Materials, 51/1, C.F. Baes, Jr., The chemistry and thermodynamics of molten salt reactor fuels, 159, Copyright (1974), with permission from Elsevier.

literature, and it is important to complete the matrix of thermophysical and thermochemical characteristics of MSR fuels.[5]

1.2.2 Pyroprocessing Applications

Like most of the technology used in civilian nuclear applications, pyroprocessing began during the Manhattan Project while investigating methods for isolating pure plutonium metal through electrolytic reduction in molten salts in 1944.[17] This technique has been applied at institutions like the Argonne National Laboratory (ANL) for on-site fuel recycling at the Integral Fast Reactor (IFR) in the late 1980s,[18] and Los Alamos National Laboratory (LANL) for the pit production process at the Plutonium Facility today.[19,20] Like the fuel cycle process, bulk electrolysis in molten chloride salt is performed in a two-electrode configuration to produce pure plutonium metal from either an oxide or impure metal feedstock. Pure plutonium metal rings are recovered following direct oxide reduction (if needed), separation from americium, and eventually serving as the anode during an electrorefining step, typically paired with pure tungsten cathode.[19,20]

Although reprocessing used nuclear fuel is not currently being pursued in the United States, decades of research have been invested in better understanding how pyroprocessing could be applied to the fuel cycle and extended into potential medical applications for the extraction of ^{99}Mo from MSR fuel.[12,21] For example, fuel from the Experimental Breeder Reactor (EBR-II) is undergoing treatment via pyroprocessing (also referred to as “electrometallurgical treatment”) for final disposition,[22] and it has been considered for online reprocessing at nuclear power plants, like in the case of the Integral

Fast Reactor concept.[23] Common electrode materials evaluated for these applications include, but are not limited to, 316 stainless steel,[8,24,25] plain carbon steel,[22] tungsten,[10,25] and even liquid metals, like cadmium.[8]

1.3 Electroanalytical Chemistry

Unlike bulk electrolysis used in pyroprocessing applications, electroanalytical chemistry hosts a suite of powerful techniques that can produce fundamental values that characterize redox reactions with popular techniques like cyclic voltammetry (CV).[26] Three-electrode cells, like in **Figure 1.2 A)**, can be used for experiments of this nature, which comprises a working electrode (WE) where current is measured during a half-cell reaction of interest, a reference electrode (RE) that serves as the other half-cell reaction and provides a constant reference potential, and a working electrode (CE) to complete the circuit with the WE, all immersed in an electrolyte containing the analyte to be studied. In CV, a potential sweep is applied between two potential values at the WE, and the resulting current profile is measured. The potential waveform (potential vs. time) is shown in **Figure 1.2 B)**, and an example voltammogram (current vs. potential) is in **Figure 1.2 C)**. Peaks in the current indicate oxidation or reduction events occurring at the surface of the WE when one oxidation state of an analyte is brought to the surface of the electrode via mass transport, converted to a different oxidation state depending on the applied potential through an electron transfer process and carried away from the surface into the bulk solution via mass transport.[27]

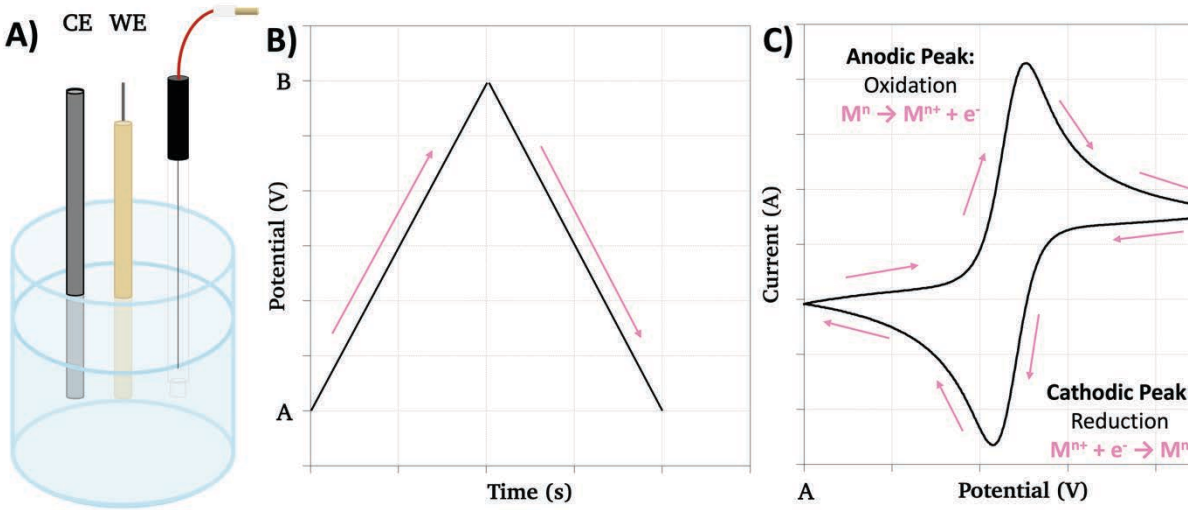

Figure 1.2 A) three-electrode cell with a counter electrode (CE), working electrode (WE), and reference electrode (RE) in the sample solution; B) potential waveform for CV and C) the resulting voltammogram with oxidation (anodic) and reduction (cathodic) peaks.

Cyclic voltammetry can be used to determine formal potentials (E^o), which indicate the potential at which a particular redox reaction occurs, diffusion coefficients (D) that describe the rate of diffusion of a species away from the surface following the redox reaction, heterogeneous electron transfer rate constants (k), which specifies the rate of the redox reaction, and the number of electrons transferred during the reaction, or electron transfer stoichiometry (n). Additionally, a range of thermodynamic information can be extracted if the temperature is varied. These calculations will be described in further detail as they are applied to molten salt electrochemistry measurements in **Chapter 6**.

These sensitive measurements can provide information that allows for elemental and oxidation state analysis based on characteristic potential values for redox reactions. Additionally, material characterization may be performed on electrodes of various compositions when used in well-studied analyte solutions. However, ensuring that the experimental infrastructure comprises resilient, reliable materials that can withstand the

given environment where measurements are performed is necessary. Electrochemical measurements are trivial tasks in simple room temperature, neutral pH, and aqueous environments. When harsh systems are of interest, like molten salts, ensuring that the electrochemical cell construction will provide meaningful results becomes increasingly challenging.

1.3.1 Boron-Doped Diamond Electrodes

1.3.1.1 Chemical Vapor Deposition for Diamond Growth

Polycrystalline diamond is typically grown via microwave plasma chemical vapor deposition (CVD) under high temperature (700-1200 °C) and high pressure (20-150 Torr) conditions onto a substrate material (i.e., ceramics and metals) that has been seeded with diamond nanoparticles in the presence of $H_2(g)$ containing a low concentration of CH_4 (1-5 %).[28,29] The CH_4 molecules are dissociated by the plasma in the CVD reactor, forming diamond (sp^3-hybridized carbon) and non-diamond (sp^2-hybridized carbon) clusters on the substrate surface. Similarly, hydrogen ions are produced from the H_2 interactions with the plasma, which selectively etch sp^2 carbon clusters from the substrate, leaving only diamond carbon to grow in a direction normal to the surface. The final polycrystalline material is then primarily sp^3-hybridized carbon, except at grain boundaries between individual crystals where there is increased disorder during the growth process, resulting in the presence of non-diamond carbon.[28]

Substrates like silicon wafers can be etched or polished, leaving pure diamond films depending on the thickness of the material. This results in two sides with distinct

morphology because the growth mechanism is such that increased thickness produces increased crystal size, given the tapered shape of individual crystals as they grow to hundreds of microns in thickness. The side with large crystals (top) will be referred to as the 'grown' side, and the portion revealed following removal of the substrate (bottom) will be referred to as the 'nucleation' side. This phenomenon is illustrated in part a) of **Figure 1.3** with accompanying example micrographs describing three regions: b) a top-down view of large diamond crystals, c) a top-down view after polishing the material, and d) a top-down view of a thin layer only a few microns in thickness with no discernable crystals.[30,31]

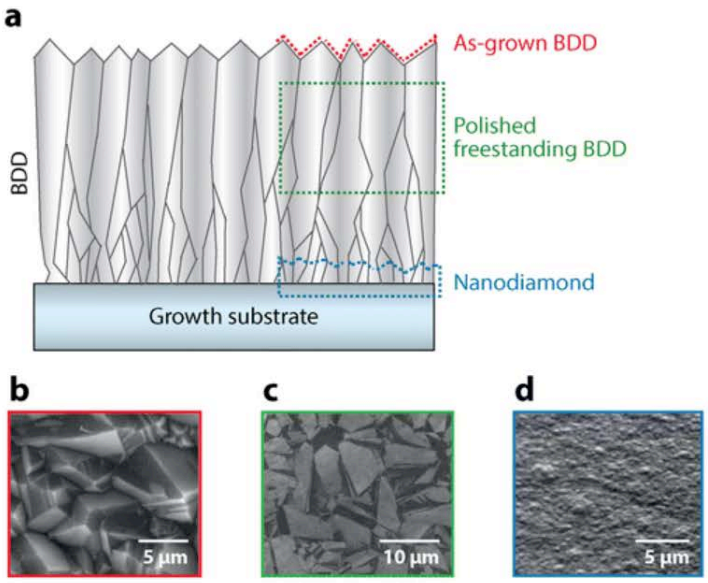

Figure 1.3 a) Schematic of boron-doped diamond grains on a growth substrate, b) rough surface of as-grown crystals, c) polished crystals, and d) nanocrystalline material.[30,31iii,iv]

[iii] Used with permission of Annual Reviews, Inc., from Boron Doped Diamond: A Designer Electrode Material for the Twenty-First Century, Samuel J. Cobb, Zoe J. Ayres, Julie V. Macpherson, 11, 2018; permission conveyed through Copyright Clearance Center, Inc.

[iv] Adapted with permission from P. W. May and Y. A. Mankelevich, "From Ultrananocrystalline Diamond to Single Crystal Diamond Growth in Hot Filament and Microwave Plasma-Enhanced CVD Reactors: a Unified Model for Growth Rates and Grain Sizes," *Journal of Physical Chemistry C,* vol. 112, no. 32, pp. 12432-12441, 2008. Copyright 2008 American Chemical Society.

This process results in a material over 95 % face-centered cubic crystalline diamond with a lattice constant of $a = 3.567$ Å, as shown in **Figure 1.4**.[28] The final product is a resilient, chemically inert material with notable strength, amongst many other positive qualities that indicate its potential applicability to a molten salt system.[32-36] However, pure diamond is an insulator with a large band gap (~5.5 eV) and, therefore, does not constitute a suitable electrode material.[28,36-38]

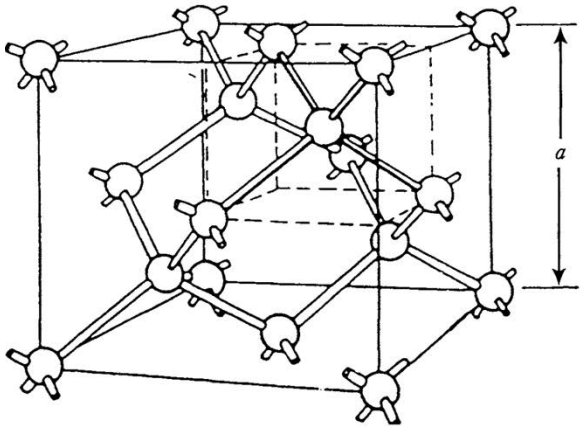

Figure 1.4 Face-centered cubic diamond structure where the dotted portion indicates a crystallographic unit cell containing two carbon atoms.[28,v]

1.3.1.2 Boron-Doped Diamond

By introducing a compound such as B_2H_6 to the source gas (CH_4 and H_2), boron atoms will be substitutionally incorporated into the diamond crystal structure. The presence of boron atoms introduces acceptor levels at 0.37 eV above the valence band maximum, changing the overall polycrystalline material from a non-conductive insulator to a p-type semiconductor suitable for electrode use.[28] However, there is a delicate balance

[v] Used with permission of Elsevier Science & Technology Journals, from Diamond Films: Chemical Vapor Deposition for Oriented and Heteroepitaxial Growth, Koji Kobashi, 2005; permission conveyed through Copyright Clearance Center, Inc.

when introducing a boron dopant, as sufficiently high concentrations (>10^{20} B-atoms/cm^3) can make the material metal-like and potentially promote graphitization during the CVD process.[28,36,39-41] Both factors may weaken the positive attributes of BDD, like the rapid electron transfer kinetics, wide solvent window, low background current, and corrosion resistance,[33,36,42,43] as the material becomes more akin to that of something like glassy carbon (non-diamond carbon). However, in the range of 10^{16}-10^{20} B-atoms/cm^3, the material will present sufficiently p-type semiconductor behavior[36] and has been described as a 'designer electrode material'[30] given its many benefits, like those listed previously. These favorable characteristics of BDD electrodes have expanded their practical applications to span wastewater treatment,[44,45] inorganic trace metal determination,[43,46] neurochemical analyses,[47,48] and measurements in harsh environments.[49-53] It is hypothesized that those benefits will extend to the complex systems of f-block redox couples and in extreme environments, like high-temperature, corrosive molten salts.

1.3.2 Molten Salt Electrochemistry

Electrochemistry is a powerful tool that has been proven beneficial to help characterize redox behavior, corrosion kinetics, and low-level detection of various molten salt systems. Some of the earliest publications regarding molten salt (also known as 'fused salt') electrochemistry came in the early nineteen hundreds before ever being considered by Manhattan Project scientists when metals like thorium were being electrodeposited out of chloride salts.[54,55] The field expanded throughout the 20th century as electroanalytical measurements and infrastructure evolved.[56-60]

Fortunately, the molten salt electrochemistry community continues to grow, and the literature is expanding exponentially to include a range of traditional electrochemical techniques that aim to probe redox couples, including, but not limited to, cyclic voltammetry, polarization, and spectroelectrochemistry.[61-78] Especially in the LiCl-KCl electrolyte, there have been many investigations of f-block elements like europium and uranium using CV on non-diamond carbon electrodes.[77,79-83] Although this arsenal of literature continues to expand, there are still many challenges in performing molten salt electrochemistry, such as the need for robust working electrodes, difficulties with reliable reference electrodes, and ensuring salt purity.

This work proposes BDD as a robust material to a contender as a WE in molten salts, considering it has proven superior to other electrodes in aqueous environments[30,36] and is quite resilient, as described in **1.3.1**. Additionally, while it has been shown that BDD is not entirely resilient in environments with high levels of oxygen at elevated temperatures,[84] successful attempts have been reported for the application of BDD as an inert anode for electrolytic reduction in molten salts even in the presence of oxides.[85-88] However, there is no evidence of BDD used for as a WE electroanalytical measurements in molten salt systems.

1.4 Organization of Dissertation

The research performed in support of this dissertation involved preliminary characterizations of aqueous systems using voltametric and SEC techniques with BDD electrodes. Then, BDD was exposed to molten chloride and fluoride salt environments to

determine its resilience before being applied as a working electrode to study Eu and U redox couples in molten chloride salts. Each chapter outlines the motivation, materials, methods, and instrumentation used in each experiment, followed by results, discussion, and conclusions.

Chapter 2 provides an overview of free-standing BDD working electrodes used to study well-known ($K_3Fe(CN)_6$, $Ru(NH_3)_6Cl_3$) and more challenging ($EuCl_3$, and $UO_2(NO_3)_2$) analytes in aqueous environments. The grown and nucleation sides of the BDD WE were isolated, allowing for comparisons between the electrochemical responses for the two distinct morphologies of the polycrystalline diamond.

Chapter 3 employs a first-of-a-kind free-standing BDD optically transparent WE that can be used for spectroelectrochemistry. Proof-of-concept experiments with aqueous $K_3Fe(CN)_6$ are used to determine redox potential and diffusion coefficients spectroelectrochemically that are easily compared to literature and previous measurements performed in **Chapter 2** using voltammetry.

Chapter 4 is the first of two parts to study BDD's response to prolonged exposure in chloride (NaCl-KCl) and fluoride (FLiNaK) molten salt systems under various conditions. Results from a variety of surface chemistry and material analyses are included for the grown and nucleation sides of each exposed sample, such as SEM, profilometry, Raman spectroscopy, XPS, and ToF-SIMS to determine if there are significant topographical or chemical changes to the BDD.

Chapter 5 is a sequel to **Chapter 4**, where the exposed samples are studied using CVs of the same well-known ($K_3Fe(CN)_6$, $Ru(NH_3)_6Cl_3$) analytes from **Chapter 2** to

determine if the molten salts induced changes to the electrochemical responses to either the grown or nucleation sides of the BDD. The size and thickness of the samples used here are slightly larger than that of **Chapter 4**, so accompanying SEM is included since the morphology of the samples' grown sides will be slightly different.

Chapter 6 uses both free-standing and thin-film BDD Wes to study f-block chloride salts ($EuCl_3$ and Ucl_3) in a LiCl-KCl (55.7-44.3 mol%) electrolyte to determine its performance as an electrode in molten chloride salts. SEM is provided for the BDD used to study europium, given the non-radioactive nature of the salt to which the material was exposed. The challenges and limitations of these experiments are also explored in this chapter.

Finally, **Chapter 7** provides an overall summary of this work with suggestions on areas for future studies. It also explores the possible industrial applications for BDD regarding fundamental studies that benefit a range of molten salt technologies, especially with respect to MSR fuels and *in situ* monitoring.

2 Aqueous Electrochemical Characterization of Free-Standing Boron-Doped Diamond

Abstract

The purpose of this chapter is to perform a preliminary characterization of the two distinct sides of free-standing boron-doped diamond (BDD) using cyclic voltammetry (CV) in aqueous environments before introducing the material to high-temperature molten salts. Two common analytes (ferri/ferrocyanide: $Fe(CN)_6^{3-/4-}$ and hexaammineruthenium: $Ru(NH_3)_6^{3+/2+}$) studied frequently using BDD electrodes are used to evaluate the grown and nucleation sides of the electrode. Since BDD is considered a high-quality working electrode material, it is also used to study two less trivial f-block analytes ($Eu^{3+/2+}$ and UO_2^{2+}/U^{4+}) with more complex redox chemistry.

The differences In response for each side of the BDD are compared using values for formal potential (E^o), diffusion coefficients (D), peak separation (ΔE_p), and electron transfer rate constants (k). Values calculated for $Fe(CN)_6^{3-/4-}$ and $Ru(NH_3)_6^{3+/2+}$ align with previous reports, and minimal differences were found between the two sides of the BDD. These cases use common methods (i.e., Randles-Sevcik equation) to determine the previously mentioned values given their relative reversibility. However, the lanthanide and actinide species exhibited quasi-reversibility and required a different approach to evaluate the diffusion and electron transfer processes for the oxidation and reduction reactions.

In these cases, values are in the expected range based on the literature available for systems as close as possible to what is used for the Eu and U studies. In each case, there were slight to moderate differences in the responses for each side of the BDD, likely due

to the crystal structures. The grown side has large crystals, while the nucleation side presents non-diamond carbon (NDC) morphology that will affect the conductivity and chemistry of the surfaces based on ratios of sp^3- to sp^2-hybridized carbon. These results present a variety of considerations that will be important as the chapters in this document progress toward the ultimate application of BDD as an electrode in high-temperature molten salts.

2.1 Introduction

Boron-doped diamond has a strong reputation as a high-quality electrode with features like wide solvent windows, low background capacitance, rapid electron transfer kinetics, and resistance to fouling compared to metal and other carbon electrodes when performing measurements like cyclic voltammetry (CV).[33,36,42,43] However, the majority of BDD working electrode designs are either thin films on a substrate, or if free-standing, the material typically has small crystal grain boundaries, is polished to a smooth surface on both sides, or is isolated to a small, single-sided surface for disc electrode designs.[36,43,89-94] However, a portion of the experiments performed in this manuscript (**Chapter 6**) employ polycrystalline material hundreds of microns in thickness where one side (grown) has crystals of about 50 – 100 μm across, which is hypothesized to be resilient in molten salt systems. Additionally, those electrodes also have a side with sub-micron grain boundaries (nucleation) that will also be exposed to the high-temperature molten salts. This variation in surface structure will affect the electrochemical response given the increased presence of highly conductive sp^2-hybridized carbon compared to the grown side (see **Figure 1.3**).

Therefore, this work uses well-known aqueous analytes (ferri/ferrocyanide: $Fe(CN)_6^{3-/4-}$ and hexaammineruthenium: $Ru(NH_3)_6^{3-/2-}$) to characterize the two distinct sides of the BDD before introducing the material to molten salt systems. It will also provide insight into the possible differences in electrochemical responses due to the significantly different morphologies of the polycrystalline surfaces. Given the wealth of literature for $Fe(CN)_6^{3-/4-}$ and $Ru(NH_3)_6^{3+/2+}$ on BDD,[89,91,95,96] the results for each side will be easily classified for relative electrode quality by comparing values like formal potential (E^o), peak separation (ΔE_p), diffusion coefficients (D), and the heterogeneous electron transfer coefficient (k).

Additionally, it is notoriously difficult to study f-block oxidation states in aqueous media, so BDD is also used to probe the $Eu^{3+/2+}$ and $U^{6+/4+}$ (as the uranyl ion) redox couples, because of its superior qualities as a working electrode.[30] There are very few published studies of these systems using techniques like cyclic voltammetry in aqueous systems and even less using BDD.[97-100] These experiments also provide a baseline for comparison as Eu and U electrochemical behavior will later be studied with BDD in molten salt systems. Again, the grown and nucleation sides of the BDD will be applied to determine if there is a preferable morphology for studying these analytes in water-based electrolytes.

2.2 Methods and Materials

Free-standing BDD (10 × 10 × 0.6 mm) from ElementSix was initially imaged with a Thermo Fisher Scientific ApreoS LoVac Scanning Electron Microscope (SEM). Before

each analyte was studied, the BDD was anodically pre-treated by scanning the potential from +2.4 to -2.8 V vs. Ag/AgCl for 50 cycles in 1 M H_2SO_4 at 100 mV/s.[101-104] After the pre-treatment, each side of the BDD (grown and nucleation) was isolated using a plate material evaluating cell from BioLogic, LLC (1 mL solution volume, exposed surface area = 0.57 cm^2), shown in **Figure 2.1**. Electrical contact was established by placing copper foil below the BDD working electrode (WE) while assembling the cell. Electrochemical measurements for Fe, Ru, and U were taken on a BASi PalmSens potentiostat, and a Metrohm AutoLab potentiostat was used for Eu measurements. Silver-silver chloride (Ag/AgCl, 3.5 M) reference electrodes (RE) used were from BASi. In the case of the anodic pre-treatment and uranyl nitrate voltammetry, double junctions filled with 1 M H_2SO_4 and HNO_3, respectively, were used. A Pt wire (d = 1 mm, 99.95% purity) from Strem Chemicals was used as the counter electrode (CE), except for the anodic pre-treatment, where a graphite rod was used as a consumable material.

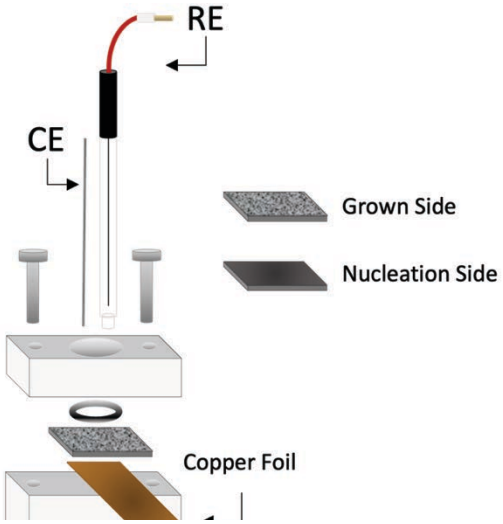

Figure 2.1 Electrochemical cell used to isolate each side of the BDD. CE: Pt wire; RE: Ag/AgCl (3.5 M KCl).

All salts and the non-uranium analytes were reagent grade from Acros Organics, and ultra-pure water (18.2 MΩ-cm) was used for all solutions using a D2798 Barnstead water purification system. The uranyl nitrate solution was prepared by dissolving solid, hydrated $UO_2(NO_3)_2$ crystals from existing inventory in 1 M HNO_3 with vigorous mixing for 10 – 15 min. Given the age of the crystals (prepared circa 2012), the exact hydrate stoichiometry is unknown; however, a final concentration of 11.3 mM [UO_2^{2+}] for the solution used here was determined with inductively coupled plasma optical emission spectroscopy (ICP-AES, $R^2 = 1$) using a PerkinElmer Optima 8000.

2.3 Scanning Electron Microscopy

The grown and nucleation sides of the BDD WE material were first analyzed using scanning electron microscopy (SEM) to visualize the distinctly different crystal structures. **Figure 2.2 A)** shows the grown side of the material with exceptionally large crystals, up to 100+ μm across, while **B)** uses twice the magnification, but grain boundaries are still not visible for the nucleation side. Increasing the magnification further in **Figure 2.2 C)** still does not present any clear grain boundaries, further emphasizing the stark contrast between the grown and nucleation sides of the BDD due to the chemical vapor deposition (CVD) growth process. Even compared to literature of large BDD crystals (up to 50 μm across), the morphology of the material in **Figure 2.2 A)** is still much greater in size than what is typically published.[105] The 'grown' side of BDD is often about 5 μm crystals.[31,43,106] The nucleation side resembles the 'nanocrystalline' diamond (NCD) previously reported for thin BDD films.[31]

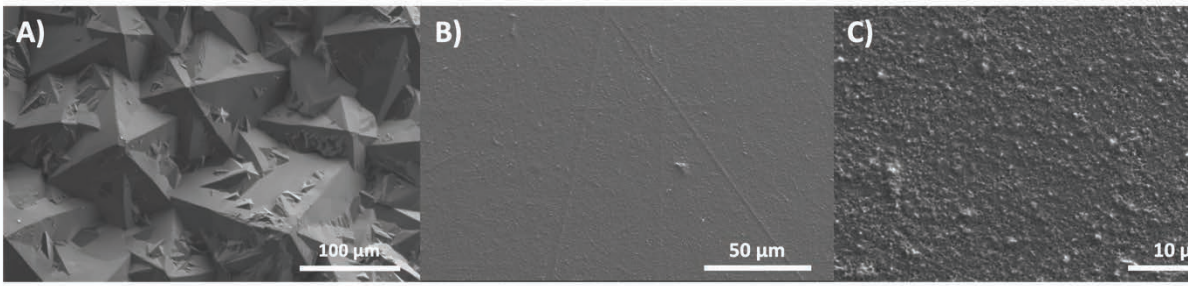

aried magnifications.

2.4 Cyclic Voltammetry

Scan rate studies were performed on the grown and nucleation sides of free-standing BDD for two well-studied transition metal complexes ($Fe(CN)_6^{3-/4-}$ and $Ru(NH_3)_6^{3+/2+}$) and two f-block species ($Eu^{3+/2+}$ and $U^{6+/4+}$). Values for formal potential (E^o), peak separation (ΔE_p), diffusion coefficients (D), and electron transfer rate constant (k) were compared for each side of the BDD and literature available for comparable systems.

2.4.1 Transition Metal Redox Chemistry

The $Fe(CN)_6^{3-/4-}$ (Eq. 1) and $Ru(NH_3)_6^{3+/2+}$ (Eq. 2) redox couples are common standards in aqueous electroanalytical chemistry, especially for characterizing and comparing electrode designs.

$$Fe(CN)_6^{3-} + e^- \rightleftharpoons Fe(CN)_6^{4-} \quad \textbf{(1)}$$

$$Ru(NH_3)_6^{3+} + e^- \rightleftharpoons Ru(NH_3)_6^{2+} \quad \textbf{(2)}$$

These two analytes have previously been applied to BDD electrodes of various compositions, morphologies, and configurations.[89,91,95,96] Because the grown side has unique crystal structures compared to much of the available literature, there is minimal evidence available to make a direct comparison. This is unlike the nucleation side, which is like most BDD electrodes described previously.

Scan rate studies (10, 25, 50, 75, 100 mV/s) were performed over three trials on each side of the BDD for the different metal ions, where each scan rate (υ) was cycled three times. The average values for E_p and i_p were used to produce the calculated values reported below. Voltammograms for the 50 mV/s scan rate are shown in **Figure 2.3** for the grown (pink) and nucleation (purple) sides of the material for **A)** $Fe(CN)_6^{3-/4-}$ and **B)** $Ru(NH_3)_6^{3+/2+}$ in 1 M KCl vs. Ag/AgCl. For both analytes, the grown and nucleation sides vary slightly in their response. However, for $Fe(CN)_6^{3-/4-}$, the nucleation side shows slightly larger peak currents and enhanced peak resolution compared to the grown side. The difference between the two sides for $Ru(NH_3)_6^{3+/2+}$ is less significant, but the grown side exhibits a slightly increased peak current compared to the nucleation side.

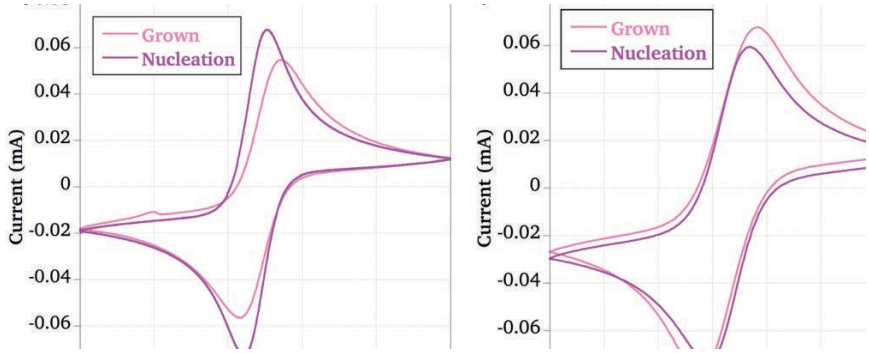

Figure 2.3 Overlays of 50 mV/s scans for 1 mM A) $Fe(CN)_6^{3-/4-}$ and B) $Ru(NH_3)_6^{3+/2+}$ in 1 M KCl on the grown (pink) and nucleation (purple) sides of free-standing BDD. RE: Ag/AgCl; CE: Pt wire.

The formal potential (E^o) can be calculated by taking the average value between the anodic ($E_{p,a}$) and cathodic ($E_{p,c}$) peak potentials using Eq. 3:

$$E^o = \frac{|E_{p,a} - E_{p,c}|}{2} \quad \textbf{(3)}$$

The formal potentials determined for $Fe(CN)_6^{3-/4-}$ differ slightly for the grown and nucleation sides but do not change for $Ru(NH_3)_6^{3+/2+}$. However, all values fall within expected ranges vs. Ag/AgCl.[91,95,107,108]

Table 2.1 Figures of merit determined for $Fe(CN)_6^{3-/4-}$ and $Ru(NH_3)_6^{3+/2+}$ in 1 M KCl using the grown and nucleation sides of free-standing BDD. *For 50 mV/s scan rate.

Analyte	BDD Side	E^o (V)	$D \times 10^{-6}$ (cm^2/s)	ΔE_p* (V)	k* $\times 10^{-3}$ (cm/s)
$Fe(CN)_6^{3-/4-}$	Grown	+0.288 ±0.0002	1.7 ±0.09	0.106 ±0.0004	1.6
	Nucleation	+0.273 ±0.0001	3.8 ±0.07	0.068 ±0.0001	17
$Ru(NH_3)_6^{3+/2+}$	Grown	-0.170 ±0.0005	3.8 ±0.1	0.095 ±0.003	2.9
	Nucleation	-0.170 ±0.0004	3.8 ±0.06	0.069 ±0.001	13

In the case of redox reactions with good reversibility, like those presented in **Figure 2.3**, the Randles-Sevcik equation for room temperature measurements (Eq. 4) can be used to determine D for the reduced or oxidized species after performing a scan rate study.

$$i_{p,a/c} = 2.69 \times 10^5 AC\sqrt{n^3 D_{R/O} v} \quad \textbf{(4)}$$

By plotting the square root of the scan rates ($\sqrt{v}$) against the anodic and cathodic peak current values ($i_{p,a/c}$), the regression slope can be used to calculate $D_{R/O}$, where D_O describes the diffusion of the oxidized species toward the electrode surface for the cathodic reaction and D_R is for the diffusion of the reduced species toward the electrode surface for the anodic reaction. Additionally, A is the surface area of the electrode, C is the concentration, and n is the electron transfer stoichiometry. In cases where reversibility is good, D should be the same for both anodic and cathodic reactions, which is the case for both $Fe(CN)_6^{3-/4-}$ and $Ru(NH_3)_6^{3+/2+}$, as shown in **Table 2.1** where $D_O = D_R$ on the grown and nucleation sides of the BDD for both analytes. However, D for the grown side when studying $Fe(CN)_6^{3-/4-}$ is slightly smaller than that for the nucleation side, and both $Ru(NH_3)_6^{3+/2+}$ studies (grown: $D = 1.7 \times 10^{-6}$ cm^2/s and nucleation: $D = 3.8 \times 10^{-6}$ cm^2/s). In all four cases (grown and nucleation for each analyte), R^2 is greater than or equal to 0.99, indicating diffusion-controlled processes, as expected.[109] These values also fall within the expected range for BDD electrodes.[91,95,107,108]

The electron transfer kinetics can be described using a method outlined by Nicholson[110] that takes the reversibility of the reaction and separation of the anodic and cathodic peaks into consideration using Eq. 5:

$$\psi = \frac{k\left(\frac{D_O}{D_R}\right)^{\frac{\alpha}{2}}}{\sqrt{\left(\frac{\pi D_O v n F}{RT}\right)}} \quad \textbf{(5)}$$

The peak separations (ΔE_p) can be used to estimate a value for ψ for each scan rate using the Nicholson method,[110] where F is Faraday's constant (96,485 A·s/mol), R is the gas constant (8.314 J/mol·K), and T is the solution temperature (298 K). Because the values for ΔE_p increase with the scan rate for $Fe(CN)_6^{3-/4-}$, it is technically a quasi-reversible system. However, it is standard to assume a reversible system with respect to the charge transfer coefficient ($\alpha = 0.5$) to determine k after calculating the values for D_O and D_R (all other terms have their usual meaning).

The values for ΔE_p and k at 50 mV/s are listed in **Table 2.1** for the grown and nucleation sides of BDD for $Fe(CN)_6^{3-/4-}$ and $Ru(NH_3)_6^{3+/2+}$. Unlike the calculated values for D, k varies significantly between the grown and nucleation sides of the BDD for both analytes. In each case, the nucleation side (10^{-2} cm/s) produced larger values for k (10^{-2} cm/s) compared to the grown side (10^{-3} cm/s). Similarly, the values for ΔE_p are smaller by 30 – 40 mV for the nucleation sides compared to the grown sides (106 vs. 68 mV for $Fe(CN)_6^{3-/4-}$ and 95 vs. 69 mV for $Ru(NH_3)_6^{3+/2+}$). Therefore, the NDC structure on the nucleation side of the BDD may have slightly better kinetics than the grown side, likely due to the increased conductivity due to the increased presence of conductive sp^2-hybridized carbon. This result confirms the initial hypothesis regarding the difference between the electrochemical response for each side. The results for both sides align with the range of values available in the literature published for small-grain BDD electrodes.[91,95,107,108,111]

2.4.2 f-Block Redox Chemistry

Lanthanide and actinide elements have large, complex electron structures that can complicate simple methods like CV (i.e., disproportionation).[112] For this reason, a different approach is required to process the results for Eu and U as analytes that fall strictly in the quasi-reversible category. Furthermore, the responses for Eu and U differ on each side of the BDD, all of which are discussed in detail in the following sections.

2.4.2.1 Europium(III) Chloride

Although most lanthanides (Ln) only exhibit the Ln^{3+} oxidation state, europium can also exist as Eu^{2+} when it loses both electrons in the 6s shell, leaving a stable half-filled 4f shell with seven remaining electrons. This stability is a unique feature compared to the Ln elements that typically only participate in three-electron reactions (III/0), except in cases like Ce, which can exhibit a (IV) oxidation state, making Eu a commonly studied electrochemical analyte for rare earth applications or as a non-radioactive surrogate for actinide (An) elements. The one-electron transfer for Eu^{3+} to Eu^{2+} is illustrated in Eq. 6:

$$Eu^{3+} + e^{-} \rightleftharpoons Eu^{2+} \quad \textbf{(6)}$$

Very few nitrate-based aqueous systems are reported in literature where Eu has been studied with voltametric techniques.[97] However, there is some published evidence that experiments were successfully performed in aqueous electrolytes to probe Eu

electrochemistry on glassy carbon,[97] and even an example of a 'conductive diamond' working electrode (thin-film BDD) that was used to study Eu and Ce.[98,99]

Like measurements in the previous section, three scan rate study trials (10, 25, 50, 75, 100 mV/s) were performed on each side of the BDD, where each scan rate was cycled three times. Again, the average values for E_p and i_p were used to perform the calculated values reported below. Voltammograms of $Eu^{3+/2+}$ in 1 M KCl for the 50 mV/s scan rate are overlain in **Figure 2.4** for the grown (pink) and nucleation (purple) sides of the material. The redox chemistry of Eu is considered quasi-reversible to a much greater degree than what is seen for $Fe(CN)_6^{3-/4-}$, which is evident in the asymmetry of the anodic and cathodic peaks. Unlike the previous measurements, the oxidation and reduction processes do not appear to behave similarly when comparing the shape of the well-resolved oxidation peaks to the reduction peaks that begin to fall within the hydrogen-gas evolution at the negative end of the solvent potential window. This behavior is observed on both sides of the BDD.

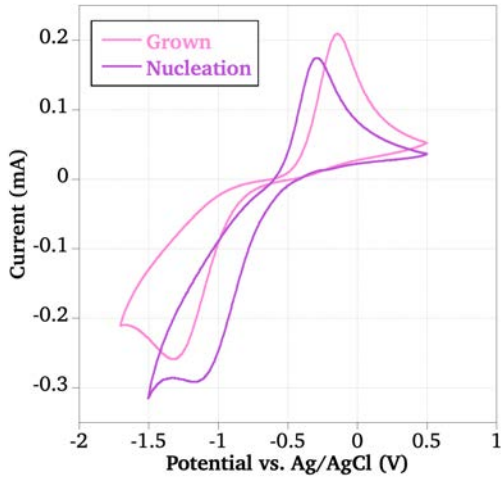

Figure 2.4 Overlays of 50 mV/s scans for 10 mM $Eu^{3+/2+}$ in 1 M KCl on the grown (pink) and nucleation (purple) sides of free-standing BDD. RE: Ag/AgCl; CE: Pt wire.

Values for E^o were calculated using Eq. 3 and are reported in **Table 2.2**. The results for each side of the BDD (grown: E^o = -0.709 V and nucleation: E^o = -0.676 V vs. Ag/AgCl) both fall within the expected range.[97,98] The slight positive shift for the nucleation side may result from the difference in kinetics seen in **Figure 2.4** compared to the grown side, likely due to the different morphologies and surface chemistry of the material.

Table 2.2 Figures of merit determined for $Eu^{3+/2+}$ in 1 M KCl using the grown and nucleation sides of free-standing BDD. *For 50 mV/s scan rate.

BDD Side	E^o (V)	$D_O \times 10^{-7}$ (cm^2/s)	$D_R \times 10^{-7}$ (cm^2/s)	ΔE_p* (V)	k* $\times 10^{-4}$ (cm/s)
Grown	-0.709 ±0.001	6.0 ±0.8	8.7 ±0.4	1.122 ±0.001	1.1
Nucleation	-0.676 ±0.004	4.6 ±0.8	3.0 ±0.2	0.767 ±0.001	1.2

The Randles-Sevcik equation (Eq. 4) used in the previous section is intended for the calculation of D for reversible (or minimally quasi-reversible) reactions. Therefore, the Berzins-Delahay equation for quasi- and irreversible redox reactions (Eq. 7) can instead be used to calculate diffusion coefficients for f-block systems like the $Eu^{3+/2+}$ couple.[67,113-115]

$$i_{p,a/c} = 0.496nFAC\sqrt{\frac{D_{R/O}(\alpha n_\alpha)Fv}{RT}} \quad (7)$$

Unlike the previous measurements, determining D first requires a calculation of the charge transfer coefficient as a function of the electron stoichiometry of the rate-limiting step, αn_α. This value was determined using Eq. 8,[67,113-115] where $E_{\frac{p}{2}}$ is the half-peak potential, which is the potential where the peak current is at half value and was collected for the anodic and cathodic peaks at each scan rate.

$$\alpha n_\alpha = \frac{1.857RT}{\left|E_p - E_{\frac{p}{2}}\right| F} \quad \textbf{(8)}$$

Like in the previous section, the anodic and cathodic reactions can be characterized by plotting i_p vs. $\sqrt{v}$ and using the slopes to determine values for D_O and D_R. The two values used for αn_α were determined by averaging the individual calculations for each scan rate for the anodic (grown: $\alpha n_\alpha = 0.323$ and nucleation: $\alpha n_\alpha = 0.422$) and cathodic (grown: $\alpha n_\alpha = 0.144$ and nucleation: $\alpha n_\alpha = 0.121$) peaks. A similar study of Eu^{3+} in IL applied this method but used only the value determined for the slowest scan rate (10 mV/s) when studying the cathodic reaction.[114] However, that value alone does not consider the changing value for αn_α at each scan rate, although the regression used to calculate D incorporates the entire range. Adjusting the value to only the slowest scan rate had a minimal impact on the final calculations (still 10^{-7} cm^2/s) provided in **Table 2.2**, so it was determined that an average over the scan rates would be an appropriate choice.

During the oxidation reaction, the diffusion of the reduced species toward the surface of the electrode was found to be similar for the grown ($D_R = 3.4 \times 10^{-7}$, $R^2 = 0.9955$) and nucleation sides ($D_R = 1.5 \times 10^{-7}$ cm^2/s, $R^2 = 0.9991$). There is literature on experiments performed in IL that corroborate these values.[115] However, for the reduction reaction, the diffusion of the oxidized species toward the surface of the electrode was found to be slightly faster for the grown side ($D_O = 1.2 \times 10^{-8}$, $R^2 = 0.9880$) compared to the nucleation side ($D_O = 6.7 \times 10^{-9}$ cm^2/s, $R^2 = 0.9809$). The grown side result of D_O

aligns with previously reported values.[114] The difference between diffusion behavior for each reaction ($D_R > D_O$) aligns with the shape of the voltammograms shown in **Figure 2.4**. All cases for the Eu couple have slower diffusion behavior compared to $Fe(CN)_6^{3-/4-}$ and $Ru(NH_3)_6^{3+/2+}$ (10^{-6} cm^2/s),[114,115] potentially as a result of the f-block valency that can be more complicated than the d-block transition metals like Fe and Ru. Regardless of the differing values, the overall linearity in each case ($R^2 > 0.9$) confirms a diffusion-controlled process for both oxidation and reduction on both sides of the material.[109]

These results also call for a different approach for determining the electron transfer rate constant. The Nicholson method can only be used for peak separations between 0.061 V and 0.212 V when approximating ψ,[110] and the separations for the grown and nucleation sides in this experiment are both too large (grown: $\Delta E_p = 1.122$ V and nucleation: $\Delta E_p = 0.767$ V for 50 mV/s). Instead, the Klingler-Kochi equation (Eq. 9) can be utilized since it does not impose any limitations to features of the voltammograms:[108,114-116]

$$k = 2.18\sqrt{D_O(\alpha n_\alpha)\frac{\nu F}{RT}} \cdot e^{\{\frac{\alpha^2 nF}{RT}(E_{p,c}-E_{p,a})\}} \quad \textbf{(9)}$$

The charge transfer coefficients (grown: $\alpha = 0.233$ and nucleation: $\alpha = 0.272$) used in these calculations were determined by averaging the anodic and cathodic values for the combined charge transfer coefficient and electron stoichiometry of the rate-limiting step value, αn_α, on each side of the BDD and dividing by the electron stoichiometry (1 e^-).

The values determined for the grown ($k = 1.1 \times 10^{-4}$ cm/s) and nucleation ($k = 1.2 \times 10^{-4}$ cm/s) sides of the BDD at 50 mV/s is at least an order of magnitude slower than

what was calculated for $Fe(CN)_6^{3-/4-}$ and $Ru(NH_3)_6^{3+/2+}$ (10^{-2} and 10^{-3} cm^2/s), but more than an order of magnitude faster than what has been previously reported for $Eu^{3+/2+}$ in IL (~4×10^{-5} cm/s at 100 °C),[114] and two orders of magnitude faster than what has been reported in perchloric acid systems on BDD (2.7×10^{-6} cm/s).[98] However, the method used to determine the latter value is not well-described, so a recalculation of that published data using the above process may improve their value.

2.4.2.2 Uranyl Nitrate

Favorable electron configurations make the U^{4+} and U^{6+} oxidation states particularly stable. For U^{6+}, the species reaches noble gas configuration ([Rn]), while for $U^{4+,}$ the unpaired electrons in the 6d (1 e^-) and 5f (3 e^-) shells are emptied, leaving the configuration as [Rn]$7s^2$ with no partially filled shells. However, U^{5+} is unstable in aqueous environments as it is much less favorable than the configurations for U^{4+} and U^{6+} and will immediately disproportionate.[117] Therefore, when performing voltametric techniques in water-containing systems, it is expected that a two-electron transfer reaction will occur. The redox reaction for the uranyl nitrate ion is illustrated below in Eq. 10:[118,119]

$$UO_2^{2+}(aq) + 4H^+(aq) + 2e^- \rightleftharpoons U^{4+}(aq) + 2H_2O\ (l) \qquad \textbf{(10)}$$

However, in the presence of nitric acid, the coordination complexes of uranyl vary based on the oxidation state of U and the concentration of nitric acid, making the redox reaction far more complex than the analytes discussed earlier in this chapter.[120,121] An

additional consideration is the possible production of solid UO_2 from the reduction of UO_2^{2+}. Fortunately, the Pourbaix diagram shown in **Figure 2.5** indicates that the 1 M HNO_3 electrolyte used for these measurements is expected to have sufficient acidity (pH = 0) such that the U^{4+} species is soluble, as opposed to inducing the precipitation of solid UO_2.[122] Additionally, no visible deposits of UO_2 were observed on the electrode following experiments.

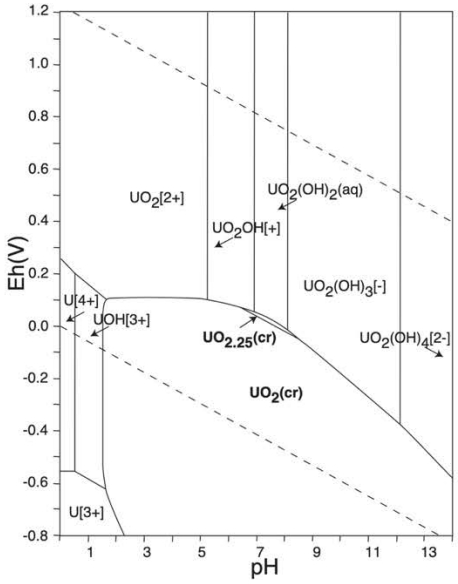

Figure 2.5 Eh-pH diagram for the system U-O-H (2). ΣU = 10^{-10}, 298.15K, 10^5 Pa.[123]

Like the previous measurements, scan rate studies were performed on each side of the BDD, except in this case, 25, 50, 75, 100, and 125 mV/s were used because 10 mV/s did not produce meaningful results considering no peaks were detected. However, the selected range successfully executed the full studies on the grown and nucleation sides required to determine *D* and *k*, and the suite of values for the BDD characterization was successfully calculated. The 50 mV/s overlays in **Figure 2.6** show similarities to the $Eu^{3+/2+}$

voltammograms in **Figure 2.4**, except in this case, the grown side has greater peak heights and peak resolution for both the oxidation and reduction reactions.

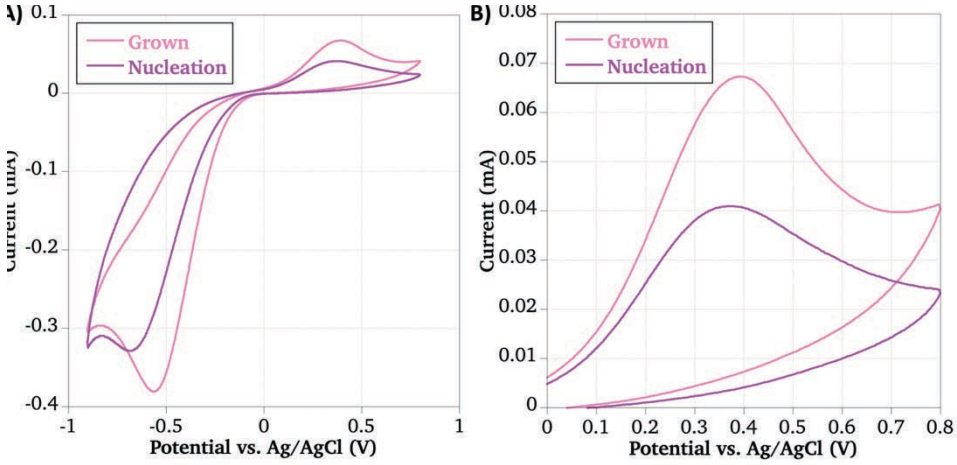

Figure 2.6 C) and nucleation (p e.

Listed in **Table 2.3** the values determined for E^o of $U^{6+/4+}$ are not equal for the grown (E^o = -0.075 V vs. Ag/AgCl) and nucleation sides (E^o = -0.139 V vs. Ag/AgCl). In contrast to the Eu results, the response on the grown side is shifted in a positive direction compared to the nucleation side. However, the discrepancy is also likely related to the kinetics of the electron transfer processes, which are still generally more resolved for the anodic than cathodic reaction (seen in **Figure 2.6**). Again, due to the complex coordination that varies between oxidation states of U in nitric acid in addition to the disproportionation of the intermediate U^{5+}, the process to transfer electrons during a voltametric measurement is nontrivial.[117,120] Additionally, the variation in reported values for E^o in aqueous environments encompasses both calculated potentials, but the literature favors the result for the nucleation side.[120]

Table 2.3 Figures of merit determined for $U^{6+/4+}$ in 1 M HNO_3 using the grown and nucleation sides of free-standing BDD. *For 50 mV/s scan rate.

BDD Side	E^o (V)	$D_O \times 10^{-8}$ (cm^2/s)	$D_R \times 10^{-8}$ (cm^2/s)	ΔE_p* (V)	$k^* \times 10^{-4}$ (cm/s)
Grown	-0.075 ±0.002	5.4 ±0.9	4.4 ±0.3	0.933 ±0.01	6.0
Nucleation	-0.139 ±0.005	7.2 ±0.8	1.4 ±0.2	0.976 ±0.002	3.9

Like for the Eu measurements, the Berzins-Delahay equation (Eq. 7) applies to this system as well, given the quasi-reversible nature of the reaction. Limited literature is available to directly compare electroanalytical figures of merit for the uranyl ion in nitrate-containing aqueous environments,[120,124] but this equation has been applied for U measurements previously.[67,113,125] The two values used for αn_α were, again, determined by averaging the individual calculations for each scan rate for the anodic (grown: αn_α = 0.245 and nucleation: αn_α = 0.285) and cathodic (grown: αn_α = 0.201 and nucleation: αn_α = 0.221) peaks. For the anodic reaction, the diffusion of the oxidized species to the surface of the electrode was found to be remarkably similar between the grown (D_R = 4.4 × 10^{-8} cm^2/s, R^2 = 0.9956) and nucleation (D_R = 1.4 × 10^{-8} cm^2/s, R^2 = 0.9907) sides. This pattern was also observed for the cathodic reaction, but the linearity of the grown side (D_O = 5.4 × 10^{-8} cm^2/s, R^2 = 0.9492) is slightly less than that of the nucleation (D_O = 2.6 × 10^{-8} cm^2/s, R^2 = 0.9831) side. Because all correlation coefficients are greater than 0.9, they can be considered diffusion-controlled processes.[109] The diffusion behavior in the present study is compared to comparable literature in **Table 2.4**. These values reported here for BDD are faster than previous measurements of $U^{6+/4+}$ chemistry in IL using a non-diamond carbon electrode,[125] but two orders of magnitude slower than what has been reported for low concentrations of HNO_3 (0.04 M or 0.05 M) on Pt.[120,126] This differs from what was found for the $Eu^{3+/2+}$ redox couple which was faster using both the grown and

nucleation sides of BDD in the present study compared to values found in the literature for IL and acidic electrolytes. In the case of measurements in IL, their value of *D* increased with temperature,[125] so it can be inferred that if the temperature were lower, the diffusion would have been slower.

Table 2.4 Diffusion coefficients of U(VI) published in literature compared to the present study.

$D_O \times 10^{-8}$ (cm^2/s)	Working Electrode	Electrolyte	T (K)	Reference
0.664	Glassy Carbon	1-Butyl-3-methylimidazolium	343	125
219	Pt	0.05 M HNO_3	298	120
330	Pt	0.04 M HNO	295	126
4.4	Free-Standing BDD – Grown Side	1 M HNO_3	298	This work
1.4	Free-Standing BDD – Nucleation Side	1 M HNO_3	298	This work

The rate constants for the grown and nucleation sides were calculated using Eq. 9 following the evaluation of diffusion behavior. The charge transfer coefficients (grown: $\alpha = 0.112$ and nucleation: $\alpha = 0.126$) used in these calculations were determined by averaging the anodic and cathodic values for the combined charge transfer coefficient and electron stoichiometry of the rate-limiting step value, αn_α, on each side of the BDD and dividing by the electron stoichiometry (2 e^-). The values determined for the grown ($k = 1.6 \times 10^{-4}$ cm/s) and nucleation ($k = 6.3 \times 10^{-5}$ cm/s) sides of the BDD at 50 mV/s differ by approximately an order of magnitude, where the grown side most closely aligns with the chemistry of Eu discussed in the previous section (10^{-4} cm^2/s) and what has been reported for $U^{6+/4+}$ in literature.[120]

2.5 Conclusions

The work presented in this chapter aims to provide a base understanding of how the morphology of BDD surfaces affects the electrochemical response when used as a working electrode. The grown and nucleation sides were compared for two analytes widely published in the literature on various forms of BDD, $Fe(CN)_6^{3-/4-}$ and $Ru(NH_3)_6^{3+/2+}$. After performing scan rate studies with CV, the values for E^o, D, $\Delta E_{p,}$ and k in each case were comparable to previous reports, but there were slight differences between the two sides. For both analytes, the kinetics were marginally faster on the nucleation side, as seen in the 50 mV/s overlays and confirmed by the values calculated for ΔE_p and k. $Ru(NH_3)_6^{3+/2+}$ is considered a reversible redox couple, and although $Fe(CN)_6^{3-/4-}$ is officially considered quasi-reversible, the electron transfer process is reversible enough that the charge transfer coefficient, α, was assumed to be 0.5 for both analytes. This decision allowed each system to be evaluated using the method outlined by Nicholson to characterize electron transfer kinetics[110] and the Randles-Sevcik equation for diffusion reactions.[109]

Because BDD is considered a high-quality electrode material, it was also used to study two more complicated redox couples: $Eu^{3+/2+}$ and UO_2^{2+}/U^{4+}. Again, the responses on the grown and nucleation sides of the material were compared using CV scan rate studies. However, in both cases, the resulting voltammograms indicate quasi-reversible behavior where the reduction peaks are less resolved and asymmetrical than the oxidation peaks for both analytes on both sides of the BDD. Additionally, the ΔE_p at each scan rate in all four cases is too wide to use the Nicholson method to determine k,[110] so a different approach was taken. First, the value for α was calculated and applied to the Berzins-

Delahay equation for quasi-reversible or irreversible reactions. The resulting values for α and D were then used in the Klingler-Kochi equation for electron transfer kinetics,[116] appropriate for quasi-reversible systems.

Most literature containing CVs of Eu and U employs the quasi-reversible method to determine D and k, but often for non-aqueous systems, given the impact of oxidizing environments on the stability of f-block oxidation states. Values for Eu and U are aligned with what aqueous and non-aqueous measurements are available, except in the case of calculating k on the grown side of the BDD for UO_2^{2+} reduction. Instead, the grown side aligns with the kinetics seen when studying Eu and previously published reports of U^{6+} reduction. While this may be an attribute of the NDC nature of the nucleation side, it is not immediately apparent as to why, in this case, it does not perform as well as the grown side. Further investigations should be conducted to probe the nuances of uranyl chemistry for BDD electrodes.

However, the differences between electrode materials and their corresponding behavior at diffusion layers have been discussed at length. Especially comparing n-type (e.g., nitrogen-doped diamond with an extra valence electron compared to carbon) to p-type (e.g., boron-doped diamond with one less valence electron compared to carbon) semiconductor electrodes, materials like BDD typically perform better for anodic reactions; in contrast, n-type materials are more suitable for cathodic mechanisms.[127] Future studies could include using n-type electrodes, like nitrogen-doped diamond, under the same conditions to study these f-block redox couples to determine if they perform better during the cathodic reactions than BDD.

Overall, the results of this study indicate there may be slight differences in the electrochemical response based on the crystal structure of BDD. Techniques like chronoamperometry and impedance spectroscopy could further investigate the differences between the grown and nucleation sides of BDD for various analytes, including f-block redox couples. While the differences observed in the present study are minor under these circumstances, they introduce new considerations for applications in molten salts to study f-block systems. Additionally, a more extensive collection of literature is available for studying Eu and U electrochemically in molten salt systems that will provide more direct comparisons to the results discussed in **Chapter 6**.

3 Aqueous Spectroelectrochemical Measurements with Free-Standing Optically Transparent Boron-Doped Diamond

Abstract

This chapter introduces a novel design for an optically transparent (OTE), free-standing, boron-doped diamond electrode (BDD) for spectroelectrochemical (SEC) applications. Given the known strength of free-standing BDD in harsh environments and the flexibility afforded by SEC techniques to investigate redox chemistry, this design could expand the application of SEC.

Preliminary characterization of the BDD OTE is described using secondary ion mass spectroscopy (SIMS) to determine the boron concentration followed by imagining with scanning electron microscopy (SEM) to investigate the structure and topography of the material after laser-drilled holes were created to produce the grid structure which allows light to pass. Additionally, cyclic voltammetry (CV) results are shown for the grid electrode (G-BDD) and a non-grid electrode (NG-BDD) to determine if the presence of non-diamond carbon (NDC) because of the lasing process influences the electrochemical response of $Fe(CN)_6^{3-/4-}$.

Finally, the G-BDD OTE was used in two capacities to study $Fe(CN)_6^{3-/4-}$. First, a thin-layer cell is shown for the determination of the standard reduction potential ($E^{o\prime}$) and electron transfer stoichiometry (n), followed by an unrestricted diffusion (semi-infinite linear diffusion) cell to calculate the diffusion coefficient (D). The results from the CV and SEC measurements are compared to prove the consistency between techniques using the

BDD OTE. However, a discussion is presented regarding the calculation of *D* based on the unique, three-region nature of the diffusion layer for this electrode design.

3.1 Introduction

While several electrochemical methods are available to characterize redox couples, spectroelectrochemistry (SEC) offers several advantages, including increased sensitivity and selectivity.[128] Additionally, it can eliminate the need for reversibility like in CV, which was shown to be challenging for quasi- or irreversible redox couples when studying f-block species in **Chapter 2**. Spectroelectrochemistry is frequently performed by combining and electrochemical technique with a spectroscopic method like UV-Visible spectrophotometry (UV-Vis) or spectrofluorometry, but several other optical detection modes have been reported (Infrared, Raman, X-ray, etc.).[129-131] For SEC with UV-Vis, observed absorbance changes occur proportionally to the applied potential and can be used to determine parameters like formal potential (E^o), thermodynamic values (ΔG_{cell}, ΔH, ΔS), diffusion coefficient (D), and electron transfer stoichiometry (n) for a given redox reaction. However, an appropriate optically transparent electrode (OTE) can be challenging to acquire, especially in harsh environments. Common OTEs include metal mesh designs from materials like Pt or Au, or transparent, conductive films like indium tin oxide or BDD on a transparent substrate.[128,132-134]

Two variations of SEC can be performed: thin-layer diffusion (TLD), which allows for the calculation of E^o, and semi-infinite linear diffusion (SID) that can describe D. The electrode configuration for SID measurements is closest to that of measurements like CV

where the diffusion layer is unrestricted, while TLD ensures that geometric structure of the electrode confines the analyte within a range that is the thickness of the diffusion layer.[135-137] Rather than oxidized or reduced species diffusing to and from the surface of an electrode in and out of the bulk solution with CV and SID, the diffusion layer is the entirety of the sample solution such that the entire sample can be uniformly electrolyzed for TLD. By applying potentials near E^o for a redox reaction, the ratio of oxidized to reduced species will change proportionally. This change can be observed using spectroscopic methods thanks to the associated color changes (like in the case of colorless ferrocyanide to yellow ferricyanide) as the ratio of the species changes. Like with CV, the redox potential is the point at which the concentration of oxidized and reduced species is equal at the surface. However, the SID technique does not restrict the surface, allowing for the determination of diffusion rates as the absorbance changes when a species is electrolyzed at the surface and then migrates to the bulk solution.

Given the opacity due to the boron-doping, BDD OTEs are typically either in the form of thin films on substrates like quartz or as a coating on a metal mesh (i.e., Nb, Ta) that contain small, macroscale holes.[128] However, these designs do not take advantage of the robust features of BDD given the lack of strength due to the minimized thickness required for optical transparency and cannot be applied to harsh environments. Additionally, literature on the use of free-standing BDD for SEC is limited.[94,138] Overall, there are few options for resilient BDD OTEs capable of withstanding harsh environments like strong acids and bases or high-temperature molten salts.

This chapter presents a free-standing BDD grid electrode (G-BDD) design for SEC measurements. The G-BDD electrode is free-standing polycrystalline diamond with holes created using laser-etching to fabricate the grid for optical transparency (discussed further in **BDD Grid** Electrode). As a proof of concept, the model 1-electron transfer ferri/ferrocyanide ($Fe(CN)_6^{3-/4-}$) redox couple was studied, in addition to the UV-Vis absorbance change from colorless to yellow when oxidizing Fe^{2+} to Fe^{3+}. Like in **Chapter 2**, $E^{o'}$, D, n, and the heterogeneous electron transfer rate constant (k) were calculated using CV for general electrode characterization. The G-BDD electrode was compared to an identical BDD electrode without the lased grid ('non-grid': NG-BDD). The resulting E^o, n, and D values were compared for the two electrodes (G-BDD vs. NG-BDD) and two techniques (SEC vs. CV). This work supports a novel grid electrode designed with resilient, high-performing material to advance fundamental redox chemistry in a variety of media.

3.2 Methods and Materials

Potassium nitrate (KNO_3), potassium chloride (KCl), potassium ferricyanide ($K_3Fe(CN)_6$), and potassium ferrocyanide trihydrate ($K_4Fe(CN)_6 \cdot 3H_2O$) were purchased from Sigma Aldrich. Sulfuric acid (H_2SO_4, trace-metal grade), sodium hydroxide (NaOH), and phosphate buffered saline (PBS) was purchased from VWR. Ultra-pure water (18.2 MΩ-cm) was used for all standard solutions using a D2798 Barnstead water purification system. Miniature silver-silver chloride (Ag/AgCl, 3.5 M) reference electrodes from eDAQ were used for all measurements. A Pt wire (d = 1 mm, 99.95% purity) from Strem Chemicals was used as the counter electrode.

All electrochemical measurements were completed using either a SP-300 (Biologic) or a PalmSens EmStat3+ (BASi). For the optical measurements, a DH-2000 BAL light source and HR4000 spectrometer from Ocean Insight were used. For the control study, an Agilent Cary 100 UV-Vis spectrophotometer was used. A JEOL JSM-5600 scanning electron microscope was used for imaging.

The voltammetry performed in this chapter is different from what was presented in **Chapter 2** in that the two distinct sides of the free-standing BDD are not being isolated. The schematic in **Figure 3.1** shows that both sides are submerged in the solution and a connection is made in the top hole described in **Section 3.2.1**. The same BASi Ag/AgCl (3.5 M) RE from **Chapter 2** was used along with a graphite CE in a shot-glass vessel. The 1 M KCl electrolyte was purged of dissolved oxygen via Ar(g) bubbling before measurements were performed.

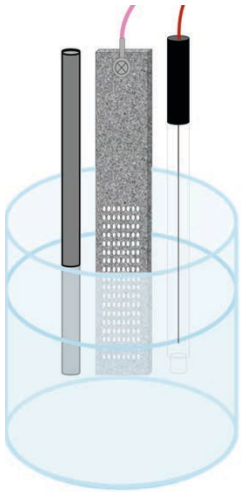

Figure 3.1 Electrochemical cell for CV measurements of a BDD WE. CE: Pt wire; RE: Ag/AgCl (3.5 M KCl).

3.2.1 BDD Grid Electrode

Free-standing BDD with custom dimensions was purchased from Elementsix, and Diamond Technology Innovations completed the laser-etching process. The dimensions of the BDD grid electrodes were 9 mm (wide) × 45 mm (long) × 0.375 mm (thick). A 3 mm diameter hole was cut at the top-center of the material for electrical connection to be made using a ring terminal. The grid was cut into the lower portion of the material in 120 rows and 10 columns of holes. Each hole was cut to 100 μm in diameter with a spacing of 150 μm (edge-to-edge). Prior to the completion of any electrochemical experiments, all BDD electrodes were cleaned following the procedure outlined by Read and Macpherson to remove non-diamond carbon.[101-104] The electrodes were placed in H_2SO_4, heated to boiling, and KNO_3 was added to saturation. The cleaned electrodes were first sonicated in deionized water, followed by sonication in ultra-pure isopropanol.

To determine *E°'*, a thin layer diffusion (TLD) electrode was constructed using strips of 0.170 mm thick polyethylene film placed on both sides of the BDD (grown and nucleation) along the long edges of the grid (left and right). Then, cut-to-size microscope slides were positioned on each side of the electrode and fixed using a quick-cure epoxy. The analyte solution was then added into the 'spacer' region and held through capillary action. Schematics of the front and side views of the assembled G-BDD is shown in **Figure 3.2**. Finally, a small amount of 1.0 M KCl was placed at the bottom of the cuvette to create an ionic connection the Ag/AgCl RE and Pt wire CE that were affixed to corners of the cuvette with the quick-cure epoxy. The grid portion of the G-BDD was placed in the center of the cuvette in the region of the light path.

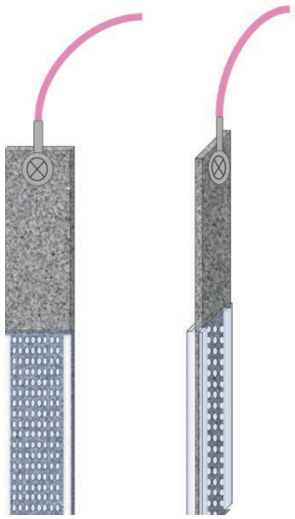

Figure 3.2 Front and side views of the assembled G-BDD with the spacer material and glass slide on each side of the electrode.

Chronoabsorptometry was performed in a similar cell to determine *D*, but the diffusion layer was not restricted, resulting in the semi-infinite diffusion (SID) observed under conditions used for techniques like CV. In this case, the cuvette was filled with the analyte solution and the grid area was fully submerged. Schematics of both the TLD and SID cell setup are shown in **Figure 3.3**.

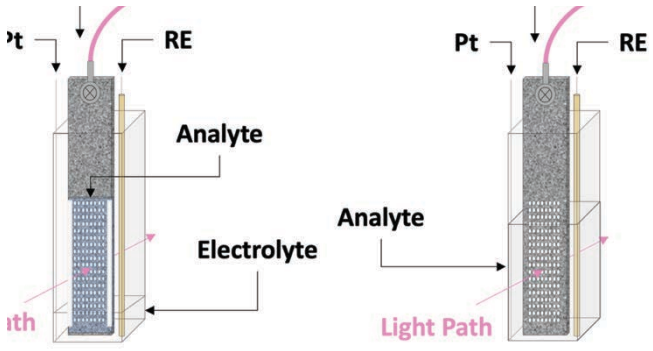

Figure 3.3 Spectroelectrochemical cells for A) thin-layer diffusion and B) semi-infinite diffusion with G-BDD OTEs; RE: Ag/AgCl; CE: Pt wire.

3.3 Grid Electrode Characterization

3.3.1 Secondary Ion Mass Spectroscopy

The boron concentration of the G-BDD electrode material was determined using secondary-ion mass spectroscopy (SIMS) measurements completed at Eurofins USA. The measurement was focused on a region near the top and away from the grid. A boron concentration of 3.0×10^{20} atoms·cm^{-3} was obtained, as shown by the SIMS depth profile in **Figure 3.4**. The reported value is based on an average of the flat region of the depth profile and is indicative of a 'medium' boron-doping level.[43] Higher or lower doping levels may be desirable for specific applications and could be adjusted accordingly in the CVD process.

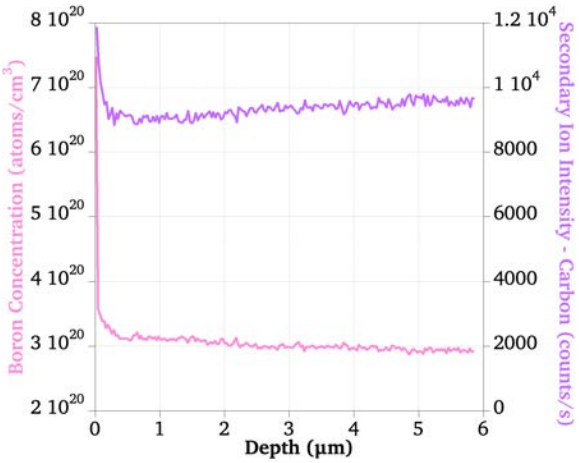

Figure 3.4 SIMS depth profile of free-standing BDD to determine B concentration.

3.3.2 Scanning Electron Microscopy

Like the BDD used in **Chapter 2**, the G-BDD grid was first topographically characterized using scanning electron microscopy (SEM). SEM micrographs in **Figure 3.5 A)** and **B)** show the grown side of the BDD material, while **C)** and **D)** show the nucleation

side. The nucleation side of free-standing BDD was initially attached to a silicon substrate which was etched away after the chemical vapor deposition (CVD) growth process. Due to the diamond seeding process that was used to deposit BDD onto the substrate, the crystal grain size is expected to be much smaller for the nucleation side than the grown side. This is evident when comparing **Figure 3.5 B)** (grown side) and **D)** (nucleation side). The crystallites appear on the order of 10 – 20 μm on the grown side, while sub-micron crystallinity was observed on the nucleation side. The laser-etching process was performed with the grown side facing the laser, and as a result **Figure 3.5 B)** and **D)** indicate that there may be a taper in the cut from the grown side to the nucleation side considering the hole diameter in **B)** is 15 – 20 μm larger than that shown in **D)**. Based on **Figure 3.5 A)** and **C)**, it also appears that the holes on the grown side present greater symmetry than those on the nucleation side.

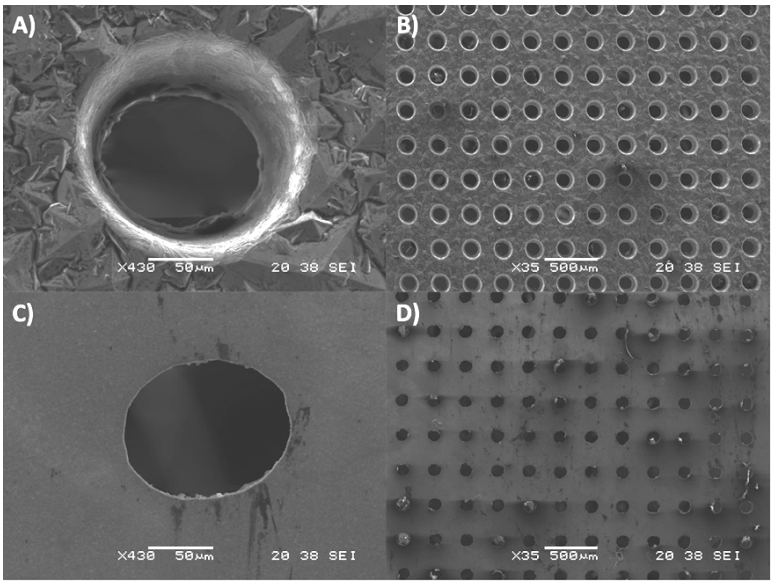

Figure 3.5 Micrographs of the grown (A,B) and nucleation (C,D) sides of the BDD OTE.

3.3.3 Cyclic Voltammetry

Cyclic voltammetry was used to assess the electrochemical performance of the BDD grid (G-BDD) electrodes. Results were compared to an identical non-grid BDD electrode (NG-BDD). This was completed to observe changes in the electrochemical response brought about by the presence of residual non-diamond carbon due to the laser-etching process. After acid cleaning the electrodes, an anodic pre-treatment in 1.0 M H_2SO_4 using CV was also performed where the potential was scanned from +2.5 V to -1.5 V at 100 $mV \cdot s^{-1}$ for 30 cycles. It is important to note that previous studies including such pre-treatment on laser-etched BDD reported pH-dependent quinone groups on the sp^2-rich lased BDD areas, but they are not expected to impact spectroelectrochemical studies.[101-104]

Voltammograms were recorded on both electrodes in 1 mM $Fe(CN)_6^{4-}$ in 1.0 M KCl before and after pre-treatment. Several redox parameters were determined and are given in **Table 3.1**. A series of CVs were recorded at varied scan rates (10 – 100 $mV \cdot s^{-1}$) within a potential window of -0.2 to +0.8 V. Each scan rate was cycled three times and repeated for three trials. The geometric surface area of the electrode submerged in solution was 6.61 cm^2 for NG-BDD and 8.01 cm^2 for G-BDD. Current interrupt *iR* compensation was completed prior to all CV measurements using 1 or 10 mA, 50 ms current pulses.[109] The uncompensated resistance was automatically accounted for (80% compensation) using the EC-Lab Software.

As seen in **Table 3.1**, the values for E^o were similar across all four electrodes, ranging from +0.279 to +0.283 V vs. Ag/AgCl, which agree with values reported for the $Fe(CN)_6^{3-/4-}$ couple on BDD.[95] The CV *i-E* curves from the scan rate study on G-BDD after

pre-treatment are shown in **Figure 3.6 A)**. Like in **Chapter 2** the quasi-reversible form of the Randles-Sevcik equation (Eq. 1) was used to produce a plot of i_p vs. $v^{1/2}$ which yielded a linear response on all electrodes, indicative of semi-infinite linear diffusion.[109] All values obtained for D ranged on the expected order of magnitude (10^{-6} cm^2/s). Values of 3.8 and 4.1 × 10^{-6} cm^2/s were obtained on anodically pre-treated G- and NG-BDD, respectively, and both align with literature (10^{-6} cm^2/s).[91]

Table 3.1 Figures of merit determined for $Fe(CN)_6^{3-/4-}$ in 1.0 M KCl using BDD with and without the grid. *For 50 mV/s scan rate.

Electrode	Pre-Treatment?	Technique	E^o (V)	$E_{p,a}$-$E_{p/2,a}$ (V)	n	$D_R \times 10^{-6}$ (cm^2/s)	ΔE_p* (V)	k* × 10^{-3} (cm/s)
G-BDD	Yes	CV	+0.279	0.058	0.97	4.1	0.064	14
G-BDD	No	CV	+0.281	0.074	0.76	5.4	0.112	1.6
NG-BDD	Yes	CV	+0.282	0.058	0.97	5.1	0.067	12
NG-BDD	No	CV	+0.283	0.067	0.84	2.9	0.096	1.8
G-BDD	Yes	SEC	+0.278	--	0.91	5.2	--	--

Also like **Chapter 2**, the method outlined by Nicholson[110] using Eq. 2 was used to determine k based on the peak separation (ΔE_p) and $D_{O/R}$ calculated for each scan rate. The values for k and ΔE_p for the 50 mV/s scan rates are listed in **Table 3.1**. In both cases, the values for the anodically treated BDD are 'improved' than the untreated electrodes where ΔE_p is smaller (64 and 67 mV vs. 112 and 97 mV for G-BDD and NG-BDD, respectively) and k is larger (10^{-2} vs. 10^{-3}).

A full scan rate study for the G-BDD after anodic treatment is shown in **Figure 3.6 A)** for 10 – 100 mV/s in 1 mM $Fe(CN)_6^{3-/4-}$ in 1 M KCl. **B)** and **C)** show CV overlays for the pre-treated G-BDD vs. pre-treated NG-BDD (**B**) and the pre-treated vs. un-treated G-BDD (**C**) at 50 mV/s. In **Figure 3.6 B)**, there is a close overlay in the response between the pre-treated G- and NG-BDD electrodes. The slight increase in the anodic response at +0.8 V is

the beginning of the surface sp^2-carbon peak observed in the KCl background (**Figure 3.7 E)**, discussed below). There is a visual difference in the pre-treated vs. un-treated G-BDD in **Figure 3.6 C)**. Like for ΔE_p and k, $E_{p,a} - E_{p/2,a}$ (**Table 3.1**) was lower on the pre-treated electrodes than the untreated BDD: 0.058 V was observed on both G- and NG-BDD, with 0.074 V and 0.067 V from their untreated counterparts. These results correspond to larger k values on the treated electrodes; pre-treated G-BDD was over an order of magnitude larger than the un-treated material, as seen in **Table 3.1**. This may suggest the presence of quinone groups on the surface due to sp^2-hybridized carbon at the lased regions of the BDD grid because of the pre-treatment process, which has been reported in literature.[101] In general, these results confirm that the pre-treatment process results in an improved response towards $Fe(CN)_6^{3/4-}$ and that the electrochemical activity is not hindered by the presence of the grid.

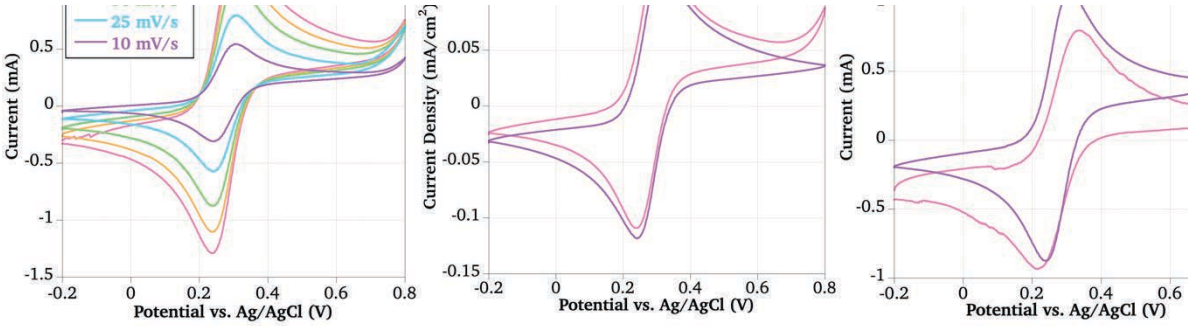

id. A) Scan rate study from 10 - 100 mV/s on the OTE; B) overlays of 50 mV/s scans on BDD with and without the grid after anodic treatment; C) overlay of 50 mV/s scans with the OTE before and after anodic treatment. RE: Ag/AgCl; CE: Pt wire.

Using the pre-treated electrodes, the potential window for both BDD electrodes was then examined in five aqueous electrolytes: 1.0 M H_2SO_4, 1.0 M NaOH, 1.0 phosphate-

buffered saline (PBS), 1.0 M KNO_3, and 1.0 M KCl. The respective CV *i-E* curves for each electrode in the electrolyte series are shown in **Figure 3.7**. A threshold of 0.4 $mA \cdot cm^{-2}$ was used in the oxygen- and hydrogen-overpotential regions to determine the anodic and cathodic potential window, as previously described by the Macpherson group.[101] In PBS, KNO_3, and KCl, the potential window was similar on both BDD electrode types, and the values determined for each electrode are listed in **Table 3.2**. These values agree with previous findings.[50-52,87,101-104,138-142] In KNO_3, an anodic peak ca. +1.2 V was observed on both electrodes, but with a larger magnitude on G-BDD (1.34 vs. 1.22 $mA \cdot cm^{-2}$). This peak has been attributed to signatures of sp^2-carbon, so the increased signal on G-BDD is expected.[101] However, in KCl, a cathodic peak appears at approximately 0 V for both electrodes. This phenomenon has not been reported in literature, but it is hypothesized that it may be a result of reaching significant current densities in the O_2 overpotential. Further discussion about this result is presented in **Chapter 5**.

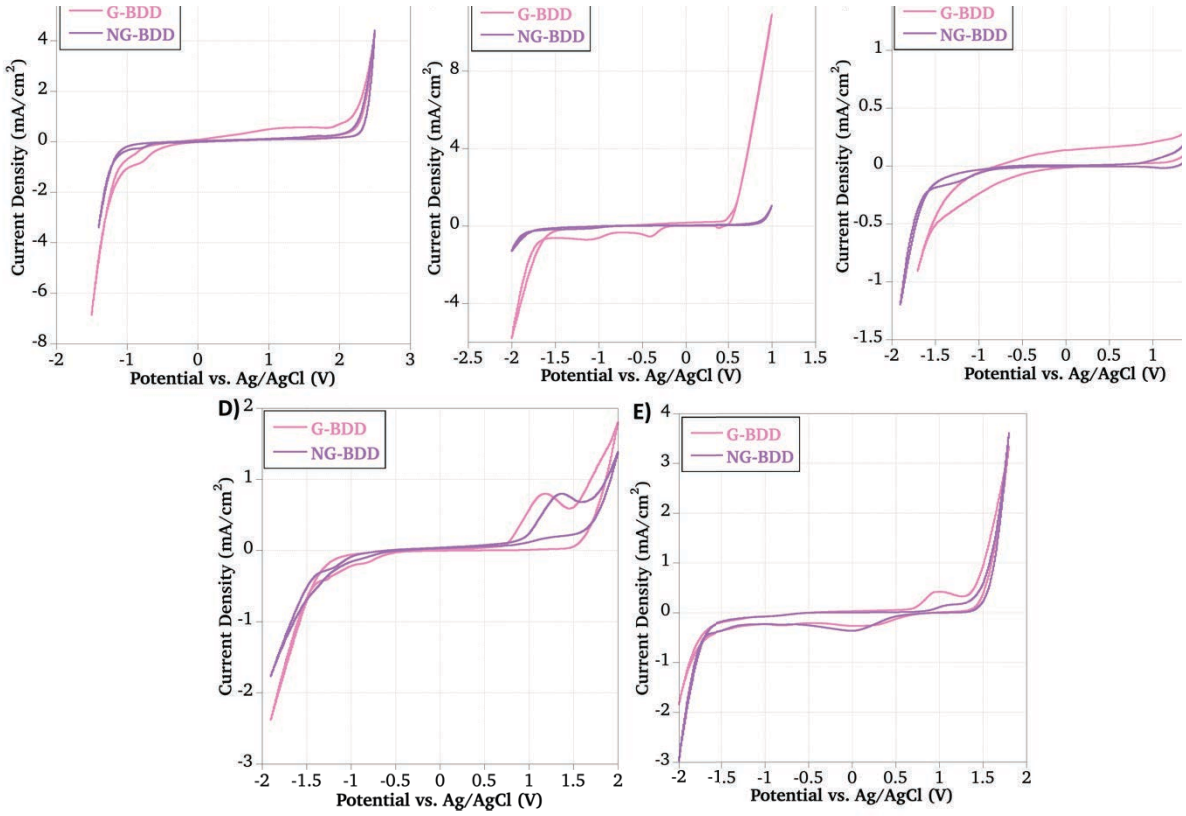

lytes.
A) 1.0 M H_2SO_4, B) 1.0 M NaOH, C) 1.0 M PBS, D) 1.0 M KNO_3, E) 1.0 M KCl. RE: Ag/AgCl with double junction for corresponding electrolyte; CE: graphite rod.

Table 3.2 Potential window magnitudes for the G- and NG-BDD electrodes in various electrolytes (1 M).

H_2SO_4		
	NG-BDD	3.16
KNO_3		
	NG-BDD	3.15

An increase in the baseline current was observed with G-BDD in 1.0 M H_2SO_4, as evident in **Figure 3.7 A)**, which caused the measurement of the anodic potential limit to be skewed. However, the oxygen overpotential was not reached until nearly +2.0 V.

Considering the baseline current, the potential window was 1.42 V with G-BDD. With baseline correction, this nearly doubles to 2.85 V, and a window of 3.16 V was observed using NG-BDD with no baseline correction needed (**Table 3.2**).

Measurements completed in 1.0 M NaOH (**Figure 3.7 B**) also yielded a difference between the potential window of the BDD electrodes. Also listed in **Table 3.2**, a potential window of 2.70 V was observed on NG-BDD, while 2.05 V was observed on G-BDD. The oxygen-overpotential (OH^- oxidation) accounted for most of the difference in the potential window (NG-BDD: 0.92 V, G-BDD: 0.50 V), again, likely due to the presence of sp^2-hybridized carbon.[36,107,143-145]

3.4 Spectroelectrochemical Measurements

The $Fe(CN)_6^{3-/4-}$ redox couple was used again since the reduced form (ferrocyanide) does not absorb light and the oxidized form (ferricyanide) exhibits strong absorption at 420 nm (ε = 1020 $M^{-1}{\cdot}cm^{-1}$). Two SEC techniques were used: thin-layer diffusion (TLD) and semi-infinite diffusion (SID). For both the TLD and SID studies, the analyte began as the colorless $Fe(CN)_6^{4-}$ and oxidizing potentials were applied to generate the yellow $Fe(CN)_6^{3-}$ solution.

3.4.1 Thin-Layer Diffusion

The TLD measurements yield E^o via a Nernst plot (log([O]/[R]) vs. E_{cell}). This regression combines the Nernst equation and the Beer-Lambert law, summarized via the modified Nernst equation (Eq. 11):[146]

$$E_{cell} = E^o + \frac{2.303RT}{nF} \log \left(\frac{Abs(O)}{Abs(R)}\right) \quad \textbf{(11)}$$

The UV-Vis spectra obtained for the TLD study is shown in **Figure 3.8 A)** along with the corresponding Nernst plot in **B)**, displaying the expected characteristic peak shape for $Fe(CN)_6^{3-}$, with a λ_{max} ca. 420 nm. In this experiment, the potential was stepped from 0 V to +0.4 V vs. Ag/AgCl in increments of 0.05 V after +0.15 V. The potential was held at each step for 5 – 8 min. until the absorbance and current stabilized. As the potential was increased, a proportional increase in the absorbance response was observed, indicating the conversion of Fe^{2+} to Fe^{3+} in the TLD cell. Using the absorbance value at λ_{max} (420 nm), a Nernst plot was generated and is shown in **Figure 3.8 B)**, exhibiting excellent linearity (R^2 = 0.999). Since the *y*-intercept of the Nernst plot yields E^o, this value was determined to be +0.278 V vs. Ag/AgCl (3.5 M KCl).

After normalizing the Ag/AgCl reference potential with a Cl^- concentration of 3.5 M for all electrodes, E^o by TLD-SEC is nearly identical in magnitude to all other measurements completed with CV (**Table 3.1**). No statistical difference in E^o was observed between TLD-SEC and CV on G-BDD (95% confidence). The slope of the Nernst plot ($0.059/n$) was used to determine n. The value observed with TLD (0.91) was also close to what was obtained using CV with pre-treated G-BDD (0.97) and NG-BDD (0.97).

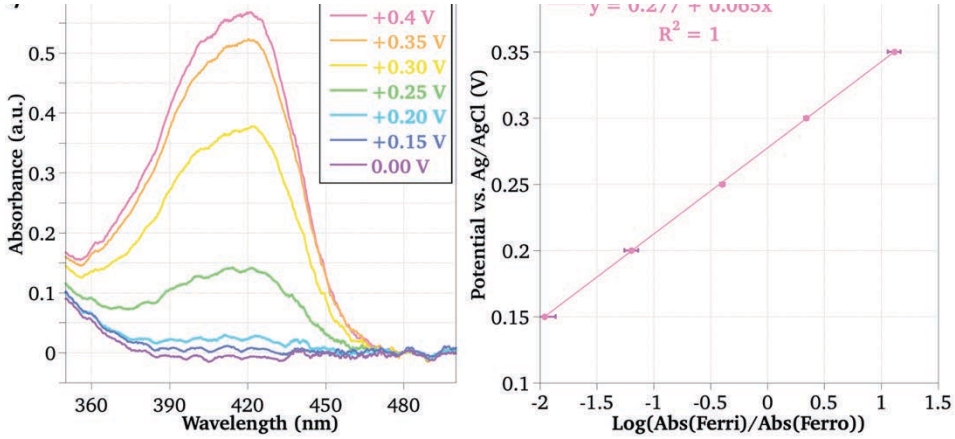

Figure 3.8 A : BDD
OTE. B) Nerr

3.4.2 Semi-Infinite Diffusion

The SID measurements were completed using chronoabsorptometry where a single potential step was applied such that the BDD grid electrode potential was held at 0 V vs. Ag/AgCl for 20 sec. before stepping to +0.8 V for 120 sec. Based on the combined CV and TLD results shown in **Figure 3.6** and **Figure 3.8 A)**, +0.8 V gave sufficient overpotential to keep the process diffusion limited. The absorbance response at 420 nm was then monitored over time before and after the potential step. Five trials were conducted for all measurements and averaged to provide the reported values.

Figure 3.9 A) shows the original *Absorbance* (*Abs*) vs. *time* (*t*) at 420 nm and **B)** displays the chronoabsorptometry plot (*Abs* vs. $t^{1/2}$), where the 0-time point is taken as the moment the potential step to +0.8 V vs. Ag/AgCl was made. In both figures, there are two regions of separate slope, indicating that G-BDD follows the trend for previous work using mini-grid electrodes.[147] The region after 3 seconds in **Figure 3.9 B)** (purple), is attributed to G-BDD exhibiting a pseudo-planar surface (discussed below). A strong linear

relationship was obtained in this region (y [a.u.] = 0.0079x [a.u./s$^{1/2}$] + 0.048 [a.u.], R^2 = 0.996).

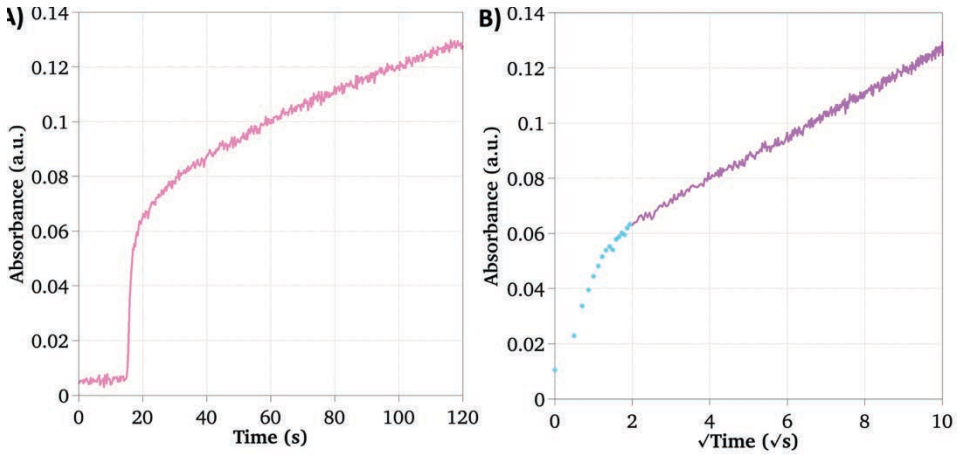

Figure 3.9 C -BDD
OTE; RE: Ag/ ion of
D.

To accurately determine D from this data, the three-dimensional geometry of the G-BDD electrode must be considered. It is different from the equation that has been classically used to define the relationship between absorbance and time after an electrochemical potential step:

$$Abs = 2\varepsilon lC\sqrt{\frac{Dt}{\pi}} \quad \textbf{(12)}$$

This equation holds for an electrode with one conductive side, where the light path only traverses one diffusion layer on the singular electrode surface (e.g., BDD thin film on one side of a quartz slide). This relationship is derived by combining the Beer-Lambert Law,

$$Abs = \varepsilon lC \quad \textbf{(13)}$$

with the charge-concentration relationship

$$Q = nFAC \quad \textbf{(14)}$$

which equation simplifies to

$$\frac{Abs}{Q} = \frac{\varepsilon l}{nFA} \quad \textbf{(15)}$$

and can be combined with the Anson equation (Eq. 16) to produce Eq. 12.

$$Q = 2nFAC\sqrt{\frac{Dt}{\pi}} \quad \textbf{(16)}$$

All terms have their usual meaning.

However, with multiple conductive sides to the OTE, the light path will include multiple, distinct diffusion layers. This was first postulated by the Murray group in 1971 using an Au grid electrode that was conducive on two sides, and they modified the *Abs* vs. $t^{1/2}$ relationship accordingly.[147]

$$Abs = 4\varepsilon lC\sqrt{\frac{Dt}{\pi}} \quad \textbf{(17)}$$

This derivation is like the described above, only now considering that the Beer-Lambert Law must be doubled since a diffusion layer would develop on both sides of their Au OTE ($Abs = 2\varepsilon lC$). It is important to note that the thickness of the Au grid electrode was no larger than ~8 μm, which is 50 times smaller than G-BDD. The Murray group reported additional theory on SEC with their Au mini-grid electrodes that is applicable to G-BDD. When evaluating the Q vs. $t^{1/2}$ response at short timescale, they mentioned that the diffusion layer is small relative to the wire dimension and linear diffusion will prevail.[147] The slope of the plot in this timescale is proportional to the microscopic surface area (A_{mic}). At sufficiently long times, the diffusion layer will become large relative to the hole and wire dimensions.[147] This will then cause the diffusion layers from individual wires to merge, linear diffusion will dominate, and the slope of the plot is proportional to the macroscopic surface area (A_{mac}). The averaged diffusion profile under this condition would cause the grid to behave as a pseudo-planar surface. In turn, the Q vs. $t^{1/2}$ response should exhibit separate short- and long-time linear segments and only in the case where $A_{mic} = A_{mac}$ will the slopes be the same.

With the *Abs* vs. $t^{1/2}$ response, Murray et al. mentioned that most of the characteristics would be like Q vs. $t^{1/2}$.[147] However, only the solution present in or above a hole would interact with the light path and the response from any solution present above an outer wire would be 'shadowed' and not optically observed.[147] This means that for linear *Abs* vs. $t^{1/2}$ response, diffusions conditions where the grid exhibits a pseudo-planar surface need to be obtained. Therefore, the electrolysis time needed to obtain the pseudo-planar

surface can be estimated by calculating the amount of time it would take to produce a diffusion profile depth one-half of the mini-grid hole size using Eq. 18:

$$\frac{C_{(x,t)}}{C^b} = 0.50 = \text{erf}\left(\frac{x}{2\sqrt{Dt}}\right) \quad \textbf{(18)}$$

where x is the hole diameter size. This could then cause the *Abs* vs. $t^{1/2}$ plot to exhibit two regions of different slope at short and long timescales, depending on the hole size.

The phenomena discussed above would be expected to hold true with G-BDD; however, the thickness of G-BDD (0.375 mm) is 50× larger than any Au mini-grid studied by the Murray group.[147] Therefore, the diffusion layer development inside the 0.1 mm diameter, 0.375 mm deep holes must also be taken into consideration, which is depicted in **Figure 3.10**. Using the equation above, the time needed to reach a pseudo-planar surface with G-BDD is approximately 3 seconds, for a theoretical value of 5×10^{-6} cm^2/s for D of $Fe(CN)_6^{4-}$. At this time point, the diffusion layer thickness is about 40 μm and walls within the conductive 'tubes' confine the electrogenerated $Fe(CN)_6^{3-}$ diffusion direction away from the electrode surface. $Fe(CN)_6^{3-}$ can travel either parallel along the walls or radially toward the center of the tubes. At a relative diffusion layer thickness of 40 μm that builds in all directions, a tube diameter of 100 μm (0.1 mm), and a length of 375 μm (0.375 mm), it is reasonable to consider the tube as an additional diffusion region through which the light path traverses, as depicted in **Figure 3.10**. Considering this third diffusion layer would cause an additional modification to the *Abs.* vs. $t^{1/2}$ relationship. The Beer-

Lambert Law would need to be tripled ($Abs = 3\varepsilon lC$) and completing the same derivation as described previously yields:

$$Abs = 6\varepsilon lC\sqrt{\frac{Dt}{\pi}} \quad \textbf{(19)}$$

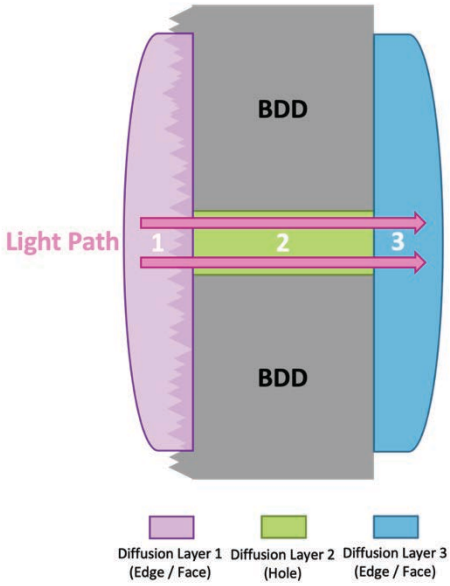

Figure 3.10 Schematic o yers for the G-BDD during SID measurements.

In the *Abs.* vs. $t^{1/2}$ plot (**Figure 3.9 B**), the time point where the slope magnitude changes is ca. 3 seconds which then produces a value that is in direct agreement with the what was calculated using Eq. 19 (the modified chronoabsorptometry equation for a three-section diffusion layer). After this, G-BDD exhibited a pseudo-planar surface (**Figure 3.9 B**). This region was then used to determine D for $Fe(CN)_6^{4-}$ using the *Abs* vs. $t^{1/2}$ relationship for 3 diffusion layers and a value of 5.2×10^{-6} cm^2/s was obtained, which is

within the expected order of magnitude based on literature, and the previously discussed CV measurements.[91,147]

For justification, if a constant of 4 is used in the *Abs* vs. $t^{1/2}$ relationship (Eq. 17) like the mesh electrode used by the Murray group,[147] D increases to 1.2×10^{-5} cm^2/s, which deviates from the expected literature value and the results gathered using CV. These results prove that 1) the SID-SEC response with G-BDD follows that published previously for other mini-grid electrodes, and 2) the constant in the chronoabsorptometry equation for G-BDD must be larger than 4 due to its characteristic thickness of 0.375 mm.

3.4.2.1 SID Control Studies

Three separate control studies were completed: 1) a benchmark with a Pt-mesh flag electrode (BASi), 2) a comparative measurement using two models of UV-Vis spectrophotometers, and 3) reversal of the G-BDD direction so that the nucleation-side, rather than the grown-side, of the electrode faced the light path.

With the Pt-mesh electrode, the same SEC cell design as G-BDD was used with 25 mM $Fe(CN)_6^{4-}$ in 1 M KCl. The resulting plots for *Abs*. vs. *t* and *Abs*. vs. $t^{1/2}$ are presented in **Figure 3.11**. Unlike for the G-BDD, the $t^{1/2}$ plot for the Pt OTE follows a linear pattern with a singular slope. To calculate D, a constant of 4 (Eq. 17) was used for two conductive sides, as suggested previously when a similar Au mesh design was used,[147] and produced a value of 7.3×10^{-6} cm^2/s for D, aligning with the literature and previous measurements using CV.[91,147] However, if a constant of 2 was used like in the original

chronoabsorptometry equation (Eq. 12), the value inflated to 2.3×10^{-5} cm^2/s, far from the expected value.

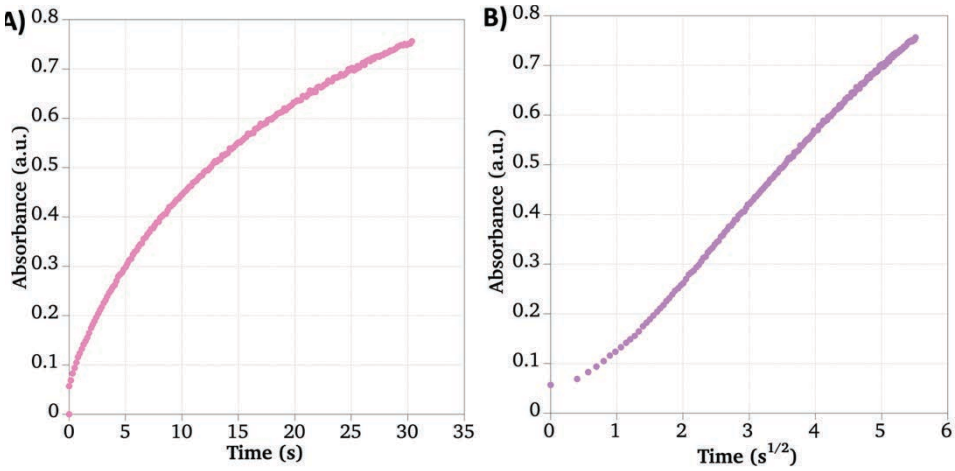

Figure 3.11 [illegible] M KCl using the Pt l[illegible] or the determination of *D*.

Additionally, a set of measurements was completed with G-BDD using a benchtop UV-Vis spectrophotometer (Agilent Cary 100). The SEC cell design was the same as with the Ocean Optics setup used previously and the concentration of $Fe(CN)_6^{4-}$ was 1.0 mM. Using a constant of 6, a value for *D* of 5.1×10^{-6} cm^2/s was determined, nearly identical to the 5.2×10^{-6} cm^2/s obtained with Ocean Optics.

Lastly, the G-BDD electrode was flipped so that the nucleation-side of the material faced the light path. Up to this point, all measurements were conducted with the grown side facing the light path. As seen in **Figure 3.5**, the holes in G-BDD were lased from the grown-side to the nucleation-side. This caused a slight taper in the hole as the laser etched through the BDD and the holes on the nucleation-side ranged 10 - 25 μm smaller in diameter than the grown-side. Considering what this means for the light path exiting a hole smaller in diameter than the entrance hole, diffraction is likely to occur with the light exiting the nucleation-

side. Internal reflection could also occur, but this was unlikely due to the BDD inside the holes. So, by reversing the G-BDD direction, the light would exit a hole with a wider diameter than it entered, and verification was needed to determine if this would affect the response.

The *Abs.* vs. $t^{1/2}$ response for when the G-BDD was reoriented such that the nucleation side faced the light source is shown in **Figure 3.12** (green-blue) and the shape of the plot is like that seen in original data where the grown side faced the light source (pink-purple). The electrolysis time (green portion, **Figure 3.12**) needed to reach a pseudo-planar surface (blue portion, **Figure 3.12**) was nearly identical to the grown-to-nucleation results ca. 3 seconds. A strong linear correlation was observed in the period where the electrode behaved pseudo-planar (y [a.u.] = $0.0074x$ [a.u./s$^{1/2}$] + 0.0388 [a.u.], R^2 = 0.996). This corresponded to a value for D of 4.59×10^{-6} cm^2/s, of which is directly in-line with that obtained with the other electrodes and measurements reported in **Table 3.1**. This indicates that the orientation of the G-BDD electrode with these dimensions does not significantly impact the *Abs*. vs. $t^{1/2}$ response. In all three cases, the control measurements support modification of the chronoabsorptometry equation to accommodate the G-BDD electrodes and development of three diffusion layers.

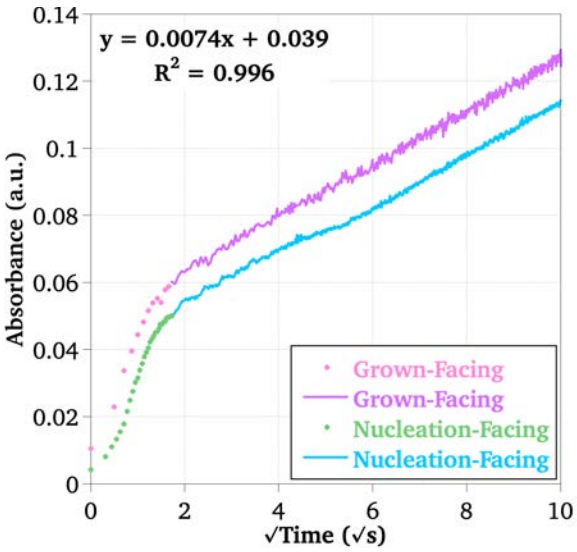

Figure 3.12 Chronoabsorptometry of 1.0 M $Fe(CN)_6^{3-/4-}$ in 1.0 M KCl using the BDD OTE. Pink to purple line: grown side facing light source; Green to Blue line: nucleation side facing light source.

While we have proposed this modification to the *Abs* vs. $t^{1/2}$ relationship to account for three diffusion layers, it is possible that the exact value for the constant lies somewhere between 4 and 6 and is dependent on several factors. For example, the electrode thickness, diameter of the grid holes, and spacing between holes could all affect the diffusion of the analyte, especially at the inner layer of the grid. Such variations were out of the scope of this thesis but will be the focus of future work to elucidate the *Abs* vs. $t^{1/2}$ relationship for SEC with electrodes like G-BDD.

3.5 Conclusions

An optically transparent, free-standing BDD grid electrode (G-BDD) was fabricated and characterized topographically, electrochemically, and spectroelectrochemically. Several important redox parameters were calculated using the $Fe(CN)_6^{3-/4-}$ redox couple, such as $E^{o'}$, D, n, and k. A pre-treatment process was used, and the response was compared

before and after. Additionally, BDD electrodes of the same dimensions without the lased grid were used as a control. Good agreement was observed between the calculated redox parameters for the two the electrodes.

Chronoabsorptometry was also completed to determine D for $Fe(CN)_6^{4-}$ and 5.2×10^{-6} cm^2/s was obtained. To calculate this value, however, modification of the traditional chronoabsorptometry equation that relates absorbance to $t^{1/2}$ (*Abs* vs. $t^{1/2}$) was required. Due to the characteristic thickness of the G-BDD OTE (0.375 mm), the light path must pass through three different diffusion layers: one on either face (two) and one within the 0.1 mm diameter, 0.375 mm thick grid holes. In the 1970s, the Murray group first published on this phenomenon on multiple conductive surfaces of OTEs and the light path traversing multiple diffusion layers. However, they used Au grid electrodes and considered them a surface with two distinct diffusion regions (increasing the constant from 2 to 4). The G-BDD OTEs used in this work contain three distinct diffusion regions and, thus, required further modification of the constant (from 4 to 6). The constant is expected to be somewhere between 4 and 6 and dependent on factors like electrode thickness, hole diameter, and hole center-to-center spacing and these features will be a focus of future work. Overall, the work reported here expands the applicability of BDD as an electrode material and spectroelectrochemical techniques as a suitable method for characterizing redox analytes in a range of environments.

4 Boron-Doped Diamond Resilience in Molten Salts Part I: Topography and Surface Chemistry Investigation

Abstract

This chapter aims to determine changes to the topography and surface chemistry of the grown and nucleation sides of BDD after exposure to as received and dried chloride and fluoride molten salts. After ten days of exposure to each environment, each side of the material was monitored using scanning electron microscopy (SEM) and profilometry to monitor topographical changes to the surface structure. Electron and optical images were collected, and the structure of the BDD was characterized with quantitative values like surface roughness for new and corroded samples.

Then, the chemistry of the material was evaluated using various techniques, including Raman spectroscopy, X-ray photoelectron spectroscopy (XPS), and Time-of-Flight Secondary Ion Mass Spectroscopy (ToF-SIMS). Based on instrument availability and prepared samples, some cases (ToF-SIMS) used only samples exposed to salts melted in the fume hood environment (air-exposed), while other measurements (XPS) only included samples exposed to dried salts in the inert glovebox environment. These impacts are considered in the discussion of results for each technique, and gaps remaining are noted in the proposed future work.

After exposure, only one sample exhibited changes to the surface structure: the grown and nucleation sides of NaCl-KCl (H). Water and oxygen in this salt system and environment likely caused the observed etching. These changes were quantified using

profilometry, and features like roughness, sharpness, and uniformity were slightly altered due to the corrosion on both sides.

Concerning the surface chemistry, none of the techniques used here detected differences between the new and exposed samples. In the Raman spectroscopy case, apparent features were present for the nucleation side, not on the grown side, but this was consistent regardless of sample treatment. This difference was not seen using XPS. A range of species were detected using ToF-SIMS, but none indicated changes to the structure or chemistry of the surface after exposure to either salt. Other methods for characterizing the surface chemistry may provide alternate results, but based on what was determined using the methods presented in this chapter, the grown and nucleation sides of BDD seem to be inert chloride and fluoride salt systems.

4.1 Introduction

Materials compatibility is a primary challenge of high-temperature molten salt environments across various industrial and lab-scale applications. For electroanalytical applications, there is a limited selection of robust working electrodes, which often leads to compromising the quality of the results. Although boron-doped diamond (BDD) has been regarded as a high-quality working electrode material, its application in molten salt systems is limited to a small collection of electrolytic reduction measurements.[85-87] However, BDD has been used successfully in various other harsh environments,[49-52] so it is hypothesized that it may be a strong contender as an electrode for sensitive measurements in molten salts.

The previous chapters have outlined the impacts of the crystallinity of BDD on the electrochemical response. Before those experiments can be extended into molten salt systems, studies are outlined here to determine if the material is resilient under extreme conditions. It is known that oxygen exposure at elevated temperatures (>600 °C) will result in etching of the surface,[84] but there is minimal work otherwise to explore how diamond would respond to high-temperature liquid salt systems. In the following work, BDD is exposed to two common molten salt systems, NaCl-KCl (50-50 mol%) and FLiNaK (46.5-11.5-42 mol% LiF-NaF-KF),[1-4,15] for ten days which is longer than most laboratory experiments would require. Additionally, the impact of using salts that are dried and melted in an inert Ar(*g*) glovebox environment versus using salts as received (stored and used in Los Alamos, NM) and melted in a fume hood under otherwise atmospheric conditions was explored.

The grown and nucleation sides of new (untreated) BDD are compared to material soaked in the hood (NaCl-KCl (H) and FLiNaK (H)) with salt that was not dried or in the glovebox with dried salt (NaCl-KCl (GB) and FLiNaK (GB)). The sample treatments are outlined in **Table 4.1**. The topography of the samples was evaluated using scanning electron microscopy (SEM), and the one sample that corroded (NaCl-KCl (H)) was imaged and measured using profilometry where metrics like surface roughness were quantified for each side of the BDD and compared before and after corrosion. Surface structures on thick BDD films are minimally reported in the literature, where the majority of BDD roughness has been studied to tailor the surface of thin films for industrial applications.[148-150] This

work expands the general characterization of large and small-grain crystal structures for BDD while describing the resilience of the material in molten salts.

Table 4.1 Sample names, salt treatment, and exposure environment.

Sample Name	Salt Treatment	Exposure Environment
NaCl-KCl (H)	None	Fume Hood
NaCl-KCl (GB)	Thermal drying in glovebox vacuum furnace antechamber	Glovebox
FLiNaK (H)	None	Fume Hood
FLiNaK (GB)	Thermal drying in glovebox vacuum furnace antechamber	Glovebox

Additionally, the surface chemistry was probed using Raman spectroscopy, X-ray photoelectron spectroscopy (XPS), and time-of-flight secondary ion mass spectroscopy (ToF-SIMS) to determine if factors like termination are affected after exposure to molten chloride and fluoride salts. However, not all samples were able to be studied with each technique, so **Table 4.2** outlines which samples were evaluated which each instrument. These methods have been used repeatedly on BDD surfaces, and many results are readily available in the literature to compare new and exposed samples.[43,151-181] However, no published work using these techniques has been employed after the material has been exposed to molten salts. This suite of instruments provides preliminary insight into the effects of these harsh systems on the grown and nucleation morphologies of BDD before it is used as an electrode in molten salt environments.

Table 4.2 Matrix describing the techniques used on each sample.

Sample	Side	SEM	Profilometry	Raman	XPS	ToF-SIMS
New	Grown	×	×	×	×	×
	Nucleation	×	×	×	×	-
NaCl-KCl (H)	Grown	×	×	×	-	×
	Nucleation	×	×	×	-	-
NaCl-KCl (GB)	Grown	×	-	×	×	-
	Nucleation	×	-	×	×	-
FLiNaK (H)	Grown	×	-	×	-	×
	Nucleation	×	-	×	-	-
FLiNaK (GB)	Grown	×	-	×	×	-
	Nucleation	×	-	×	×	-

4.2 Methods and Materials

In all cases, the BDD samples were placed at the bottom of Coors alumina crucibles with the grown side facing up. All salts used (NaCl, KCl, LiF, NaF, KF) were from ThermoScientific and reagent grade (>99%). Each salt system was mixed to the eutectic composition to minimize the overall melting point: NaCl-KCl (50-50 mol%) that melts at approximately 657 °C[1,3] and FLiNaK (46.5-11.5-42 mol% LiF-NaF-KF) at approximately 454 °C.[2,4] The salts melted in the fume hood were weighed, mixed, and ground by hand with mortar and pestle before being added to the BDD samples in alumina crucibles. Salts melted in the glovebox environment were first dried as separate constituents within a vacuum oven antechamber on a VAC NexGen inert Ar(*g*) atmosphere (<1 ppm H_2O, <1 ppm O_2) glovebox. The chloride and fluoride salts were dried in two separate runs (NaCl and KCl followed by LiF, NaF, and KF), each under the same temperature profile: 100 °C for 6 hours, 150 °C for 6 hours, and 200 °C for 72 hours. The Pyrex jars containing each salt were covered in aluminum foil with holes to release water during drying. Once dried and introduced to the glovebox, the salts were weighed, mixed, and ground by hand with mortar and pestle before being added to the BDD samples in alumina crucibles.

The fume hood salts were melted using a ThermoScientific Thermolyne Benchtop Muffle Furnace. The dried salts in the glovebox were melted in an MTI KSL-1100X High Temperature Muffle Furnace. While the furnace was running in the glovebox or while salts were dried in the vacuum oven antechamber, a PolyScience DuraChill Portable Chiller was kept at 5 °C and circulated through the doors of the antechamber and fan system inside the glovebox. The internal temperature of the glovebox remained below 18 °C for the duration of all furnace operations. The salts were held at approximately 50 °C above their respective melting points (700 °C for NaCl-KCl and 500 °C for FLiNaK) for ten days. The FLiNaK temperature was chosen to ensure melting while minimizing salt creep throughout the exposure, as higher temperatures encouraged the salt to escape the crucible over the edges.

The grown and nucleation sides of free-standing BDD (5 × 5 × 0.45 mm) from ElementSix were first imaged through scanning electron microscopy (SEM) with a ThermoFisher Scientific ApreoS LoVac Scanning Electron Microscope. Surface roughness was evaluated via profilometry using a KEYENCE VK-1000X 3D Laser Optical Microscope. Surface chemistry was studied using a HORIBA XploRA Conical Raman Microscope with a 532 nm laser, a ThermoFisher Scientific Nexsa G2 X-ray Photoelectron Spectrometer, and a Kore Analytical Time-of-Flight Secondary Ion Mass Spectrometer.

Raman spectroscopy is a non-destructive technique that was used to study the vibrational modes of a given species by taking advantage of photon inelastic scattering after a laser is reflected off the sample. The resulting spectrum provided insight into the components of the sample via characteristic peaks at known wavenumbers. For XPS, X-ray

photons at a known energy and wavelength are used to excite and eject photoelectrons from various orbitals in the atoms of the sample. The ejected photoelectrons are detected, and the elemental composition can be described by the resulting count and kinetic energy (KE) of the detected electrons. Subtracting the KE of the electrons from the KE of the incoming photons, the characteristic binding energy (BE) of the ejected electron can be used to describe the element and electron orbital from where it originated. Finally, ToF-SIMS uses particle beams to dislodge species (ions, molecules, or fragments) from the surface of the sample, which are accelerated toward a detector. The 'time-of-flight' for the species corresponds to the mass of the sample, and a resulting mass spectrum (measured using a mass/charge ratio: m/z) is produced with characteristic peaks for various elements or isotopes.

4.3 BDD Topography

After removal from frozen salt castings, the BDD samples were sonicated in water to remove excess salt and dried with ethanol before analysis. The surface morphology of new and exposed BDD was first studied using scanning electron microscopy (SEM) to visually determine changes to the crystal structure on the grown and nucleation sides. The one sample that showed etching to the surfaces was then evaluated using profilometry to quantify changes to the surface structure, including a topographical height map and roughness factor calculations.

4.3.1 Scanning Electron Microscopy

The BDD coupons used in the following measurements are slightly different morphologies from those used in the previous chapters. In this case, the overall thickness is 0.45 mm, slightly smaller than in **Chapter 2** (0.6 mm) and slightly larger than the material used for the optically transparent electrode in **Chapter 3** (0.375 mm). The grown and nucleation sides of the material used in this body of work are shown in **Figure 4.1**. The grown side in **A)** still has large crystals and is distinctly different from the nucleation side in **B)**, where the surface texture is indicative of where the substrate was previously adhered. The surface structure of the 'bottom' of polycrystalline material corresponds to where crystal sizes start small (μm scale) during the CVD process and grow up to 50 – 100 μm for samples of this thickness.

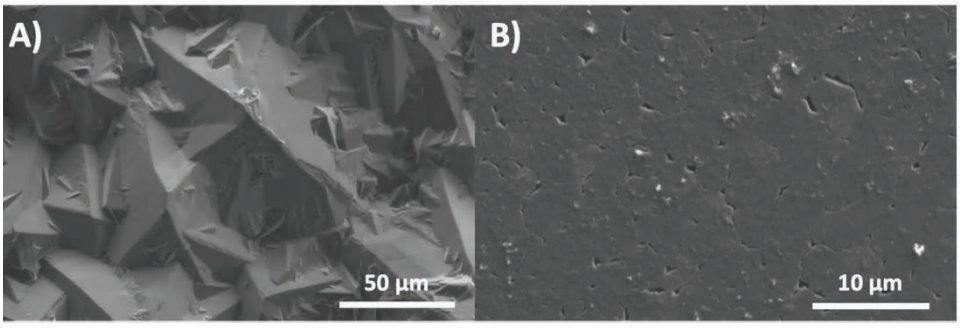

Figure 4.1 SEM of the A) grown and B) nucleation sides of new BDD.

After ten days in the NaCl-KCl (H) environment, there is a significant difference on the grown side of the material, as seen in **Figure 4.2 A)**. Corrosion has occurred at the grain boundaries, at the edges connecting the facets of each crystal, and even in select areas where holes developed on some of the facets of the crystals. This feature follows the expected trend where sp^2-hybridization at the grains would be susceptible to etching

compared to the broader surfaces primarily composed of sp^3-hybridized carbon.[84] Delocalized electrons associated with the sp^2 planes between sp^3 crystal structures are more readily available to react with species like oxygen than larger crystal surfaces where electrons are already occupied in the lattice. However, after the salt was dried and the exposure was performed under oxygen and moisture-free conditions (NaCl-KCl (GB)), the surface appeared unchanged, which is highlighted in **Figure 4.2 B)**.

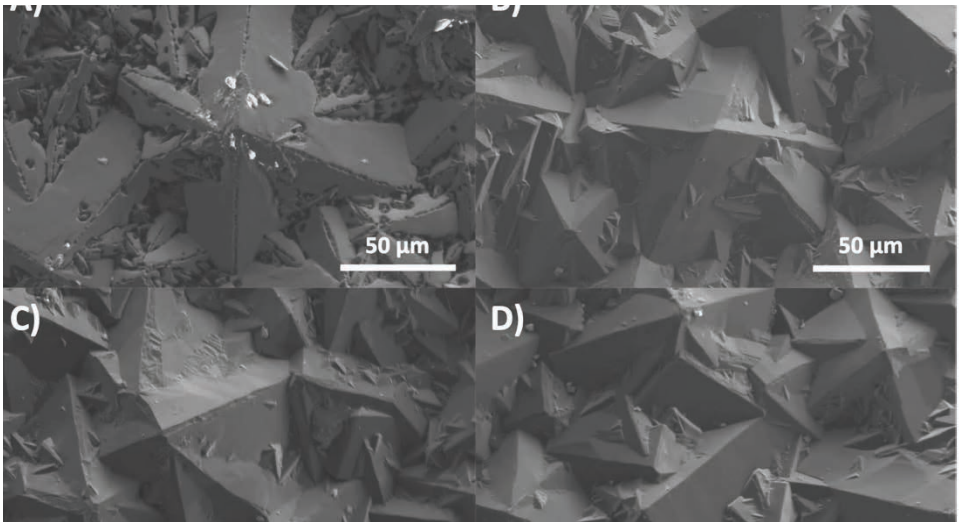

Figure 4.2 SEM of the grown sides of the A) NaCl-KCl (H), B) NaCl-KCl (GB), C) FLiNaK (H), and D) FLiNaK (GB) BDD samples.

However, the untreated fluoride salt in the air system (FLiNaK (H)) also shows no change to the surface in **Figure 4.2 C)**, which is also the case for the dried glovebox fluoride salt melt (FLiNaK (GB), **Figure 4.2D**). Therefore, the grown side of the BDD is most certainly resistant in systems that contain only trace levels of oxygen and moisture, but there is a stark difference between the NaCl-KCl (H) and FLiNaK (H) samples, although neither used dried salt and both were exposed to air for the duration of the soak. Previous

reports of high-temperature oxygen exposure for diamond results in etching like what is seen for the NaCl-KCl (H) sample,[84] indicating that it is possible that the corrosion exhibited here is a result of the increased deliquescence of chloride versus fluoride salts.[182,183] Furthermore, in previous studies where the surface of BDD was fluorinated using non-salt methods, no changes were observed using SEM.[151] Additionally, the 200 °C discrepancy between the temperatures where the chloride (700 °C) and fluoride (500 °C) salts were held should be considered. There is a possibility that corrosion was induced by maintaining a higher temperature, but a logical expectation would be to see at least some degree of etching, even if minimal, on the FLiNaK (H) sample.

For the nucleation side, the NaCl-KCl (H) in **Figure 4.3 A)** again has the most significant transformation compared to the other exposed samples. The grains are more well-defined than the new or other exposed samples, and a degree of crystallinity has appeared across the surface. However, the three other samples may also have some degree of etching at the grain boundaries, as seen in **Figure 4.3 B)**, **C)**, and **D)**, which could be a result of the proximity to the Al_2O_3 crucible considering the nucleation side was face-down for the duration of the exposures. If oxygen escaped the ceramic during the ten-day soak, it would be in direct contact with the nucleation side of the BDD. Nevertheless, the effect is minimal, and the surfaces of NaCl-KCl (GB), FLiNaK (H), and FLiNaK (GB) resemble the micrograph in **Figure 4.1 B)** of the nucleation side of the new BDD.

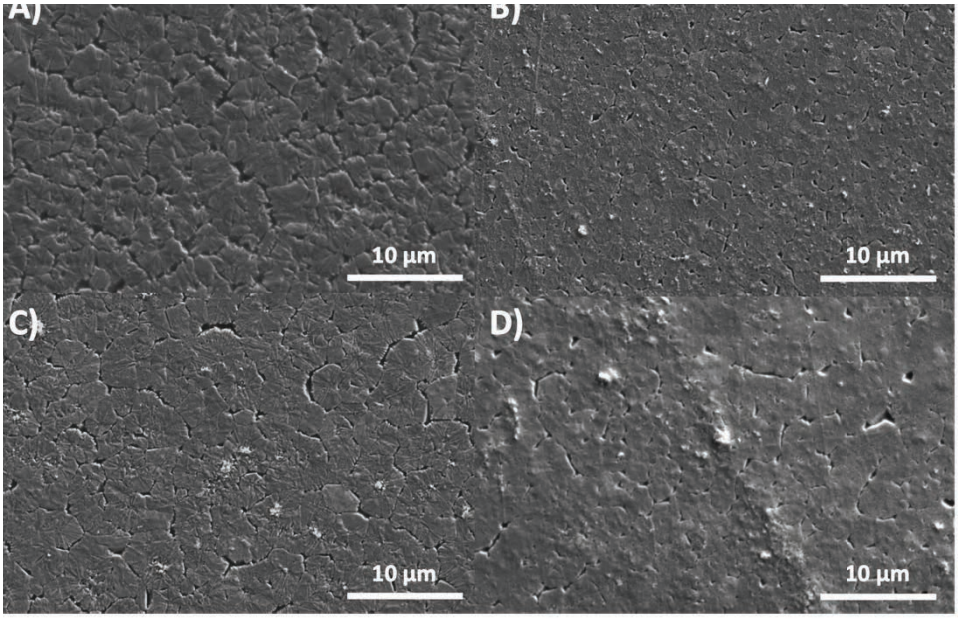

Figure 4.3 S[illegible] nd D) FLiNaK (GB)

4.3.2 Profilometry

Following SEM imaging, the material was examined using profilometry to characterize the roughness of the BDD before and after corrosion occurred. Because corrosion was only seen on the NaCl-KCl (H) sample, the grown and nucleation sides of that piece were compared to the new BDD using profilometry. The topographic features of the other samples were unchanged after exposure based on SEM, so the measurements would be comparable to the new material. After optical images were taken with the microscope, laser scanning across the surface fabricated a three-dimensional height map of the material. The resulting map is accompanied by values for a variety of surface descriptors outlined in **Table 4.3**.[184] The arithmetical mean height (S_a /µm) or 'roughness,' is determined by taking the absolute value of the height difference at each point compared to the mean of the surface. The maximum height (S_z /µm) is the sum of the largest peak

height value and the largest pit depth value. The texture aspect ratio (S_{tr}, 0-1) describes the overall uniformity of the texture where lower values correspond to more uniform surfaces The arithmetic mean peak curvature (S_{pc} /mm^{-1}) indicates rounder surfaces with smaller values and sharper surfaces with larger values. The developed interfacial area ratio (S_{dr}, %) quantifies the percentage of additional surface area that is contributed by texture. Diamond and BDD surface roughness have been studied, but not always using profilometry and often for thin films (nm to tens of μm in thickness) with roughness values on the nm scale.[152-159] The other values determined using profilometry in this study have not been extensively evaluated for diamond, and little to no literature is available for free-standing BDD.

Table 4.3 Quantified material surface descriptors from profilometric measurements.[184]

Characteristic	Symbol	Unit or Value Range	Description
Arithmetical Mean Height	S_a	μm	Roughness
Maximum Height	S_z	μm	Highest peak
Texture Aspect Ratio	S_{tr}	0 - 1	Uniformity
Arithmetic Mean Peak Curvature	S_{pc}	mm^{-1}	Sharpness
Developed Interfacial Area Ratio	S_{dr}	%	Additional surface area due to texture

The material was initially examined using the optical microscope such that an image of the entire sample was constructed for the grown and nucleation sides of the new and NaCl-KCl (H) BDD, shown in **Figure 4.4**. This magnification shows no visible difference between the new and exposed material on the grown side. However, the nucleation side was affected, given the dark ring that appeared around the edge of the sample. Additionally, there are ring-like patterns at various locations across the surface. The center of the nucleation side for the new and exposed pieces was investigated further,

indicated by points **(i)** in **Figure 4.4 B)** and **D)**. Additionally, the inner and outer rings in **C)** are studied closer, as indicated by points **(ii)** and **(iii)** in **D)**. The purple horizontal streaks in **A)** and **C)** are artifacts of the image processing, like the large grid that appears in **B)**.

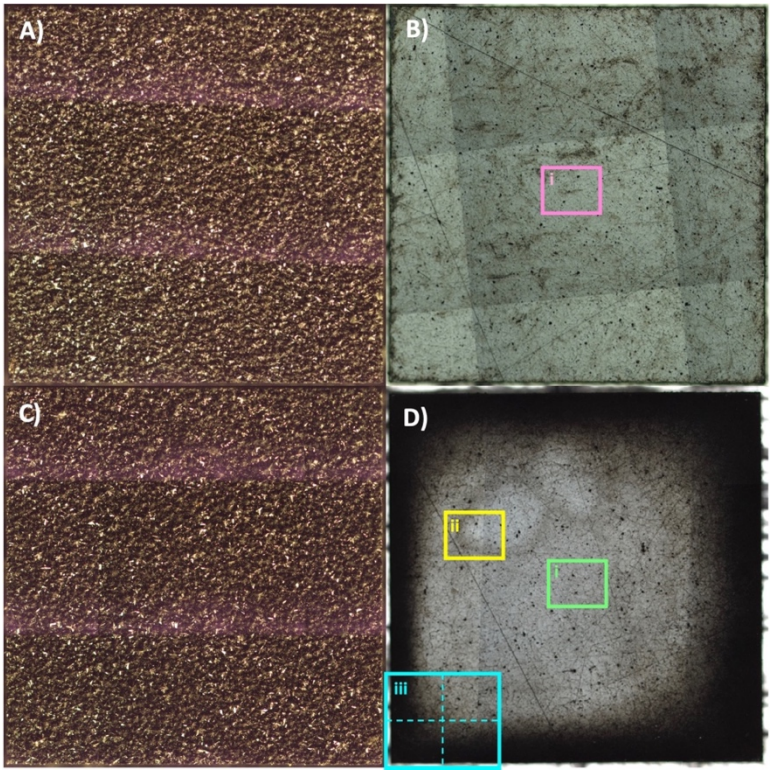

Figure 4.4 Optical images of the grown and nucleation sides of (A and B) new and (C and D) NaCl-KCl (H) exposed BDD.

The grown side of the new BDD was evaluated. An increased magnification of **Figure 4.4 A)** is shown in **Figure 4.5** using an optical image (**A**), a two-dimensional height map (**B**), and multiple angles of a three-dimensional height map (**C**). In the height maps, the maximum relative peak height value (64.247 μm) corresponds to the red regions at the highest points of each crystal, and the relative minimum value (12.922 μm) corresponds to the blue regions describing grain boundaries between the structures. The

height map ranges for the grown side of the new and NaCl-KCl (H) samples are listed in **Table 4.4**.

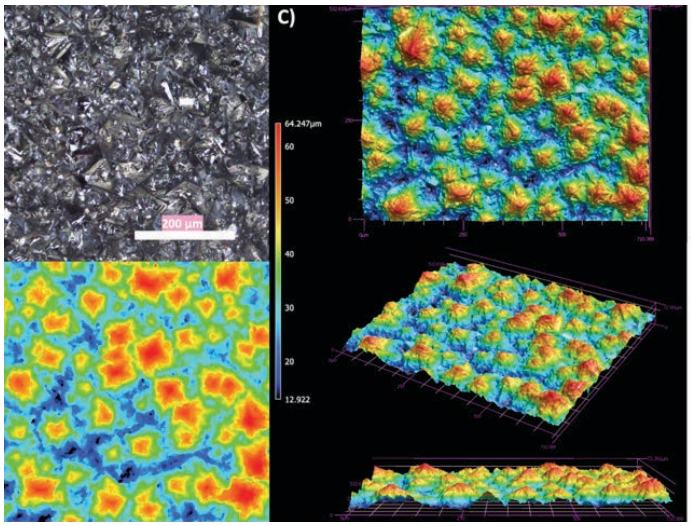

Figure 4.5 Surface structure analysis of the grown side of new BDD. A) optical image with increased magnification, B) 2-dimensional height map, and C) various angles of a 3-dimensional height map.

Table 4.4 Height map ranges for the grown side of the new and NaCl-KCl (H) samples.

NaCl-KCl (H)	62.625	8.632

When comparing the SEM images between **Figure 4.1** and **Figure 4.2**, there is a clear difference between the new and NaCl-KCl (H) BDD samples where the chloride-exposed material experienced corrosion across the surface. However, when viewed by profilometry, those differences are not apparent in either the higher magnification optical image or the height maps shown in **Figure 4.6**, which is an increased magnification of the surface shown in **Figure 4.4 C)**. In this case, the maximum relative peak height is 62.625 µm, and the valleys are lowest at 8.632 µm (**Table 4.4**). These values are comparable to what was determined for the area observed on the new sample, and the difference could

result from the non-homogeneity of the grown side of BDD grown to this thickness. Increased sampling and statistical analysis could be performed to understand better the significance of any differences determined here, which extends to the quantified surface characteristics discussed below.

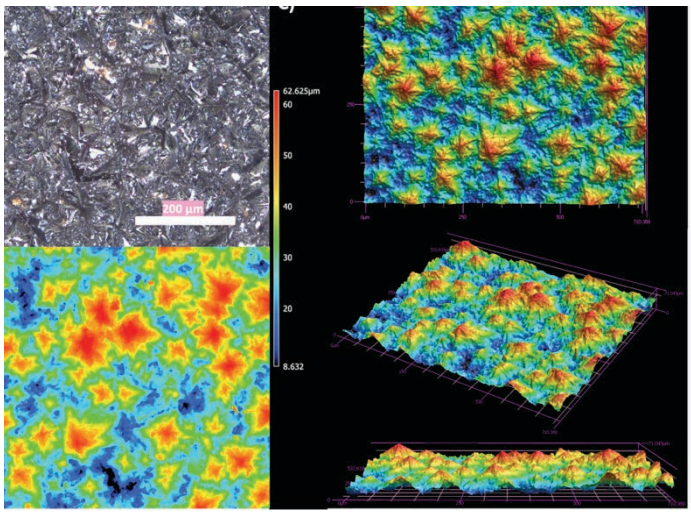

Figure 4.6 Surface structure analysis of the grown side of NaCl-KCl (H) exposed BDD. A) optical image with increased magnification, B) 2-dimensional height map, and C) various angles of a 3-dimensional height map.

Various characteristics of the surface were quantified and are listed in **Table 4.5**. In the regions analyzed for the new BDD, S_a (roughness) was calculated to be 8.71 µm, which is significantly greater than what is typically reported for BDD films (typically nanoscale),[152-158] but not much larger than what was determined for the NaCl-KCl (H) sample, 8.63 µm. However, the diamond films where profilometry has been performed were often significantly thinner and, therefore, had smaller crystals, resulting in smoother surfaces. Additionally, S_z in the studied areas was found to be 72.4 and 71.0 µm, S_{tr} is 0.919 and 0.902, S_{pc} is 3332 and 3319 mm^{-1}, and S_{dr} is 1.01 and 1.17 for the new and NaCl-KCl (H) samples, respectively. These values are similar in both cases, and each

corresponds to large maximum peak heights for non-uniform surfaces with sharp structures. On the new material, an excess of 1% of the surface area is attributed to the texture of the crystals, and this value increased to 17% after corrosion occurred. While this difference is not visible in the profilometry figures, it corresponds to the etching seen in the SEM micrographs at the grain boundaries, edges between the facets on each crystal, and on the facets in some areas. Values of this nature are not readily available in previous reports for polycrystalline BDD to make reasonable comparisons. However, this information provides a relative baseline to compare with the NaCl-KCl (H) sample.

Table 4.5 Surface roughness characterization of the grown side of BDD before and after exposure to NaCl-KCl (H).

Sample	Side	S_a (μm)	S_z (μm)	S_{tr} (0-1)	S_{pc} (mm^{-1})	S_{dr} (%)
New	Grown	8.71	72.4	0.919	3332	1.01
NaCl-KCl (H)	Grown	8.63	71.0	0.902	3319	1.17

The nucleation side of the BDD shows a vastly different topography, which is evident using both SEM and profilometry. **Figure 4.7** is a magnification of region **(i)** in **Figure 4.4 B)** and includes an optical image of the region (**A**), a two-dimensional height map (**B**), and multiple angles of a three-dimensional height map (**C**). Here, the highest measured surface is only 11.563 μm, and the lowest is 10.357 μm, a significantly smaller difference compared to the surface structures of the grown side. This range is compared to that of the NaCl-KCl (H) sample in **Table 4.6**. In this case, there are select locations with taller structures, but most of the surface falls along the lower end of the height spectrum.

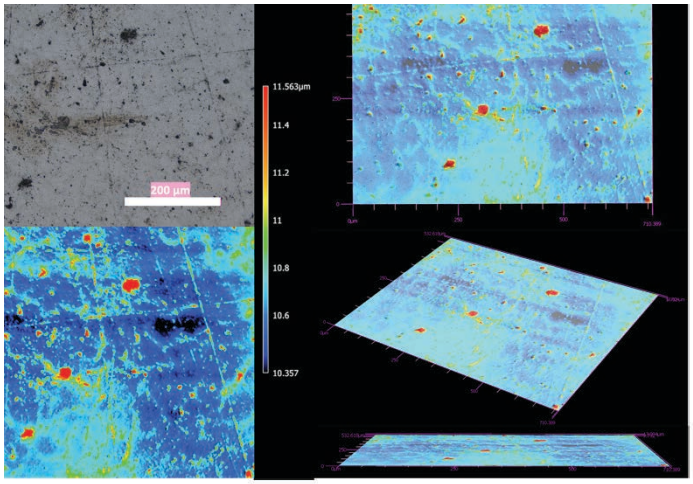

Figure 4.7 Surface structur nage with increased magnification, B) 2-dimensional height map, and C) various angles of a 3-dimensional height map.

Table 4.6 Height map ranges for the nucleation side of the new and NaCl-KCl (H) samples.

The NaCl-KCl (H) nucleation side shows a different height distribution than the new piece. **Figure 4.8** magnifies region **(i)** in the middle area of **Figure 4.4 D)**. The internal and external rings will be discussed in more detail below. For this area, instead of most of the surface residing in the lower end of the height spectrum, the corroded piece exhibits significantly more of the surface at the mid-range (9.049 to 7.816 µm, listed in **Table 4.6**). Additionally, roughness increases across the material regardless of the height in each area, which corroborates the increase in grain boundary depth shown in **Figure 4.3 A)**. The peak height in this region is also slightly lower than the lowest portions measured on the new sample. However, further sampling and analysis should be performed to calculate standard errors for each sample and determine if there is statistical significance between the samples.

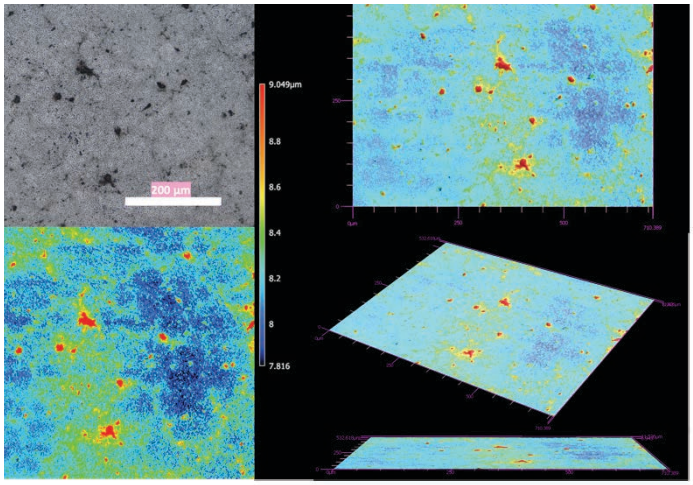

Figure 4.8 Surface structur BDD. Central region (i): A) optical image with increased magnification, B) 2-dimensional height map, and C) various angles of a 3-dimensional height map.

Figures of merit describing the nucleation side of each sample are listed in **Table 4.7**. Significantly different from the grown side, the value for S_a for the nucleation side of the new material was calculated as 0.120 µm. This value increased to 0.136 µm for the NaCl-KCl (H) sample, which is expected given the change in texture observed visually and the smaller scale of the height distribution for the nucleation sides overall. Although much less than the grown side, these values for roughness are still relatively large for what has been previously reported for BDD films (nanometer to sub-nanometer scale).[152-158] Additionally, S_z in the studied areas on the nucleation sides was found to be 4.47 and 4.58 µm, S_{tr} is 0.623 and 0.712, S_{pc} is 362.0 and 547.4 mm^{-1}, and S_{dr} is 0.0129 and 0.0252 for the new and NaCl-KCl (H) samples, respectively. Each of these descriptors is significantly smaller than what was observed for the grown sides. In both cases, each sample corresponds to much smaller maximum peak heights for moderately non-uniform surfaces with rounder structures than the grown side of the respective samples. On the new

material, an excess of 0.0129% of the surface area is attributed to the texture of the surface, and this value increased to 0.0252% after corrosion occurred. Again, these contributions are fractions of what was observed for the large crystals on the grown side, but the value almost doubled after exposure to the air-exposed salt system.

Table 4.7 Surface roughness characterization of the nucleation side of BDD before and after exposure to NaCl-KCl (H).

Sample	Side	S_a (μm)	S_z (μm)	S_{tr} (0-1)	S_{pc} (mm^{-1})	S_{dr} (%)
New	Nucleation	0.120	4.47	0.623	362.0	0.0129
NaCl-KCl (H)	Nucleation	0.136	4.58	0.712	547.4	0.0252

On both samples, the grown sides are significantly taller, sharper, less uniform, and the texture contributes much more to the overall surface area. These differences quantify the visual observations via SEM, optical images, and height maps. The grown and nucleation sides changed in different ways when comparing the new and exposed samples. The changes were minimal on the grown side after exposure. The roughness, maximum peak height, and sharpness decreased very slightly, while the uniformity and additional surface area because of texture both slightly increased. The physical structure of the crystals in the BDD did not truly change shape, but the way the value for sharpness is calculated affected the overall description due to the corrosion observed on the surface in various areas.

After exposure on the nucleation side, the roughness and maximum peak height increased. Although the material did not grow, the value for S_z is determined by considering the highest height value combined with the lowest, and because of the corrosion, the lowest point on the surface increased the overall ‘maximum peak height’

calculation. Additionally, the uniformity decreased, the sharpness increased, and the surface area contributed by texture increased. These factors support the increased texture in the height maps when comparing **Figure 4.7** and **Figure 4.8**.

Two unexpected features appeared on the nucleation side of the NaCl-KCl (H) sample. Multiple small, dark rings appeared in the upper portion of **Figure 4.4 D)**, and a large dark ring appeared around the edge of the whole sample. Measurements were performed in each of these areas. An increased magnification optical image of region **(ii)** in **Figure 4.4 D)** is shown in **Figure 4.9 A)** along with a two-dimensional (**B**) and three-dimensional (**C**) height map. This portion of the surface represents the bottom left edge of one of the small rings where the height ranges from 9.066 μm to 7.716 μm. The ring pattern is visible in the optical image and height maps, indicated by the slightly darker and yellow vertical area. These color variations indicate that the ring is elevated compared to most of the surface, but an explanation for this is unclear. One possible explanation could be related to oxygen release from the Al_2O_3 crucible during the exposure, producing a bubble of air between the crucible bottom and nucleation side (facing down) of the BDD. This would selectively etch the central portions of the material more rapidly than the edges. However, previously published tests of Al_2O_3 corrosion resistance in NaCl-KCl, specifically, found that little-to-no change was found to the surface of the ceramic after 400 hours of exposure to the salt at 800 °C,[185] meaning the likelihood of an entire oxygen bubble forming during the present study (250 hours at 700 °C) is highly unlikely. A similar process that may explain this phenomenon would be if the BDD etching process resulted in the production of gases like CO_2 that may have been trapped, further reacting with the

surface of the material and unable to escape. Again, this mechanism requires further investigation before a conclusion can be made.

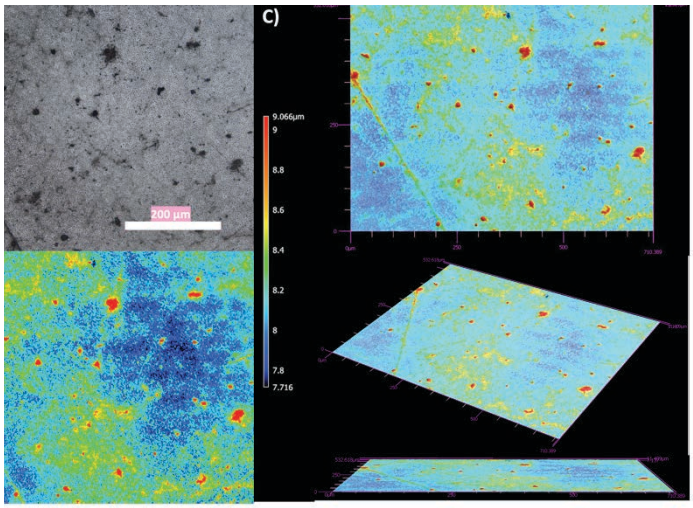

Figure 4.9 Surface structure analysis of the nucleation side of NucPKR (1) exposed BDD. Internal ring region (ii): A) optical image with increased magnification, B) 2-dimensional height map, and C) various angles of a 3-dimensional height map.

The large ring encompassing the four edges of the sample was investigated by increasing the magnification of four areas in the bottom left corner, region **(iii)** in **Figure 4.4 D)**. The four areas are illustrated using optical images (left) and two-dimensional height maps (right) in **Figure 4.10**. The four regions are not a perfect stitching of the bottom left corner but generally represent that sample area. The heights range from 9.537 µm to 7.756 µm, comparable to those observed in the previous areas. However, like in the case of the smaller internal ring, the dark regions observed in the optical image of the bottom corner correspond to the larger end of the height spectrum. Again, there is no explanation for this feature that is immediately obvious and should be the focus of further investigation.

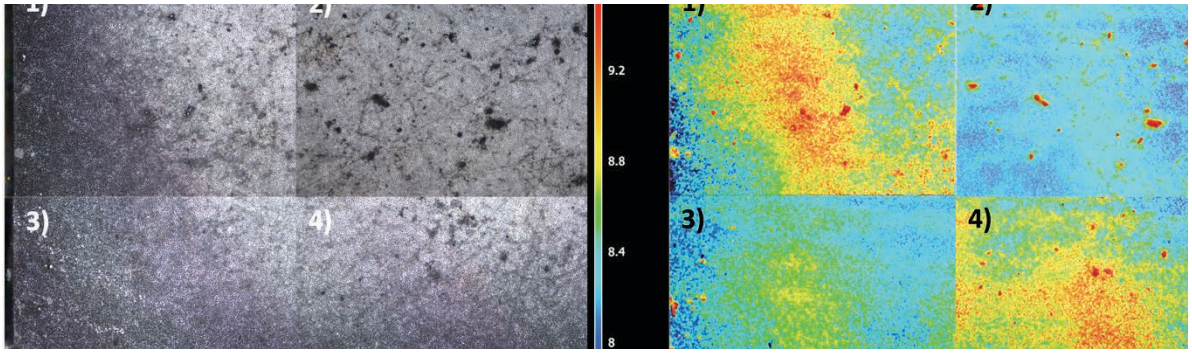

Figure 4.10 Surface structure analysis of the nucleation side of NaCl-KCl (H) exposed BDD with optical images (left) and their corresponding height maps (right). External ring region (iii): 1) left side edge, 2) central region, 3) corner edge, 4) bottom edge.

4.4 BDD Surface Chemistry

To determine if the exposure to molten salts changed the surface of the BDD, the grown and nucleation sides were investigated using Raman spectroscopy, X-ray photoelectron spectroscopy (XPS), and Time-of-Flight Secondary Ion Mass Spectroscopy (ToF-SIMS). Each technique uses a unique approach to probing the BDD crystal structure and exploring material composition.

4.4.1 Raman Spectroscopy

The first measurement performed to study the surface chemistry of the grown and nucleation sides of the material was Raman spectroscopy. Raman has been used extensively to study BDD in various forms, primarily identifying sp^3 and sp^2 hybridized carbon, residual silicon from the substrate material, and boron incorporation.[43,156,160-172]

The grown and nucleation sides of the new BDD were first analyzed as a baseline measurement to compare the exposed samples. The spectra are overlain in **Figure 4.11**,

and it is clear to see that the primary features present include the sharp sp^3 peak at 1332 cm^{-1} on the grown side, which corresponds to the first-order diamond Raman line expected at 1330 cm^{-1} for C-C stretching, whose slight positive shift is indicative of the large grain size.[165,169,172] The same sharp sp^3 peak appears within the broader features associated with the G peak for amorphous carbon ranging from 1520-1580 cm^{-1}.[165] In this case, the sp^3 peak is at precisely 1330 cm^{-1} due to the smaller grain size for the nucleation side. It is expected that a 520 cm^{-1} first-order silicon Raman peak[165] would appear, considering the nucleation side was previously attached to a silicon substrate during the chemical vapor deposition (CVD) growth process, but if present, it is lost in the noise caused by a broad peak around 500 cm^{-1}. These results correspond to the expected carbon structures associated with the large crystals on the grown side that are primarily sp^3 carbon, and the increased grain boundaries on the nucleation side introduce a significant amount of sp^2 carbon. However, the origin of the peak at approximately 1240 cm^{-1} is unclear. There have been reports of broad peaks in the regions of 500 cm^{-1} and 1230 cm^{-1} that may be associated with damage to the crystal structure because of the ion beam (consistent with the phonon density of states of diamond), or they may be indicative of boron incorporation into the lattice.[161,163-166] Both phenomena are plausible explanations, but the likely source is doping at boron concentrations $\geq 10^{20}$ cm^{-3} and various reports of this result.[162-164,167,169]

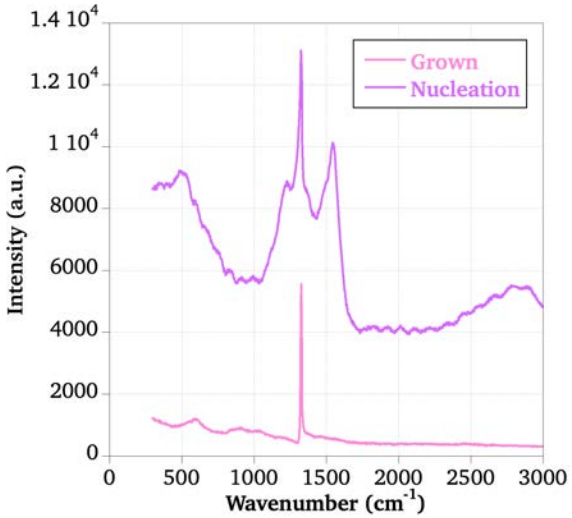

Figure 4.11 Raman spectra of the grown and nucleation sides of new BDD.

After exposure to the molten salts, it was anticipated that the surface chemistry would be altered, potentially with respect to termination of the surface where various species can form bonds with the surface or carbon hybridization as the crystals are etched (in the case of the NaCl-KCl (H) sample) converting sp^3 to sp^2 carbon. Typically, BDD surfaces are either oxygen or hydrogen-terminated; however, previous studies have found minimal changes in Raman spectra based on termination.[160] Minimal work has been performed in the chlorination of BDD, but quite a few reports are available for surface fluorination and studied with Raman spectroscopy. For example, plasma-induced fluorination and chlorination of BDD found no change with respect to the sp^3 and sp^2 carbon, and no other changes were reported.[151,173,176] However, with Raman spectroscopy at 1096, 1251, and 1347 cm^{-1}, C-F stretching was observed for BDD that was grown using a BF_3 source during the CVD process (as opposed to B_2H_6, for example) [169]. Yet another study used a thermal reaction of elemental fluorine with undoped diamond and found the same three peaks for C-F stretching as the BF_3-sourced BDD.[186] Furthermore, fluorine was

physisorbed for BDD film via electrochemical modification in tetrabutylammonium tetrafluoroborate and studied with Raman spectroscopy, but the resulting peaks were most likely a result of the monolayer composition as opposed to direct C-F bonding.[170] Of these examples, none involve the exposure of BDD to high-temperature halogen salts to provide a clear expectation of what should be observed on either the grown or nucleation sides of the material in the present study.

Raman spectra of the grown and nucleation sides on new, NaCl-KCl (H), NaCl-KCl (GB), FLiNaK (H), and FLiNaK (GB) samples are shown in **Figure 4.12 A)** and **B)**. Although there may be variation in intensities, the same features seen on the new samples are present for the exposed material, with no new artifacts to report. Compared to previous studies that claimed to chlorinate or fluorinate the surface of BDD, the material in this case seems unchanged. The same responses for sp^2, sp^3, B, and Si are present, but the anticipated peaks for C-F, any indication of possible C-Cl formation, or any other factor published previously for halogenation of BDD surfaces are absent. The lack of change in the Raman spectra does not necessarily rule out changes to the surface chemistry, considering plasma-induced fluorination or chlorination did not change Raman spectra.[151,173] However, any changes that may have occurred do not reflect what has been previously reported in the literature for other techniques to incorporate F or Cl into the material.[169,170] Further investigation is required to fully characterize the surfaces of BDD after exposure to chloride and fluoride salts.

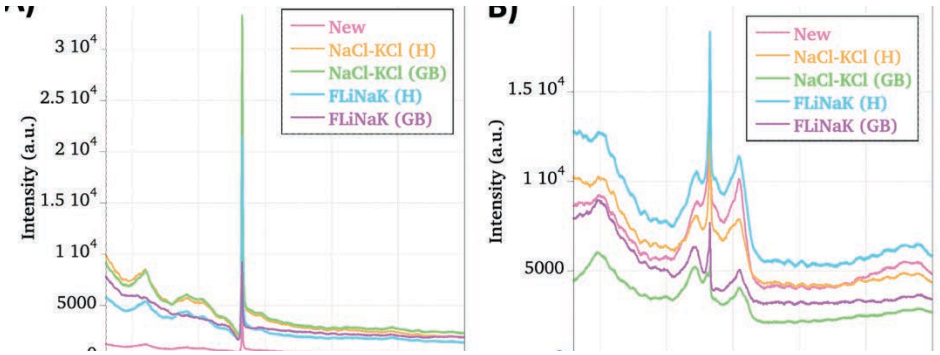

Figure 4.12 Raman spectra of the A) grown and B) nucleation sides of new, NaCl-KCl (H), NaCl-KCl (GB), FLiNaK (H), and FLiNaK (GB) exposed material.

4.4.2 X-ray Photoelectron Spectroscopy

X-ray photoelectron spectroscopy (XPS) is another non-destructive technique that can further explore surface chemistry through elemental identification at and just below the surface of the material (nm scale). If bonds like C-F or C-Cl are formed on the surface of the BDD after exposure to NaCl-KCl or FLiNaK, XPS should be able to describe these features. In the case of C, for example, the photoelectrons detected typically originate from the core 1s orbital in BDD with a BE of 284 eV.[170,187-192] Due to logistical constraints, the following measurements include new, NaCl-KCl (GB), and FLiNaK (GB), but not NaCl-KCl (H) or FLiNaK (H). It is not expected that corrosion or the air-exposed environment would affect the results based on the lack of change in SEM images (outside of corrosion seen for NaCl-KCl (H)) and Raman shifts. On the new samples, the primary peak expected is the C1s representative of C-C bonds on the surface, and this is observed at 284 eV for both the grown and nucleation samples seen in **Figure 4.13**.[170,187-193]

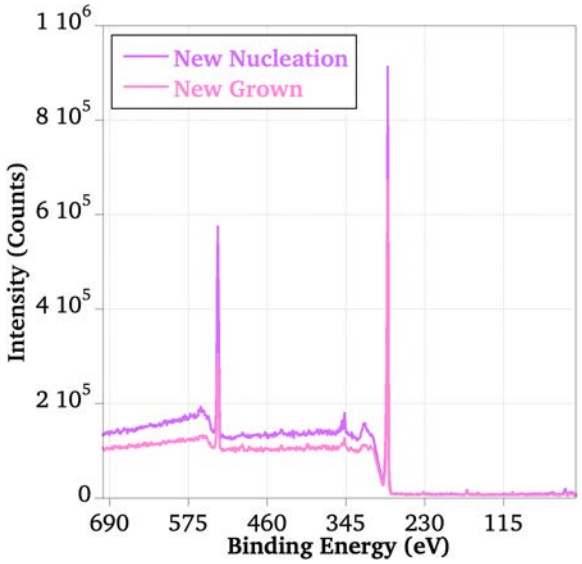

Figure 4.13 XPS of the grown and nucleation sides of new BDD.

There is literature available identifying differences in carbon hybridization by observing slight positive shifts in BE (<1 eV),[194] so it is possible that this phenomenon would be observed when comparing each side of the BDD. Although the increased presence of sp^2 hybridized carbon on the nucleation side as shown by Raman spectroscopy, the delocalized electrons in the pi bonding of polycrystalline diamond are not in the form of C=C double-bonding like in hydrocarbon molecules but rather serve as connecting planes between sp^3 hybridized material. Therefore, it is expected that both sides would have similar, if not identical, features of single C-C bonds.[195] In addition to evidence of carbon, there is a strong O1s peak at 532 eV representative of C-O bonding on the surface of each side.[190,193] Reports of BDD XPS spectra do not include the presence of B (expected at 190 eV),[170,191] which is reflected for both the grown and nucleation sides.

Like Raman spectroscopy, several studies have been published for XPS spectra following the fluorination and occasional chlorination of BDD using various

methods.[151,170,173-176] If fluorination occurs in the form of C-F bonds on the surface, a peak at 687 eV is expected for the F1s photoelectron ejection.[170,174-176,193,196] Again, there is a significant gap in the literature regarding the chlorine functionalization on the surface of BDD, but one example using plasma-induced chlorination corroborates other samples of material with C-Cl chemistry that have shown peaks at 200 eV for this feature (Cl2p photoelectrons).[173,197] However, **Figure 4.14** shows that the spectra for the grown (**A**) and nucleation (**B**) sides of new, NaCl-KCl (GB), and FLiNaK (GB) samples have identical features. Again, the C1s and O1s peaks are the only two significant peaks, and they appear at the expected BE values based on literature and when compared to the new material. Unlike previous reports of fluorinated BDD surfaces, there is no presence of an F1s peak, or in the case of general C-Cl bonds, there is no evidence for the Cl2p peak.

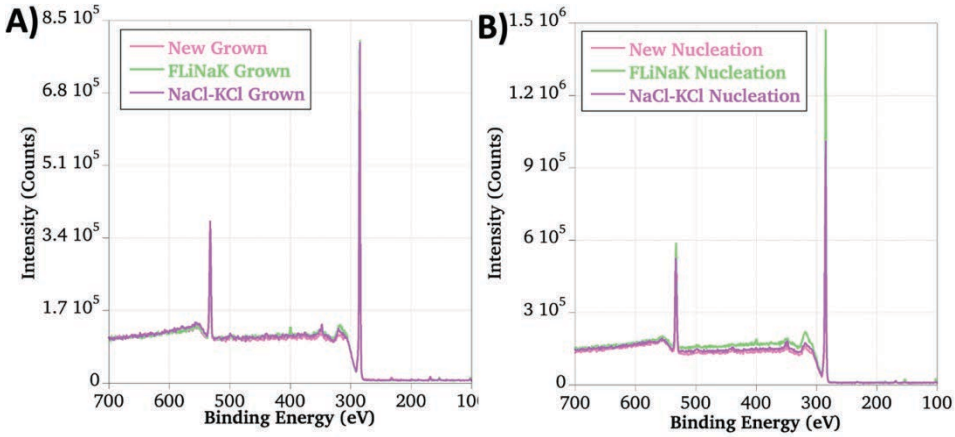

Figure 4.14 X
exposed mate

As in the case of Raman spectra, there is no apparent difference between the new and exposed samples using XPS to characterize the surface chemistry of BDD. When comparing to previous claims of fluorination and C-Cl bonds, neither side of any sample

shows the presence of these features. Only C1s and O1s peaks are present, indicating only C-C and C-O bonding were detectable using this technique. Given the sensitivity of XPS and the results discussed in the previous section, it may be inferred that the material is inert in molten chloride and fluoride salts. However, further analysis may be performed to understand better if other changes aside from halogenation have occurred on the surfaces of the material, like ToF-SIMS.

4.4.3 Time-of-Flight Secondary Ion Mass Spectroscopy

Time-of-flight secondary ion mass spectroscopy (ToF-SIMS) is yet another non-destructive analysis technique sensitive to compositions of sample surfaces to nm scale depths. This technique has been applied to materials comprising both diamond and non-diamond carbon,[178,198-202] and has been extended to BDD where the primary characteristics include principal components[203] in the form of hydrocarbon, $H_xC_yO_z$ compound, borocarbon, and borohydride ion fragments.[177-181] However, the only comparable literature for this study with respect to material changes after a surface treatment is a measurement performed on an undoped, single-crystal diamond after exposure to LiCl-KCl for five days which found Li leaching into the crystal lattice.[204] Still, there is no readily available literature where diamond material exposed to fluoride salts, where polycrystalline diamond is exposed to molten salts, or where diamond doped with boron is exposed to molten salts of any kind have been studied using this method, much like the techniques discussed previously in this chapter.

The grown side of the new, NaCl-KCl (H), and FLiNaK (H) samples were measured using ToF-SIMS after a light sputtering with Ar^+ for 2 minutes prior to analysis to remove surface contaminants. A 250 × 250 μm region was analyzed using a $^{69}Ga^+$ liquid metal ion gun at a base pressure of 5×10^{-10} Torr. Although the BDD was dried with ethanol after removing the salt with sonication in deionized water, there was apparent off-gassing while the samples were being introduced to the instrument. The ion sputtering pre-treatment likely helped to remove much of the species that would be present because of the remaining water.

Each sample showed various levels of the same species and the individual isotopes detected along with principal components as negative or positive ion fragments are listed in **Table 4.8**. The elements included in the detection of negative ion fragments include H, C, O, F, Na (not identified as an individual isotope peak, only as a part of a fragment ion), and Cl, and the positive ion fragments were composed of H, Li, B, C, Na, and K. However, the new sample should not have salt components on the surface (Li, Na, K, F, or Cl), the NaCl-KCl (H) sample should not have Li or F species, and the FLiNaK (H) sample should not have Cl-containing fragments. One explanation could be related to the off-gassing of water during sample introduction which may have induced cross-contamination. The levels to which this occurred is discussed in more detail below for each sample.

Table 4.8 Isotopes and principal components in the negative and positive fragment ions detected for the grown side of the BDD samples.

Fragment Ion Charge	Isotope Peaks	Principal Components
Negative	$^1H^-$, $^{12}C^-$, $^{16}O^-$, $^{19}F^-$, $^{35}Cl^-$, $^{37}Cl^-$	$^{12}C_2^-$, $^{12}CH^-$, $^{12}C_2{}^1H^-$, $^{12}C_2{}^1H_2^-$, $^{12}C_x{}^1H_y^-$, $^{16}O^1H^-$, $^{23}Na^1H^-$, $^{35}Cl^1H^-$, $^{37}Cl^1H^-$,
Positive	$^1H^+$,$^6Li^+$, $^7Li^+$, $^{10}B^+$, $^{11}B^+$, $^{12}C^+$, $^{23}Na^+$, $^{39}K^+$, $^{40}K^+$, $^{41}K^+$	$^{12}C_2{}^+$, $^{12}C_2H_x{}^+$, $^{12}C^1H^+$, $^{12}C^1H_2{}^+$, $^{12}C^1H_3{}^+$, $^6Li_2{}^+$, $^7Li_2{}^+$, $^{23}Na^1H^+$, $^{39}K^1H^+$, $^{40}K^1H^+$

The negative and positive ion fragment patterns for the new sample are shown in **Figure 4.15 A)** and **B)**, respectively. The negative pattern has significant $^{1}H^{-}$ and $^{16}O^{-}$ peaks and a range of hydrocarbons. Additionally, there was some evidence of $^{19}F^{-}$, $^{35}Cl^{-}$, and $^{37}Cl^{-}$ isotopes, where the Cl appeared at the expected isotopic ratio of 75-25 % (^{35}Cl-^{37}Cl),[205] in addition to ClH^{-} compounds containing both isotopes at the appropriate ratio. The positive fragment pattern included hydrocarbons in addition to relatively large amounts of Na and the three naturally occurring isotopes of K (A = 39, 40, and 41). However, the K isotopes did not align exactly with the expected 93.25-0.01-6.73 % ratio,[206] which is likely due to the presence of $^{39}KH^{+}$ and $^{40}KH^{+}$, which affected the remaining fragment pattern and increased the relative amount of $^{41}K^{+}$ identified.

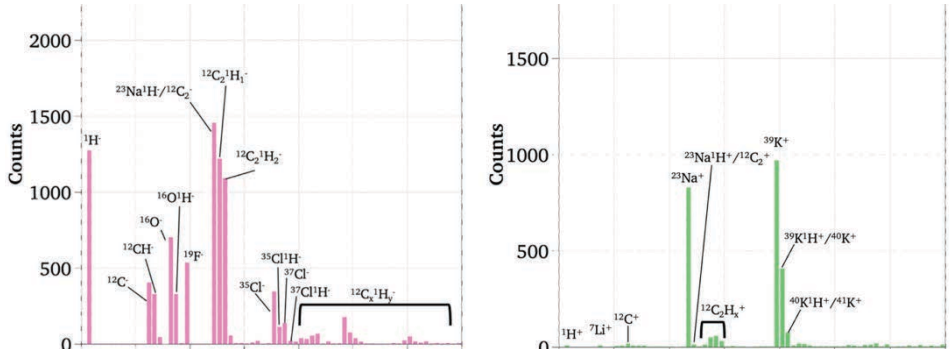

Figure 4.15 A) Negative and B) positive ion fragment patterns for the grown side of new BDD.

The resulting ion fragment patterns for the NaCl-KCl (H) sample are shown in **Figure 4.16** where **A)** describes the negative ion fragments and **B)** describes the positive ion fragments. Both patterns were like that of the new sample, but in the negative ion fragments, the two Cl isotopes had a much larger presence, as expected. However, the

$^{35/37}ClH^-$ was not detected in this measurement, which indicates that it may have been a product of the cross-contamination during the water off-gassing during sample introduction. Additionally, the presence of $^{16}O^-$ and $^{19}F^-$ decreased significantly compared to the new sample, and there was minimal detection of hydrocarbons within the mass range of 40 to 60 m/z. The positive fragment pattern was also like the new sample, but a mass 24 m/z peak developed, which was identified as either $^{12}C_2^+$ or $^{23}Na^1H^+$. The peak for isotopic $^{23}Na^+$ decreased compared to the new sample, therefore, $^{23}Na^1H^+$ is likely to be present due to the trace amounts of NaCl salt that likely remained following exposure.

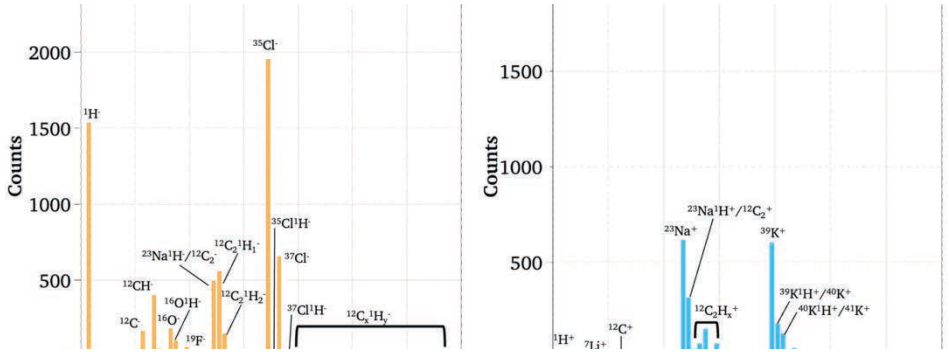

Figure 4.16 A) Negative and B) positive ion fragment patterns for the grown side of NaCl-KCl (H) BDD.

The negative and positive ion fragment patterns for the FLiNaK (H) sample are shown in **A)** and **B)** of **Figure 4.17**. Much like the new sample, the negative fragment pattern shows a large $^1H^-$ peak and evidence of $^{35/37}ClH^-$. However, the intensities of $^{16}O^-$ and $^{19}F^-$ were greater than for either of the other two samples, and overall, the ion intensity yields were largest for this sample with respect to both the negative and positive ion fragments. The positive fragment pattern is very similar to that of the new sample, but

with greater intensities for $^{23}Na^+$ and all three isotopes of K^+, which corresponds to the exposure to NaF and KF.

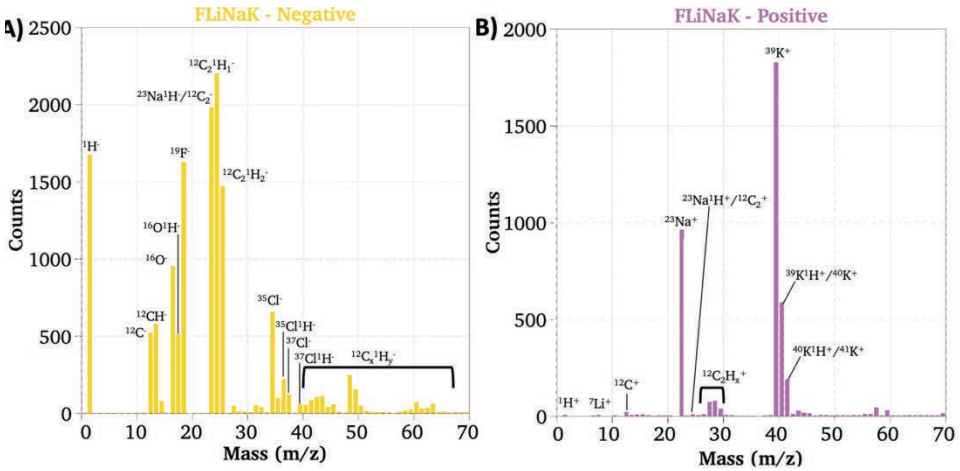

Figure 4.1)D.

Additionally, light weight principal components may appear at low mass values but can be overshadowed by the intense peaks of larger species with higher mass values. Therefore, the positive ion fragment patterns for additional species (< 20 m/z) are shown in **Figure 4.18** for the new (**A**), NaCl-KCl (H) (**B**), and FLiNaK (H) (**C**) samples. A range of hydrocarbon ion fragments appeared, like at higher masses, in addition to $^1H^+$ peaks for each sample at greater intensities for NaCl-KCl (H) and FLiNaK (H). Additionally, the two naturally occurring isotopes for Li (A = 6 and 7) and B (A = 10 and 11) were visible. Unlike the previous reports for ToF-SIMS of BDD,[177-181] there are no BH or BC principal components on any of the three samples, only signals for the two naturally occurring isotopes. Additionally, the B isotopes should follow a ratio of 20-80 % for ^{10}B-^{11}B and the Li isotopes are expected to appear at a ratio of 7.6-92.4 % for ^6Li-^7Li.[207,208] The FLiNaK (H) sample showed the greatest intensity for the ^7Li, which corresponds to the LiF exposure in

the FLiNaK, and it was also the only sample to show both isotopes at the expected ratio. This trend, in addition to the generally higher intensity yields on the previously discussed fragment patterns for the FLiNaK (H) sample, may be a result of the large $^{16}O^-$ peak, which is known to enhance secondary ion yield for electropositive species (e.g., Li, B, Na, and K isotopes).[209,210] Furthermore, the $^{16}O^-$ peaks for the new and NaCl-KCl (H) samples which are lower and lowest, respectively, which aligns with their relative intensities for positive fragment ion patterns. The higher intensity of B isotopes for the FLiNaK (H) sample compared to the new and NaCl-KCl (H) samples supports this hypothesis as well. However, regardless of the $^{16}O^-$ peak intensity for NaCl-KCl (H), the lower mass hydrocarbon positive ion fragments are relatively strong intensity yields, which may be a result of the corrosion observed using SEM that could have graphitized the BDD due to high-temperature oxygen exposure given the non-dried salt melted under non-inert conditions.[84]

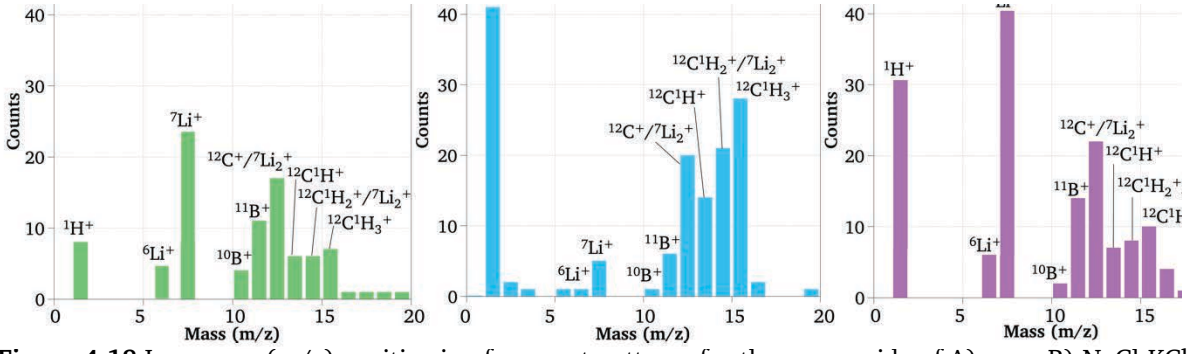

Figure 4.18 Low mass (m/z) positive ion fragment patterns for the grown side of A) new, B) NaCl-KCl (H), and C) FLiNaK (H) BDD.

The culmination of data from ToF-SIMS of the new, NaCl-KCl (H), and FLiNaK (H) samples provided a wealth of information regarding the species at the surface of the

material. However, species that did not appear were indications of changes to the surface with respect to termination or bonding of the carbon to salt species, including C-F or C-Cl bonds that would be expected following the fluorination or chlorination of the BDD. The salt components that appeared are, instead, likely the result of the highly sensitive technique detecting residual, trace levels of salt on the surface that remained even after sonication.

4.5 Conclusions

In this chapter, the surface structure and chemistry of the grown and nucleation sides of BDD were investigated before and after exposure to NaCl-KCl and FLiNaK either in air or using thermally dried salts in an inert glovebox. The surface of the BDD was visually inspected using SEM to determine morphological changes or lack thereof, for the grown and nucleation sides after exposure. Like the previous chapters, the free-standing BDD showed two distinctly different crystal structures on the grown and nucleation sides, given the thickness of the material. The only notable change visually observed was for the NaCl-KCl (H) sample, where corrosion was observed at grain boundaries, the edges between facets of individual crystals, and, in some cases, holes appeared on the facets of the crystals.

On the sample that did experience corrosion (NaCl-KCl (H)), profilometry was performed to quantify changes to the surface, like roughness, uniformity, and sharpness. The values were significantly different for the grown and nucleation sides on the new and exposed material, given the differences viewed using SEM and the optical microscope

portion of the profilometry measurement. After exposure, there was a slight change to the surface due to etching on the grown and nucleation sides. More surface locations should be sampled since there are inherent differences for any given portion of the large crystals on the grown side to determine the statistical significance of these differences. Another feature observed using this technique was a series of dark rings that appeared on the nucleation side of the BDD after exposure to the water and oxygen-containing NaCl-KCl. It is unclear why they developed, especially considering the rings are greater in height than the rest of the nucleation side. This phenomenon requires further investigations regarding corrosion mechanisms and environmental variations, including moisture content in the salt, temperature, and crucible material during exposure.

The surface chemistry was also studied using a complementary suite of techniques that approach speciation and elemental analysis from various perspectives by probing distinctive features of the sample, including molecular vibrations (Raman), photoelectric excitation (XPS), and mass spectroscopy of dislodged portions of the material (ToF-SIMS). There was virtually no change after exposure to the grown or nucleation sides in the chloride or fluoride samples. Although ToF-SIMS provided the only indication of salt components, their speciation indicates that they are likely residual from exposure rather than evidence of changes to the surface chemistry (i.e., termination or bond formation).

However, while Raman was used to study all four exposed samples, XPS was only performed on the GB samples, and ToF-SIMS was only performed on the H samples, given their readiness at the time of instrument availability. Further studies could include XPS on the NaCl-KCl (H) and FLiNaK (H) samples, but differences are unlikely given that the only

variation seems to be corrosion that occurred on the chloride sample. Additionally, steps could be taken to better clean and dry the surfaces of the BDD before performing ToF-SIMS, but this would not be likely to affect the formation of C-F or C-Cl bonds. If measurements were performed on the NaCl-KCl (GB) sample to compare with the NaCl-KCl (H) sample, it could be possible to compare the presence of hydrocarbons that may have been a result of graphitization due to corrosion only seen on the NaCl-KCl (H) sample.

Although no significant changes were observed using these techniques, other approaches must be taken to investigate to deem BDD a completely inert material in molten chloride and fluoride salts. For example, contact angle analysis, atomic force microscopy, and auger electron spectroscopy each measure other features of the samples to explore changes to surface chemistry. However, based on the results discussed in this chapter, a preliminary material analysis of BDD after exposure to chloride and fluoride salt indicates that it is most likely unchanged.

5 Boron-Doped Diamond Resilience in Molten Salts Part II: Aqueous Electrochemical Response Investigation

Abstract

This chapter is a sequel to what was discussed previously, aiming to characterize the electrochemical performance of boron-doped diamond (BDD) after exposure to molten chloride and fluoride salts for extended periods of time. Following the same procedure used before, the material was exposed to NaCl-KCl (700 °C) and FLiNaK (500 °C) either in as-received salts in air or in dried salts in an inert Ar(*g*) glovebox environment for ten days. The coupons were then studied in a side-isolating cell that allowed for electrochemical measurements on either the grown (top, large crystals) or nucleation (bottom, nanometer scale grain boundaries) using two common analytes, (ferri/ferrocyanide: $Fe(CN)_6^{3-/4-}$ and hexaammineruthenium: $Ru(NH_3)_6^{3+/2+}$), in a KCl electrolyte. Each analyte exploits different electron transfer mechanisms, either inner- or outer-sphere, that describe different portions of the diffusion layer of an electrode. Together, performing cyclic voltammetry (CV) scan rate studies of each system on the two sides of the new and exposed BDD samples should be useful in monitoring changes to the surface of the electrodes at the Inner Helmholtz Plane (IHP) with $Fe(CN)_6^{3-/4-}$, or farther into the diffusion double-layer at the Outer Helmholtz Plane (OHP) with $Ru(NH_3)_6^{3+/2+}$.

Previous studies of fluorinated and chlorinated BDD provided a baseline of expected changes for the solvent potential windows and any possible changes to CV for $Fe(CN)_6^{3-/4-}$ and $Ru(NH_3)_6^{3+/2+}$. However, although there were some changes observed for each of the three studies, they did not align with what has been previously reported, like widening of

potential windows and peak separations. Instead, slight differences were found for diffusion or electron transfer kinetics, but all values determined still fell within the expected values for measurements on BDD. It was concluded, however, that whatever changes had occurred had a more significant impact on $Fe(CN)_6^{3-/4-}$ rather than $Ru(NH_3)_6^{3+/2+}$, which was anticipated based on their electron transfer mechanisms.

Ultimately, the changes seen to the electrochemical responses of the grown and nucleation sides of BDD do not align with the expectations for fluorination and chlorination that have been previously described (e.g., slower electron transfer kinetics). Therefore, the alterations that have occurred are likely due to another undetermined change. Further investigation is required to better understand these changes. However, those changes were not significant enough to eliminate BDD as a potentially useful electrode in molten salt systems considering all values generally fell within the expected ranges, and exposures lasted far longer than laboratory-scale experiments would require.

5.1 Introduction

If boron-doped diamond (BDD) is to be used as an electrode in molten salts, it is imperative to determine changes to its electrochemical performance in addition to the physical and surface chemistry analysis after exposure to chloride and fluoride systems. In **Chapter 2**, two common aqueous analytes (ferri/ferrocyanide: $Fe(CN)_6^{3-/4-}$ and hexaammineruthenium: $Ru(NH_3)_6^{3+/2+}$) were used to characterize the differences in response based on the morphologies of the grown and nucleation sides of free-standing BDD given the extensive literature available using the same working electrode material to

measure these species.[89,91,95,96] This chapter will build upon the previous measurements of aqueous species each side of free-standing BDD in **Chapter 2** and continue discussions from the materials science investigation from **Chapter 4**. Cyclic voltammetry (CV) scan rate studies were performed to determine formal potentials (E^o), peak separations (ΔE), diffusion coefficients (D), and heterogeneous electron transfer rate constants (k) for $Fe(CN)_6^{3-/4-}$ and $Ru(NH_3)_6^{3+/2+}$ on the grown and nucleation sides of free-standing BDD after exposure to molten NaCl-KCl and FLiNaK.

Although there were no significant changes to the topography or surface chemistry of the material after exposure in **Chapter 4**, this chapter uses highly sensitive electrochemical methods that may uncover impacts that could not be detected using the previous techniques. It is hypothesized that measurements like CV scan rate studies can further explore impacts that the molten salt systems may have on the performance of BDD as an electrode. In addition to the materials characterization explored in the previous chapter (i.e., scanning electron microscopy, Raman, x-ray photoelectron spectroscopy), literature regarding the halogenation of BDD surfaces often includes CVs of $Fe(CN)_6^{3-/4-}$ and $Ru(NH_3)_6^{3+/2+}$ which can be used for reference for the salt-exposed samples investigated in the present study.

Two different sizes of free-standing BDD were used for the previous chapter (5 × 5 mm) and this chapter (10 × 10 mm) and were simultaneously exposed to the same four environments: NaCl-KCl (700 °C) and FLiNaK (500 °C) without drying and in the fume hood, or after drying and in an inert Ar(g) glovebox for ten days (see **Table 5.1**). Again, scanning electron microscopy (SEM) was used to image the grown and nucleation sides of

new, NaCl-KCl (H), NaCl-KCl (GB), FLiNaK (H), and FLiNaK (GB) BDD samples since the material used for these experiments needed to be large enough to fit in the side-isolating electrochemical cell. The increase in surface area of the BDD was also slightly thicker, so any differences in crystalline structure compared to the smaller samples were captured using SEM. Finally, aqueous electrochemical measurements were performed for each side of each sample via CV scan rate studies of $Fe(CN)_6^{3-/4-}$ and $Ru(NH_3)_6^{3+/2+}$ in KCl.

Table 5.1 Sample names, salt treatment, and exposure environment.

Sample Name	Salt Treatment	Exposure Environment
NaCl-KCl (H)	None	Fume Hood
NaCl-KCl (GB)	Thermal drying in glovebox vacuum furnace antechamber	Glovebox
FLiNaK (H)	None	Fume Hood
FLiNaK (GB)	Thermal drying in glovebox vacuum furnace antechamber	Glovebox

The electron transfer mechanisms for the redox reactions of $Fe(CN)_6^{3-/4-}$ and $Ru(NH_3)_6^{3+/2+}$ describe different regions of the electrode double-layer. Inner- and outer-sphere electron transfer processes either involve direct (inner) or indirect (outer) interactions between the electrode and the coordinated ligand of an electroactive metal complex.[202-213] In the case of an inner-sphere electron transfer, the mechanism is sensitive to the surface of the electrode material as the redox reaction occurs at the Inner Helmholtz Plane (IHP) via the complexed metal with the coordination spheres maintained. In the case of an outer-sphere transfer, a solvated layer of the electrolyte (e.g., KCl in H_2O) is maintained between the electroactive species and the surface of the electrode, such that the Outer Helmholtz Plane (OHP) is the plane of closest approach, making the redox reaction less dependent upon the surface of the electrode. Therefore, with the goal of monitoring changes to electrochemical response at the IHP and OHP, a wide range of

insights could result from using analytes with inner- and outer-sphere electron transfer mechanisms to determine changes to an electrode's performance before and after something like molten salt exposure.

In many cases, both $Fe(CN)_6^{3-/4-}$ and $Ru(NH_3)_6^{3+/2+}$ have both been classified as outer-sphere mechanisms.[111,211,214-219] However, there has been debate with respect to the mechanisms for $Fe(CN)_6^{3-/4-}$ when using carbon, especially BDD, working electrodes.[95,111,176,218,220,221] In acidic environments, outer-sphere mechanisms have been reported,[111,220,222] but in salt systems like KCl and phosphate-buffered saline, inner-sphere electron transfer has been observed.[95,111,151,176,223] Regardless of the actual mechanism, $Fe(CN)_6^{3-/4-}$ on polycrystalline BDD has ultimately been considered surface sensitive with respect to functionalization and surface chemistry for various forms of carbon electrodes,[95,143,176,221,224] and is assumed to extend that feature to the measurements performed in this chapter. For the present study, using $Fe(CN)_6^{3-/4-}$ and $Ru(NH_3)_6^{3+/2+}$ should speak to electrochemical responses that can be seen in the IHP (electrode surface) or OHP (solvent layer mediator) after exposure to NaCl-KCl or FLiNaK.

The fluorination of BDD surfaces have been found to have significant impacts on the electrochemical responses of the material and some examples are reported in **Table 5.2**.[151,172,173,176] Responses for $Fe(CN)_6^{3-/4-}$ changed significantly, even under acidic conditions, while those for $Ru(NH_3)_6^{3+/2+}$ were virtually unchanged after fluorination or chlorination.[151,173,176] In one case, the peak separation seen for $Fe(CN)_6^{3-/4-}$ on plasma fluorinated BDD increased from 0.170 V to over 1.5 V while that for $Ru(NH_3)_6^{3+/2+}$ increased from 0.1 V to just 0.22 V.[151] This study also found a decrease in the kinetics,

even for $Ru(NH_3)_6^{3+/2+}$ on fluorinated BDD, to which they attributed to possible 'downward bending' of the band gap resulting in a decreased density of states at the Fermi level considering the outer-sphere mechanism would not be affect to changes on the surface of the material. While this feature is beyond the scope of the present study, it could be one explanation any changes to the response for $Ru(NH_3)_6^{3+/2+}$ if there is any change for this analyte after salt exposure. This further strengthens the argument for an inner-sphere electron transfer mechanism for $Fe(CN)_6^{3-/4-}$ to compliment results provided by $Ru(NH_3)_6^{3+/2+}$. There was even work to explore the impact of BDD fluorination on the kinetics of the $Eu^{3+/2+}$ redox couple under aqueous conditions.[196] Like for $Fe(CN)_6^{3-/4-}$, the peak separation increased significantly, speaking to a decrease in the overall kinetics of the electron transfer.

Table 5.2 Electrochemical changes of fluorinated BDD electrodes reported in literature.

BDD Treatment	Aqueous Analyte	Electrochemical Response	Reference
CF_4 plasma exposure	$Fe(CN)_6^{3-/4-}$	• ΔE_p: 1.3 V increase • k: Decreased	151
	$Ru(NH_3)_6^{3+/2+}$	• ΔE_p: 0.12 V increase • k: Decreased	
Cl_2 and CF_4 plasma exposure	$Fe(CN)_6^{3-/4-}$	• ΔE_p: >1.2 V increase • k: Decreased	173
	$Ru(NH_3)_6^{3+/2+}$	• ΔE_p: No change • k: No change	
CF_4 plasma exposure	KCl	• Negative $H_2(g)$ shift	176
	$Fe(CN)_6^{3-/4-}$	• k: Decreased	
	$Ru(NH_3)_6^{3+/2+}$	• No change	
CF_4 plasma exposure	$Fe(CN)_6^{3-/4-}$	• ΔE_p increased • k: Decreased	195
	$Eu^{3+/2+}$	• ΔE_p increased • k: Decreased	
	$HClO_4$	• 5 V Potential window	

Multiple studies in the literature have shown that the solvent potential windows for fluorinated species extended in the negative direction after fluorination and chlorination,

such that the hydrogen gas evolution appeared at more negative potentials compared to new BDD.[151,176,193] Additionally, these reports included that additional anodic peaks appeared and were attributed to a layer of fluorocarbon polymer that formed on the surface.[151,176,193] Evaluating the solvent windows and performing scan rate studies of species like $Fe(CN)_6^{3-/4-}$ and $Ru(NH_3)_6^{3+/2+}$ could provide insight to surface changes of the BDD after exposure to the salts. Although the measurements in the previous chapter did not indicate significant differences, the increased sensitivity of electrochemical methods could expose even subtle changes to the material.

5.2 Methods and Materials

The preparation, exposure, cleaning, and SEM imaging in this chapter is identical to that of **Chapter 4**. However, in this case the 10 × 10 × 0.6 mm BDD from ElementSix is used in order to utilize the same plate material evaluation cell from Biologic, LLC, (1 mL solution volume, exposed surface area = 0.57 cm^2) used in **Chapter 2** (**Figure 2.1**) because the smaller coupons (5 × 5 mm) would not be large enough to create a seal with the o-ring to retain the solution. The same chemicals used in the aqueous measurements in **Chapter 2** were used here as well, but no anodic pre-treatment was performed on the new or exposed material to create a direct comparison when performing the electrochemical measurements. Additionally, these measurements were performed on a Gamry Interface 1010 potentiostat. The same Ag/AgCl (3.5 M KCl) reference electrode (BASi) from **Chapter 2** was used, but with the Pt wire counter electrode that accompanied the side-isolating cell from Biologic.

5.3 Scanning Electron Microscopy

The free-standing BDD used for the following measurements are identical to what was used in **Chapter 2** (seen in **Figure 2.2**), and thicker with slightly different morphology than the smaller samples used in **Chapter 4** (new material seen in **Figure 4.1**). The large crystals of the grown side and nano-diamond structure of the nucleation side of BDD are shown in **Figure 5.1 A)** and **B)**. Compared to the smaller coupons, the crystals on the grown side are slightly larger, and the texture of the nucleation side is also different than what was observed previously. Instead of clear grains that show the base of the crystal growth, this material does not have observable grain boundaries at the same magnification. This feature is likely a result of the etching or polishing process that was used to remove the silicon substrate after the growth process during manufacturing. This may be a feature to consider given the impact morphology has shown in previous measurements, but this difference is inevitable for the current study and should be the focus of future work.

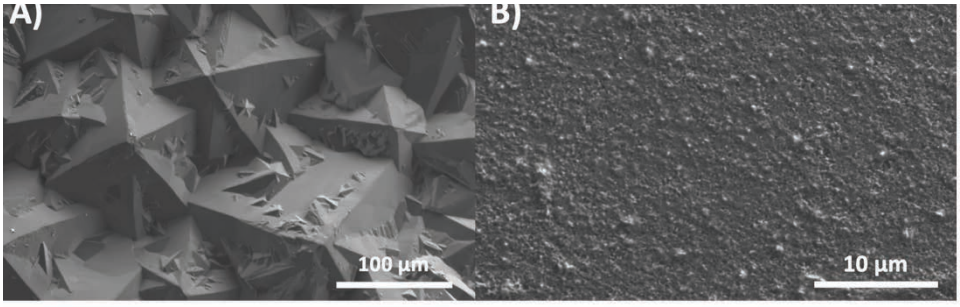

Mirroring what was seen for the smaller coupons in **Chapter 4**, after exposure to the four systems, the material is virtually unchanged except for the NaCl-KCl (H) sample. The micrograph in **Figure 5.2 A)** shows a similar pattern of corrosion that was seen in **Figure 4.2 A)** at the grain boundaries, edges between facets on each crystal, and some areas of the crystal faces. However, the NaCl-KCl (GB), FLiNaK (H), and FLiNaK (GB) samples show no evidence of etching, further supporting the idea that the NaCl-KCl (H) environment is uniquely harsh, likely due to the increased presence of moisture which introduces oxygen that is known to corrode diamond at high temperatures.[84,182,183] This result confirms that the material responds similarly to the four exposure conditions regardless of the moderate differences in morphologies.

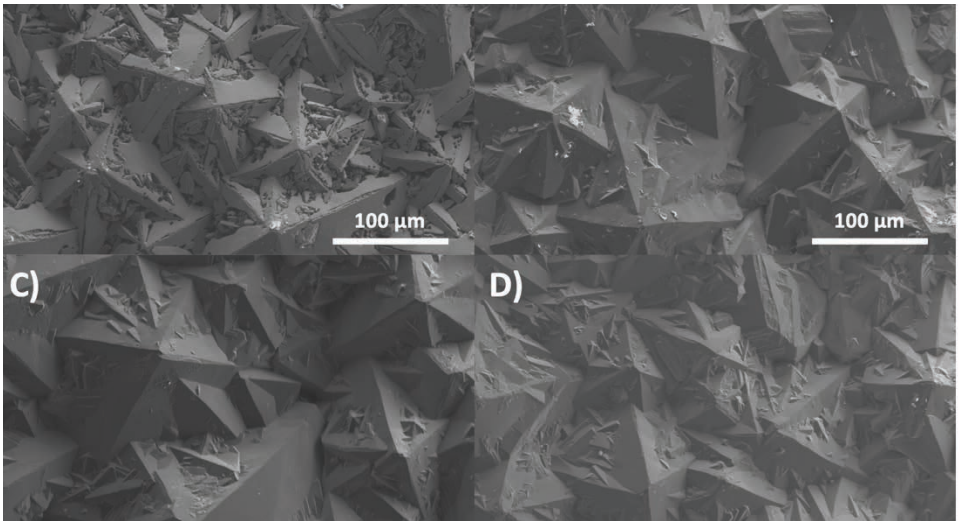

Figure 5.2 SEM of the grown sides of the A) NaCl-KCl (H), B) NaCl-KCl (GB), C) FLiNaK (H), and D) FLiNaK (GB) BDD samples.

The nucleation side of the material also responded similarly to what was observed in the previous chapter. There is a moderate degree of change on each of the samples with

the greatest change seen on the NaCl-KCl (H) sample shown in **Figure 5.3**. Additionally, for samples like NaCl-KCl (H) and FLiNaK (GB) in **A)** and **D)**, the grain boundaries seen in the smaller samples in **Figure 4.3** which may be related to the etching and polishing process, or simple due to the general variation that can occur. For example, the FLiNaK (GB) sample in **Figure 5.3 D)** shows artifacts from where the diamond nanoparticle was seeded into the original substrate through a scratching technique, leaving behind a negative of that pattern in the final surface structure. Instead, the morphology difference could perhaps be a result of moderate corrosion to the surface. Samples NaCl-KCl (GB) and FLiNaK (H) also show a degree of corrosion where, although more aligned with the roughness seen in the new sample in **Figure 5.1 B)**, there is a slight increase in the presence of pitting across the surface. Again, the material was grown side up such that the nucleation side was in direct contact with the alumina crucible where oxygen may have escaped during the exposure. The measurements in **Chapter 4** did not indicate this caused significant changes on the smaller samples where this phenomenon was more prominent, but electrochemical investigations may be able to detect impacts from this effect.

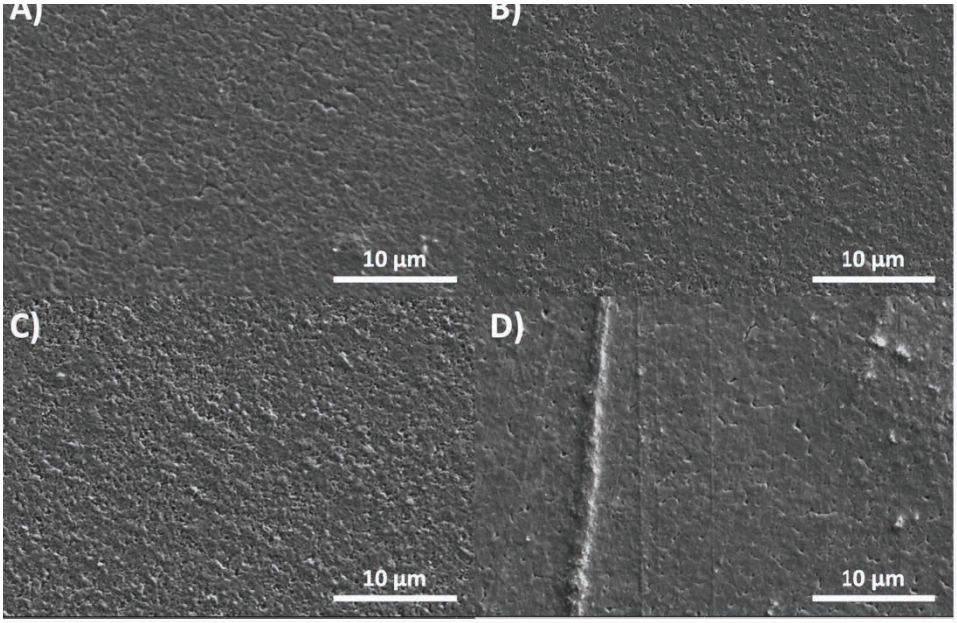

Figure 5.3 Sl l D) FLiNaK (GB)

5.4 Cyclic Voltammetry

Like previous chapters have shown, CV is a powerful technique that can be used to probe electroactive analytes and evaluate electrode performance. In this case, CV was chosen to characterize free-standing BDD electrodes after exposure to molten NaCl-KCl and FLiNaK by comparing solvent potential windows for KCl and various figures of merit for $Fe(CN)_6^{3-/4-}$ and $Ru(NH_3)_6^{3-/2-}$, including E^o, ΔE, D, and k. The geometric surface area exposed for each experiment in the side-isolating cell was 0.57 cm^2.

5.4.1 Solvent Potential Windows

When comparing the optically transparent grid and non-grid BDD in **Chapter 3**, the current density limit for the oxygen and hydrogen evolution was ±0.4 mA/cm^2. In some cases, a baseline correction was used for samples with an increased background

capacitance that would otherwise skew the actual working window area. This approach is adopted in the present study as well. Additionally, anodic peaks at +1.2 V vs. Ag/AgCl were observed for the measurements in 1 M KCl that were attributed to the presence of sp^2 carbon which rightfully increased for the grid electrode given the lasing process that graphitized some of the diamond crystal lattice.

In this case, the grown side of the new material was measured and a window with approximately equal current densities for the oxygen and hydrogen overpotentials was selected: +1.75 V to -2.0 V at 100 mV/s. This scan range was used as a standard for the remaining samples. Based on the previous results for **Chapter 3**, the solvent potential windows for 1 M KCl were expected to be approximately 3 V. However, those BDD electrodes had been anodically pre-treated in 1 M H_2SO_4 while the samples in this chapter have not. This will likely impact the solvent windows on both side of the material since the surface is not necessarily hydrogen-terminated.

The grown and nucleation responses on new BDD are shown in **Figure 5.4**. At approximately +1.2 V an anodic peak appeared for the nucleation side which corresponds to the measurements performed in 1 M KCl in **Chapter 3**. Because this feature is attributed to the presence of sp^2 hybridized carbon,[101] this result corroborates the morphology of the nucleation side has far more grain boundaries compared to the nucleation side. Additionally, the Raman spectroscopy performed in **Chapter 4** detected sp^2 non-diamond carbon.

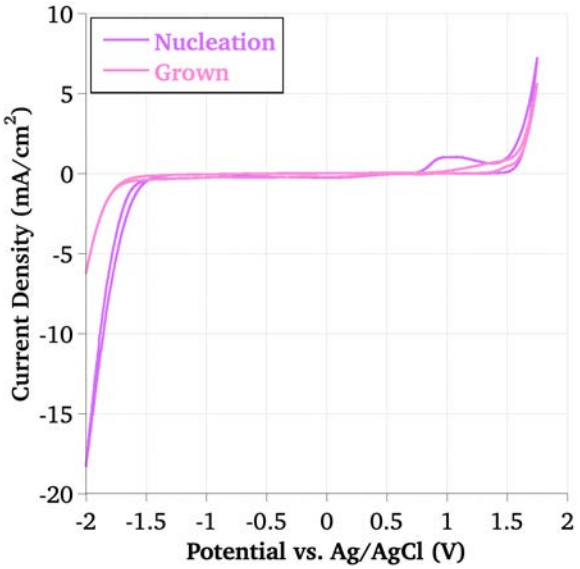

Figure 5.4 Solvent potential windows for 1 M KCl on the grown (purple) and nucleation (pink) sides of new BDD. RE: Ag/AgCl; CE: Pt wire.

The potential windows calculated for each side are reported in **Table 5.3**. The grown side was found to be 2.88 V and the nucleation side was 2.98 V, including the anodic sp^2 peak such that the positive end was chosen at the valley between the anodic peak and oxygen overpotential. If this peak was not included, the potential window decreases to 2.31 V. Although the window is slightly smaller for the grown side, the hydrogen overpotential region of the solvent window is more negative on the grown side. Overall, the responses on both the grown and nucleation sides are slightly smaller, but comparable to the results seen for the anodically treated material in **Chapter 3**.

Table 5.3 Solvent potential windows and oxygen and hydrogen evolution onset potentials vs. Ag/AgCl for 1 M KCl on the grown and nucleation sides of each BDD sample.

Treatment	Side	Potential Window (V)	$O_2(g)$ vs. Ag/AgCl (V)	$H_2(g)$ vs. Ag/AgCl (V)
New	Grown	2.88	+1.20	-1.70
New	Nucleation	2.98	+0.84	-1.47

It has been shown that functionalization like fluorination and chlorination will have an impact on solvent potential windows.[151,176,193] Previous reports describe an extension in the negative direction, and even the presence of additional anodic peaks after these forms of halogenation. However, these phenomena are not observed for salt-exposed material. After exposure to NaCl-KCl and FLiNaK in the fume hood and glovebox, the potential windows show slightly different features in various ways. The responses on the grown side of the new (pink), NaCl-KCl (H) (orange), NaCl-KCl (GB) (green), FLiNaK (H) (blue), and FLiNaK (GB) (purple) are illustrated in **Figure 5.5**.

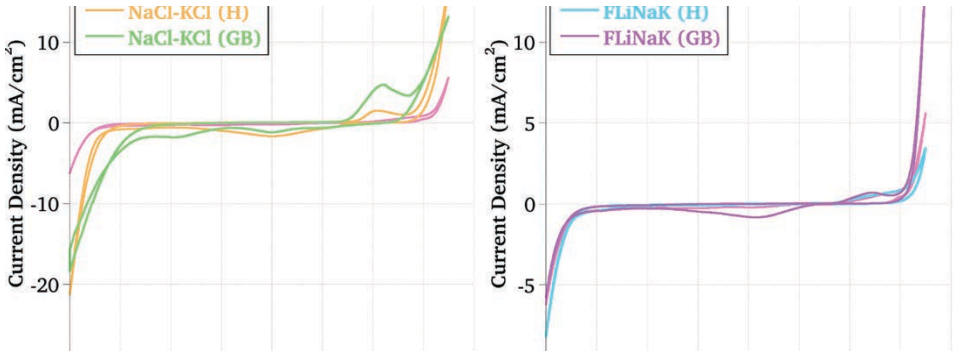

Figure 5.5 Solvent potential windows for 1 M KCl on the grown side of new (pink), NaCl-KCl (H, orange), NaCl-KCl (GB, green), FLiNaK (H, blue), and FLiNaK (GB, purple) BDD. RE: Ag/AgCl; CE: Pt wire.

The NaCl-KCl (H), NaCl-KCl (GB), and FLiNaK (GB) sample shows an additional broad cathodic peak around 0 V which was also observed for the material used for **Chapter 3** where both sides of the BDD were simultaneously exposed to the solvent during measurements. This is likely attributed to the large current density achieved at the positive overpotential, which may induce a reduction event of some kind. The 0 V cathodic peak seems to correspond with the magnitude of the oxidative overpotential, so this

phenomenon should be studied further to better understand the mechanism of the reaction. However, it does not have significant implications for the current study.

Unexpectedly, the sp^2 carbon peak at +1.2 V is seen on the NaCl-KCl (H), NaCl-KCl (GB), and FLiNaK (GB) samples although these were performed on the grown side. It may be possible that corrosion observed on the NaCl-KCl (H) sample could have residual non-diamond carbon following graphitization of the diamond crystal lattice, but this does not explain the NaCl-KCl (GB) and FLiNaK (GB) samples that did not show corrosion. Additionally, none of these samples had detectable levels of sp^2 carbon when performing Raman spectroscopy in **Chapter 4**, which may simply speak to the sensitivity of electrochemical methods. The FLiNaK (H) is the most comparable to the new material on the grown side. However, it does not show the reported features expected for fluorinated material, like wider overall window and additional anodic peaks.[151,176,193]

The solvent potential windows for the nucleation side are shown in **Figure 5.6**. Interestingly, the sp^2 peak which would be expected for all nucleation measurements does not appear for the NaCl-KCl (H), FLiNaK (H), or FLiNaK (GB) samples. Like on the grown side, this peak appears on the nucleation side of NaCl-KCl (H) sample at an equally large current magnitude (4.71 mA/cm^3 on the grown side and 4.78 mA/cm^3 on the nucleation side), compared to just 1.02 mA/cm^3 on the new piece and only 0.69 mA/cm^3 for the grown side of the FLiNaK (GB) sample. If this peak does in fact correspond to the presence of sp^2 carbon, it conflicts with the lack of corrosion seen via SEM, and lack of detection using Raman spectroscopy in **Chapter 4** considering sp^2 carbon was seen for all of the nucleation sides of each sample, but not detected most of the potential windows.

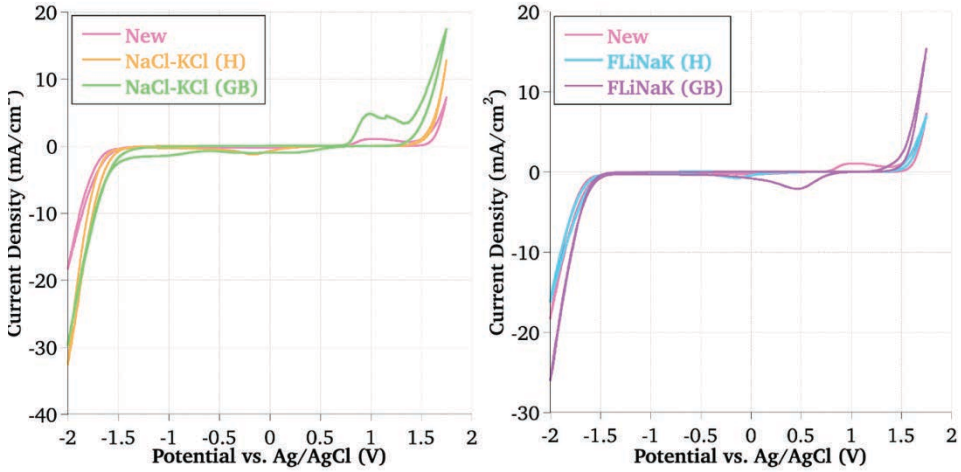

Figure 5.6 S l (H, orange), NaCl-KCl (GB, green), FLiNaK (H, blue), and FLiNaK (GB, purple) BDD. RE: Ag/AgCl; CE: Pt wire.

The calculated values for the solvent potential windows are listed in **Table 5.4**. Throughout each of the measurements, the windows ranged from as small as 2.67 V on the nucleation side of NaCl-KCl (GB) to as large as 3.28 V for the grown side of FLiNaK (GB). Overall, NaCl-KCl (GB) has the smallest windows for both the grown and nucleation sides, even with the presence of the anodic sp^2 carbon peak, while no clear pattern has otherwise arisen for the other samples or grown versus nucleation sides. Ultimately, none of these results correspond to the impacts reported by chlorination or fluorination of the surface of BDD electrodes.

Table 5.4 Solvent potential windows and oxygen and hydrogen evolution onset potentials vs. Ag/AgCl for 1 M KCl on the grown and nucleation sides of each BDD sample.

NaCl-KCl (C	Grown	2.69	+1.33	-1.36
FLiNaK (G	Nucleatic	2.81	+1.32	-1.49

5.4.2 Ferri/Ferrocyanide

Scan rate studies (10, 25, 50, 75, 100 mV/s) were performed over three trials on each side of the BDD for each system, where each scan rate (υ) was cycled three times. The average values for E_p and i_p were used to perform the calculated values reported below. As the surface-sensitive analyte, it is expected that $Fe(CN)_6^{3-/4-}$ (1 mmol, 1 M KCl) will expose any changes to the material surface that have not yet been identified using surface chemistry or potential window measurements in previous sections. Additionally, like what was seen in **Chapter 2**, the differences between the grown and nucleation morphologies can also be explored using the results from CV scan rate studies even without the anodic pre-treatment. The overlays of the 50 mV/s scans for each side of the new material are show in **Figure 5.7**, and like in the previous studies, the nucleation side shows higher resolution peaks compared to the grown side.

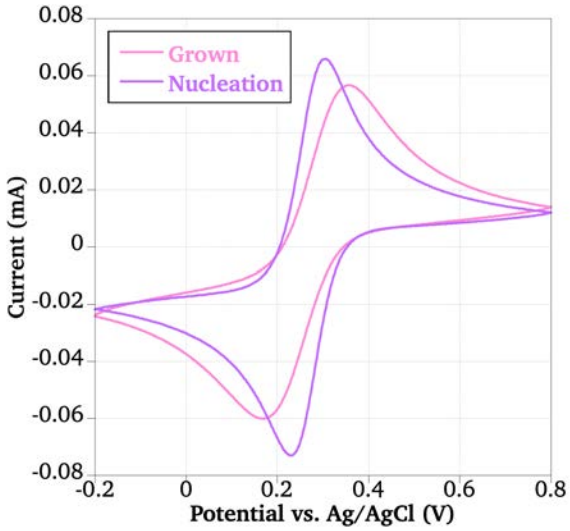

Figure 5.7 Overlays of 50 mV/s scans for 1 mM $Fe(CN)_6^{3-/4-}$ in 1 M KCl on the grown (pink) and nucleation (purple) sides of new free-standing BDD. RE: Ag/AgCl; CE: Pt wire.

The scan rate studies repeated on the grown and nucleation sides of each exposed sample showed variation in the electrochemical responses that ranged from slight to moderate. The 50 mV/s scan rate overlays for the grown and nucleation sides of each sample are presented in **Figure 5.8 A)** and **B)** respectively. The least change is seen between the new and NaCl-KCl (H) material on the nucleation sides. In the case of the grown and nucleation sides, the two FLiNaK exposures resulted in the most significant change. The FLiNaK (H) sample shows an increase in peak current while the FLiNaK (GB) sample shows a decrease in peak current. With respect to differences between the grown and nucleation sides, the NaCl-KCl (H) and NaCl-KCl (GB) samples show much better kinetics on the nucleation sides compared to the grown sides. Additionally, although the peak current increased after exposure, the FLiNaK (H) sample does not have the same sharp resolution on the grown side like what is seen for the nucleation side. Overall, the worst response on the grown side is the NaCl-KCl (GB) while the worse response on the nucleation side is for FLiNaK (GB).

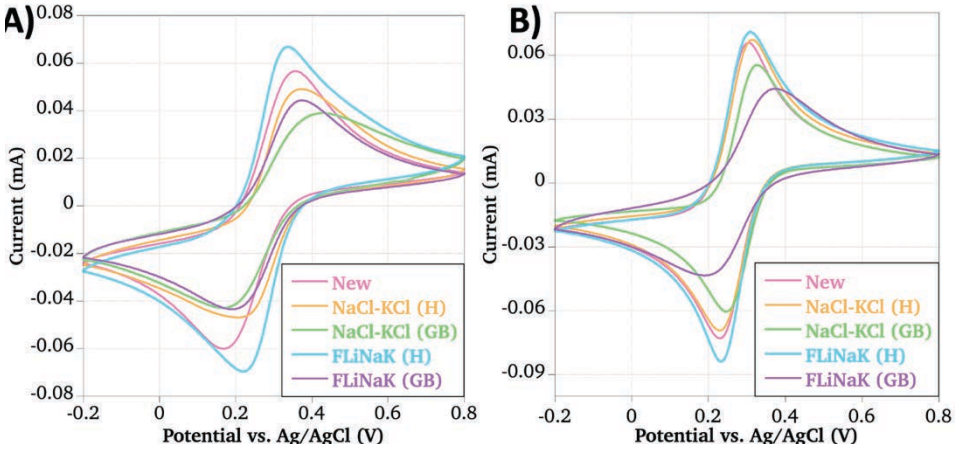

Figure 5.8 Overlays of 50 mV/s scans for 1 mM $Fe(CN)_6^{3-/4-}$ in 1 M KCl on the A) grown and B) nucleation sides of new (pink), NaCl-KCl (H, orange), NaCl-KCl (GB, green), FLiNaK (H, blue), and FLiNaK (GB, purple) BDD samples. RE: Ag/AgCl; CE: Pt wire.

Like for the previous chapters using scan rate studies, characteristics like E^o, D, ΔE_p, and k have been calculated for the grown and nucleation sides of each sample to quantify the performance of the electrode material. These values are listed in **Table 5.5**. Again, the values for E^o were calculated using Eq. 3 which averages the anodic and cathodic peak potentials. The values determined for each surface extend from +0.263 V to +0.286 V vs. Ag/AgCl but fall within the expected range.[91,95,107,108] Because of how E^o is calculated, it is not expected that it would change based on surface chemistry but rather serves as a standard of comparison and baseline for electrode quality. In this case, the consistency is the first good sign that BDD can generally still perform well after exposure to each molten salt environment.

Table 5.5 Figures of merit for 1 mM $Fe(CN)_6^{3-/4-}$ in 1 M KCl vs. Ag/AgCl on the grown and nucleation sides of BDD after various treatments. *For 50 mV/s scan rate.

Treatment	Side	E^o (V)	$D \times 10^{-6}$ (cm^2/s)	ΔE_p* (V)	k* $\times 10^{-3}$ (cm/s)
New	Grown	+0.263 ±0.0007	1.7 ±0.02	0.190 ±0.00002	0.48
New	Nucleation	+0.267 ±0.0003	3.8 ±0.07	0.076 ±0.0	8.4
NaCl-KCl (H)	Grown	+0.286 ±0.0003	1.7 ±0.05	0.133 ±0.0003	0.17
NaCl-KCl (H)	Nucleation	+0.272 ±0.0003	3.8 ±0.1	0.084 ±0.0	4.8
NaCl-KCl (GB)	Grown	+0.270 ±0.002	0.43 ±0.04	0.262 ±0.0007	0.26
NaCl-KCl (GB)	Nucleation	+0.287 ±0.0002	3.8 ±0.08	0.081 ±0.0003	6.1
FLiNaK (H)	Grown	+0.279 ±0.0004	3.8 ±0.3	0.121 ±0.0003	1.7
FLiNaK (H)	Nucleation	+0.272 ±0.0008	6.8 ±0.1	0.076 ±0.0	9.7
FLiNaK (GB)	Grown	+0.286 ±0.004	1.7 ±0.1	0.185 ±0.0003	0.48
FLiNaK (GB)	Nucleation	+0.286 ±0.0	3.8 ±0.08	0.182 ±0.0	0.73

The diffusion coefficients for the anodic and cathodic reactions were calculated using the Randles-Sevcik equation (Eq. 4). In each case the values for D_O and D_R were equal and are reported as one value for D in **Table 5.5**. The rate of diffusion ranges from as fast as 6.8×10^{-6} ±0.1 cm^2/s for the FLiNaK (H) nucleation side to as slow as 4.3×10^{-7} ±0.4 cm^2/s for the NaCl-KCl (GB) grown side. The behavior of the NaCl-KCl (H) and

FLiNaK (GB) samples mirrored what was calculated for both the grown and nucleation sides of the new BDD. The FLiNaK (H) grown and nucleation sides both resulted in faster diffusion than their counterparts for the new material, and the nucleation sides of each sample saw faster diffusion than the grown sides. These results generally align with the CVs seen in **Figure 5.8**. Regardless of the rate of diffusion, each scan rate study produced linear plots for i_p versus $\sqrt{v}$ with $R^2 > 0.99$ which indicates semi-infinite linear diffusion, and all of the values still fall within the expected range for measurements on BDD.[91,95,107,108]

For almost all samples, the Nicholson method was yet again chosen to determine the heterogeneous electron transfer rate constant via Eq. 5.[110] However, this approach only applies for peak separations less than 0.212 V. Therefore, because ΔE_p for the grown side of NaCl-KCl (GB) was 0.262 V, the Klingler-Kochi method (Eq. 9) was used instead.[116] The charge transfer coefficient, αn_α (equal to α for a one electron transfer) was determined to be 0.391 using Eq. 8 as opposed to 0.5 which was assumed for the other calculations given the near reversibility observed in the other cases, which was also done in **Chapter 2** and **Chapter 3**. However, all of the values for k calculated fell within the expected range (10^{-4} to 10^{-3} cm/s) for $Fe(CN)_6^{3-/4-}$ on BDD.[91,95,107,108,111] The fastest kinetics were seen for the nucleation side of the FLiNaK (H) sample, and the slowest on the grown side of the NaCl-KCl (GB) sample. Additionally, one common trend is that the nucleation side consistently shows faster kinetics via larger values for k and smaller ΔE_p across all samples, like what was seen for D and in **Chapter 2**.

The figures of merit discussed in **Table 5.5** are also illustrated visually for the grown side of each sample in **Figure 5.9** where the values for E^o (pink) and ΔE_p (purple) are to

the left and D (green) and k (blue) are to the right. These visual overviews provide a clear comparison for how these characteristics change after exposure to each environment. The E^o values changed very little across the sample set, but the two pieces exposed in the fume hood have the smallest ΔE_p, the NaCl-KCl (GB) sample has the largest, and the FLiNaK (GB) changed the least compared to the new material. However, the D and k are clearly the greatest for FLiNaK (H), and the two air-exposed samples differ. The increased peak current seen for the FLiNaK (H) sample in **Figure 5.7** increased D significantly, which ultimately also increased k compared to the NaCl-KCl (H) material. Additionally, the wide ΔE_p for the NaCl-KCl (GB) material extends to the resulting values for D and k which are clearly small compared to the other samples. However, the k for NaCl-KCl (H) is still smallest overall but has an equal value for D compared to the new and FLiNaK (GB) material. These plots paint a complicated picture with respect to the quality of the grown sides of the BDD after exposure to the salt, and that there is no clear trend of improvement or decreased performance for all values in either chloride or fluoride salts.

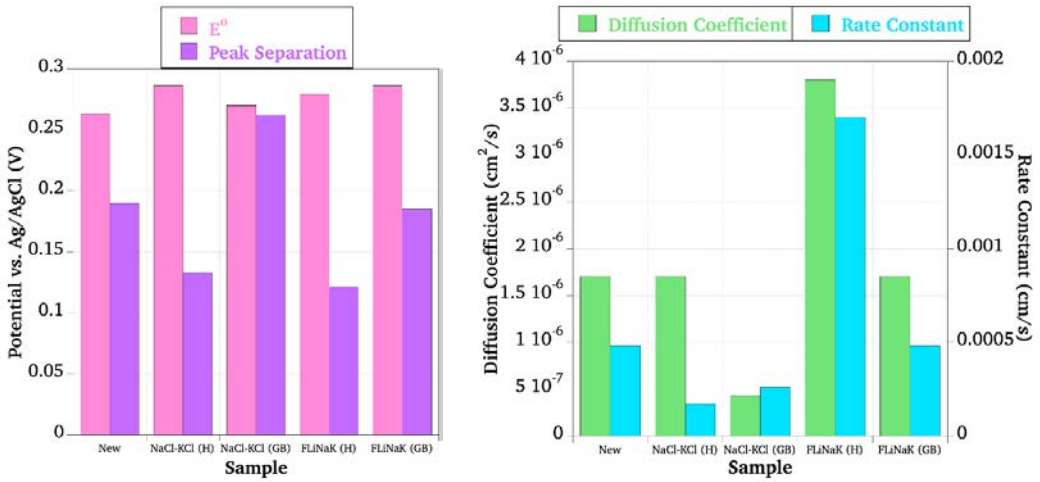

Figure 5.9 Formal potentials (pink), peak separations (purple), diffusion coefficients (green), and rate constants (blue) for 1 mM $Fe(CN)_6^{3-/4-}$ in 1 M KCl vs. Figures of merit for 1 mM $Fe(CN)_6^{3-/4-}$ in 1 M KCl vs. Ag/AgCl on the grown side side of BDD after various treatments.

Similar plots describing E^o (pink) and ΔE_p (purple) are to the left and D (green) and k (blue) are shown in **Figure 5.10**. In this case, E^o is still constant across samples, and now ΔE_p also changed very little until the FLiNaK (GB) sample. Like on the grown side, the values for D and k were largest for the FLiNaK (H) sample. Additionally, the wide separation for FLiNaK (GB) corresponds to the significantly smaller k when paired with a moderate calculation for D that aligns with the new and NaCl-KCl exposed samples. Compared to the grown side, the nucleation side seems to have slightly faster diffusion and electron transfer kinetics compared to the grown side which, again, aligns with what was found in the work reported in **Chapter 2**.

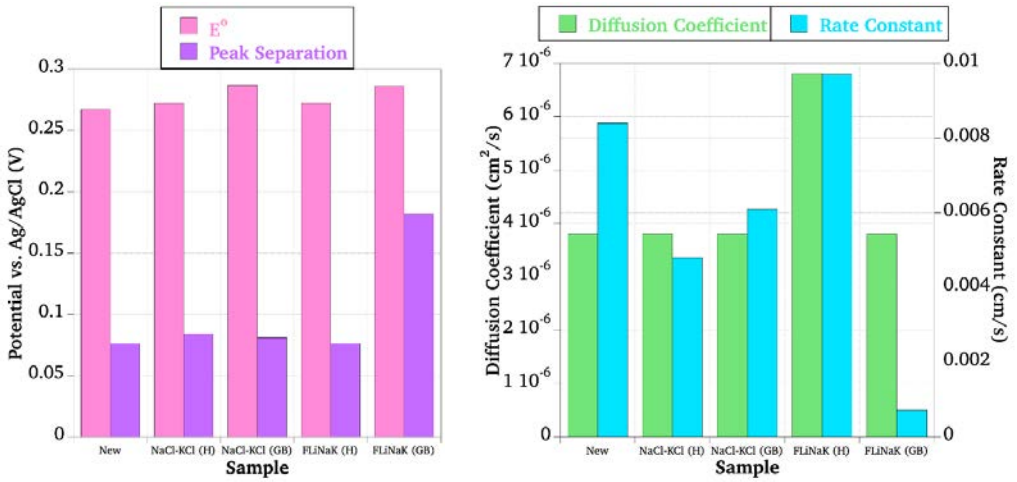

Figure 5.10 Formal potentials (pink), peak separations (purple), diffusion coefficients (green), and rate constants (blue) for 1 mM $Fe(CN)_6^{3-/4-}$ in 1 M KCl vs. Ag/AgCl on the nucleation side of BDD after various treatments.

Although the measurements performed to characterize various aspects of the surface chemistry in the previous chapter do not show differences after exposure, it seems as though not only is there a difference between the fluoride and chloride exposed

material, but the environment in which the exposure occurred may have an impact. While NaCl-KCl (H) was the only sample to show clear corrosion, it appears that some changes yet to be understood have occurred to the material as determined by the inner-sphere electron transfers performed by $Fe(CN)_6^{3-/4-}$.

5.4.3 Hexaammineruthenium(III/II) Chloride

Again, scan rate studies (10, 25, 50, 75, 100 mV/s) were performed over three trials on each side of the BDD for each system, where each υ was cycled three times and the average values for E_p and i_p were used to perform the calculated values reported below. Because $Ru(NH_3)_6^{3+/2+}$ (1 mmol, 1 M KCl) exhibits outer-sphere electron transfer mechanisms, it is expected that changes to the electrode surface will have less of an impact on the response. This has been observed even in the cases of confirmed fluorination and chlorination of BDD electrodes, especially when comparing to measurements of $Fe(CN)_6^{3-/4-}$.[151,173,176]

The 50 mV/s scans for 1 mmol $Ru(NH_3)_6^{3+/2+}$ performed on the grown and nucleation sides of new BDD are shown in **Figure 5.11**. In this case, there is minimal change in the response due to the differences in morphology compared to $Fe(CN)_6^{3-/4-}$, and compared to what was observed for the anodically pre-treated material in **Chapter 2**. The response on the grown side shows greater resolution and improved kinetics compared to $Fe(CN)_6^{3-/4-}$, which furthers the argument that $Ru(NH_3)_6^{3+/2+}$ is less surface-sensitive.

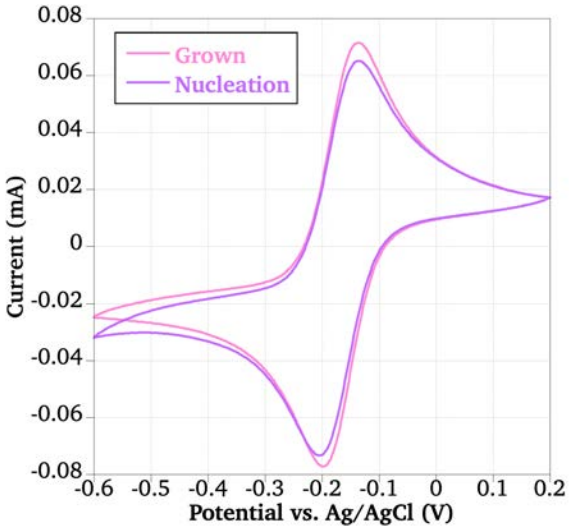

Figure 5.11 Overlays of 50 mV/s scans for 1 mM $Ru(NH_3)_6^{3+/2+}$ in 1 M KCl on the grown (pink) and nucleation (purple) sides of new free-standing BDD. RE: Ag/AgCl; CE: Pt wire.

Overlays of the 50 mV/s scans for the new, NaCl-KCl (H), NaCl-KCl (GB), FLiNaK (H), and FLiNaK (GB) samples are presented in **Figure 5.12** where the response for the grown side are in **A)** and those for the nucleation side are in **B)**. On the grown side, the voltammograms are nearly identical as expected, except in the case of FLiNaK (H). The anodic and cathodic peaks have lower current magnitudes and are much less resolved. This change indicates a change to the kinetics of the electron transfer, but because this reaction does not occur at the surface of the material the cause it not immediately apparent. This pattern is not observed for the nucleation side. All responses are generally aligned with the new sample, including the FLiNaK (H) BDD which almost perfectly overlaps the other traces and has a well resolved cathodic peak with a slightly larger current magnitude. Instead, the only trace with a noticeable difference is for FLiNaK (GB), but the peak resolution is maintained and only the current magnitude has decreased slightly for the anodic and cathodic reactions.

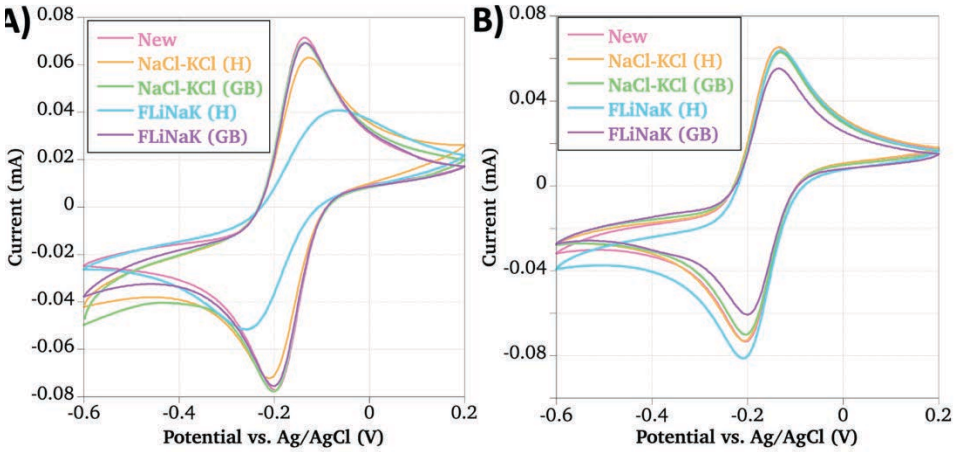

Figure 5.12 (
sides of new (
BDD. RE: Ag/AgCl; CE: Pt wire.

The responses for each side of the samples are listed in **Table 5.6**. The values for E^o were again calculated using Eq. 3 with minimal variation across measurements and all fall within the expected range.[91,95,107,108,151,173,176] Because there is good reversibility for these measurements, it is expected that, so long as the reference electrode is in proper working order, this value would not waiver.

Table 5.6 Figures of merit for 1 mM $Ru(NH_3)_6^{3+/2+}$ in 1 M KCl vs. Ag/AgCl on the grown and nucleation sides of BDD after various treatments. *For 50 mV/s scan rate.

NaCl-KCl	Grow	-0.168 ±0.0002	3.8 ±0.1	0.083 ±0.(	5.3
FLiNaK	Nuclea	-0.170 ±0.0004	6.8 ±0.06	0.079 ±0.(	7.0

The diffusion was quantified using the Randles-Sevcik equation (Eq. 4), and most of the samples resulted in equal values for D_O and D_R, except in the case of the grown side of FLiNaK (H) and are listed in **Table 5.6**. However, including that measurement, the plot of i_p versus $\sqrt{v}$ resulted in $R^2 > 0.99$, indicating diffusion-controlled processes, as expected. The rates of diffusion for all other samples are generally faster than what was observed for the $Fe(CN)_6^{3-/4-}$, but at an order of magnitude of 10^{-6} cm^2/s, they all fall within the expected range for measurements using BDD.[91,95,107,108,151,173,176] However, the anodic reaction for the FLiNaK (H) grown side slowed to 10^{-7} cm^2/s, which corresponds with the poor resolution of the anodic peak seen in **Figure 5.12 A)**. This result is particularly interested considering the measurements performed on quasi-reversible f-block species in **Chapter 2** saw faster diffusion for the reduction process rather than the oxidation process. Even the slower diffusion coefficient is within the range of values expected based on previously published literature.[91,95,197,108,151,173,176]

The distance between the anodic and cathodic peaks were less than 0.212 V for each side of each sample, therefore the Nicholson method was used to calculate *k* with Eq. 5.[110] Like for *D*, the values calculated for the rate of electron transfer are generally faster than what was seen for $Fe(CN)_6^{3-/4-}$, but still fall within the expected range.[91,95,197,108,151,173,176] Although the grown side of the FLiNaK (H) sample had uneven diffusion rates for oxidation and reduction, only D_O is used for the calculation of *k* and therefore did not have a significant impact.

A visual analysis of the $Ru(NH_3)_6^{3+/2+}$ figures of merit for the grown sides of the BDD samples in **Figure 5.13** show that E^o (pink) is consistent across all of the samples.

Additionally, ΔE_p (purple) was constant except for the FLiNaK (H) material which was more than twice as large as the next widest separation (NaCl-KCl (H)). The values for D on the new, NaCl-KCl (GB), and FLiNaK (GB) samples were equal, and the calculation for k was unchanged from the new to NaCl-KCl (GB) sample. However, D and k for NaCl-KCl (H) and FLiNaK (H) decreased. As expected, the FLiNaK (H) sample shows the greatest decrease in diffusion and electron transfer kinetics which corresponds to the poor resolution seen in **Figure 5.12**.

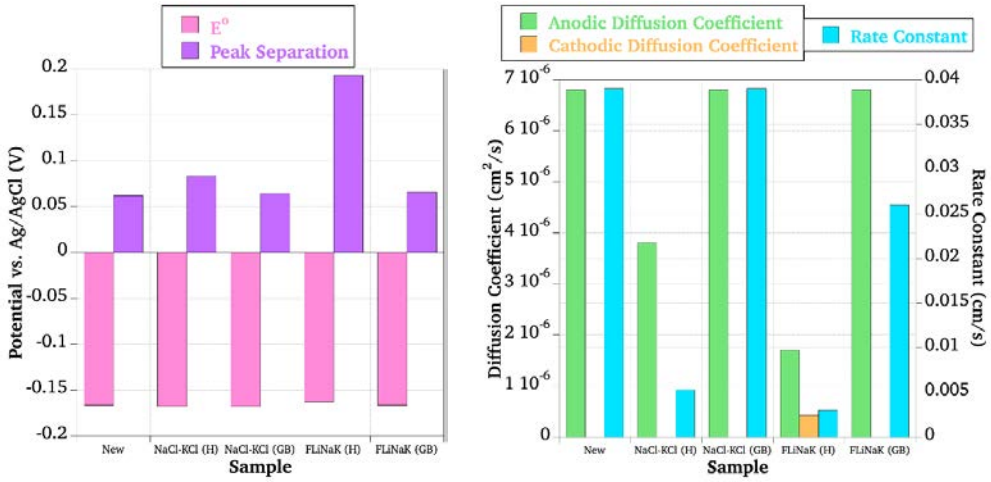

Figure 5.13 Formal potentials (pink), peak separations (purple), diffusion coefficients (green and orange), and rate constants (blue) for 1 mM $Ru(NH_3)_6^{3+/2+}$ in 1 M KCl vs. Ag/AgCl on the grown side of BDD after various treatments.

On the nucleation side, described in **Figure 5.14**, there is very little change across E^o, and minimal variation is seen between the new and exposed samples for ΔE_p where the FLiNaK (H) material gave slightly larger and FLiNaK (GB) gave slightly smaller separations. The diffusion did not change after exposure for the NaCl-KCl (H) or FLiNaK (H) samples, but their kinetics decreased slightly because of the slight differences in features like ΔE_p. Additionally, the variation seen on this side is much less than what was

seen on the grown side which ranged over an order of magnitude, while the nucleation side range is less than an order of magnitude overall. One explanation could be related to the differences in hybridization, possibly indicating that whatever changes may have occurred have a proclivity to affect sp^3 carbon compared to sp^2 carbon. This result needs to be further explored to confirm this hypothesis.

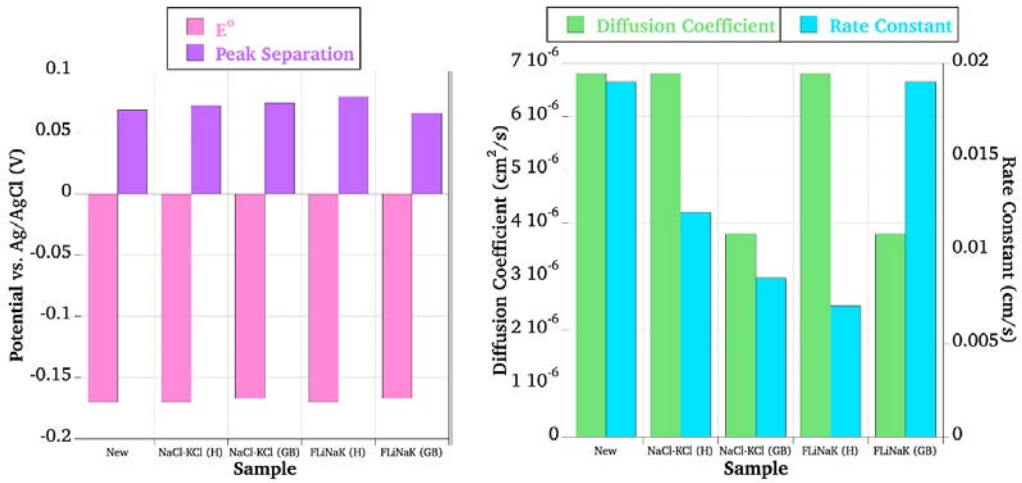

Figure 5.14 Formal potentials (pink), peak separations (purple), diffusion coefficients (green), and rate constants (blue) constants for 1 mM $Ru(NH_3)_6^{3+/2+}$ in 1 M KCl vs. Ag/AgCl on the nucleation side of BDD after various treatments.

As expected, the responses for $Ru(NH_3)_6^{3+/2+}$ do not exhibit changes as a result of exposure to the four salt systems like what was seen for the $Fe(CN)_6^{3-/4-}$ study. However, there was a small degree of variation in the quantification of electrode performance using the calculated figures of merit, and the voltammogram for the grown side of the FLiNaK (H) sample was a clear outlier with decreased anodic and cathodic i_p and less resolved peaks. This was reflected in the calculated values for ΔE_p, D, and k. The cause of this difference is unclear considering the response for $Ru(NH_3)_6^{3+/2+}$ should not be depending on the surface of the electrode given its outer-sphere electron transfer mechanism.[151,173,176]

Therefore, changes to the $Ru(NH_3)_6^{3+/2+}$ response may indicate an impact to the OHP portion of the diffusion layer for this portion of the material. This finding requires further investigation with other electrochemical methods and materials characterization techniques.

5.5 Conclusions

The work in this chapter aimed to characterize the electrochemical performance of BDD exposed to chloride and fluoride molten salts either in air, or in an inert glovebox with dried salt. Preliminary SEM to image the material showed the same results as the smaller coupons used in the material characterization chapter, where no changes were observed on the grown side other than corrosion seen on the NaCl-KCl (H) sample, likely due to the increased presence of oxygen and moisture. The nucleation sides all showed minor degrees of corrosion, which is possibly due to the removal of loosely attached sp^2 carbon at the grain boundaries produced during the growth process after exposure to the high temperature liquid. Like the previous free-standing BDD studies in this manuscript, the grown and nucleation sides of the material showed vastly different morphologies that have had impacts on the response, so each side was isolated for comparative measurements.

It was expected that fluorination or chlorination to the surface will have implications for the solvent potential windows in the KCl electrolyte and scan rate studies for $Fe(CN)_6^{3-/4-}$ on BDD based on what was previously reported in literature, assuming $Fe(CN)_6^{3-/4-}$ exhibits inner-sphere electron transfer behavior. The measurements on

$Ru(NH_3)_6^{3+/2+}$ were not expected to change following exposure as an outer-sphere electron transfer mechanism. These hypotheses were not clearly confirmed or contradicted. There were some slight changes to solvent potential windows and voltammograms for $Fe(CN)_6^{3-/4-}$, but not in the ways that have been previously observed for fluorinated or chlorinated material. There were not significant increases to the potential windows or ΔE_p. Instead, there were slight changes to the diffusion and kinetics of the electrode transfer mechanisms, but all values still fell within the expected ranges for measurements on BDD.

Additionally, the voltammograms for $Ru(NH_3)_6^{3+/2+}$ were generally unchanged after exposure, as expected. However, the grown side of FLiNaK (H) drastically decreased in peak resolution, saw a small increase in ΔE_p, and decreases in D and k. Again, the outer-sphere electron transfer for this analyte is not as sensitive to the surface of the electrode, so this result is potentially related to another feature of the double-layer changing. One previous study discussed a similar change for $Ru(NH_3)_6^{3+/2+}$ where they claimed the band gap for the material conductivity was altered after fluorination, so this may be one possible explanation.[151,173,176]

Yet, in previous cases where fluorination was monitored using these analytes, they provided accompanying measurements like Raman spectroscopy or x-ray photoelectron spectroscopy (XPS), like what was performed in **Chapter 4**. In those cases, differences were detected for changes in carbon hybridization or the presence of C-F or C-Cl bonds on the surface. There was no evidence for these bonds for the measurements reported in the previous chapter, so it is not a likely explanation, including for the FLiNaK (H) response change for $Ru(NH_3)_6^{3+/2+}$ discussed above. Therefore, more work is required to fully

understand the changes that have occurred to the material either through different approaches to electrochemical measurements or other instrumental analysis to probe the surface chemistries. Overall, the changes observed do not rule out the usefulness of BDD as an electrode for *in situ* measurements of analytes in molten salt systems so long as precautions are taken to limit the presence of oxygen and moisture to limit corrosion. However, even after corrosion occurred, the electrode performance still aligned with literature values for each sample.

6 Electrochemical Characterization of f-Block Elements with Boron-Doped Diamond in Molten Chloride Salts

Abstract

Boron-doped diamond (BDD) has been thoroughly investigated using various techniques to probe the surface chemistry and evaluate its resilience in molten salts. This chapter uses the material to perform electroanalytical measurements in molten chloride salts. Previous findings reported in this manuscript determined minimal impact on the surface chemistry, such as corrosion and surface termination, but some changes were observed electrochemically. Therefore, the present work will determine if the quality of BDD performance will translate to harsh molten salt environments by performing cyclic voltammetry (CV) to study the $Eu^{3+/2+}$ and $U^{4+/3+}$ redox couples. Values like formal potentials (E^o), diffusion coefficients (D), peak separations (ΔE_p), and heterogeneous electron transfer rate constants (k) were calculated and aligned with what has been published in the literature. Additionally, when it was possible to perform measurements at multiple temperatures, the Gibbs free energy (ΔG), enthalpy (ΔH), and entropy (ΔS) were determined, and each fell within the expected ranges.

Additionally, a comparison is included for how electrochemical responses differ for Eu using free-standing and thin-film BDD, which have stark differences in morphology, which was also discussed in earlier chapters and has been shown to influence electrode performance. Lastly, there was an opportunity to use BDD in measurements of U in LiCl-KCl and $MgCl_2$-NaCl electrolytes, significantly influencing the redox reaction. Compared to graphite and W working electrodes, BDD performed well in the $MgCl_2$-NaCl, where the

presence of Mg^{2+} has been previously found to selectively stabilize lower oxidation states, making techniques like CV challenging.

Overall, the results collected only began to scratch the surface of what could be possible with BDD electrodes in molten salt environments. The experiments were generally successful, but questions are posed based on interesting results in certain circumstances. Further work is required to understand the potential and complete limitations of the material. Continued efforts should be made to optimize electrode designs regarding features like doping levels, geometry, and crystallinity (material thickness) to produce the best results. Electrodes comprising BDD material have a promising future in molten salt electroanalytical chemistry.

6.1 Introduction

Electroanalytical measurements have been performed in molten salts over many decades, and the interest in molten salt electrochemistry continues to grow.[54-65] However, experimental infrastructure is challenging to establish given the limited selection of materials that can withstand the high temperature and corrosive nature of molten salts. Because there are no trivial designs for thermodynamic reference electrodes in fluoride salts, they are not yet the focus of this work. Electroanalytical methods in chloride salt systems are well established and the materials of construction available for lab-scale applications are accessible. For example, working electrodes are typically made of metals like tungsten (W),[68,225-229] or non-diamond carbon (NDC) like graphite or glassy carbon.[72,77,79-83,230-237] It has been argued that metal and NDC electrodes do not perform as

well as boron-doped diamond (BDD) in traditional aqueous environments,[30,36] and it is hypothesized that this feature will translate into molten salt systems. Additionally, materials like graphite are known to foul or decompose in the harsh environment of molten salts, experiencing changes to the diffusion layer and intercalation of Li^+ into the graphite surface at sufficiently negative potentials (less than -1.2 V vs. Ag/AgCl) and formation of Li_2C_2 compounds.[236]

Diamond electrodes have been used previously in chloride molten salts, but the available literature is limited to oxide-containing systems generally for pyroprocessing applications rather than electroanalytical techniques like CV to probe features like electron transfer kinetics.[85-88] There is a wealth of literature available for analytical measurements of Eu and U species in molten salts using NDC electrodes,[77,79-83] but BDD is a novel material for this application. Therefore, there is also no discussion in the literature about the impact of crystal morphology on electrochemical responses in molten salts, which is also discussed below.

In this chapter, 0.1 mol% $EuCl_3$ and UCl_3 in LiCl-KCl were measured using CV to evaluate solvent potential windows and determine values like formal potentials (E^o), diffusion coefficients (D), peak separations (ΔE_p), heterogeneous electron transfer rate constants (k) via scan rate studies. When using the free-standing BDD working electrode, it was possible to repeat the experiment at multiple temperatures, which enabled thermodynamic calculations for Gibbs free energy (ΔG^o), enthalpy (ΔH^o), and entropy (ΔS^o). Additionally, the impact of morphology of the BDD electrode on the electrochemical response is explored. Free-standing BDD and thin-film BDD-coated tantalum (Ta) rod

electrodes were used to study $Eu^{3+/2+}$ in LiCl-KCl. Both electrode designs were imaged using scanning electron microscopy (SEM) after the experiments to determine changes to the surface topography after exposure to the salt systems. However, when performing measurements of $U^{4+/3+}$, only thin-film BDD electrodes were available. In this case, the impact of changing the electrolyte salt was observed by comparing LiCl-KCl and $MgCl_2$-NaCl systems, which has been a research area of interest based on recent publications that explore the impact of cation size and charge on analyte oxidation state stability.[75,238]

6.2 Methods and Materials

A portion of the work performed in this chapter was performed with new infrastructure under development at the University of Nevada, Las Vegas (UNLV), and other experiments used pre-existing infrastructure available at the Los Alamos National Laboratory (LANL). At UNLV, the free-standing BDD was used to study $Eu^{3+/2+}$ before an inert glovebox environment was available, and all other measurements were performed in the gloveboxes at LANL. The differences in experimental design and the impacts of those changes are discussed below. In each case the total salt solution was approximately 20 g. A matrix of the experimental conditions is provided in **Table 6.1**.

Table 6.1 Matrix of experimental conditions for molten salt electrochemical measurements.

Analyte	Electrolyte	Working Electrode	Counter Electrode	Reference Electrode	Environment
$EuCl_3$	LiCl-KCl	Free-Standing BDD	Graphite Block	Ag/AgCl	Benchtop
$EuCl_3$	LiCl-KCl	BDD-Coated Ta Rod	W Rod	Ag/AgCl	Glovebox
UCl_3	LiCl-KCl	BDD-Coated Ta Rod	W Rod	Ag/AgCl	Glovebox
UCl_3	$MgCl_2$-NaCl	Small Area BDD-Coated Ta Rod	W Rod	$Mg/MgCl_2$	Glovebox

6.2.1 Non-inert Measurements

At UNLV, $Eu^{3+/2+}$ was studied using free-standing BDD exposed to air, which provided an opportunity to determine the performance of BDD under particularly harsh conditions since oxygen and moisture were not prevented from impacting the system. A schematic of the Ag/AgCl RE and three-electrode cell is shown in **Figure 6.1**, including the 1 × 5 × 0.35 mm piece of BDD used as the working electrode (WE). The electrical contact was made via a 3 mm diameter (d) hole lased in the top like the grid electrodes used in **Chapter 3**. A Zn-plated steel nut and bolt set were used to attach the BDD to a graphite block that kept the potentiostat lead entering the heating zone of the furnace. A similar graphite block was used as the counter electrode (CE). Following a design seen widely throughout literature,[83,232,239-244] an Ag/AgCl reference electrode (RE) was constructed by adding a 1 mol% AgCl (99.9%, Strem Chemicals) in LiCl-KCl (55.7-44.3 mol%)[238] solution to a thin-wall Pyrex nuclear magnetic resonance (NMR) tube (d = 5 mm, Wilmad LabGlass) with an Ag wire (d = 0.25 mm; 99.995%). The 99%+ purity anhydrous LiCl and KCl salts were acquired from Acros Organics. The analyte solution was 0.1 mol% $EuCl_3$ (99.9% anhydrous, Strem Chemicals) in the same LiCl-KCl solvent salt. All salts were prepared by weighing and then hand-grinding with a mortar and pestle on the benchtop before being added to either the crucible or NMR tube in the case of the RE.

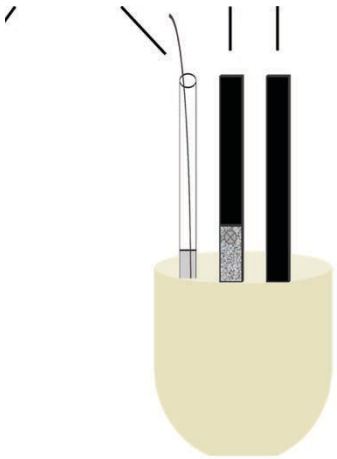

Figure 6.1 Electrochemical cell for $EuCl_3$ ir DD working electrode. RE: 1 mol% AgCl in LiCl-KCl; CE: Graphite.

An MTI KSL-1200X muffle furnace with a custom-designed hole in the top allowed for electrical contact between the potentiostat leads and electrodes in the crucible while at temperature. Images of the furnace and electrochemical cell are shown in **Figure 6.2**. As seen in **A)**, copper (Cu) wire was attached to Cu clips used to make electrical contact with the graphite of the WE and CE and suspend the RE NMR tube. The potentiostat leads were attached to the Cu wires of the WE and CE and the Ag wire of the RE. A top-down view of the three-electrode cells at 450 °C can be seen in **B)**, and the electrodes at room temperature are in **C)**. Measurements were performed using a Biologic SP-300 potentiostat. After the experiment, a JEOL JSM-5600 scanning electron microscope was used to image the BDD.

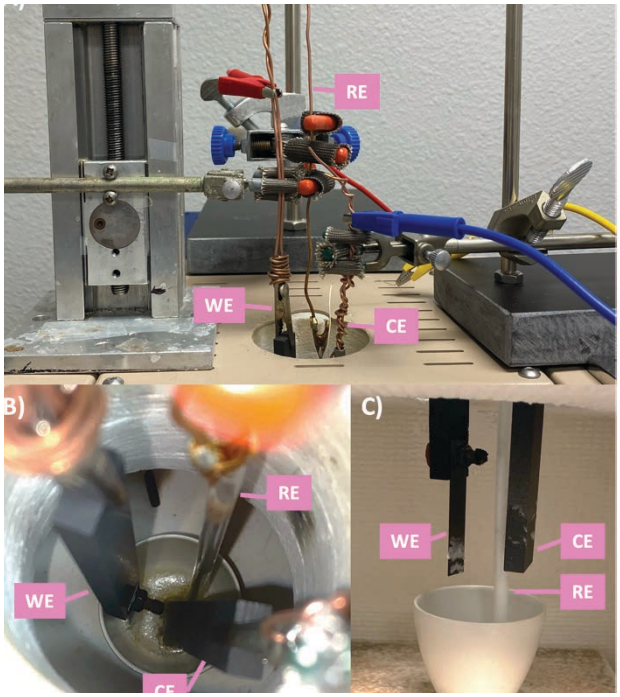

Figure 6.2 Molten salt electrochemistry infrastructure at UNLV used for $EuCl_3$ in LiCl-KCl measurements. A) Electrical connections for the WE, RE, and CE at the top hole of the muffle furnace; B) Top-down view of the crucible at 450 °C showing WE, RE, and CE; C) View inside the furnace at 25 °C after the experiment showing WE, RE, and CE.

6.2.2 Inert Measurements

Polycrystalline BDD-coated Ta rods (d = 0.4 cm, 13 cm long, 5 μm BDD film thickness) were purchased from MSE Supplies with a reported doping level of 2500 ppm, which corresponds to the boron/carbon ratio of the source gas rather than the crystal lattice, but often results in 'medium' doping levels like the other BDD used in this manuscript (see **Figure 3.4**).[43] A bare rod immersed in the salt was used when studying Eu and U in LiCl-KCl (shown in **Figure 6.3**), but the original purpose of performing measurements stemmed from a separate project at LANL that aimed to investigate 'small area working electrodes' (SAWE), unrelated to the work initially planned for this manuscript.[75] There was an opportunity to include a BDD-coated rod electrode whose

surface area (SA) was minimized by covering most of the rod, except for a small portion at one end to be the exposed area (SA = 0.0040 cm^2) and approximately 3 cm at the other end to create electrical contact, with Cotronics Corp Resbond 989 Hi-Purity Alumina Ceramic Adhesive. The Resbond coating was applied and left to dry overnight, followed by cures at 65 °C for 24 hours and 200 °C for 24 hours in an MTI GSL-1500X tube furnace.

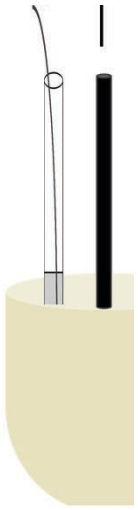

Figure 6.3 Electrochemical cell for $EuCl_3$ and UCl_3 in LiCl-KCl with BDD-coated Ta rod working electrode. RE: Ag/AgCl (exchangeable with Mg/$MgCl_2$); CE: W.

Two other SAWE designs were the original focus of the measurements performed in $MgCl_2$-NaCl and were constructed slightly differently. Disc electrodes are a standard design in aqueous electrochemistry where a circular surface area is the only exposed portion of a conductive material that is otherwise insulated. For molten salts, this was accomplished by taking either a graphite rod (d = 0.305 cm, 99.9995%, Alfa Aesar) or W wire (d = 0.0762 cm, 99.95%, Midwest Tungsten Service) inserted into MgO tubes (Tateho Ozark) that were filled with liquid Resbond. After the same drying and curing

process, the ends of the electrodes were sanded to expose only the ends of either the rod or wire (graphite SA = 0.073 cm^2, W SA = 0.0046 cm^2). This process was not performed for the BDD electrode as the inner diameter of the MgO sheaths was too small for the rod, and the sanding process would also risk compromising the BDD coating. Schematics of the graphite and W SAWEs are shown in **Figure 6.4** with a photo of the BDD SAWE.

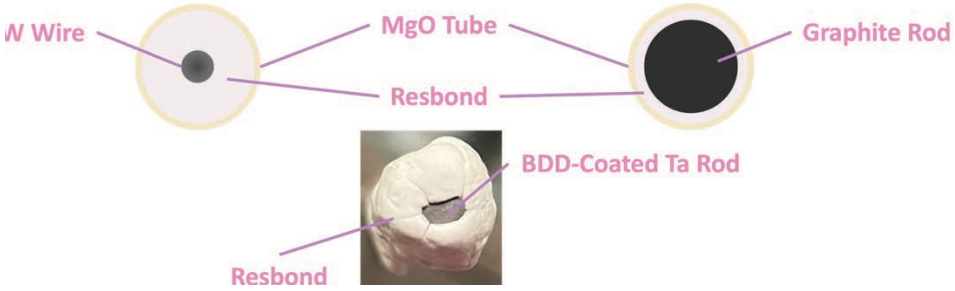

Figure 6.4 Bottom faces of W, graphite, and BDD SAWEs used to study UCl_3 in $MgCl_2$-NaCl at 550 °C.

The W rods (d = 0.3175 cm, 99.95%, Midwest Tungsten Service) used as CEs were sanded before each measurement. In the LiCl-KCl solvent salts, the same Ag/AgCl RE design discussed for the UNLV experiments was used where a 1 mol% AgCl (99.99%, Thermo Fisher Scientific) solution in LiCl-KCl and Ag wire (d = 0.1016 cm, 99.9%, Alfa Aesar) were added to Corning Pyrex borosilicate NMR tubes (outer diameter = 5 mm, inner diameter = 4.2 mm).[83,232,239-244] The measurements performed in the $MgCl_2$-NaCl solvent also aimed to validate using a novel Mg/$MgCl_2$ RE designed by researchers at LANL, and their process was followed for preparation.[74] A Mg rod (d = 0.3175 cm, 99.935%, ESPI Metals) and the $MgCl_2$-NaCl mixture were added to a custom-designed MgO tube (Tateho Ozark), where a 2.54 cm porous plug was fitted to one end to serve as the frit.

The team at LANL had pre-existing infrastructure suitable for electroanalytical chemistry in molten salts, shown in **Figure 6.5**. An MTI KSL-1100X muffle furnace had a custom hole cut in the top with a graphite cap designed in-house using the local machine shop on site. The graphite cap holes were drilled and tapped to house Swagelok fittings to support electrodes. For fully conductive electrode materials like the CE comprising a bare W rod, a MgO sheath was used to secure the W rod and prevent electrical contact with the graphite cap. Additionally, for this work, insulation material was placed under the cap because the BDD rod, when mounted, was slightly too tall, and the cap needed to be elevated to ensure the WE did not touch the bottom of the crucible during measurements since that was the location of the exposed surface.

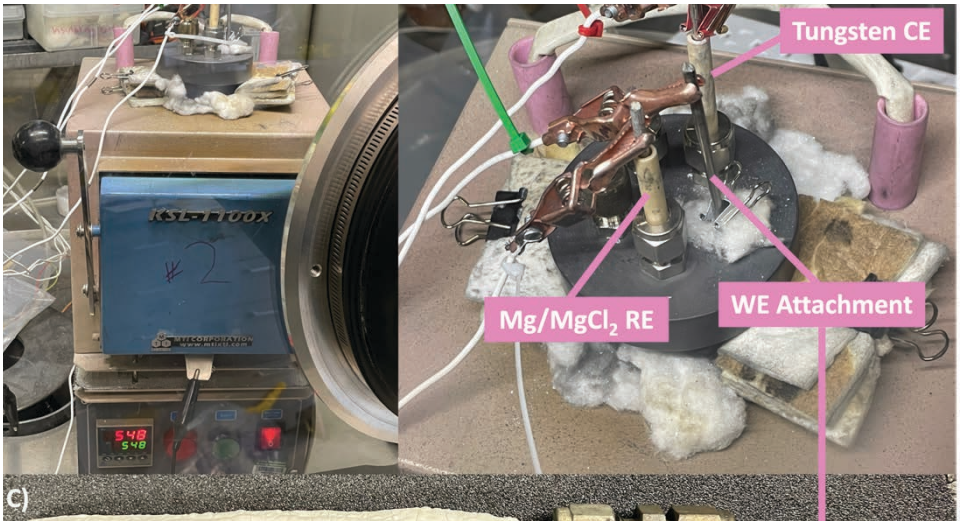

Figure 6.5 Molten salt electrochemistry infrastructure at LANL used for $EuCl_3$ and UCl_3 in LiCl-KCl and $MgCl_2$-NaCl measurements. A) Muffle furnace with grounding strip and graphite cap with feedthroughs to secure electrodes; B) Graphite cap with $Mg/MgCl_2$ RE (exchangeable with Ag/AgCl design), working electrode extension (exchangeable with W, graphite, and BDD electrodes), and W CE housed in a ceramic sheath; C) Example WE mount showcasing BDD-coated Ta rod covered with Resbond to restrict surface area to bottom end when submerged in salt.

A stainless-steel tongue fed through the bottom of the door and was placed under a stainless-steel cup inside the furnace. The crucible was placed in the cup to serve as secondary containment in the event of a spill and to create a Faraday cage by grounding the system through a lead connecting the steel tongue and the glovebox frame (seen in **Figure 6.5 A**). Small binder clips were useful in suspending or securing portions of the infrastructure, like in **B)**.

The WE mount served as an extension for electrical contact as the electrodes were not long enough to reach through the graphite cap while in the salt solution. For the BDD rod, a 0.4 cm Swagelok outfitted with Teflon ferrules held the exposed end of the electrode (0.3175 cm components for graphite and W electrodes) and was connected to an adaptor for a stainless-steel rod (d = 0.635 cm) acquired from the scrap metal in the machine shop. This design is shown for the BDD rod in **Figure 6.5 C)**.

All electrolyte salts (LiCl, KCl, NaCl, $MgCl_2$ from Alfa Aesar, >99% purity) used in the experiments at LANL were dried following procedures outlined by laboratory standard operating procedures like in **Chapter 4** and **Chapter 5** using the same vacuum oven antechamber attached to the VAC NEXGEN Ar(*g*) glovebox (<0.5 ppm moisture, <0.5 ppm O_2). However, the $MgCl_2$ procedure was slightly different to avoid forming MgOHCl side products that can form from rapid reactions between H_2O and $MgCl_2$ at high temperatures.[74,245] The vacuum oven antechamber was held at 117 °C, 180 °C, and 240 °C, for 20 hours each. The chloride salts (LiCl, KCl, NaCl, and $MgCl_2$) were weighed after drying and introduction to the glovebox. The LiCl-KCl was combined at the 55.7-44.3

mol% eutectic ratio and 48-52 mol% for $MgCl_2$-NaCl. The $EuCl_3$ (99.99% anhydrous, Sigma Aldrich) and UCl_3 (prepared by TerraPower) were added to their respective mixtures at concentrations of 0.1 mol% and mixed before being added to either Al_2O_3 (Coors) or MgO crucibles (Tateho Ozark) for measurements in LiCl-KCl or $MgCl_2$-NaCl, respectively.

Measurements of LiCl-KCl systems were performed with CH Instruments 1140C potentiostats, and a Biologic SP-50 potentiostat was used for those in $MgCl_2$-NaCl. All experiments were performed in VAC NexGen Ar(*g*) gloveboxes (<0.5 ppm moisture, <0.5 ppm O_2) outfitted with PolyScience Durachill chillers to regulate the temperature while furnaces were operating. Current interrupt *iR* compensation was determined for all measurements before each procedure began. A Thermo Fisher Scientific ApreoS LoVac scanning electron microscopy was used to image the BDD rod from the $EuCl_3$ measurements.

6.3 Europium Trichloride

Like the discussions of, the $Eu^{3+/2+}$ redox couple described in Eq. 6 was chosen as a non-radioactive f-block species before embarking on experiments with U. There is a wealth of literature for CV of Eu in molten chloride salts to compare the values calculated in the following sections (e.g., E^o, D, and k) that will be discussed in detail below. Experiments were successfully performed on free-standing BDD and BDD-coated Ta rod electrodes in LiCl-KCl at 450 °C.

$$Eu^{3+} + e^- \rightleftharpoons Eu^{2+} \quad \textbf{(6)}$$

6.3.1 Free-Standing BDD

In previous chapters (**2** and 5), it was possible to isolate the 'grown' (large crystal) or 'nucleation' (smooth side resulting from the removal of the growth substrate) sides and compare the electrochemical responses of each. In the present study, the experimental design is like in **Chapter 3** when performing CV on the grid and non-grid free-standing BDD such that both the grown and nucleation sides of the material were exposed to the solution and participated in the measurement. Regardless, it is anticipated that based on the culmination of results in the previous chapters, free-standing BDD should be capable of successfully measuring the $Eu^{3+/2+}$ redox couple and surviving the LiCl-KCl environment for the duration of the experiment. Scanning electron microscopy (SEM) was performed on the material submerged in the salt and exposed to the high-temperature air of the furnace during the experiment to visualize any changes to the topography.

6.3.1.1 Cyclic Voltammetry

Scan rate studies at 10, 25, 50, 75, and 100 mV/s (three trials of three cycles for each scan rate) were performed at 450, 550, and 650 °C in 0.11 mol% $EuCl_3$ in LiCl-KCl with a graphite block CE and Ag/AgCl RE. The exact concentration that can be used for calculations was translated to 31.1 mmol based on an assumed LiCl-KCl density of 1.6 g/mL at 450°C.[245] The surface area of the BDD exposed to the salt was 2.11 cm^2 (1 cm^2 on the grown and nucleation sides plus the side and bottom edges of the material). Again,

this experiment was performed before an inert glovebox environment was available and performed on the benchtop exposed to air.

Before the $EuCl_3$ was added, a scan of the solvent potential window was performed at 450 °C to first determine the working region between the $Cl_2(g)$ evolution at the positive region and reduction of Li metal at the negative region (comparable to the production of $O_2(g)$ at the anodic overpotential or $H_2(g)$ at the cathodic overpotential observed in water-based solutions), also referred to as the 'solvent decomposition' regions. The resulting voltammogram at 100 mV/s is shown in **Figure 6.6** and provides a working window of approximately 3 V. This is slightly smaller than what has been reported in the literature for W, Mo, and graphite electrodes (ca. 3.25 – 3.75 V).[66,76,237,242,247-249] This discrepancy may result from multiple uncontrolled variables during the measurement. No purification steps were taken for salt drying to remove moisture-related species (e.g., hydroxides) or a pre-electrolysis process to remove impurities via electrodeposition. Additionally, IR compensation was not first performed before the measurement, which may explain voltage loss caused by the electrolyte between the WE and RE. However, the region where the $Eu^{3+/2+}$ is expected to appear ($E^o \sim +3$ V vs. Ag/AgCl at 450 °C)[79,81,235] falls well between the two decomposition portions of the solvent window.

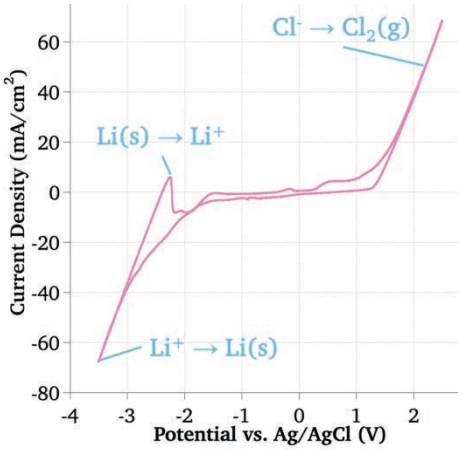

Figure 6.6 Potential windo BDD in air at 450 °C. RE: 1 mol% AgCl in LiCl-KCl; CE: Graph

The scan rate study on free-standing BDD at 450 °C for 10, 25, 50, 75, and 100 mV/s is shown in **Figure 6.7 A)**, accompanied by the plot of peak currents over the square roots of each scan rate ($\sqrt{\nu}$) in **B)**. Each scan rate was cycled three times and performed over three trials. Despite the previously discussed sources of error due to the lack of purification or controlled environment, the oxidation and reduction peaks are well-resolved, and the anodic and cathodic peak regression have high correlation coefficients (>0.999), indicating semi-infinite linear diffusion.[109]

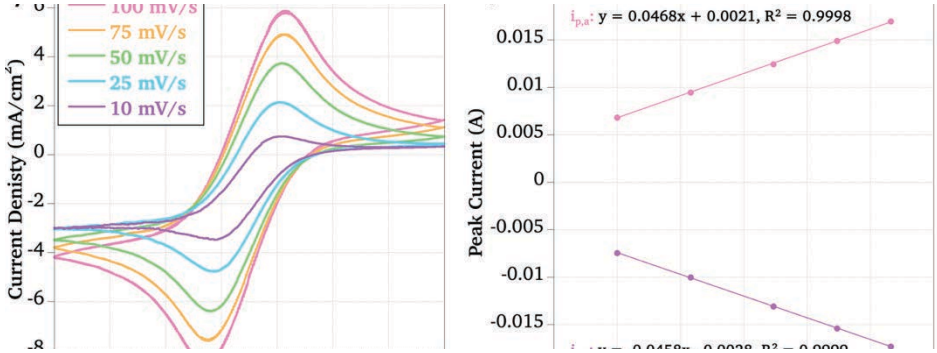

Figure 6.7 Scan rate study of 31.1 mmol $EuCl_3$ in LiCl-KCl on free-standing BDD at 450 °C in air. RE: 1 mol% AgCl in LiCl-KCl; CE: Graphite.

Because this initial measurement was successful, the temperature was increased to 550 and then 650 °C to repeat the scan rate studies. Overlays of the 50 mV/s scans are shown in **Figure 6.8**. From 450 to 550 °C, the anodic peak resolution is consistent and shifts positively, as expected. However, the cathodic peak shows a significant decrease and possible shift in the background current based on the angle of the voltammogram. By 650 °C, the scan quality significantly decreased such that the anodic peak is poorly resolved, and noise is present in the signal at both ends of the voltammogram window. This decline may indicate an issue with the electrode response or electrical connection, but scan rate studies with multiple trials and cycles were successfully performed at each temperature.

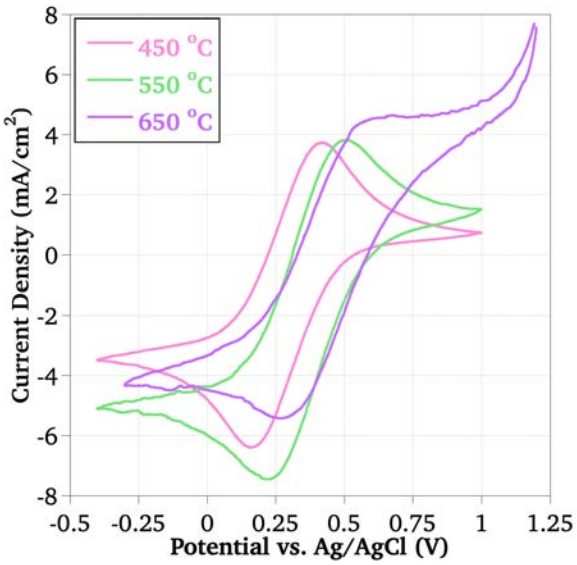

Figure 6.8 Overlays of 50 mV/s scans at 450, 550, and 650 °C for 31.1 mmol $EuCl_3$ in LiCl-KCl on free-standing BDD in air. RE: 1 mol% AgCl in LiCl-KCl; CE: Graphite.

The issue quickly became apparent after the furnace was cooled to room temperature. The electrical contact between the graphite block and BDD via Zn-plated steel is shown in **Figure 6.9**. Significant corrosion has occurred, almost certainly due to

the prolonged exposure to high temperatures in air, resulting in oxidation of the metal components. This damage is the most likely source of decline in measurement quality and could likely be prevented by performing experiments under oxygen and water free conditions.

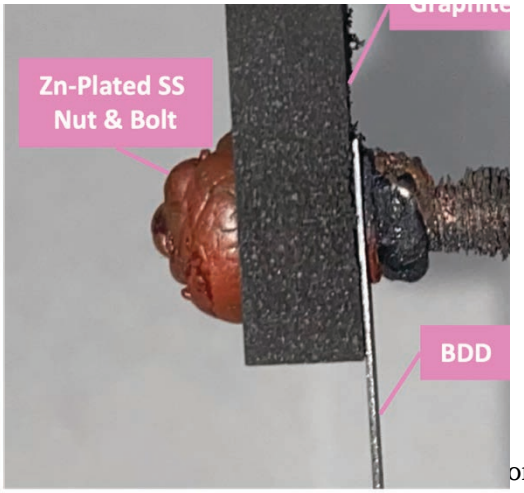

Figure 6.9 Side view of cor or BDD electrode from CV of $EuCl_3$ in LiCl-KCl at 450, 550, and

Although the signal quality was compromised over time, the successful scan rates still resulted in peak current versus $\sqrt{\nu}$ with regressions >0.99 for 450 and 550 °C and >0.9 for 650 °C. Therefore, the E^o and D were calculated and are listed in **Table 6.2** for each temperature. Based on the Nernst equation (Eq. 20), E^o was expected to increase as the temperature was increased.

$$E_{cell} = E^o_{cell} - \frac{RT}{nF} \ln \left(\frac{[Red]}{[Ox]}\right) \quad \textbf{(20)}$$

This trend was observed and reported below and aligned with values reported in the literature versus Ag/AgCl.[235,250]

Table 6.2 Formal potentials and diffusion coefficients determined for 31.1 mmol $EuCl_3$ in LiCl-KCl at 450, 550, and 650 °C with free-standing BDD.

T (°C)	*E* vs. Ag/AgCl (V)	$D_O \times 10^{-5}$ (cm^2/s)	$D_R \times 10^{-5}$ (cm^2/s)
450	+0.288 ±0.0006	1.6 ±0.01	1.7 ±0.04
550	+0.358 ±0.001	1.9 ±0.08	2.3 ±0.09
650	+0.439 ±0.002	1.6 ±0.5	0.9 ±0.2

The Randles-Sevcik equation (Eq. 4) is commonly used to determine Eu diffusion coefficients in molten chloride salts.[67,69,71] The values for the diffusion of the oxidized and reduced species are reported in **Table 6.2** for the three temperatures. Values in the literature typically fall within 10^{-6} – 10^{-5} cm^2/s,[72,235] aligning with the present results. The diffusion was expected to increase as temperature increased,[70] and this trend was observed for the first temperature step. However, the value collected for 650 °C decreased, most likely due to decreased electrical contact quality. The nut and bolt connecting the BDD to the graphite block mount was severely corroded (seen in **Figure 6.9**) which likely had a significant influence on the quality of the measurement and is confirmed by the poor resolution of the 50 mV/s scan in **Figure 6.8**. At that temperature, the peak current measurements are likely skewed for higher values, supported by the declining correlation coefficient.

The three scan rate studies also provided information regarding the kinetics of the electron transfer through values for ΔE_p and k. The Nicholson method for determining k using Eq. 5 is commonly applied to Eu in molten chloride salts.[69-73,110] However, the increased temperature must be considered for ΔE_p and ψ, a value defined by Nicholson to

calculate k as a function of ΔE_p. The appropriate adjustment can be made using Eq. 21 and Eq. 22 with a charge transfer coefficient (α) value of 0.5 based on the process outlined by Kuznetsov et al.[70,72,73]

$$\Delta E_{p,298} = \frac{\Delta E_{p,T} \cdot 298}{T} \quad \textbf{(21)}$$

$$\psi_T = \psi_{298}\sqrt{\frac{T}{298}} \quad \textbf{(22)}$$

The adjustments for 450, 550, and 650 °C are presented in **Table 6.3** and the corresponding k values for 50 mV/s scans in **Table 6.2** align with previous reports for $Eu^{3+/2+}$ in chloride salts, presenting the expected trend of increasing electron transfer rate at higher temperatures.[69-73]

Table 6.3 Peak separation and ψ adjusted for salt temperature with resulting k for the 50 mV/s scan rate.

T (K)	$\Delta E_{p,T}$ (mV)	$\Delta E_{p,298}$ (mV)	ψ_T	ψ_{298}	$k \times 10^{-3}$ (cm/s)
723	244 ±0.001	101 ±0.001	0.6	0.93	6.1
823	245 ±0.005	88.7 ±0.005	0.8	1.3	9.3
923	235 ±0.006	75.9 ±0.006	1.8	3.1	12

Although the quality of scans began to decrease at higher temperatures, the peak potentials were still easily delineated, meaning the values for E^o for each scan rate study could be used to explore thermodynamic descriptions of the $Eu^{3+/2+}$ redox couple. The relationship between E^o and the Gibbs free energy (ΔG^o) is outlined in Eq. 23.

$$\Delta G^o = -nFE^o \quad \textbf{(23)}$$

Additionally, ΔG^o also corresponds to the enthalpy (ΔH^o) and entropy (ΔS^o) of the reaction that can be determined using a regression of the free energy over multiple temperatures via Eq. 24.

$$\Delta G^o = \Delta H^o - T\Delta S^o \quad \textbf{(24)}$$

Most literature first adjusts the reference potential to that of the Cl solvent decomposition at the positive end of the potential window, which is a temperature-dependent shift from Ag/AgCl.[232,237,251,252] One published method outlines the process of converting reference potentials based on the temperature of the salt during measurement and the concentration of AgCl in the RE design.[239,253] First, the apparent standard potential of the Ag/AgCl redox couple ($E^{o\prime}_{Ag/AgCl}$) is determined for the given temperature using Eq. 25.

$$E^{o\prime}_{Ag/AgCl} = -1.076 + 0.0001672T \quad \textbf{(25)}$$

Then, this value is corrected via the Nernst equation to consider the mole fraction (X_{AgCl}) via Eq. 26 to determine the relative cell potential, which can then be used to convert to and from the $Cl^-/Cl_2(g)$.

$$E^{o}_{Ag/AgCl} = E^{o\prime}_{Ag/AgCl} - \frac{RT}{nF}\ln\left(X_{AgCl}\right) \quad \textbf{(26)}$$

In the present study, 1 mol% AgCl ($X_{AgCl} = 0.01$) conversion to the $Cl^-/Cl_2(g)$ reference for 450, 550, and 650 °C shifted the potential -1.242, -1.26, and -1.29 V, respectively.

A linear regression was performed for ΔG^o across the three studied temperatures, shown in **Figure 6.10**. The y-intercept and slope equate to ΔH^o and ΔS^o, respectively, and the regression is highly linear (R^2>0.99). Although the measurement quality decreased as the temperature increased, the RE was stable, and peaks were still resolved well enough to determine the energetics of the reaction. The values for ΔG^o at each temperature (-92.0, -87.5, and -81.9 kJ/mol) and resulting ΔH^o (-128.8 kJ/mol) and ΔS^o (-50.7 J/mol·K) almost exactly match what has been reported for $Eu^{3+/2+}$ in LiCl-KCl.[80] These values are listed alongside the corresponding temperatures and E^o for both reference potentials in **Table 6.4** and comparative literature values in **Table 6.5**.

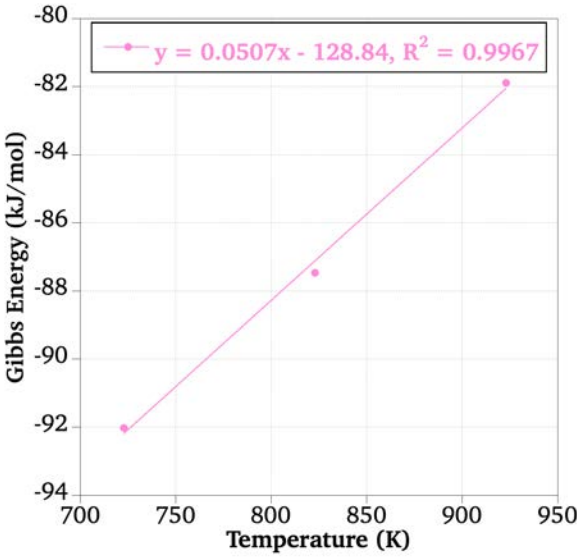

Figure 6.10 Regression of Gibbs energy vs. $Cl^-/Cl_2(g)$ for 31.1 mmol $EuCl_3$ in LiCl-KCl at 450, 550, and 650 °C with free-standing BDD.

Table 6.4 Thermodynamic calculations for 31.1 mmol $EuCl_3$ in LiCl-KCl at 450, 550, and 650 °C with free-standing BDD vs. Ag/AgCl and adjusted Cl^-/Cl_2 reference.

T (°C)	E^o vs. Ag/AgCl (V)	E^o vs. Cl^-/Cl_2 (V)	ΔG^o (kJ/mol)	ΔH^o (kJ/mol)	ΔS^o (J/mol·K)	R^2
450	+0.288 ±0.0006	-0.954 ±0.0006	-92.0 ±0.6	-128.8 ±2.4	-50.7 ±2.9	0.9967
550	+0.358 ±0.001	-0.902 ±0.001	-87.5 ±1			
650	+0.439 ±0.002	-0.851 ±0.002	-81.9 ±2			

Table 6.5 Thermodynamic calculations compared to literature values.

T (°C)	ΔG^o(kJ/mol)	ΔH^o(kJ/mol)	ΔS^o(J/mol·K)	Reference
450	-92.0 ±0.6	-128.8 ±2.4	-50.7 ±2.9	This Work
550	-87.5 ±1			
650	-81.9 ±2			
450	-92.4 ±0.19	-128 ±0.2	-49 ±0.08	80
550	-87.8 ±0.19			
650	-82.5 ±0.19			

6.3.1.2 Scanning Electron Microscopy

After performing the solvent potential window scan at 450 °C and scan rate studies at 450, 550, and 650 °C, SEM was used to image the grown side of the material. An image was collected in the region submerged in the salt and a portion above the liquid level exposed to the high-temperature air of the furnace. Based on the results of **Chapter 4** and **Chapter 5**, the source of corrosion after BDD was exposed to molten salts was likely moisture and oxygen present in the salts that were not purified and melted in air. Therefore, it is expected that significantly more corrosion is expected in the upper region of the material that was in direct contact with the furnace air for the duration of the experiments. The furnace temperature was above 400 °C for roughly 8 hours and cycled approximately 150 times for the potential window and scan rate study voltammograms.

A schematic of the WE design with the regions exposed to either salt or air is on the left in **Figure 6.11** To the right are micrographs of one area in each region showing the large crystalline structures expected for the grown side of free-standing material seen in

the previous chapters. Both regions show white across the surfaces, indicating the presence of salt residual that remained after cleaning with water via sonication. Although the top region was not directly submerged in the solution, the salt may have volatilized during the experiment. However, etching occurred at the grain boundaries and between the facets of each crystal, much like what was previously observed on corroded samples in **Chapter 4** and **Chapter 5**. However, the portion of the BDD that was only in the salt does not show any apparent corrosion, which further strengthens the previous arguments that the source of corrosion is high-temperature oxygen or moisture rather than the salt system directly, which is a theory supported by literature where high-temperature oxidation is described.[84]

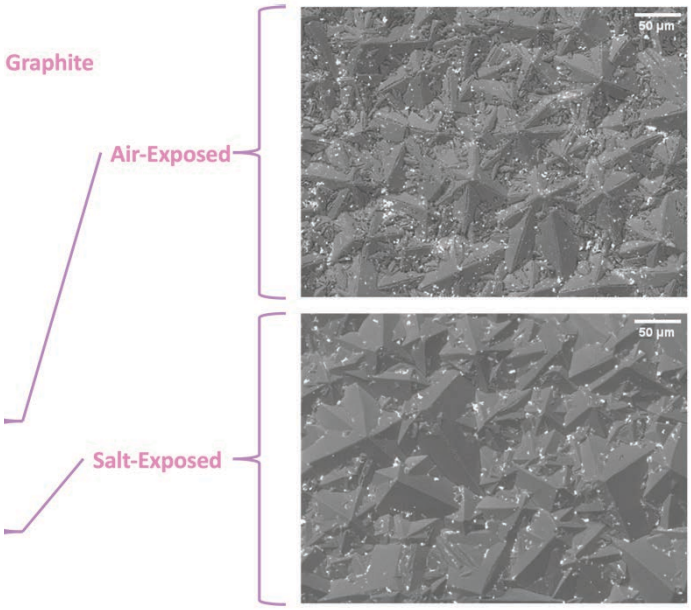

Figure 6.11 SEM of free-sta 50, and 650 °C. The top portion was not exposed ed in the salt for the duration of the experiment.

6.3.2 Thin-Film BDD

Large pieces (longer than the coupons used in **Chapter 5**) of free-standing BDD are challenging to grow; therefore, they are expensive and take significant time to acquire.

Therefore, the only electrode material available during these experiments performed at LANL was BDD-coated Ta rods that could be more easily purchased from a supplier within a reasonable time. However, by performing scan rate studies for $EuCl_3$ in LiCl-KCl with this material, a comparison can be made between the electrical performance of free-standing and thin-film BDD. Because the system was not radioactive, the electrode was also imaged using SEM after the experiment.

6.3.2.1 Cyclic Voltammetry

A scan rate study was performed for 0.1 mol% (28.2 mmol in this measurement)[246] $Eu^{3+/2+}$ in LiCl-KCl using the thin-film BDD electrode at 100, 200, 300, 400, and 500 mV/s. In this case, the slower scan rates used previously (10 – 100 mV/s) did not produce meaningful voltammograms that could be used to perform calculations to quantify electrode performance. Additionally, there were apparent issues with the construction of the Ag/AgCl reference electrode, which were observed when the potential window was shifted too far in the positive direction. Positive shifts have been observed by other researchers when AgCl concentrations are sufficiently low,[253] but it is unclear as to why this was not an issue that occurred in the previous measurement, in the many publications that also use this design, or the following measurement of U in the next section. However, it is trivial to calibrate the reference potential of the potential window and scan rate study to the onset of chlorine solvent decomposition in the background scan and then adjust to the equivalent of 1 mol% Ag/AgCl using Eq. 25 and Eq. 26.[239,253] An attempt was made to increase the temperature and repeat the scan rate study. However, the response quality

was too poor to utilize for quantification. Therefore, the experiment was limited to just one temperature out of concern for the BDD rod electrode but still allowed for calculations of E^o, D, ΔE_p, and k at 450 °C.

The potential window measured in LiCl-KCl at 450 °C using the thin-film BDD electrode is shown in **Figure 6.12** where the original data is overlaid with the shifted potential to align with the Cl solvent decomposition (-2.3 V shift) and Li solvent decomposition (+1.4 V shift). Like what was seen using the free-standing BDD, the literature indicates that the oxidation of Cl^- to $Cl_2(g)$ should appear in the range of +1.25 to +1.5 V vs. Ag/AgCl and the reduction of Li^+ to Li metal occurs between approximately -2.25 V and -2.75 V vs. Ag/AgCl.[66,76,237,242,247-249] The Cl_2/Cl(g) and Li^+/Li reactions both serve as standard references in LiCl-KCl[72,230,254,255] and their reliability is confirmed as the solvent decomposition onsets were consistent over time. Additionally, the anodic and cathodic peaks from the scan rate study discussed below did not shift in potential, indicating that the RE used was precise, even if inaccurate.

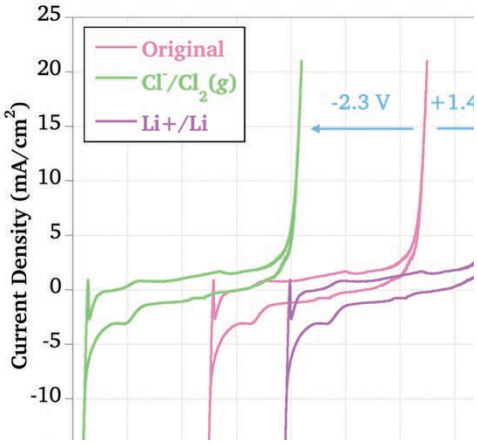

Figure 6.12 Potential window at 100 mV/s for LiCl-KCl on thin-film BDD at 450 °C with reference potentials adjusted to $Cl^-/Cl_2(g)$ (green) and Li^+/Li (purple). CE: W.

The solvent window shows a relatively large background current density (approximately 2 A/cm^2) compared to what was observed using the free-standing material (approximately 1.5 mA/cm^2). One explanation for this difference may be related to the carbon hybridization of the differing morphologies. The thin-film BDD, at only 5 μm in thickness, has many small grain boundaries and, therefore, a relatively high sp^2 content compared to the free-standing material. The fine grain surface may ultimately increase the conductivity compared to the free-standing material with large crystals on the grown side at 350 μm thick, where one-half of the surface is primarily sp^3-hybridized carbon. With this feature being considered, the working region of the solvent window is still approximately 3 V, like the free-standing material, for the distance between the Cl and Li solvent decomposition regions.

Another important consideration is the purity of the salt. Anodic and cathodic peaks appear approximately 0.5 V positive from the Li reduction and are mostly likely the result of hydroxide contamination in the form of LiOH.[256] This indicates that the thermal drying and pre-electrolysis procedures did not wholly remove moisture from the system before melting. However, no other species appear within the window, and the regions where the Eu and U redox couples are expected should be unaffected.

The scan rate study normalized to the $Cl^-/Cl_2(g)$ reference is shown in **Figure 6.13 A)** for scan rates 100 – 500 mV/s, where each was cycled three times and performed over three trials. With E^o at -0.942 V vs. $Cl^-/Cl_2(g)$, this result aligns well with literature for $Eu^{3+/2+}$ in chloride molten salts[72,230,255] in addition to the results normalized using the free-

standing BDD in the previous study. Additionally, if the CVs are instead normalized to the Li^+/Li reference, the resulting E^o at +2.75 V exactly agrees with what has been previously reported.[254] When adjusted to the 1 mol% Ag/AgCl reference after normalization to either of the decomposition potentials[239,253] E^o was +0.300 V which aligns nicely with what was determined using the free-standing BDD at 450 °C, agreeing with expected values.[235,250] The total surface area exposed to the salt (3.9 cm^2) was determined by measuring the salt level after removing the electrode from the graphite cap at temperature.

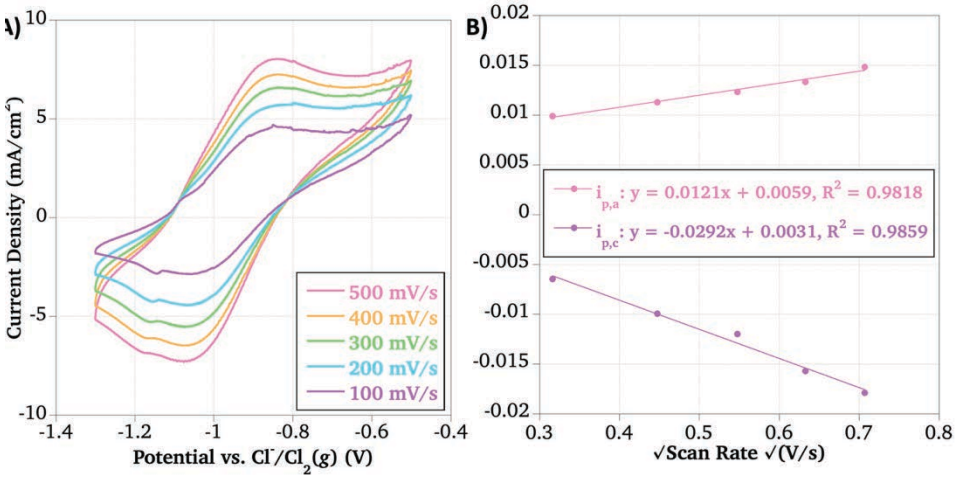

Figure 6.13 Scan rate study of 28.2 mmol $EuCl_3$ in LiCl-KCl on thin-film BDD at 450 °C. Reference: $Cl^-/Cl_2(g)$; CE: W.

The plot of peak current versus $\sqrt{\nu}$ in **Figure 6.13 B)** for the anodic and cathodic reactions produced relatively linear regressions, but both correlation coefficients are slightly weaker than what was collected using the free-standing material at the same temperature ($R^2 = 0.98$ for thin-film BDD vs. $R^2 > 0.99$ for free-standing BDD). However, the trend is still overall linear and allowed for the calculations of D. Figures of merit are listed in **Table 6.6** for E^o at all three reference potentials, and D was determined using the Randles-Sevcik equation (Eq. 4).

Table 6.6 Formal potentials and diffusion coefficients determined for 28.2 mmol $EuCl_3$ in LiCl-KCl at 450 °C with free-standing BDD recalibrated for Ag/AgCl using $Cl^-/Cl_2(g)$ and Li^+/Li.

E^o vs. $Cl^-/Cl_2(g)$ (V)	E^o vs. Li^+/Li (V)	E^o vs. Ag/AgCl (V)	$D_O \times 10^{-6}$ (cm^2/s)	$D_R \times 10^{-6}$ (cm^2/s)
-0.942 ±0.001	+2.75 ±0.001	+0.300 ±0.001	2.4 ±0.3	0.41 ±0.06

In some cases, D has been reported using the Berzins-Delahay method (Eq. 7) for scan rates faster than 500 mV/s because the reversibility of the reaction is compromised,[72] but because the study was performed with 100 – 500 mV/s scan rates, the Randles-Sevcik equation was still provided reasonable results. The regressions for peak current over $\sqrt{\nu}$ are not as strong as those calculated for the measurements at 450 and 550 °C using the free-standing BDD, but $R^2 > 0.9$ for both the anodic and cathodic reactions. In comparable studies, D is typically expected within 10^6 - 10^{-5} cm^2/s,[67,69-72,232,235] which is in line with D_o, but D_R was determined to be slightly slower than anticipated at 4.1×10^{-7} cm^2/s. However, an instance has been reported where a graphite rod WE produced D in the range of 10^{-10} cm^2/s,[255] so one possible explanation could be the similar hybridization (presence of sp^2) of the carbon affecting the diffusion. However, based on the quality of the measurements seen in **Figure 6.13 A)**, it is most likely related to increased resistance indicated by the angle of the voltammograms, which could have skewed the resulting peak current values that directly impact the calculation of D.

As for the free-standing material, the Nicholson method with temperature-adjusted parameters and $\alpha = 0.5$ was used to determine k.[69-73,110] In this case, the room temperature and high temperature ΔE_p and ψ values with the resulting k for 300 mV/s are listed in **Table 6.7**. Regardless of the relatively slow diffusion of Eu^{2+}, k falls within the expected range and aligns closely with what was calculated for the free-standing BDD.[69-73]

Table 6.7 Peak separation and ψ adjusted for salt temperature with resulting *k* for the 300 mV/s scan rate.

T (K)	$\Delta E_{p,T}$ (mV)	$\Delta E_{p,298}$ (mV)	ψ_T	ψ_{298}	k (cm/s)
723	208 ±1	85.7 ±1	0.9	1.4	5.4×10^{-3}

6.3.2.2 Scanning Electron Microscopy

After the scan rate study at 450 °C was complete, the furnace temperature was increased to 550 °C, and the measurements were attempted again. However, no usable signal was acquired. After the furnace cooled to room temperature, it became clear why there may have been issues compared to CVs like what was collected on the free-standing BDD. The electrode was removed from the salt, revealing that the coating had chipped off the rod at the end of the submerged portion. Therefore, it is likely that the Ta rod was involved in the electrochemical response observed in the previous section. Images were collected with SEM to evaluate the damage further. Three images of the rod end are stitched together to produce **Figure 6.14**. It is hypothesized that the temperature ramping may have been too rapid when heating to 450 and 550 °C, resulting in thermal unequal expansion of the BDD coating and its Ta substrate, causing the thin coating to crack and separate from the rod. This feature also appears primarily where a 'seam' exists in the coating because of the chemical vapor deposition (CVD) process as the Ta is coated horizontally, then rotated to coat the other side. The edge of the coatings would possibly serve as points of weakness when presented with extreme environments.

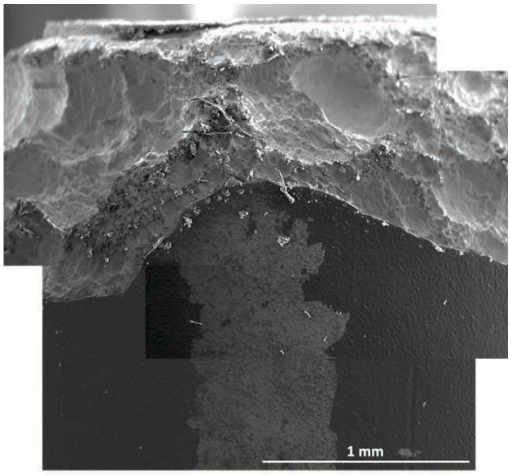

Figure 6.14 Stitched SEM ıre to LiCl-KCl at 450 and 550 °C.

However, images were also acquired before exposure to provide a thin-film polycrystalline BDD topography baseline. **Figure 6.15 A)** shows a micrograph of a new rod not yet exposed to salt. The grain structure is entirely different from what was observed on either the grown or nucleation sides of the free-standing BDD. In this case, the crystal structures are described in the literature as 'cauliflower nanodiamond carbon' based on the resemblance of the vegetable in the crystal structure.[257] Additionally, the used electrode was imaged in a region submerged in the salt but away from the damaged portion at the rod end in **Figure 6.15 B)**. In this case, there is no apparent change to the coating or crystal structure, even after exposure to various temperatures in molten chloride salt.

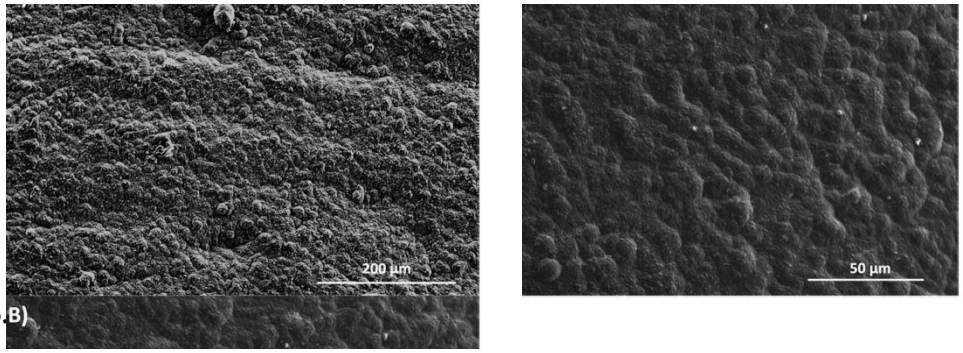

Figure 6. B) C.

6.4 Uranium Trichloride

The BDD-coated rod electrodes were used to perform CVs of UCl_3 in LiCl-KCl and $MgCl_2$-NaCl (48-52 mol%) electrolytes. Free-standing material long enough to perform molten salt electroanalytical measurements was not available in this case but is a proposed area of future work following the success observed in measurements of $EuCl_3$ discussed in the previous section. Attempts were made to use the BDD coupons used in the exposure tests of **Chapter 4** and **Chapter 5**, but the small area was challenging to selectively expose to the salt while also ensuring the electrical connection was resilient. Those measurements were ultimately unsuccessful for many reasons related to the available infrastructure.

The same furnace design used for $EuCl_3$ measurements with the BDD rod electrode was also employed in this section. In the LiCl-KCl electrolyte, a bare rod was used in the salt. However, one feature of the project that provided the opportunity to use BDD to study UCl_3 in $MgCl_2$-NaCl was the development of small area working electrodes (SAWE) that aimed to increase resolution and sensitivity. Therefore, the BDD rod electrode was modified with Resbond by covering all but a small portion of one end, which was exposed

to the salt, and approximately 3 cm in length at the other end to allow for electrical connections.

6.4.1 LiCl-KCl Electrolyte

The solvent potential window of LiCl-KCl using the bare BDD rod electrode was measured again before UCl_3 was introduced. The result was expected to be identical to what was collected before studying Eu in the previous section. However, the voltammogram presented in **Figure 6.16** shows that the overall current density is significantly lower, and the presence of LiOH appears to be less prominent with only a slight cathodic wave appearing just before the Li solvent decomposition.[256] Additionally, this window does align with the potentials expected for the Cl and Li overpotential regions at each end of the CV.[66,76,228,237,242,247-249] Compared to what was observed on the free-standing BDD, this window is well-resolved, and the solvent decomposition features are not affected by issues with resistance, which may be a combination of improved electrical connection and the use of *iR* compensation performed before the measurement.

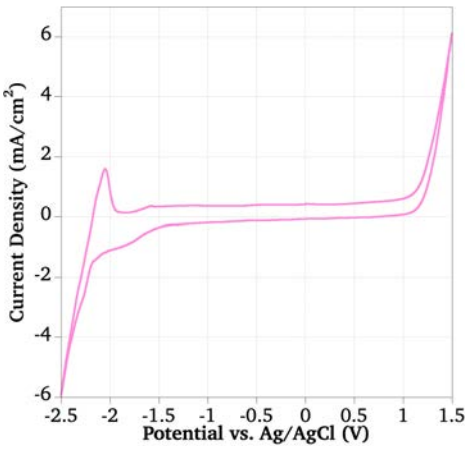

Figure 6.16 Potential window at 100 mV/s for LiCl-KCl on thin-film BDD at 450 °C. RE: 1 mol% AgCl in LiCl-KCl; CE: W.

Unlike the measurements of $EuCl_3$ using the thin-film rod electrode, the scan rate study of 0.1 mol% (27.7 mmol)[51] $U^{4+/3+}$ was successfully captured using the slower scan rates, 10, 25, 50, 75, and 100 mV/s where each was cycled three times and performed over three trials. As seen in **Figure 6.17 A)**, there is virtually no noise across the scans, and like for the solvent window, resistance does not appear to affect the shape of the voltammograms. Additionally, the regressions for the anodic and cathodic peak heights over $\sqrt{\nu}$ have strong correlation coefficients, both larger than 0.99.

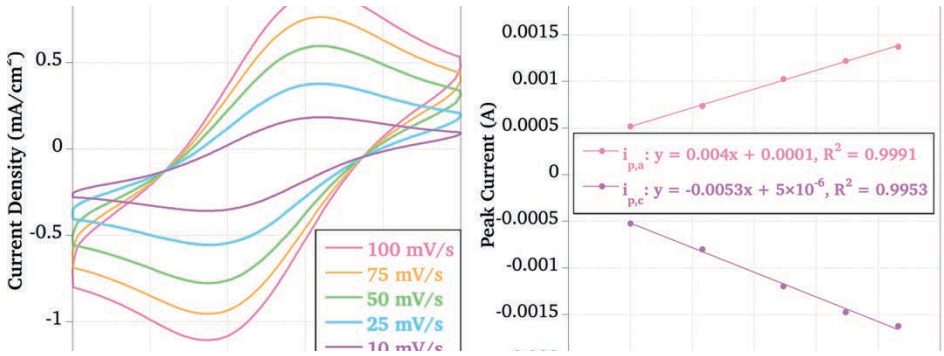

Figure 6.17 Scan rate study of 27.2 mmol UCl_3 in LiCl-KCl on thin-film BDD at 450 °C. RE: 1 mol% AgCl in LiCl-KCl; CE: W.

The results may have improved compared to the $Eu^{3+/2+}$ study because the temperature ramp rate was slower (100 °C/h) upon initial heating, and measurements at 550 °C were not attempted due to logistical limitations at the time of the experiment in hopes of preserving the thin coating. Because the rod was then contaminated with radioactive material, it could not be taken to the LANL electron microscopy laboratory, and it was too large to fit in the local benchtop SEM that could handle actinide samples.

However, it was concluded that no significant damage occurred via visual inspection. An image of the electrode end after exposure is shown in **Figure 6.18**.

Figure 6.18 nts in UCl_3 in LiCl-KCl at 450 °C.

Taking the average potential between the anodic and cathodic peaks provided a value for E^o that aligns with the literature using Ag/AgCl, and this holds for the $U^{4+/3+}$ redox couple when normalized to the $Cl^-/Cl_2(g)$ reference Eq. 25 and Eq. 26.[69,78,232,239,258,259] The values for E^o are provided in **Table 6.8** alongside D_O and D_O that were calculated using the Randles-Sevcik equation like for the $EuCl_3$ measurements and similar studies published in the literature.[69,232,259,260] However, the diffusion is expected to occur at a rate within the range of 10^{-6} – 10^{-5} cm^2/s, and the values calculated for the CVs collected using the thin-film BDD rod electrode are slower by two orders of magnitude (10^{-8} cm^2/s). The calculation of D is directly affected by the magnitude of the peak currents considering the slope of their regression across $\sqrt{\nu}$. In **Figure 6.17** it is clear to see that the current response is on the order of less than 1 mA/cm^2. For a surface area of 3.4 cm^2 (determined by the salt level after removal from the graphite cap while at temperature), the current density was significantly lower than what was observed when studying $Eu^{3+/2+}$ using either the free-standing BDD or the BDD-coated rod in the previous section. This result is curious,

considering the higher conductivity of the BDD coating compared to the free-standing material due to the varied ratios of sp^3 and sp^2 hybridized carbon.

Table 6.8 Formal potentials and diffusion coefficients determined for 27.2 mmol UCl_3 in LiCl-KCl at 450 °C with thin-film BDD vs. 1 mol% AgCl in LiCl-KCl.

E^o vs. Ag/AgCl (V)	E^o vs. $Cl^-/Cl_2(g)$ (V)	$D_O \times 10^{-8}$ (cm^2/s)	$D_R \times 10^{-8}$ (cm^2/s)
-0.349 ±0.0004	-1.591 ±0.0004	2.3 ±0.08	4.1 ±0.3

Additionally, the response presented here does not align with previously measured using the same electrode design. One possible explanation could be the chipping observed before, which may have increased the current response thanks to the involvement of the exposed Ta rod. An argument could be made for the relatively large surface area affecting the diffusion behavior compared to something like a wire or disc electrode design, but it is, in fact, a slightly smaller exposed surface than what was used to study $EuCl_3$. That study produced values for D within the expected range (10^{-6} cm^2/s), so it seems like an unlikely explanation.

Calculations related to the kinetics of the reaction are also nuanced compared to the previous measurements reported in this chapter, and values for ΔE_p, ψ, and k are listed in **Table 6.9**. In the studies reported above, converting the required parameters to the appropriate temperature equivalent was trivial. In this case, the original ΔE_p was only 0.134 V, and the adjusted value decreased to 0.055 V.[69-73] The Nicholson method is limited to 0.061 V $< \Delta E_p <$ 0.212 V,[110] and the resulting ψ is estimated to the maximum table value of 20, although it would actually be larger. The temperature adjusted value of 31 for ψ and yielded a value of 5.4×10^{-3} cm/s for k, which is still relatively large considering the influence both D_O and D_R have on the calculation of k (see Eq. 5). The expected order

of magnitude is faster based on literature (10^{-3} cm/s),[69,70] but the approximations required to produce this value bring its validity into question. According to the Nernst equation, at standard conditions (T = 298 K), the pink portion of Eq. 27 will equate to a separation of 0.059 V / n, meaning that ΔE_p = 0.055 V for a 1 e^- transfer is smaller than theoretically possible.

$$E_{cell} = E^o_{cell} - \frac{2.303RT}{nF} log \frac{[Red]}{[Ox]} \quad \textbf{(27)}$$

When adjusted for 450 °C, the ideal separation becomes 0.143 V / n. Again, the value collected at temperature (0.134 V) is also abnormal. While the explanation for this narrow separation is unclear, there is an alternative for calculating k that does not consider this detail.

Table 6.9 Peak separation and ψ adjusted for salt temperature with resulting k for the 50 mV/s scan rate using the Nicholson and Klingler-Kochi methods.

T (K)	$\Delta E_{p,T}$ (mV)	$\Delta E_{p,298}$ (mV)	ψ_T	ψ_{298}	k^N (cm/s)	$k^{K\text{-}K}$ (cm/s)	αn_α
723	134 ±1	55.0 ±1	20	31	5.4×10^{-3}	9.6×10^{-2}	1.1

The Klingler-Kochi approach to quantifying k was also considered.[116] In this method, Eq. 8 and Eq. 9 can be used to determine the charge transfer coefficient, αn_α, and k. The result using this method is quite good and aligns with the literature.[69,70] The rate constant calculated using the Nicholson equation is denoted as k^N, and $k^{K\text{-}K}$ is used for Klingler-Kochi in **Table 6.9**.

6.4.2 $MgCl_2$-NaCl Electrolyte

To compliment the LiCl-KCl system, BDD was also used to measure 0.1 mol% $U^{4+/3+}$ in a $MgCl_2$-NaCl (48-52 mol%) electrolyte. While confirming previous results on graphite and W disc small area working electrodes (SAWE) for a separate project, a thin-film BDD rod electrode surface area was restricted to a small portion of one end. Previous trials of CV with the graphite and W SAWEs were not successful in capturing oxidation or reduction peaks, and the task was to repeat the attempt once more before proceeding with a publication regarding the electromotive force of $U^{3+/0}$ in the $MgCl_2$-NaCl system.[75] The $Mg/MgCl_2$ RE in use aligns the $Mg^{2+/0}$ reaction at 0 V, which nearly overlapped the $U^{3+/0}$ couple during measurements. Because it is known that $U^{3+/4+}$ appears approximately +1.2 V from the $U^{3+/0}$, anodic and cathodic responses are expected to appear near +1.2 V vs. $Mg/MgCl_2$.[69,75,77,225,232]

In **Figure 6.19 A)**, the response collected using the graphite SAWE shows some evidence of the oxidation reaction at ca. +1.3 V vs. $Mg/MgCl_2$, the expected region if E^o = +1.2 V. However, the reduction peak is much less prominent in the +1.1 V region. Together, these peaks encapsulate the expected +1.2 V potential for E^o, but the resolution is poor, like when these measurements were first performed. Next, the W SAWE in **B)** was deployed. In this case, there is no evidence of U^{3+} oxidation, only an anodic peak at approximately +2 V, hypothesized to result from W chemistry that can occur at more extreme potentials.[75] The reduction peak at +1.15 V can likely be attributed to the reduction of U^{4+}, but overall, the $U^{4+/3+}$ is not easily identified using this electrode material. Ultimately, the results from these two measurements confirmed what had been

measured previously for this project. Before the furnace was brought down to room temperature, the BDD SAWE was mounted in the graphite cap while at temperature. Based on the results from the $EuCl_3$ experiment, there were significant concerns regarding the rapid thermal expansion of the electrode material and a poor electrochemical response. Instead, U^{3+} oxidation and U^{4+} reduction is detected on each side of +1.2 V, illustrated in **C)**. Unfortunately, because the BDD was only introduced just before taking down the electrochemical cell, there was no opportunity to perform a scan of the $MgCl_2$-NaCl solvent window. This response should be pursued in future explorations of this system using BDD.

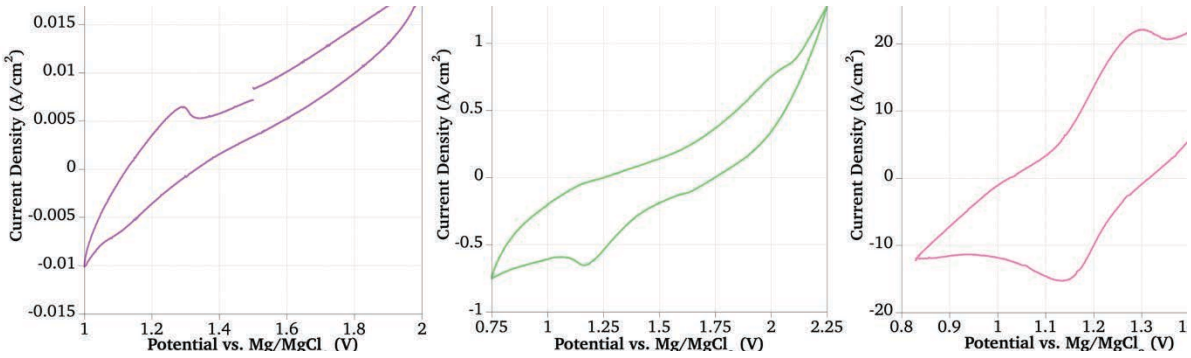

Figure 6.19 100 mV/s voltammograms of 0.1 mol% UCl_3 in $MgCl_2$-NaCl at 550 °C vs. $Mg/MgCl_2$ on graphite (purple), tungsten (green), and BDD (pink) SAWEs. RE: $Mg/MgCl_2$; CE: W.

Because both peaks were relatively well resolved using BDD, E^o was determined to be +1.22 V vs. $Mg/MgCl_2$. This reference was converted to 5 mol% Ag/AgCl using a method outlined by the team at LANL for this project. This reference was normalized to $Cl^-/Cl_2(g)$, and then 1 mol% Ag/AgCl with Eq. 25 and Eq. 26.[239,253] The four adjusted values for E^o are listed in **Table 6.10**, and the values for $Cl^-/Cl_2(g)$ and 1 mol% Ag/AgCl both agree nicely with what was measured using the bare BDD rod electrode in the LiCl-KCl electrolyte and therefore with values reported in the literature.[69,78,232,239,258,259]

Table 6.10 Formal potentials for $U^{4+/3+}$ adjusted for each reference.

$Mg/MgCl_2$ (V)	**5 mol% Ag/AgCl (V)**	**$Cl^-/Cl_2(g)$ (V)**	**1 mol% Ag/AgCl (V)**
+1.22	-0.457	-1.60	-0.357

Another group at LANL recently studied one possible explanation for why detecting the $U^{4+/3+}$ in $MgCl_2$-NaCl was challenging. In a study where CV was performed on $LnCl_3$ in a variety of alkali and alkaline earth chloride electrolyte salts, a pattern was detected related to the ionic radii and electron density of solvent cations and the stabilization of oxidation states of lanthanides in the salt.[238] It was found that the larger, 2+ charge cations (e.g., Mg^{2+} and Ca^{2+}) shifted the redox potential for $Eu^{3+/2+}$ +0.5 V compared to the measurements in KCl, favoring the lower oxidation state. Therefore, if this trend were to extend to actinides, it is likely that the presence of Mg^{2+} in the present study could make the oxidation of U^{3+} to U^{4+} nontrivial. Yet, the BDD electrode was still capable of detecting both the oxidation and reduction mechanisms at the expected potential, unlike graphite and W, which are commonly used to measure $U^{4+/3+}$ in LiCl-KCl.[69,78,232,239,258,259]

When comparing the responses in the LiCl-KCl and $MgCl_2$-NaCl, there is a significant difference in the current density, although the two BDD rods were from the same batch order. The electrical conductivity of the two electrolytes was researched, and it has been found that at 550 °C, LiCl-KCl is reported to have an electrical conductivity of 2.1 S/cm,[261] but the one available study reporting the 48-52 mol% $MgCl_2$-NaCl mixture reported temperatures only down to 633 °C.[262] That publication recorded a conductivity of 1.75 S/cm, and because electrical conductivity decreases as temperature decreases, it

would most certainly be less conductive than LiCl-KCl at 550 °C. Therefore, this characteristic does not explain the lower current magnitude in LiCl-KCl.

The other primary difference between these measurements of UCl_3 is the geometry of the surface area exposed to the salt. For LiCl-KCl, a bare rod was submerged with a total exposed area of 3.4 cm^2, including one end and a portion of the cylindrical surface. However, the SAWE design only exposed a small region on the end, making the design comparable to that of a disc electrode design with a surface area restricted to 0.004 cm^2. The literature shows that geometry can impact CV resolution but not necessarily the current magnitude.[263] The geometry may, however, significantly impact the direction of diffusion based on the drastic difference between the double-layer size and shape between the two electrode designs.[264] This comparison is much like what was discussed in **Chapter 3**, where the holes in the grid BDD electrode design introduced a new component to the diffusion mechanism, adding another region of analyte interactions to consider. Again, this difference is unlikely to explain the current density difference observed for the $U^{4+/3+}$ studies.

Finally, the literature presented the most plausible source for the extreme difference in current density. When the size of electrodes is drastically reduced to micron-scale surface areas, they can be classified as 'microelectrodes' whose ultra-small conductive region is much smaller than the resulting diffusion layer. This difference can also enhance the focus of analyte detection and create relatively large current density responses.[265,266] In one case, micro-tip electrodes produced current densities on the order of A/cm^2.[266] Although the BDD SAWE used in the present study is not a small enough surface area to

qualify as a microelectrode, the significant reduction in exposed BDD, especially compared to the bare rod, is likely the reason for such a significant difference between their resulting current densities.

6.5 Conclusions

This chapter aims to further strengthen the argument supporting the consideration of BDD as a resilient electrode in molten salts by deploying BDD working electrodes to study f-block redox couple in molten chloride electrolytes. Measurements were performed using free-standing and thin-film material, in one case comparing the detection and characterization of the $Eu^{3+/2+}$ redox couple in LiCl-KCl. Using the thin-film rod electrode, $U^{4+/3+}$ was studied in LiCl-KCl and $MgCl_2$-NaCl to determine the effect of electrolyte composition on the stability of favorable oxidation states. Additionally, there was an opportunity to discuss the influence of surface area, further exploring the various configurations of BDD electrodes and the quality of their responses.

Free-standing BDD had greater peak resolution compared to the thin-film material. Although it would be ideal to use this form of BDD in UCl_3-containing salts as well, this it is generally less accessible compared to thin-film BDD coatings on substrates like the Ta rods used here given the time and financial cost associated with growing large surface area free-standing material. However, thin-film BDD may have the potential to perform high-quality measurements, like free-standing material, based on the limited applications described here. The electrode design could be optimized by varying features like the thickness of the film, doping levels of the boron, and geometry of the substrate in order to

increase resilience and conductivity. Additionally, the reduced surface area concept should be explored further by refining the process to expose limited portions of the film with the intention of increasing current density for measurements like CV.

7 Conclusions

Molten salt technology is rapidly expanding and the urgency for quality, reliable measurements is greater than ever. With the rise of molten salt reactors (MSRs) in the advanced nuclear reactor fleet and growing interests in used fuel recycling and reprocessing, it is imperative that there is a library of robust materials available to consider at industry and laboratory-scale applications. Additionally, techniques like electrochemistry can provide valuable information regarding redox potentials of fuel salt systems and corrosion mechanisms for materials of construction. This manuscript proposed boron-doped diamond (BDD) as a resilient material that can withstand the harsh conditions of high-temperature molten salts while also performing as a robust electrode for *in situ* measurements. The literature exploring the use of BDD in molten salts is extremely limited,[85-88] and impacts to the surface chemistry of the material or quality of the electrode performance has not yet been reported for chloride or fluoride salt exposure. This work contributes a novel material proven to be resilient in both chloride and fluoride molten salts, and capable of performing as a working electrode for *in situ* analytical measurements of f-block species.

A range of measurements have been performed to characterize free-standing BDD electrodes using electrochemical, microscopic, and spectroscopic methods. First, the grown and nucleation sides of the material was imaged using scanning electron microscopy (SEM) to visualize the difference in topography for each side. Then, aqueous electrochemistry was performed on the grown and nucleation sides of BDD electrodes to compare the impact of crystal structure and morphology on the quality of the response.

Cyclic voltammetry (CV) scan rate studies were used to quantify the oxidation and reduction processes at the electrode surface by calculating the formal potential (E^o), diffusion coefficient (D), peak separation (ΔE), and heterogeneous electron transfer rate constant (k). Potassium ferricyanide ($K_3Fe(CN)_6$) and hexaammineruthenium(III) chloride ($Cl_3Ru(NH_3)_6$) are two common analytes that are well-reported in the literature and are commonly used on BDD electrodes, but typically on thin-film material that more closely resembles the nucleation side of free-standing material compared to the grown side. Additionally, two f-block analytes, $EuCl_3$ in KCl and $UO_2(NO_3)_2$ in HNO_3, were investigated on each side of the BDD electrode and characterized using the same techniques and calculations. Overall, the responses were well-aligned with expected literature ranges, but the electron transfer kinetics and diffusion rates were slightly faster on the nucleation side for each analyte. The most likely explanation for this difference is the morphology, specifically the hybridization of the carbon on each side. For the grown side with large crystals, the surface is primarily sp^3-hybridized, while the nucleation side has vastly smaller grain boundaries, which results in more sp^2-hybridized carbon. Because sp^2 carbon is more conductive than sp^3, this ratio difference may explain why the response was slightly improved on the nucleation side compared to the grown side. Therefore, there does seem to be an impact on measurement quality when morphology is modified, which will potentially have implications for electrode designs considered for molten salt applications.

Another powerful electrochemical technique incorporates spectroscopic methods to perform spectroelectrochemistry (SEC). One of the primary benefits of SEC measurements includes the feature that reversibility is not a necessary feature of the redox couple being

studied, which does drastically improve results for methods like CV. Because the actinides and lanthanides of interest in molten salts often lack good reversibility, SEC may be a helpful technique to provide high-quality results to describe fuel salts. In this chapter, ultraviolet-visible (UV-Vis.) spectroscopy was used to monitor the absorbance change of $Fe(CN)_6^{4-}$ from colorless to yellow as it was oxidized to $Fe(CN)_6^{3-}$ using a novel optically transparent electrode (OTE) constructed using free-standing BDD material with holes lased to allow light to pass through. Typical BDD OTEs are nanoscale thickness films on quartz substrates which would not survive in a harsh environment like molten salts. However, free-standing BDD may have the resilience to perform in salts, and using this design, can also be used to extend SEC techniques to harsh environments. The holes of the G-BDD were first described using SEM of the grown and nucleation sides to determine the texture and uniformity of the holes. Measurements using CV were then performed on the OTE grid BDD (G-BDD) and a non-grid electrode (NG-BDD) to determine the impact of lasing the material on the electrochemical response. There was a slight difference which, again, is likely attributed to the hybridization of the carbon since the lasing process graphitizes the diamond crystals, leaving behind sp^2 carbon in the holes. However, an anodic pre-treatment improved the response and likely helped to clear the surface.

Then, two types of SEC measurements were performed either with a restricted diffusion layer (thin-film diffusion) to determine E^o by monitoring the spectrum as applied potentials were stepped from 0 V to +0.4 V vs. Ag/AgCl (around the expected E^o). The resulting absorbance value at the spectrum peak was plotted against the potential using a Nernst plot, whose linear regression equated to the Nernst equation and provided a value

for E^o that aligned with the CVs and literature. Then, the diffusion layer was not restricted, allowing for the measurement of D by monitoring only the absorbance of the peak wavelength over time with chronoabsorptometry. The absorbance increased when the potential is stepped once from 0 V to +0.8 V vs. Ag/AgCl. By converting the plot of absorbance over time to the square root of time, two linear regions were identified. The literature uncovered that the geometry of the OTE can affect the diffusion behavior based on how many diffusion 'regions' exist for each design. It was determined that for the G-BDD, there are three distinct diffusion regions: one on each side of the free-standing BDD, and one within the holes. A modified form of the chronoabsorptometry equation was proposed to account for this feature and the resulting value for D aligned with literature and what was calculated using CV. Depending on the survivability of free-standing BDD in molten salts, this success indicates that the G-BDD may be a suitable OTE selection for performing *in situ* SEC.

Following the successful aqueous measurements, free-standing BDD resilience in chloride and fluoride molten salts was investigated. BDD coupons were subjected to 10 days of exposure in either NaCl-KCl (700 °C) or FLiNaK (500 °C) with as-received salts using furnaces in a fume hood (H) or with thermally dried salts using furnaces in an inert Ar(*g*) glovebox (GB) producing four unique samples identified as NaCl-KCl (H), NaCl-KCl (GB), FLiNaK (H), and FLiNaK (GB). The grown and nucleation sides of the samples were first imaged using SEM which revealed that the surfaces were largely unchanged, except in the case of the NaCl-KCl (H) sample which showed a noticeable amount of corrosion to both the grown and nucleation sides, primarily appearing at the grain boundaries and

edges between the facets of the large crystals on the grown side. This insinuates that those regions, which happen to be the location of sp^2 hybridized carbon, are the likely targets for etching. Additionally, because only the NaCl-KCl (H) sample was affected, it is assumed that the increased presence of moisture in that salt compared to the FLiNaK (H) or dried salts introduced volatile oxygen at the high temperature, inducing a decomposition reaction. This sample was then measured using profilometry which creates a height map of the surfaces and collects values for descriptors for surface roughness, uniformity, maximum height, sharpness, and the degree to which the roughness contributes to additional surface area. The maps for the grown and nucleation sides of NaCl-KCl (H) and calculated values were compared to the new material. The grown and nucleation sides were vastly different, as expected, but the new and exposed material changed minimally regardless of the corrosion seen using SEM.

The grown and nucleation side of each sample was also measured using Raman spectroscopy to investigate the surface chemistry with respect to speciation. Again, the grown and nucleation sides produced significantly difference responses, particularly with respect to the presence of only the singular, sharp sp^3 peak for the grown side and multiple peaks on the nucleation side that identify both sp^3 and sp^2 carbon, which aligns with the expected chemistry of the two morphologies. Interestingly, there was no change after exposure to the salts and the spectra of the four samples align with the new material. Additionally, X-ray photoelectron spectroscopy (XPS) was performed on the grown and nucleation sides of new, NaCl-KCl (GB) and FLiNaK (GB) material as a different approach to probe the surfaces. Similarly, the grown and nucleation sides showed, again, in this

case, the grown and nucleation sides had nearly identical spectra showing C-C bonding and C-O bonding. This was also the case for the exposed samples. In the literature, many papers have reported the fluorination of BDD and resulting XPS, indicating the presence of C-F bonding which did not appear on either side of the FLiNaK (GB) sample. Similarly, there was no evidence of C-Cl bonding for NaCl-KCl (GB). Finally, time-of-flight secondary ion mass spectroscopy (ToF-SIMS) was performed to explore yet another method of investigating the surface of BDD, this time measuring new material, NaCl-KCl (H), and FLiNaK (H). Yet again, the results indicated that there were no significant changes to the surface chemistry of the BDD samples after exposure to the chloride and fluoride salts. There is a wide array of other techniques that can be used to continue studying the material after exposure, but the suite of measurements included in this chapter indicate that there may not be a significant change to the surface of the grown or nucleation sides of BDD after exposure to either chloride or fluoride exposed material.

Like in the first study discussed, $Fe(CN)_6^{3-/4-}$ and $Ru(NH_3)_6^{3+/2+}$ are common electrochemistry analytes that have been reported frequently in the literature using BDD electrodes. They are complimentary analytes for analyzing changes to electrode surfaces since $Fe(CN)_6^{3-/4-}$ is considered to follow and inner-sphere electron transfer mechanism, which should be more sensitive to changes at the surface of the electrode; and $Ru(NH_3)_6^{3+/2+}$ uses an outer-sphere electron transfer mechanism which is less-sensitive to changes at the surface. Following measurements of 1 M KCl solvent potential window measurements on each side of new, NaCl-KCl (H), NaCl-KCl (GB), FLiNaK (H), and FLiNaK (GB) BDD samples, scan rate studies were performed with CV using $Fe(CN)_6^{3-/4-}$ and

$Ru(NH_3)_6^{3+/2+}$. The quality of the measurements were compared using E^o, D, ΔE_p, and k and found that, as expected, more changes occurred to the responses for $Fe(CN)_6^{3-/4-}$ compared to $Ru(NH_3)_6^{3+/2+}$. However, none of the changes were significant enough to diverge from the expected ranges based on the new material and values published in literature.

Each of the previous chapters were the foundation to ultimately use BDD as a working electrode in molten salts to study f-block species. First, free-standing BDD was used to study $EuCl_3$ in LiCl-KCl at 450, 550, and 650 °C. At each temperature, scan rate studies using CV were successfully completed and E^o, D, ΔE_p, and k are reported. Additionally, the thermodynamics of the reaction were investigated thanks to the multiple temperatures studied. All the values calculated almost perfectly aligned with what has been published in literature and the resolution of the measurements at 450 °C were exceptional. However, this measurement was performed on the benchtop in salts that were not dried before the experiment. As the temperature increased, the quality of the response decreased. After the furnace cooled to room temperature, it became quickly apparent that this was due to the deteriorating electrical connection as the Zn-coated steel nut and bolt corroded. Despite this challenge, the calculations still produced good results. Therefore, it is expected that using this material in a more controlled environment should further improve the results and allow for measurements at higher temperatures.

However, when the work transferred to the Los Alamos National Laboratory (LANL) from the University of Nevada, Las Vegas (UNLV), free-standing material long enough to perform such measurements was not available and the following measurements instead

used thin-film BDD coated on Ta rods. First, the $EuCl_3$ scan rate study in LiCl-KCl at 450 °C was repeated using a thin-film rod electrode with dried salts in an inert Ar(*g*) glovebox. In this case, the result did not produce peaks that were as well-resolved compared to what was collected using the free-standing BDD at UNLV, but the calculated values for E^o, D, ΔE_p, and k also generally aligned with measurements reported in literature. However, when the temperature was increased to 550 °C, the response deteriorated past a point of collecting useful information and the experiment was terminated. Then, it was discovered that the coating had chipped which may be a result of rapid heating and possible thermal expansion differences between the Ta of the substrate and the coating.

When a similar measurement was performed to study UCl_3 in LiCl-KCl, the first temperature ramp was performed more slowly, and the results were more stable throughout the measurement. In this case, the scan rate study was only performed at 450 °C, but the rod was not damaged following the measurement. The values for E^o, D, ΔE_p, and k for the $U^{4+/3+}$ redox couple were successfully determined. While E^o, ΔE_p, and k produced similar results to what has been published previously, D was ultimately much slower (two orders of magnitude) than what was expected. The overall peak current was very low, which has a direct influence on the values calculated for D. A direct comparison cannot be made to the $EuCl_3$ measurement in the case that the chipping occurred before the ramping where perhaps Ta participated in the response. There is work needed to better develop an appropriate design for using this electrode geometry.

Finally, there was an opportunity to incorporate a BDD rod electrode into another project at LANL where UCl_3 was being studied in a $MgCl_2$-NaCl electrolyte at 550 °C. In

this case, small area working electrodes (SAWE) were of interest, and the BDD was modified to reduce the surface area to a mere fraction of what was exposed in the previous measurements. It was also compared to the graphite and W disc SAWEs originally planned for these measurements. It was not feasible to perform an entire scan rate study at that time, but when comparing even just single scans using each electrode showed that only the BDD design was able to show the oxidation and reduction peaks for $U^{4+/3+}$ clearly while graphite and W could not. This difference may be attributed to the impact of electrolyte cation strength on the stabilization of different oxidation states and the inability for graphite and W to overcome that factor, while BDD was successful. Additionally, the current density was remarkably high for the BDD SAWE compared to the bare rod used in LiCl-KCl, which may be a result of restricting the surface area significantly like the phenomenon observed with microelectrodes in aqueous applications. This design, along with the free-standing material, should be refined and considered for the LiCl-KCl electrolyte experiments for $EuCl_3$ and UCl_3.

The results presented in this work introduced a multitude of pathways for further investigations that should be pursued to better understand the role of BDD in molten salt electrochemistry. These directions include, but are not limited to, further investigation of surface chemistry changes and electrode performance after exposure to salts (e.g., capacitance measurements, electrochemical impedance spectroscopy, other material characterization methods), the influence of crystal morphology on the electrochemical response in molten salts, and electrode design optimization for molten salt measurements, for example. Now that it is clear BDD will survive molten salts, especially free-standing

material, the G-BDD design should be applied to perform SEC in molten salt systems to study f-block analytes that can be challenging with techniques like CV. Additionally, the changes (or lack thereof) to the surface after exposure to chloride and fluoride salt for an extended period could be further investigated using a range of other techniques, but changes observed in the current study are minimal-to-none. Furthermore, the ideal morphologies and designs should be further explored to optimize electrochemical responses in high-temperature molten salts.

In addition to laboratory-scale measurements, BDD could be considered for more far-reaching applications such as elemental speciation, corrosion monitoring, and low-level detection using a suite of techniques reaching far beyond CV in MSR systems or fuel cycle technologies. If the corrosion mechanism observed for exposure to oxygen in the system could be better understood and even quantified, it may be possible to use BDD as an oxygen-monitor. Additionally, if there is success in using BDD for low-level detection, there could be an opportunity to apply the electrode for material accountability and nonproliferation applications within the MSR and pyrochemical fuel cycle systems. As further studies explore BDD in molten salt systems, there could be a range of other ways in which this invaluable material could benefit molten salt technologies.

References

[1] J. Lonergan, V. Goncharov, M. Swinhart, K. Makovsky, M. Rollog, B. McNamara, R. Clark, D. Cutforth, C. Armstrong, X. Guo and P. Paviet, "Thermodynamic investigation of the NaCl-KCl salt system from 25 to 950 °C," *Journal of Molecular Liquids,* vol. 391, no. Part A, p. 122591, 2023.

[2] C. N. A. C. Z. Bahri, W. M. Al-Areqi, M. '. F. M. Ruf and A. A. Majid, "Characteristic of molten fluoride salt system LiF-BeF2 (Flibe) and LiF-NaF-KF (Flinak) as coolant and fuel carrier in molten salt reactor (MSR)," *AIP Conference Proceedings,* vol. 1799, no. 1, p. 040008, 2017.

[3] M. Brostrom, S. Enestam, R. Backman and K. Makela, "Condensation in the KCl-NaCl system," *Fuel Processing Technology,* vol. 105, pp. 142-148, 2013.

[4] H. W. Hoffman and J. Lones, "Fused Salt Heat Transfer Part II. Forced convection heat transfer in circular tubes containing NaF-KF-LiF eutectic," Oak Ridge, 1955.

[5] J. C. Ard, J. A. Yingling, K. E. Johnson, J. Schorne-Pinto, M. Aziziha, C. M. Dixon, M. S. Christian, J. W. McMurray and T. M. Besmann, "Development of the Molten Salt Thermal Properties Database--Thermochemical (MSTDB-TC), example applications, and LiCl-RbCl and UF3-UF4 system assessments," *Journal of Nuclear Materials,* vol. 563, p. 153631, 2022.

[6] E. Gonzalez-Roubaud, D. Perez-Osorio and C. Preito, "Review of commercial thermal energy storage in concentrated solar power plants: Steam vs. molten salts," *Renewable and Sustainable Energy Reviews,* vol. 80, pp. 133-148, 2017.

[7] H. G. MacPherson, "Molten-Salt Reactor Program Status Report," U.S. Atomic Energy Commission, Oak Ridge, 1958.

[8] J. J. Laidler, J. E. Battles, W. E. Miller, J. P. Ackerman and E. L. Carls, "Development of pyroprocessing technology," *Progress in Nuclear Energy,* vol. 31, no. 1-2, pp. 131-140, 1997.

[9] J.-H. Yoo, C.-S. Seo, E.-H. Kim and H.-S. Lee, "A Conceptual Study of Pyropressing for Recovering Actinides from Spent Oxide Fuels," *Nuclear Engineering and Technology,* vol. 40, no. 7, pp. 581-592, 2008.

[10] E.-Y. Choi and S. M. Jeong, "Electrochemical processing of spent nuclear fuels: An overview of oxide reduction in pyroprocessing technology," *Progress in Natural Science: Materials International,* vol. 25, no. 6, pp. 572-582, 2015.

[11] M. S. Coops, J. B. Knighton and L. J. Mullins, "Technology Review Report: Pyrochemical Processing of Plutonium," in *American Chemical Society Symposium on Plutonium Chemistry*, Kansas City, 1982.

[12] M. F. Simpson, "Fundamentals of Spent Nuclear Fuel Pyroprocessing," in *Nuclear Fuel Reprocessing and Waste Management*, vol. 2, J. Zhang, Ed., Hackensack, New Jersey: World Scientific Publishing Co. Pte. Ltd., 2019, pp. 27-54.

[13] Oak Ridge National Laboratory, "Earth Day 1970," *Oak Ridge National Laboratory Review,* vol. 25, no. 3&4, pp. 149-155, 1992.

[14] J. H. Shaffer, "Preparation and Handling of Salt Mixtures for the Molten Salt Reactor Experiment," U.S. Atomic Energy Commission, Oak Ridge, 1971.

[15] C. F. Baes Jr, "The chemistry and thermodynamics of molten salt reactor fuels," *Journal of Nuclear Materials,* vol. 51, no. 1, pp. 149-162, 1974.

[16] M. Fratoni, D. Shen, G. Ilas and J. Power, "Molten Salt Reactor Experiment Benchmark Evaluation," U.S. Department of Energy, Berkeley, 2020.

[17] A. H. Compton, "July Meeting with Dr. C. A. Thomas on Final Purification and Metallurgy of 49," U.S. Department of Energy, Argonne, 1944.

[18] L. Burris, M. Steindler and W. Miller, "A Proposed Pyrometallurgical Process for Rapid Recycle of Discharged Fuel Materials from the Integral Fast Reactor," Argonne National Laboratory, Argonne, 1984.

[19] N. S. S. Staff, "Pit production explained," Los Alamos National Laboratory, 13 December 2021. [Online]. Available: https://discover.lanl.gov/publications/national-security-science/2021-winter/pit-production-explained/. [Accessed 10 January 2024].

[20] T. Paget, J. McNeese, K. Fife, M. Jackson and R. Watson, "Molten Salt Chemistry of Plutonium," in *Plutonium Handbook*, 2nd ed., vol. 1, D. L. Clark, D. A. Geeson and R. J. Hanrahan, Jr, Eds., La Grange Park, Illinois: American Nuclear Society, 2019, pp. 201-286.

[21] J. Moon, K. Myhre, H. Andrews and J. McFarlane, "Potential of electrolytic processes for recovery of molybdenum from molten salts for 99Mo production," *Progress in Nuclear Energy,* vol. 152, p. 104369, 2022.

[22] G. L. Fredrickson, M. N. Patterson, D. Vaden, G. G. Galbreth, T.-S. Yoo, J. Price, E. J. Flynn and R. N. Searle, "History and Status of Spent Fuel Treatment at the INL Fuel Conditioning Facility," *Progress in Nuclear Energy,* vol. 143, p. 104037, 2022.

[23] J. P. Ackerman, "Chemical Basis for Pyrochemical Reprocessing of Nuclear Fuel," *Industrial and Engineering Chemistry Research,* vol. 30, pp. 141-145, 1991.

[24] A. Burak, J. Chamberlain and M. F. Simpson, "Study of entrainment of Li2O in product from direct electrolytic reduction of UO2 in molten LiCl–Li2O. Part 1: Post-processing and analysis techniques," *Journal of Nuclear Materials,* vol. 529, p. 151913, 2020.

[25] A. Merwin and D. Chidambaram, "Alternate Anodes for the Electrolytic Reduction of UO2," *Metallurgical and Materials Transactions A,* vol. 46, pp. 536-544, 2014.

[26] P. T. Kissinger and W. R. Heineman, "Cyclic Voltammetry," *Journal of Chemical Education,* vol. 60, no. 9, pp. 702-706, 1983.

[27] D. Pletcher, "In Introduction to Electrode Reactions," in *A First Course in Electrode Processes*, 2nd Edition ed., Cambridge, RSC Publishing, 2009, pp. 1-47.

[28] K. Kobashi, "Diamond - Structure and CVD Growth," in *Diamond Films: Chemical Vapor Deposition for Oriented and Heteroepitaxial Growth*, Oxford, Elsevier Ltd., 2005, pp. 9-13.

[29] R. C. Burns and G. J. Davis, "Growth of Synthetic Diamond," in *The Properties of Natural and Synthetic Diamond*, J. E. Field, Ed., San Diego, California: Academic Press Limited, 1992, pp. 395-422.

[30] S. J. Cobb, Z. J. Ayres and J. V. Macpherson, "Boron Doped Diamond: A Designer Electrode Material for the Twenty-First Century," *Annual Review of Analytical Chemsitry,* vol. 11, pp. 463-484, 2018.

[31] P. W. May and Y. A. Mankelevich, "From Ultrananocrystalline Diamond to Single Crystal Diamond Growth in Hot Filament and Microwave Plasma-Enhanced CVD Reactors: a Unified Model for Growth Rates and Grain Sizes," *Journal of Physical Chemistry C,* vol. 112, no. 32, pp. 12432-12441, 2008.

[32] Y. Sato and M. Kamo, "Synthesis of Diamond from the Vapor Phase," in *The Properties of Natural and Synthetic Diamond*, J. E. Fields, Ed., San Diego, California: Academic Press Limited, 1992, pp. 423-469.

[33] S. Huang, J. E. Weis, S. Costa, M. Kalbac and M. S. Dresselhaus, "Properties of Carbon: An Overview," in *Electrochemistry of Carbon Electrodes*, vol. 16, R. C. Alkire, P. N. Bartlett and J. Lipkowski, Eds., Weinheim, Wiley-VCH, 2015, pp. 1-29.

[34] J. Lee, D. A. Tryk, A. Fujishima and S.-M. Park, "Electrochemical generation of ferrate in acidic media at boron-doped diamond electrodes," *Chemistry Communications,* pp. 486-487, 2002.

[35] Z. V. Zivcova, O. Frank, V. Petrak, H. Tarabkova, J. Vacik, M. Nesladek and L. Kavan, "Electrochemistry and in situ Raman spectroelectrochemistry of low and high quality boron doped diamond layers in aqueous electrolyte solution," *Electrochmica Acta,* vol. 87, pp. 518-525, 2013.

[36] J. V. Macpherson, "The Use of Conducting Diamond in Electrochemistry," in *Electrochemistry of Carbon Electrodes*, vol. 16, R. C. Alkire, P. N. Bartlett and J. Lipkowski, Eds., Weinheim, Wiley-VCH Verlag GmbH & Co., 2015, pp. 163-210.

[37] A. M. Stoneham, "Diamond: Recent Advances in Theory," in *The Properties of Natural and Synthetic Diamond*, J. E. Field, Ed., San Diego, California: Academic Press Limited, 1992, pp. 3-34.

[38] A. T. Collins, "Band Structure," in *Handbook of Industrial Diamonds and Diamond Films*, M. A. Prelas, G. Popovici and L. K. Bigelow, Eds., New York, New York: Marcel Dekker, Inc., 1998, pp. 1-17.

[39] H. Sternschulte, T. Albrecht, K. Thonke, R. Sauer, M. Grieβer and M. Grasserbauer, "Cathodoluminescence Studies of Bound Excitons and Near Band Gap Emission Lines in Boron- and Phosphorous-Doped CVD-Diamonds," *MSR Online Proceedings Library,* vol. 423, p. 693, 1996.

[40] R. E. Clausing, "Diamond Morphology," in *Handbook of Industrial Diamonds and Diamond Films*, M. A. Prelas, G. Popovici and L. K. Bigelow, Eds., New York, New York: Marcel Dekker, Inc., 1998, pp. 19-47.

[41] K. Nishimura, K. Das, J. T. Glass, K. Kobashi and R. J. Nemanich, "Electrical Properties of B Doped CVD Grown Polycrystalline Diamond Films," in *The Physics and Chemistry of Carbides, Nitrides and Borides*, vol. 185, R. Freer, Ed., Norwell, Massachusetts: Kluwer Academic Publishers, 1990, pp. 183-194.

[42] H. V. Patten, K. E. Meadows, L. A. Hutton, J. G. Iacobini, D. Battistel, K. McKelvey, A. W. Colburn, M. E. Newton, J. V. Macpherson and P. R. Unwin, "Electrochemical Mapping Reveals Direct Correlation between Heterogeneous Electron-Transfer Kinetics and Local Density of States in Diamond Electrodes," *Angewandte Chemie International Edition,* vol. 51, no. 28, pp. 7002-7006, 2012.

[43] J. v. Macpherson, "A Practical Guide to Using Boron Doped Diamond in Electrochemical Research," *Physical Chemistry and Chemical Physics,* vol. 17, no. 5, pp. 2935-2949, 2015.

[44] M. A. Q. Alfar, S. Ferro, C. A. Martinez-Huitle and Y. M. Vong, "Boron Doped Diamond Electrode for the Wastewater Treatment," *Journal of the Brazilian Chemical Society,* vol. 17, no. 2, pp. 227-236, 2006.

[45] T. Mackuľak, E. Medvecká, A. Vojs Staňová, P. Brandeburová, R. Grabic, O. Golovko, M. Marton, I. Bodík, A. Medveď o-vá, M. Gál, M. Planý, A. Kromka, V. Špalková, A. Škulco-vá, I. Horáková and M. Vojs, "Boron Doped Diamond Electrode -- The Elimination of Psychoactive Drugs and Resistant Bacteria from Wastewater," *Vacuum,* vol. 171, p. 108957, 2020.

[46] A. Manivannan, D. A. Tryk and A. Fujishima, "Detection of Trace Lead at Boron-Doped Diamond Electrodes by Anodic Stripping Analysis," *Electrochemical and Solid-State Letters,* vol. 2, no. 9, pp. 455-456, 1999.

[47] M. Brycht, S. Baluchova, A. Taylor, V. Mortet, S. Sedlakova, L. Klimsa and K. Schwarzova-Peckova, "Comparison of electrochemical performance of various boron-doped diamond electrodes: Dopamine sensing in biomimicking media used for cell cultivation," *Bioelectrochemistry,* vol. 137, p. 107646, 2021.

[48] L. Zhang, J.-q. Yang, Y. Luo, J.-c. Shang and X.-h. Jiang, "Simultaneous determination of eleven compounds related to metabolism of bioamines in rat cortex and hippocampus by HPLC-ECD with boron-doped diamond working electrode," *Journal of Pharmeceutical and Biomedical Analysis,* vol. 118, pp. 41-51, 2016.

[49] N. Mitani and Y. Einaga, "The Simple Voltammetric Analysis of Acids Using Highly Boron-Doped Diamond Macroelectrodes and Microelectrodes," *Journal of Electroanalytical Chemistry,* vol. 626, no. 1-2, pp. 156-160, 2009.

[50] S. Gupta, M. Muralikiran, J. Farmer, L. R. Cao and R. G. Downing, "The Effect of Boron Doping and Gamma Irradiation on the Structure and Properties of Microwave Chemical Vapor Deposited Boron-Doped Diamond Films," *Journal of Material Research,* vol. 24, no. 4, pp. 1498-1512, 2009.

[51] C. J. Maher, C. Bouyer, T. L. Griffiths, S. Legand, G. Leturcq, M. Miguirditchian and M. Sarsfield, "Impact of Uranium Carbide Organics Treated by Prolonged Boiling

and Electrochemical Oxidation upon Uranium and Plutonium Solvent Extraction," *Radiochmica Acta,* vol. 106, no. 2, pp. 95-106, 2018.

[52] E. A. Ekimov, V. Ralchenko and A. Popovich, "Synthesis of Superconducting and Thermal Stability," *Diamond and Related Materials,* vol. 50, pp. 15-19, 2014.

[53] Y. Kado, T. Goto and R. Hagiwara, "Stability of a Boron-Doped Diamond Electrode in Molten Chloride Systems," *Diamond and Related Materials,* vol. 18, no. 9, pp. 1186-1190, 2009.

[54] M. Moissan and O. Honigschmid, "Sur la Preparation du Thorium," *Annales de chimie et de physique,* vol. 8, no. 8, pp. 182-192, 1906.

[55] H. von Wartenberg, "Uber Thorium," *Zeitschrift fur Elektrochemie,* vol. 15, no. 22, pp. 866-872, 1909.

[56] W. Kroll, "The Fused Salt Electrolysis for the Production of Metal Powders," *Transitions of the Electrochemical Society,* no. 87, pp. 551-569, 1945.

[57] I. K. Delimarskii and B. Markov, Electrochemistry of Fused Salts, Washington, DC: The Sigma Press, 1961.

[58] H. A. Laitinen and R. A. Osteryoung, "Electrochemistry in Molten Salts," in *Fused Salts*, B. R. Sundheim, Ed., New York, NY: McGraw-Hill Book Company, 1964, pp. 255-300.

[59] A. Alabyshev, M. Lantratov and A. Morachevski, Reference Electrodes for Fused Salts, Washington, DC: The Sigma Press, 1965.

[60] G. J. Janz, "Electrochemical Properties," in *Molten Salts Handbook*, Cambridge, MA: Academic Press, 1967, pp. 265-357.

[61] I. B. Polovov, V. A. Volkovich, J. M. Charnock, B. Kraj, R. G. Lewin, H. Kinoshita, I. May and C. A. Sharrad, "In Situ Spectroscopy and Spectroelectrochemistry of

Uranium in High-Temperature Alkali Chloride Molten Salts," *Inorganic Chemistry,* vol. 47, no. 17, pp. 7474-7482, 2008.

[62] D. Rappleye, M. L. Newton, C. Zhang and M. F. Simpson, "Electroanalytical measurements of binar-analyte mixture in molten LiCl-KCl eutectic: Uranium(III)- and Magnesium(II)-Chloride," *Journal of Nuclear Materials,* vol. 486, pp. 369-380, 2017.

[63] S. Guo, E. Wu and J. Zhang, "Investigation of electrochemical kinetics for La(III)/La reaction in molten LiCl-KCl eutectic salt using potentiometric polarization," *Journal of Nuclear Materials,* vol. 510, pp. 414-420, 2018.

[64] J.-C. Fondanaiche, "Voltammetrie du chlorure d'uranyle dans l'eutectique LiCl-KCl," Commissariat a l'Energie Atomique - France, Fontenay-aux-Roses, 1965.

[65] H. Tang and B. Pesic, "Electrochemical behavior of LaCl3 and morphology of La deposit on molybdenum substrate in molten LiCl-KCl eutectic salt," *Electrochimica Acta,* vol. 119, pp. 120-130, 2014.

[66] L. Cassayre, J. Serp, P. Soucek, R. Malmbeck, J. Rebizant and J.-P. Glatz, "Electrochemistry of thorium in LiCl-KCl eutectic melts," *Electrochimica Acta,* vol. 52, no. 26, pp. 7432-7437, 2007.

[67] N. Hege, J. Jackson and J. Shafer, "Review--Fundamental Uranium Electrochemistry and Spectroscopy in Molten Salt Systems," *Journal of the Electrochemical Society,* vol. 170, p. 016503, 2023.

[68] T.-J. Kim, D.-H. Ahn, S.-W. Paek and Y. Jung, "Study on Electrodeposition of Ce(III) at a Tungsten Electrode in a LiCl-KCl Molten Salt Solution," *International Journal of Electrochemical Science,* vol. 8, no. 7, pp. 9180-9186, 2013.

[69] S. A. Kuznetsov, H. Hayashi, K. Minato and M. Gaune-Escard, "Electrochemical Behavior of Some Thermodynamic Properties of UCl4 and UCl3 Dissolved in a LiCl-KCl Eutectic Melt," *Journal of the Electrochemical Society,* vol. 152, p. C203, 2005.

[70] S. A. Kuznetsov and M. Gaune-Escard, "Electrochemical transient techniques for study of the electrochemistry and thermodynamics of nuclear materials in molten salts," *Journal of Nuclear Materials,* vol. 389, no. 1, pp. 108-114, 2009.

[71] S. A. Kuznetsov and M. Gaune-Escard, "Kinetics of electrode processes and thermodynamic properties of europium chlorides dissolved in alkali chloride melts," *Journal of Electroanalytical Chemistry,* vol. 595, pp. 11-22, 2006.

[72] S. A. Kuznetsov and M. Gaune-Escard, "Redox electrochemistry and formal standard redox potentials of the Eu(III)/Eu(II) redox couple in an equimolar mixture of molten NaCl-KCl," *Electrochimica Acta,* vol. 46, no. 8, pp. 1101-1111, 2001.

[73] S. A. Kuznetsov, S. V. Kuznetsova and P. T. Stangrit, "Cathodic reduction of hafnium tetrachloride in an equimolar sodium-chloride potassium-chloride melt," *Soviet Electrochemistry,* vol. 26, no. 1, pp. 55-60, 1990.

[74] C. R. Lhermitte, S. S. Parker, J. M. Jackson and M. J. Monreal, "Communication--Mg2+/0 as a Reliable Reference Electrode for Molten Chloride Salts," *Journal of the Electrochemical Society,* vol. 168, no. 6, p. 066501, 2021.

[75] C. R. Lhermitte, H. K. Patenaude, S. S. Parker, J. M. Jackson and M. J. Monreal, "Electrochemical behavior and electromotive force measurements of molten U3+/U0 MgCl2-NaCl," *Electrochimica Acta,* under review.

[76] P. Masset, C. Apostolidis, R. J. M. Konings, R. Malmbeck, J. Rebizant, J. Serp and J.-P. Glatz, "Electrochemical behavior of neptunium in the molten LiCl-KCl eutectic," *Journal of Electroanalytical Chemistry,* vol. 603, no. 2, pp. 166-174, 2007.

[77] B. P. Reddy, S. Vandarkuzhali, T. Subramanian and P. Venkatesh, "Electrochemical studies on the redox mechanism of uranium chloride in molten LiCl-KCl eutectic," *Electrochimica Acta,* vol. 49, no. 15, pp. 2471-2478, 2004.

[78] O. Shirai, T. Iwai, Y. Suzuki, Y. Sakamura and H. Tanaka, "Electrochemical behavior of actinide ions in LiCl-KCl eutectic melts," *Journal of Alloys and Compounds,* Vols. 271-273, pp. 685-688, 1998.

[79] C. Caravaca, G. Cordoba and M. J. Tomas, "Electrochemical Study of Europium Trichloride in Molten Eutectic LiCl-KCl," in *8th Information Exchange Meeting on P&T*, Las Vegas, 2004.

[80] C. A. Schroll, S. Chatterjee, T. G. Levitskaia, W. R. Heineman and S. A. Bryan, "Electrochemistry and Spectroelectrochemistry of Europium(III) Chloride in 3LiCl-KCl from 643 to 1123 K," *Analytical Chemistry,* vol. 85, no. 20, pp. 9924-9931, 2013.

[81] M. R. Bermejo, F. de la Rosa, E. Barrado and Y. Castrillejo, "Cathodic behavior of europium (III) on glassy carbon, electrochemical formation of Al4Eu, and oxoacidity reactions in the eutectic LiCl-KCl," *Journal of Electroanalytical Chemistry,* vol. 603, no. 1, pp. 81-95, 2007.

[82] J. Ge, Q. Yang, Y. Wang, W. Zhuo, M. Du and J. Zhang, "Selective Electrodeposition of Europium and Samarium in Molten LiCl-KCl with Copper and Aluminum Electrodes," *Journal of the Electrochemical Society,* vol. 167, no. 2, p. 022501, 2020.

[83] G.-Y. Kim, D. Yoon, S. Paek, S.-H. Kim, T.-J. Kim and D.-H. Ahn, "A study on the electrochemical deposition behavior of uranium ion in a LiCl–KCl molten salt on solid and liquid electrode," *Journal of Electroanalytical Chemistry,* vol. 682, pp. 128-135, 2012.

[84] J. Ryl, M. Cieslik, A. Zielinski, M. Ficek, B. Dec, K. Darowicki and R. Bogdanowicz, " High-Temperature Oxidation of Heavy Boron-Doped Diamond Electrodes: Microstructural and Electrochemical Performance Modification," *Materials,* vol. 13, no. 4, p. 964, 2020.

[85] Y. Kado, T. Goto and R. Hagiwara, "Behavior of a Boron-Doped Diamond Electrode in Molten Chlorides Containing Oxide Ion," in *Zero-Carbon Energy: Proceedings of the First International Symposium of the Global COE Program "Energy Science in the*

Age of Global Warming--Toward CO2 Zero-emission Energy System", T. Yao, Ed., Kyoto, Springer, 2010, pp. 234-239.

[86] T. Goto, Y. Kado and R. Hagiwara, "Boron-Doped Diamond Electrodes in Molten Chloride Systems," in *Molten Salts Chemistry: From Lab to Applications*, F. Lantelme and H. Groult, Eds., Burlington, Massachusetts: Elsevier, 2013, pp. 187-205.

[87] Y. Kado, T. Goto and R. Hagiwara, "Stability of a boron-doped diamond electrode in molten chloride systems," *Diamond and Related Materials,* vol. 18, no. 9, pp. 1186-1190, 2009.

[88] W. Park, J.-K. Kim, J.-M. Hur, E.-Y. Choi, H. S. Im and S.-S. Hong, "Application of a boron doped diamond (BDD) electrode as an anode for the electrolytic reduction of UO2 in Li2O–LiCl–KCl molten salt," *Journal of Nuclear Materials,* vol. 432, no. 1-3, pp. 175-181, 2013.

[89] L. Hutton, M. E. Newton, P. R. Unwin and J. V. Macpherson, "Amperometric Oxygen Sensor Based on a PlatinumNanoparticle-Modified Polycrystalline Boron DopedDiamond Disk Electrode," *Analytical Chemistry,* vol. 81, pp. 1023-1032, 2009.

[90] Z. V. Zivcova, V. Mortet, A. Taylor, A. Zukal, O. Frank and L. Kavan, "Electrochemical characterization of porous boron-doped diamond prepared using SiO2 fiber template," *Diamond and Related Materials,* vol. 87, pp. 61-69, 2008.

[91] R. Jarosova, P. De Sousa Bezerra, C. Munson and G. Swain, "Assessment of heterogeneous electron-transfer rate constants for soluble redox analytes at tetrahedral amorphous carbon, boron-doped diamond, and glassy carbon electrodes," *Physica Status Solidi (a),* vol. 213, no. 8, pp. 2087-2098, 2016.

[92] I. Gonzalez-Gonzalez, E. R. Fachini, M. A. Scibioh, D. A. Tryk, M. Tague, H. D. Abruna and C. R. Cabrera, "Facet-Selective Platinum Electrodeposition at Free-standing Polycrystalline Boron-Doped Diamond Films," *Langmuir,* vol. 25, no. 17, pp. 10329-10336, 2009.

[93] R. G. Compton, J. S. Foord and F. Marken, "Electroanalysis at Diamond-Like and Doped-Diamond Electrodes," *Electroanalysis,* vol. 15, no. 17, pp. 1349-1363, 2003.

[94] S. Haymond, J. K. Zak, Y. Show, J. E. Butler, G. T. Babcock and G. M. Swain, "Spectroelectrochemical responsiveness of a freestanding, boron-doped diamond, optically transparent electrode toward ferrocene," *Analytical Chimica Acta,* vol. 500, pp. 137-144, 2003.

[95] M. C. Granger and G. M. Swain, "The Influence of Surface Interactions on the Reversibility of Ferri/Ferrocyanide at Boron-Doped Diamond Thin-Film Electrodes," *Journal of the Electrochemical Society,* vol. 146, p. 4551, 1999.

[96] F. Marken, C. A. Paddon and D. Asogan, "Direct cytochrome c electrochemistry at boron-doped diamond electrodes," *Electrochemistry Communications,* vol. 4, no. 1, pp. 62-66, 2022.

[97] M. Van de Voorde, B. Geboes, T. V. H. K. Vander Hoogerstraete, T. Cardinaels and K. Binnemans, "Stability of europium(II) in aqueous nitrate solutions," *Dalton Transactions,* vol. 48, pp. 14758-14768, 2019.

[98] S. Ferro and A. De Battisti, "Electrochemistry of the aqueous europium(III)/europium(II) redox couple at conductive diamond electrodes," *Journal of Electroanalytical Chemistry,* vol. 533, pp. 177-180, 2002.

[99] S. Ferro and A. De Battisti, "Electrochemistry of the aqueous ceric/cerous redox couple at conductive diamond and gold electrodes," *Physical Chemistry Chemical Physics,* vol. 4, pp. 1915-1920, 2002.

[100] Y. Suzuki, T. Nankawa, T. Ozaki, T. Ohnuki, A. J. Francis, Y. Enokida and I. Yamamoto, "Electrochemical Studies on Uranium in the Presence of Organic Acids," *Journal of Nuclear Science and Technology,* vol. 44, p. 1227, 2007.

[101] Z. J. Ayers, J. C. Newland, M. E. Newton and J. V. Macpherson, "Controlled sp2 Functionalization of Robust and Nernstian pH Electrodes," *Analytical Chemistry,* vol. 88, no. 1, pp. 974-980, 2016.

[102] A. Lucio and J. Macpherson, "Combined Voltammetric Measurement of pH and Free Chloride Speciation Using a Micro-Spot sp2 Bonded Carbon-Boron Doped Diamond Electrode," *Analytical Chemistry,* vol. 92, no. 24, pp. 16072-16078, 2020.

[103] A. J. Lucio, R. E. P. Meyler, M. A. Edwards and J. v. Macpherson, "Investigation of sp2-Carbon Pattern Geometry in Boron-Doped Diamond Electrodes for the Electrochemical Quantification of Hypochlorite at High Concentrations," *ACS Sensors,* vol. 5, no. 3, pp. 789-797, 2020.

[104] T. L. Read, S. J. Cobb and J. v. Macpherson, "An sp2 patterned boron doped diamond electrode for the simultaneous detection of dissolved oxygen and pH," *ACS Sensors,* vol. 4, no. 3, pp. 756-763, 2019.

[105] Z. Liu, S. Baluchova, Z. Li, Y. Gonzalez-Garcia, C. E. Hall and J. G. Buijnsters, "Unravelling microstructure-electroactivity relationships in free-standing polycrystalline boron-doped diamond: A mapping study," *Acta Materialia,* vol. 166, p. 119671, 2024.

[106] R. Bogdanowicz, M. Ficek, N. Malinowska, S. Gupta, R. Meek, P. Niedzialkowski, M. Rycewicz, M. Sawczak, J. Ryl and T. Ossowski, "Electrochemical performance of thin free-standing boron-doped diamond nanosheet electrodes," *Journal of Electroanalytical Chemistry,* vol. 862, p. 114016, 2020.

[107] M. Granger, M. Witek, J. Xu, J. Wang, M. Hupert, A. Hanks, M. Koppang, J. Butler, G. Lucazeau, M. Mermoux, J. Strojek and G. Wain, "Standard Electrochemical Behavior of High-Quality Boron-Doped Polycrystalline Diamond Thin-Film Electrodes," *Analytical Chemistry,* vol. 72, no. 16, pp. 3693-3804, 2000.

[108] M. G. Trachioti, A. C. Lazanas and M. I. Prodromidis, "Shedding light on the calculation of electrode electroactive area and heterogeneous electron transfer rate constants at graphite screen-printed electrodes," *Microchimica Acta,* vol. 190, p. 251, 2023.

[109] A. J. Bard and L. R. Faulkner, "Potential Sweep Methods," in *Electrochemical Methods: Fundamentals and Applications*, 2nd Edition ed., New York, New York: John Wiley & Sons, Inc., 2001, pp. 226-260.

[110] R. S. Nicholson, "Theory and application of cyclic voltammetry for measurement of electrode reaction kinetics," *Analytical Chemistry,* vol. 37, no. 11, pp. 1351-1355, 1965.

[111] J. F. Cassidy, R. C. de Carvalho and A. J. Betts, "Use of Inner/Outer Sphere Terminology in Electrochemistry--A Hexacyanoferrate II/III Case Study," *Electrochem,* vol. 4, no. 3, pp. 313-349, 2023.

[112] V. P. Shilove, A. M. Fedoseev and B. F. Myasoedov, "Disproportionation of Actinides in Aqueous and Organic Media," *Radiochemistry,* vol. 64, pp. 323-337, 2022.

[113] P. Delahay, "Voltammetry and Polarography and Continuously Changing Potential," in *New Instrumental Methods in Electrochemistry: Theory, Instrumentation, and Applications to Analytical and Physical Chemistry*, New York, New York: Interscience Publishers, Inc., 1954, pp. 115-145.

[114] C. Jagadeeswara Rao, K. A. Venkatesan, K. Nagarajan, T. G. Srinivason and P. R. Vasudeva Rao, "Electrochemical behavior of europium (III) in N-butyl-N-methylpyrrolidinium bis(trifluoromethylsulfonyl)imide," *Electrochimica Acta,* vol. 54, no. 20, pp. 4718-4725, 2009.

[115] R. Nagaishi, M. Arisaka, T. Kimura and Kitatsuji, "Spectroscopic and electrochemical properties of europium(III) ion in hydrophobic ionic liquids under controlled condition of water content," *Journal of Alloys and Compounds,* vol. 431, pp. 221-225, 2007.

[116] R. J. Klingler and J. K. Kochi, "Electron-transfer kinetics from cyclic voltammetry. Quantitative description of electron reversibility," *Journal of Physical Chemistry,* vol. 85, no. 12, pp. 1731-1741, 1981.

[117] C. J. Rao, K. A. Venkatesan, K. Nagarajan and T. G. Srinivasa, "Dissolution of uranium oxides and electrochemical behavior of U(VI) in task specific ionic liquid," *Radiochimica Acta,* vol. 96, pp. 403-409, 2008.

[118] I. Grenthe, J. Fuger, R. J. M. Konings, R. J. Lemire, A. B. Muller, C. Nguyen0Trung Cregu and H. Wanner, "Standards and Conventions," in *Chemical Thermodynamics of Uranium*, Issy-les-Moulineaux, OECD Nuclear Energy Agency, 2004, pp. 9-28.

[119] R. Guillaumont, T. Fanghanel, V. Neck, J. Fuger, D. A. Palmer, I. Grenthe and M. H. Rand, "Selected Data for Uranium," in *Update on the Chemical Thermodynamics of Uranium, Neptunium, Plutonium, Americium and Technetium*, Issy-les-Moulineaux, OEC Nuclear Energy Agency, 2003, pp. 43-78.

[120] S. Mishra, S. K., C. J. Rao, C. Mallika and U. K. Mudali, "Electrochemical studies on the reduction of uranyl ions in nitric acid-hydrazine media," *Journal of Electroanalytical Chemistry,* vol. 776, pp. 127-133, 2016.

[121] A. Ikeda-Ohno, C. Hennig, S. Tsushima, A. C. Scheinost, G. Bernhard and T. Yaita, "Speciation and Structural Study of U(IV) and -(VI) in Perchloric and Nitric Acid Solutions," *Inorganic Chemistry,* vol. 48, no. 15, pp. 7201-7210, 2009.

[122] B. W. Edenborough and R. G. Robins, "High Temperature rH/pH Diagrams for the System Uranium(VI)-Nitrate-Water," *Electrochimica Actaa,* vol. 14, pp. 1285-1295, 1969.

[123] N. Takeno, "Atlas of Eh-pH diagrams: Intercomparison of thermodynamic databases," National Institute of Advanced Industrial Science and Technology, 2005.

[124] P. Giridhar, K. A. Venkatesan, S. Subramaniam, T. G. Srinivasan and P. Vasudeva Rao, "Extraction of uranium (VI) by 1.1 M tri-n-butylphosphate/ionic liquid and the feasibility of recovery by direct electrodeposition from organic phase," *Journal of Alloys and Compounds,* vol. 448, no. 1-2, pp. 104-108, 2008.

[125] P. Giridhar, K. A. Venkatesan, T. G. Srinivasan and P. R. Vasudeva Rao, "Electrochemical behavior of uranium(VI) in 1-butyl-3-methylimidazoliumchloride and thermal characterization of uranium oxide deposit," *Electrochimica Acta,* vol. 52, pp. 3006-3012, 2007.

[126] Y. Wang, X. Dong, Y. Lu, Y. Liu, X. Cao, J. Chen and C. Xu, "Electrochemical and spectrochemical analysis of U(VI) reduction in nitric acid solutions," *Journal of Electroanalytical Chemistry,* vol. 874, p. 114482, 2020.

[127] N. Sato, "Electrical Double Layer at Electrode Interfaces," in *Electrochemistry at Metal and Semiconductor Electrodes*, New York, Elsevier, 1998, pp. 119-199.

[128] W. R. Heineman, "Spectroelectrochemistry: The Combination of Optical and Electrochemical Techniques," *Journal of Chemical Education,* vol. 60, no. 4, pp. 305-308, 1983.

[129] Z. V. Živcová, O. Frank, V. Petrák, H. Tarábková, J. Vacík, M. Nesládek and L. Kavan, "Electrochemistry and in Situ Raman Spectroelectrochemistry of Low and High Quality Boron Doped Diamond Layers in Aqueous Electrolyte Solution," *Electrochimica Acta,* vol. 87, pp. 518-525, 2013.

[130] K. Ashley and S. Pons, "Infrared Spectroelectrochemistry," *Chemical Reviews,* vol. 88, pp. 673-695, 1988.

[131] K. Takao, S. Takao, A. C. Scheinoist and C. H. Bernhard, "In situ spectroelectrochemical investigation of Pt(II/IV) oxidation in aqueous solution using X-ray absorption spectroscopy," *Inorganica Chimica Acta,* vol. 363, no. 4, pp. 802-806, 2010.

[132] J. K. Zak, J. E. Butler and G. M. Swain, "Diamond Optically Transparent Electrodes: Demonstration of Concept with Ferri/Ferrocyanide and Methyl Viologen," *Analytical Chemistry ,* vol. 73, no. 5, pp. 908-914, 2001.

[133] C. A. Rusinek, M. F. Becker, R. Rechenberg, N. Kaval, K. Ojo and W. R. Heineman, "Polymer-Coated Boron Doped Diamond Optically Transparent Electrodes for Spectroelectrochemical Sensors," *Electroanalysis,* vol. 28, no. 9, pp. 2228-2236, 2016.

[134] N. Wächter, C. Munson, R. Jarošová, I. Berkun, T. Hogan, R. C. Rocha-Filho and G. M. Swain, "Structure, Electronic Properties, and Electrochemical Behavior of a

Boron-Doped Diamond/Quartz Optically Transparent Electrode," *ACS Applied Material Interfaces,* vol. 8, no. 42, pp. 28325-28337, 2016.

[135] Q. Cao, Z. Shao, D. K. Hensley, N. Lavrik and B. J. Venton, "Influence of Geometry on Thin Layer and Diffusion Processes at Carbon Electrodes," *Langmuir,* vol. 37, no. 8, pp. 2667-2676, 2021.

[136] Q. Cao, P. Puthongkham and B. J. Venton, "Review: new insights into optimizing chemical and 3D surface structures of carbon electrodes for neurotransmitter detection," *Analytical Methods,* vol. 11, no. 3, pp. 247-261, 2019.

[137] L. B. Anderson and C. N. Reilley, "Thin-layer electrochemistry: Steady-state methods of studying rate processes," *Journal of Electroanalytical Chemistry,* vol. 10, no. 4, pp. 295-305, 1965.

[138] S. Goia, M. A. P. Turner, J. M. Woolley, M. D. Horbury, A. J. Borrill, J. J. Tully, S. J. Cobb, M. Staniforth, N. D. M. Hine, A. Burriss, J. v. Macpherson, B. R. Robinson and V. G. Stavros, "Ultrafast Transient Absorption Spectroelectrochemistry: Femtosecond to Nanosecond Excited-State Relaxation Dynamics of the Individual Components of an Anthraquinone Redox Couple," *Chemical Science,* vol. 13, no. 2, pp. 486-496, 2022.

[139] J. Xu, Y. Yokota, R. A. Wong, Y. K. Kim and Y. Einaga, "Unusual Electrochemical Properties of Low-Doped Boron-Doped Diamond Electrodes Containing sp2 Carbon," *Journal of the American Chemical Society,* vol. 142, no. 5, pp. 2310-2316, 2020.

[140] J. Sun, H. Lu, H. Lin, L. Du, W. Huang, H. Li and T. Cui, "Electrochemical oxidation of aqueous phenol at low concentrations using Ti/BDD electrode," *Separation and Purification Technology,* vol. 88, pp. 116-120, 2012.

[141] W. C. Poh, K. P. Log, W. D. Zhang, Y. J.-S. Sudhiranja and F.-S. Sheu, "Biosensing Properties of Diamond and Carbon Nanotubes," *Langmuir,* vol. 20, no. 13, pp. 5484-5492, 2004.

[142] R. Trouillion, D. O'Hare and Y. Einaga, "Effect of doping level on the biological stability of hydrogenated boron doped diamond electrodes," *Physical Chemistry Chemical Physics,* vol. 13, no. 5422-5429, 2011.

[143] J. A. Bennett, J. Wang, Y. Show and G. M. Swain, "Effect of sp2-Bonded Non-diamond Carbon Impurity on the Response of Boron-Doped Polycrystalline Diamond Thin-Film Electrodes," *Journal of the Electrochemical Society,* vol. 151, p. E306, 2004.

[144] H. B. Martin, A. Argoitia, U. Landau, A. B. Anderson and J. C. Angus, "Hydrogen and Oxygen Evolution on Boron-Doped Diamond Electrodes," *Journal of the Electrochemical Society,* vol. 143, p. L133, 1996.

[145] R. L. McCreery, "Advanced Carbon Electrode Materials for Molecular Electrochemistry," *Chemical Review,* vol. 108, no. 7, pp. 2646-2687, 2008.

[146] Y. Dai, D. Proshlykov, J. Zak and G. Swain, "Optically transparent diamond electrode for use in IR transmission spectroelectrochemical measurements," *Analytical Chemistry,* vol. 79, no. 19, pp. 7526-7533, 2007.

[147] M. Petek, T. Neal and R. Murray, "Spectroelectrochemistry--Application of optically transparent minigrid electrodes under semi-infinite diffusion conditions," *Analytical Chemistry,* vol. 43, no. 8, pp. 1069-1074, 1971.

[148] F. H. Sun, Z. M. Zhang, M. Chen and H. S. Shen, "Improvement of adhesive strength and surface roughness of diamond films on Co-cemented tungsten carbide," *Diamond and Related Materials,* vol. 12, no. 3-7, pp. 711-718, 2003.

[149] X. Wang, J. Zhang, B. Shen, T. Zhang and F. Sun, "Fracture and solid particle erosion of micro-crystalline, nano-crystalline and boron-doped diamond films," *International Journal of Refractory Metals and Hard Materials,* vol. 45, pp. 31-40, 2014.

[150] Z. Zhang, D. Ziang, Z. Zhang, Y. Zhang and B. Zhao, "Study on tribology and cutting performance of boron doped diamond composite coated tools," *International Journal of Refractory Materials and Hard Materials,* vol. 117, p. 106385, 2023.

[151] C. Yamaguchi, K. Natsui, S. Iizuka, Y. Tateyama and Y. Einaga, "Electrochemical properties of fluorinated boron-doped diamond electrodes via fluorine-containing plasma treatment," *Physical Chemistry Chemical Physics,* vol. 21, pp. 13788-13794, 2019.

[152] T. H. Borst and O. Weis, "Boron-Doped Homoepitaxial Diamond Layers: Fabrication, Characterization, and Electronic Applications," *physica status solidi (a),* vol. 154, no. 1, pp. 423-444, 1996.

[153] H. Zeng, P. U. Arumugam, S. Siddiqui and J. A. Carlisle, "Low temperature boron doped diamond," *Applied Physical Letters,* vol. 102, no. 22, p. 223108, 2013.

[154] P. Gluche, M. Adamschik, A. Vescan, W. Ebert, F. Szucs, H. J. Fecht, A. Floter, R. Zachai and E. Kohn, "Application of highly oriented, planar diamond (HOD) films of high mechanical strength in sensor technologies," *Diamond and Related Materials,* vol. 7, no. 6, pp. 779-782, 1998.

[155] T. H. Borst, P. C. Munzinger and O. Weis, "Characterization of undoped and doped homeopitaxial diamond layers produced by mircowave plasma CVD," *Diamond and Related Materials,* vol. 3, no. 4-6, pp. 515-519, 1994.

[156] L. A. Hutton, J. G. Iacobini, E. Bitziou, R. B. Channon, M. E. Newton and J. V. Macpherson, "Examination of the Factors Affecting the Electrochemical Performance of Oxygen-Terminated Polycrystalline Boron-Doped Diamond Electrodes," *Analytical Chemistry,* vol. 85, no. 15, pp. 7230-7240, 2013.

[157] S. Gupta and G. P. Vierkant, " Surface Roughness and Critical Exponent Analyses of Boron- Doped Diamond Films Using Atomic Force Microscopy Imaging: Application of Autocorrelation and Power Spectral Density Functions," *Electronic Materials,* vol. 43, no. 9, pp. 3436-3448, 2014.

[158] C. Zhang, J. Wu and D. Fu, "Fractals in several electrode materials," *Applied Surface Science,* vol. 313, pp. 750-754, 2014.

[159] B. Koslowski, S. Strobel, M. J. Wenig, R. Martschat and P. Ziemann, "On the roughness of hydrogen-plasma treated diamond(100) surfaces," *Diamond and Related Materials,* vol. 7, no. 2-5, pp. 322-326, 1998.

[160] L. Kavan, Z. V. Zivcova, V. Petrak, O. Frank, P. Janda, H. Tarabkova, M. Nesladek and V. Mortet, "Boron-doped Diamond Electrodes: Electrochemical, Atomic Force Microscopy and Raman Study towards Corrosion-modifications at Nanoscale," *Electrochimica Acta,* vol. 179, pp. 626-636, 2015.

[161] V. Mortet, A. Taylor, Z. V. Zivcova, D. Machon, O. Frank, P. Hubik, D. Trmouilles and L. Kavan, "Analysis of heavily boron-doped diamond Raman spectrum," *Diamond and Related Materials,* vol. 88, pp. 163-166, 2018.

[162] V. Mortet, I. Gregora, A. Taylor, N. Lambert, P. Ashcheulov, Z. Gedeonova and P. Hubik, "New perspectives for heavily boron-doped diamond Raman spectrum analysis," *Carbon,* vol. 168, pp. 319-327, 2020.

[163] M. Bernard, C. Baron and A. Deneuville, "About the origin of the low wave number structures of the Raman spectra of heavily boron doped diamond films," *Diamond and Related Materials,* vol. 13, p. 896, 2004.

[164] M. Bernard, A. Deneuville and P. Muret, "Non-destructive determination of the boron concentration of heavily doped metallic diamond thin films from Raman spectroscopy," *Diamond and Related Materials,* vol. 13, p. 282, 2004.

[165] S. Prawer and R. J. Nemanich, "Raman spectroscopy of diamond and doped diamond," *The Philosophical Transactions of the Royal Society A,* vol. 362, no. 1824, pp. 2537-2565, 2004.

[166] S. Prawer, K. W. Nugent and D. N. Jamieson, "The Raman spectrum of amorphous diamond," *Diamond and Related Material,* vol. 7, p. 106, 1998.

[167] F. Pruvost, E. Bustarret and A. Deneuville, "Characteristics of homoepitaxial heavily boron-doped diamond films from their Raman spectra," *Diamond and Related Materials,* vol. 9, pp. 295-299, 2000.

[168] M. Ficek, M. Sobaszek, M. Gnyba, J. Ryl, L. Golunski, M. Smietana, J. Jasinski, P. Caban and R. Bogdanowicz, "Optical and electrical properties of boron doped diamond thin conductive films deposited on fused silica glass substrates," *Applied Surface Science,* vol. 387, pp. 846-856, 2016.

[169] F. Okino, Y. Kawaguchi, H. Touhara, K. Momota, M. Nishitani-Gamo, T. Ando, A. Sasaki, M. Yoshimoto and O. Odawara, "Preparation of boron-doped semiconducting diamond films using BF3 and the electrochemical behavior of the semiconducting diamond electrodes," *Journal of Fluorine Chemistry,* vol. 125, pp. 1715-1722, 2004.

[170] T.-C. Kuo, R. L. McCreery and G. M. Swain, "Electrochemical Modification of Boron-Doped Chemical Vapor Deposited Diamond Surfaces with Covalently Bonded Monolayers," *Electrochemical and Solid-State Letters,* vol. 2, no. 6, pp. 288-290, 1999.

[171] A. C. Ferrari and J. Robertson, "Origin of the 1150 cm-1 Raman mode in nanocrystalline diamond," *Physical Reviews B,* vol. 63, p. 121405, 2001.

[172] J. H. T. Luong, K. B. Male and J. D. Glenon, "Boron-doped diamond electrode: synthesis, characterization, functionalization and analytical applications," *Analyst,* vol. 134, pp. 1965-1979, 2009.

[173] T. Kondo, H. Ito, K. Kusakabe, K. Ohkawa, Y. Einaga, A. Fujishima and T. Kawai, "Plasma etching treatment for surface modification of boron-doped diamond electrodes," *Electrochimica Acta,* vol. 52, pp. 3840-3848, 2007.

[174] V. S. Smentkowski and J. T. Yates Jr., "Fluorination of Diamond Surfaces by Irradiation of Perfluorinted Alkyl Iodides," *Science,* vol. 271, pp. 193-195, 1996.

[175] V. S. Smentkowski, J. T. Yates Jr., X. Chen and W. A. Goddard III, "Fluorination of diamond -- C4F9I and CF3I photochemistry on diamond (100)," *Surface Science,* vol. 370, pp. 209-231, 1997.

[176] T. Kondo, K. Ito, K. Kusakabe, K. Ohkawa, K. Honda, Y. Einaga, A. Fujishima and T. Kawai, "Characterization and electrochemical properties of CF4 plasma-treated boron-doped diamond surfaces," *Diamond and Related Materials,* vol. 17, no. 1, pp. 48-54, 2008.

[177] K. G. Saw, "Tof-Sims Fragment Pattern Analysis Of Boron-Doped Chemical Vapor Deposition Diamond," in *Proceedings of the 8th International Conference on Multidisciplinary Research*, Pulau Pinang, 2019.

[178] S. Torrengo, R. Canteri, R. Del'Anna, L. Minati, A. Pasquarelli and G. Speranza, "XPS and ToF-SIMS investigation of nanocrystalline diamond oxidized surfaces," *Applied Surface Science,* vol. 276, pp. 101-111, 2013.

[179] K. W. Wong, L. J. Huang, Y. Hung, S. T. Lee and R. W. M. Kwok, "Depletion of surface boron of heavily boron-doped diamond films by annealing," *Diamond and Related Materials,* vol. 8, pp. 1006-1010, 1999.

[180] M. N. Drozdov, Y. N. Drozdov, M. A. Lobaev and P. A. Yunin, "New Cluster Secondary Ions for Quantitative Analysis of the Concentration of Boron Atoms in Diamond by Time-of-Flight Secondary-Ion Mass Spectrometry," *Technical Physics Letters,* vol. 44, no. 4, pp. 297-300, 2018.

[181] O. L. Eryilmaz and A. Erdemir, "TOF-SIMS and XPS characterization of diamond-like carbon films after tests in inert and oxidizing environments," *Wear,* vol. 265, pp. 244-254, 2008.

[182] A. Karmen and H. Haut, "Detection of heteroatoms in gas-liquid chromatographic effluents by ion-exchange flame excitation and ionzation," *Journal of Chromatography,* vol. 99, pp. 394-356, 1974.

[183] G. Zong, Z.-B. Zhang, J.-H. Sun and J.-C. Xiao, "Preparation of high-purity molten FLiNaK salt by the hydrofluorination process," *Journal of Fluorine Chemistry,* vol. 197, pp. 134-141, 2017.

[184] Keyence, "Introduction to Surface Roughness Measurement," Keyence Corporation of America, Itasca, 2018.

[185] T. Nagaoka, K. Kita and N. Kondo, "Hot corrosion of Al2O3 and SiC ceramics by KCl-NaCl molten salt," *Journal of the Ceramic Society of Japan,* vol. 123, no. 8, pp. 685-689, 2015.

[186] T. Ando, K. Yamamoto, M. Matsuzawa, Y. Takamatsu, S. Kawasaki, F. okino, H. Touhara, M. Kamo and Y. Sato, "Direct interaction of elemental fluorine with diamond surfaces," *Diamond and Related Materials,* vol. 5, pp. 1021-1025, 1996.

[187] S. Ghodbane, D. Ballutaud, A. Deneuville and C. Baron, "Influence of boron concentration on the XPS spectra of the (100) surface of homoepitaxial boron-doped diamond films," *physica status solidi (a),* vol. 203, no. 12, pp. 3147-3151, 2006.

[188] S. Ghodbane, D. Ballutaud, F. Omnes and C. Agnes, "Comparison of the XPS spectra from homoepitaxial [111], [100] and polycrystalline boron-doped diamond films," *Diamond and Related Materials,* vol. 19, pp. 630-636, 2010.

[189] M. Wang, N. Simon, C. Decorse-Pascanut, M. Bouttemy, A. Etcheberry, M. Li, R. Boukherroub and S. Szunerits, "Comparison of the chemical composiiton of boron-doped diamond surfaces upon different oxidation processes," *Electrochimica Acta,* vol. 54, pp. 5818-5824, 2009.

[190] C. H. Goeting, F. Marken, A. Gutierrez-Sosa, R. G. Compton and J. S. Foord, "Electrochemically induced surface modifications of boron-doped diamond electrodes: an X-ray photoelectron spectroscopy study," *Diamond and Related Materials,* vol. 9, pp. 390-396, 2000.

[191] F. Jia, Y. Bai, F. Qu, J. Zhao, C. Zhuang and X. Jiang, "Effect of B/C ratio on the physical properties of highly boron-doped diamond films," *Vacuum,* vol. 84, no. 7, pp. 930-934, 2010.

[192] R. Hoffmann, A. Kriele, H. Obloh, J. Hees, M. Wolfer, W. Smirnov, N. Yang and C. E. Nebel, "Electrochemical hydrogen termination of boron-doped diamond," *Applied Physics Letters,* vol. 97, p. 052103, 2010.

[193] G. Sine, L. Ouattara, M. Panizza and C. Comninellis, "Electrochemical Behavior of Fluorinated Boron-Doped Diamond," *Electrochemical and Solid-State Letters,* vol. 6, no. 9, pp. D9-D11, 2003.

[194] H. Kabir, H. Zhu, J. May, K. Hamal, Y. Kan, T. Williams, E. Echeverria, D. N. McIlroy, D. Estrada, P. H. Davis, T. Pandhi, K. Yocham, K. Higginbotham, A. Clearfield and I. F. Cheng, "The sp^2-sp^3 carbon hybridization content of nanocrystalline graphite from pyrolyzed vegetable oil, comparison of electrochemistry and physical properties with other carbon forms and allotropes," (2019). *Carbon, 144*, 831-840.

A. Mezzi and S. Kaciulis, "Surface investigation of carbon films: from diamond to graphite," *Surface and Interface Analysis,* vol. 42, pp. 1082-1084, 2010.

[195]

[196] S. Ferro and A. De Battisti, "Physicochemical Properties of Fluorinated Diamond Electrodes," *Journal of Physical Chemistry B,* vol. 107, no. 31, pp. 7567-7573, 2003.

[197] J. Du, D. Wang, C. A. Wilkie and J. Wang, "An XP investigation of thermal degredation and charring on poly(vinyl chloride)-clay nanocomposites," *Polymer Degredation and Stability,* vol. 79, no. 2, pp. 319-324, 2003.

[198] M. N. Drozdov, A. E. Ieshkin, O. A. Streletskiy, O. Y. Nishchak, S. F. Belykh and A. Tolstoguzov, "TOF-SIMS for carbon hybridization state analysis," *Carbon,* vol. 186, pp. 83-90, 2022.

[199] F. Awaja, T.-T. Wong, D. Putzer, M. Thaler, A. al Taee and T. O'Brien, "Molecular descriptions of functionalised multi layered diamond like/ amorphous carbon coatings," *Materials Today Communciations,* vol. 19, pp. 433-440, 2019.

[200] E. Staryga, G. W. Bqk, J. Rogowski, M. Knapik, A. Rylski and K. Fabisiak, "Application of Time-of-Flight Secondary Ion Mass Spectroscopy to study diamond-like carbon films," *Diamond and Related Materials,* vol. 16, no. 4-7, pp. 1312-1315, 2007.

[201] A. Deslandes, M. Jasieniak, M. Ionescu, J. G. Shapter, C. Fairman, J. J. Gooding, D. B. Hibbert and J. S. Quinton, "ToF-SIMS characterization of methane- and hydrogen-plasma-modified garphite using principal component analysis," *Surface and Interface Analysis,* vol. 41, no. 3, pp. 216-224, 2009.

[202] H. Yin, H.-G. Boyne, P. Ziemann, B. Dohuard, L. Houssiau, F. Renaux, M. Hecq and C. Bittencourt, "Purity of epitaxial cubic BoronNitride films on (001) Diamond - A prerequisite for their doping," *Diamond and Related Materials,* vol. 17, no. 3, pp. 276-282, 2008.

[203] D. J. Graham and L. J. Gamble, "Back to the basics of time-of-flight secondary ion mass spectrometry data analysis of bio-related samples. II. Data process and display," *Biointerphases,* vol. 18, p. 031201, 2023.

[204] E. Lukosi, A. Alghamdi, D. Hamm, C. Launiere, R. Milburn, C. Pereira, P. Vilmercati and H. Weitering, "Electrical and material effects of molten salt and temperature on diamond," *Diamond and Related Materials,* vol. 128, p. 109222, 2022.

[205] M. Bonifacie, "Chlorine Isotopes," in *Encyclopedia of Geochemistry: A Comprehensive Reference Source on the Chemistry of the Earth*, Cham, Springer International Publishing, 2018, pp. 244-248.

[206] K. Wang, W. Li, S. Li, Z. Tian, P. Koefoed and X.-Y. Zheng, "Geochemistry and cosmochemistry of potassium stable isotopes," *Geochemistry,* vol. 81, no. 3, p. 125786, 2021.

[207] M. R. Palmer and G. H. Swihart, "Boron Isotope Geochemistry: An Overview," in *Boron: Mineralogy, Petrology, and Geochemistry*, Boston, De Gruyter, 1996, pp. 709-744.

[208] T. B. Coplen, J. A. Hopple, J. K. Bohlke, H. S. Peiser, S. E. Rieder, H. R. Krouse, K. J. R. Rosman, T. Ding, R. D. Vocke Jr., K. M. Revesz, A. Lamberty, P. Taylor and P. De Bievre, "Compilation of Minimum and Maximum Isotope Ratios of Selected Elements in Naturally Occurring Terrestrial Materials and Reagents," U.S. Department of the Interior, Reston, 2002.

[209] J. C. Lee, H. J. Kang, K. J. Kim, Y. S. Kim and D. W. Moon, "Oxygen enhanced secondary ion emission of Fe and Co by TOF-SIMS and ISS/DR," *Surface Science,* vol. 324, no. 2-3, pp. 338-344, 1995.

[210] R. N. S. Sodhi, "Time-of-flight secondary ion mass spectrometry (TOF-SIMS):-versatility in chemical and imaging surface science," *Analyst,* vol. 129, pp. 483-487, 2004.

[211] S. Tanimoto and A. Ichimura, "Discrimination of Inner- and Outer-Sphere Electrode Reactions by Cyclic Voltammetry Experiments," *Journal of Chemical Education,* vol. 90, pp. 778-781, 2013.

[212] L. M. Torres, A. F. Gil, L. Galicia and I. Gonzalez, "Understanding the difference between inner- and outer-sphere mechanisms: An electrochemical experiment," *Journal of Chemical Education,* vol. 73, no. 8, pp. 808-810, 1996.

[213] E. J. Piechota and G. J. Meyer, "Introduction to Electron Transfer: Theoretical Foundatinos and Pedagogical Examples," *Journal of Chemical Education,* vol. 96, pp. 2450-2466, 2019.

[214] H. Taube, "Mechanisms of Oxidation-Reduction Reactions," *Journal of Chemical Education,* vol. 45, no. 7, pp. 452-461, 1968.

[215] J. C. Curtis and T. J. Meyer, "Outer-Sphere Charge Transfer in Mixed-Metal Ion Pairs," *Inorganic Chemistry,* vol. 21, no. 4, pp. 1562-1571, 1982.

[216] K. K. Cline, M. T. McDermott and R. L. McCreery, "Anomalously Slow Electron Transfer at Ordered Graphite Electrodes: Influence of Electronic Factors and Reactive Sites," *Journal of Physical Chemistry,* vol. 98, no. 20, pp. 5314-5319, 1994.

[217] S. Ranganathan, T.-C. Kuo and R. L. McCreery, "Facile Preparation of Active Glassy Carbon Electrodes with Activated Carbon and Organic Solvents," *Analytical Chemistry,* vol. 71, no. 16, pp. 3574-3580, 1999.

[218] X. Ji, C. E. Banks, A. Crossley and R. G. Compton, " Oxygenated Edge Plane Sites Slow the Electron Transfer of the Ferro-/Ferricyanide Redox Couple at Graphite Electrodes," *ChemPhysChem,* vol. 7, no. 6, pp. 1337-1344, 2006.

[219] P. Chen, M. A. Fryling and R. L. McCreery, "Electron Transfer Kinetics at Modified Carbon Electrode Surfaces: The Role of Specific Surface Sites," *Analytical Chemistry,* vol. 67, no. 18, pp. 3115-3122, 1995.

[220] I. Duo, C. Levy-Clement, A. Fujishima and C. Comninellis, "Electron transfer kinetics on boron-doped diamond Part I: Influence of anodic treatment," *Journal of Applied Electrochemistry,* vol. 34, pp. 935-943, 2004.

[221] K. K. Cline, M. T. McDermott and R. L. McCreery, "Anomalously Slow Electron Transfer at Ordered Graphite Electrodes: Influence of Electronic Factors and Reactive Sites," *Journal of Physical Chemistry,* vol. 98, no. 20, pp. 5314-5319, 1994.

[222] I. Dui, A. Fujishima and C. Comninellis, "Electron transfer kinetics on composite diamond (sp3)-graphite (sp2) electrodes," *Electrochemistry Communications,* vol. 5, no. 8, pp. 695-7000, 2003.

[223] L. Xiong, C. Batchelor-McAuley, K. R. Ward, C. Downing, R. S. Hartshorne, N. S. Lawrence and R. G. Compton, "Voltammetry at graphite electrodes: The oxidation of hexacyanoferrate (II) (ferrocyanide) does not exhibit pure outer-sphere electron transfer kinetics and is sensitive to pre-exposure of the electrode to organic solvents," *Journal of Electroanalytical Chemistry,* vol. 661, pp. 144-149, 2011.

[224] T. Watanabe, Y. Honda, K. Kanda and Y. Einaga, "Tailored design of boron-doped diamond electrodes for various electrochemical applications with boron-doping

level and sp2-bonded carbon impurities," *physica status solidi (a),* vol. 211, no. 12, pp. 2709-2717, 2014.

[225] D. Rappleye, K. Teaford and M. F. Simpson, "Investigation of the effects of uranium(III)-chloride concentration on voltammetry in molten LiCl-KCl eutectic with a glass sealed tungsten electrode," *Electrochimica Acta,* vol. 219, pp. 721-733, 2016.

[226] L. Swain, S. Ghosh, G. Pakhui and B. P. Reddy, "Redox Behavior of Moisture in LiCl-KCl Eutectic Melts: A Cyclic Voltammetry Study," *Nuclear Technology,* vol. 207, no. 1, pp. 119-146, 2021.

[227] L. Swain, G. Pakhui, A. Jain and S. Ghosh, "Electrochemical behavior of LiCl-KCl eutectic melts containing moisture as impurity. Part I: Inert tungsten electrode," *Journal of Electroanalytical Chemistry,* vol. 910, p. 116125, 2022.

[228] S. Vandarkuzhali, N. Gogoi, S. Ghosh, B. P. Reddy and K. Nagarajan, "Electrochemical behavior of LaCl3 at tungsten and aluminum cathodes in LiCl-KCl eutectic melt," *Electrochimica Acta,* vol. 59, pp. 245-255, 2012.

[229] M. Zhang, J. Ge, J. Zhang and L. E. Liu, "Redox potential measurement of AgCl in molten LiCl-KCl salt using chronopotentiometry and potentiodynamic scan techniques," *Electrochemistry Communications,* vol. 105, p. 106498, 2019.

[230] A. Uehara, O. Shirai, T. Nagai, T. Fuji and H. Tamana, "Spectroelectrochemistry and Electrochemistry of Europium Ions in Alkali Chloride Melts," in *Zeitschrift fur Naturforschung A*, Hammamet, 2007.

[231] M. Mohamedi, S. Martinet, J. Bouteillon and J. C. Poignet, "Comprehensive examination of the electrochemistry of indium in the molten LiCl-KCl eutectic," *Electrochimica Acta,* vol. 44, no. 5, pp. 797-803, 1998.

[232] R. O. Hoover, M. R. Shaltry, S. Martin, K. Sridharan and S. Phongikaroon, "Electrochemical studies and analysis of 1-10wt% UCl3 concentrations in molten LiCl-KCl eutectic," *Journal of Nuclear Material,* vol. 452, no. 1-3, pp. 389-396, 2014.

[233] S. D. James, "Undervoltage deposition of Alkali Metal at Carbon Electrodes in the LiCl-KCl Eutectic Melt," *Journal of the Electrochemical Society,* vol. 122, no. 7, p. 921, 1975.

[234] P. Cui, B. Qin, A. M. Martinez and G. M. Haarberg, "Electrochemical Behavior of Indium in LiCl-KCl Molten Salts," *International Journal of Electrochemical Science,* vol. 14, no. 6, pp. 5064-5074, 2019.

[235] T.-J. Kim, Y.-J. Jung, S.-H. Kim, S.-W. Paek and D.-H. Ahn, "Elucidation of Electrode Reaction of EuCl3 in LiCl-KCl Eutectic Melts through CV Curve Analysis," *Bulletin of the Koren Chemical Society,* vol. 32, no. 3, pp. 863-866, 2011.

[236] S. Suganthi, G. Pakhui and S. Ghosh, "Electrochemical investigations on cathodic reduction processes at graphite electrode in LiCl-KCl eutectic melt," *Journal of Electroanalytical Chemistry,* vol. 954, p. 118019, 2024.

[237] C. Sun, Q. Xu, X. Zou, H. Cheng and X. Lu, "A new method to determine AgCl(1% mol)/Ag electrode potential versus the standard chloride electrode potential in a LiCl-KCl eutectic," *Electrochemistry Communications,* vol. 130, p. 107111, 2021.

[238] M. M. MacInnes, Z. R. Jones, B. Li, N. H. Anderson, B. E. R., I. M. DiMucci, C. Eiroa-Lledo, K. E. Knope, M. Y. Livshits, S. A. Kozimore, V. Mocko, K. A. Pace, F. R. Rocha and B. Stein, "Using molten salts to probe outer-coordination sphere effects on lanthanide(III)/(II) electron-transfer reactions," *Dalton Transactions,* vol. 50, pp. 15696-15710, 2021.

[239] K. Sridharan, M. Simpson and J. Bresee, "Thermal Properties of LiCl-KCl Molten Salt for Nuclear Waste Separation," U.S. Department of Energy Nuclear Energy University Program, Madison, 2012.

[240] C. P. Fabian, V. Luca, P. Chamelot, L. Massot, C. Caravaca and G. R. Lumpkin, "Experimental and Simulation Study of the Electrode Reaction Mechanism of La3+ in LiCl-KCl Eutectic Molten Salt," *Journal of the Electrochemical Society,* vol. 159, no. 4, p. F63, 2012.

[241] J. Park, S. Choi, S. Sohn and I. S. Hwang, "Cyclic Voltammetry on Zr, Sn, Fe, Cr and Co in LiCl-KCl Salts at 500 oC for Electrorefining of Irradiated Zircaloy-4 Cladding," *Journal of the Electrochemical Society,* vol. 164, no. 12, p. D744, 2017.

[242] Y. J. Park, Y. J. Jung, S. K. Min, Y. H. Cho, H.-J. Im, J.-W. Yeon and K. Song, "A Quartz Tube Based Ag/Ag+ Reference Electrode with a Tungsten Tip Junction for an Electrochemical Study in Molten Salts," *Bulletin of the Korean Chemical Society,* vol. 30, no. 1, pp. 133-136, 2009.

[243] C. P. Fabian, V. Luca, T. H. Le, A. M. Bond, P. Chamelot, L. Massot, C. Caravaca, T. L. Hanley and G. R. Lumpkin, "Cyclic Voltammetric Experiment - Simulation Comparisons of the Complex Mechanism Associated with Electrochemical Reduction of Zr4+ in LiCl-KCl Eutectic Molten Salt," *Journal of the Electrochemical Society,* vol. 160, no. 2, p. H81, 2012.

[244] M. Zhang, J. Ge, J. Zhang and L. E. Liu, "Redox potential measurement of AgCl in molten LiCl-KCl salt using chronopotentiometry and potentiodynamic scan techniques," *Electrochemistry Communications,* vol. 105, p. 106498, 2019.

[245] W. Ding, J. Gomez-Vidal, A. Bonk and T. Bauer, "Molten chloride salts for next generation CSP plants: Electrolytical salt purification for reducing corrosive impurity," *Solar Energy Materials and Solar Cells,* vol. 199, pp. 8-15, 2019.

[246] K. Duemmler, Y. Lin, M. Woods, T. Karlsson, R. Gakhar and B. Beeler, "Evaluation of thermophysical properties of the LiCl-KCl system via ab initio and experimental methods," *Journal of Nuclear Materials,* vol. 559, p. 153414, 2022.

[247] Z.-h. Wang, D. Rappleye and M. F. Simpson, "Voltammetric Analysis of Mixtures of Molten Eutectic LiCl-KCl Containing LaCl3 and ThCl4 for Concentration and DIffusion Coefficient Measurement," *Electrochimica Acta,* vol. 191, pp. 29-43, 2016.

[248] Z. Wang, D. Rappleye, C. S. Yang and M. F. Simpson, "Application of Voltammetry for Electroanalytical Measurements of Concentrations in LaCl3-MgCl2 Mixtures in Eutectic LiCl-KCl," *Journal of the Electrochemical Society,* vol. 163, no. 10, p. H912, 2016.

[249] G. D. Cordoba, A. Laplace, J. Lacquement and C. Caravaca, "Electrochemical Behavior of Np in the Molten LiCl-KCl Eutectic," *Journal of the Electrochemical Society,* vol. 154, no. 1, p. F16, 2006.

[250] B. Y. Kim and J.-I. Yun, "Reduction of Trivalent Europium in Molten LiCl-KCl Eutectic Observed by In-Situ Laser Spectroscopic Techniques," *ECS Electrochemistry Letters,* vol. 2, no. 11, p. H54, 2013.

[251] L. Yang and R. G. Hudson, "Some Investigations of the Ag/AgCl in LiCl-KCl Eutectic Reference Electrode," *Journal of the Electrochemical Society,* vol. 106, no. 11, pp. 986-990, 1959.

[252] P. Gao, X. Jinn, D. Wang, X. Hu and G. Z. Chen, "A quartz sealed Ag/AgCl reference electrode for CaCl2 based molten salts," *Journal of Electroanalytical Chemistry,* vol. 579, no. 2, pp. 321-328, 2005.

[253] O. Shirai, T. Nagai, A. Uehara and H. Yamana, "Electrochemical properties of the Ag+|Ag and other reference electrodes in the LiCl-KCl eutectic melts," *Journal of Alloys and Compounds,* vol. 456, no. 1-2, pp. 498-502, 2008.

[254] T. Zhu, W. Huang and Y. Gong, "Electrochemical separation of uranium from lanthanide (La, Eu, Gd) fluorides in molten LiCl-KCl," *Separation and Purification Technology,* vol. 235, p. 116227, 2020.

[255] J. Ge, B. Cai, F. Zhu, Y. Gao, X. Wang, Q. Chen, M. Wang and S. Jiao, "Natural Convection in Molten Salt Electrochemistry," *Journal of Physical Chemistry B,* vol. 127, pp. 8669-8680, 2023.

[256] M. Gonzalez, A. Burak, S. Guo and M. F. Simpson, "Identification, measurement, and mitigation of key impurities in LiCl-LiO2 used for direct electrolytic reduction of UO2," *Journal of Nuclear Materials,* vol. 510, pp. 513-523, 2018.

[257] P. W. May, W. J. Ludlow, M. Hannaway, P. J. Heard, J. A. Smith and K. N. Rosser, "Raman and conductivity studies of boron-doped microcrystalline diamond,

facetted nanocrystalline diamond and cauliflower diamond films," *Diamond and Related Materials,* vol. 17, no. 2, pp. 105-117, 2008.

[258] D. L. Hill, J. Perano and R. A. Osteryoung, "An Electrochemical Study of Uranium in Fused Chlorides," *Journal of the Electrochemical Society,* vol. 107, no. 8, p. 698, 1960.

[259] P. Masset, D. Bottomley, R. Konings, R. Malmbeck, A. Rodrigues, J. Serp and J.-P. Glatz, "Electrochemistry of Uranium in Molten LiCl-KCl Eutectic," *Journal of the Electrochemical Society,* vol. 152, no. 6, p. A1109, 2005.

[260] C. E. Thalmeyer, S. Bruckenstein and D. M. Gruen, "Chronopotentiometric determination of interdiffusion coefficients and heats of interdiffusion in molten salts," *Journal of Inorganic Nuclear Chemistry,* vol. 26, pp. 347-357, 1964.

[261] A. Salyulev and A. Potapov, "Electrical Conductivity and Molar volume of (LiCl-KCl)eut.-CsCl Molten Mixtures," *Journal of Chemical & Engineering Data,* vol. 68, no. 6, pp. 1334-1342, 2023.

[262] R. W. Huber, E. V. Potter and H. W. St. Clair, Electrical conductivity and density of fused binary mixtures of magnesium chloride and other chlorides, Pittsburgh: U.S. Department of the Interior, 1952.

[263] A. Molina, J. Gonzalez, M. C. Henstridge and R. G. Compton, "Voltammetry of Electrochemicall Reversible Systems at Electrodes of Any Geometry: A General, Explicit Analytical Characterization," *Journal of Physical Chemistry C,* vol. 115, pp. 4054-4062, 2011.

[264] K. R. Ward, N. S. Lawrence, R. S. Hartshorne and R. G. Compton, "The theory of cyclic voltammetry of electrochemically heterogeneous surfaces: comparison of different models for surface geometry and applications to highly ordered pyrolytic graphite," *Physical Chemistry Chemical Physics,* vol. 14, pp. 7264-7275, 2012.

[265] K. Stulik, C. Amatore, K. Holub, V. Marecek and W. Kutner, "Microelectrodes. Definitions, characterization, and applications," *Pure and Applied Chemistry,* vol. 72, no. 8, pp. 1483-1492, 2000.

[266] C. C. McIntyre and W. M. Grill, "Finite Element Analysis of the Current-Density and Electric Field Generated by Metal Microelectrodes," *Annals of Biomedical Engineering,* vol. 29, pp. 277-235, 2001.

Curriculum Vitae

Hannah K. Patenaude
U.S. Department of Energy University Nuclear Leadership Program Fellow
hpatenaude@lanl.gov | LinkedIn | ORCID: 0000-0002-6790-4659

EDUCATION

2020 – 2024	**Doctor of Philosophy,** Radiochemistry *Department of Chemistry & Biochemistry* *University of Nevada, Las Vegas* Grade Point Average: 3.98
2015 – 2020	**Bachelor of Science,** Chemistry **Bachelor of Arts,** Communication Studies *Cum Laude	Honors College* *University of Nevada, Las Vegas* Grade Point Average: 3.56

Relevant Coursework

CHEM 793	Electrochemistry
CHEM 793	Molten Salt Chemistry (SAMOSAFER)
CHEM 793	Nuclear Policy
CHEM 795	Computational Thermodynamics of Nuclear Materials
COM 418	Rhetoric of Science
HPS 602/603	Radiation Detection & Laboratory
ME 655	Fundamentals of Nuclear Engineering
ME 758	Accelerator Applications in Nuclear Engineering
RDCH 701	Applied Nuclear Physics
RDCH 702	Radiochemistry
RDCH 710	Actinide Chemistry

RESEARCH EXPERIENCE

2022 – Present **Seaborg Graduate Research Fellow (C-Division)**, *Inorganic, Isotope, and Actinide Chemistry & Glenn T. Seaborg Institute, LANL*
Mentors: Marisa Monreal, Ph.D. & Franz Freibert, Ph.D.
Continuation of dissertation research through partnership between Los Alamos National Laboratory (LANL) and University of Nevada, Las Vegas (UNLV) through the Chemistry Division. Electroanalytical chemistry of depleted uranium and thorium chloride and fluoride molten salts using boron-doped diamond electrodes. Various molten salt electroanalytical chemistry and materials science experiments are of interest. Development of electrochemical capabilities within C-IIAC. Support from LANL LDRD funding for actinide research and the Seaborg Institute.

2020 – 2024	**Graduate Research Assistant**, *Radiochemistry Program, UNLV* Advisors: Cory Rusinek, Ph.D. & Kenneth Czerwinski, Ph.D. Spectroelectrochemical investigation of chloride and fluoride molten salt reactor fuel systems containing U, Pu, fission products, and corrosion products while studying the corrosion of Boron-doped diamond electrodes. Modeling molten salt systems with Thermochimica. Established project infrastructure: new gloveboxes, furnaces, spectrometers, potentiostats, electrodes, and radiological laboratory. Mentor undergraduate researchers. Collaboration with Pacific Northwest National Laboratory (PNNL) and LANL.
2018 – 2024	**Graduate Research Assistant**, *Department of Communication Studies, UNLV* Primary Investigator: Emma Frances Bloomfield, Ph.D. Conduct research on the rhetoric of science, specifically regarding the use of nuclear power in the United States. Organizing personal narratives, compiling relevant data and analytics to explain the American view of nuclear applications. Constructed the Nuclear Communication Certificate, now housed at UNLV.
Summer 2022	**Seaborg Graduate Research Fellow (NEN-Division)**, *Systems Design and Analysis & Glenn T. Seaborg Institute, LANL* Mentors: Franz Freibert, Ph.D. & Vedant Mehta, Ph.D. Summer research project to study the Manhattan Project-era Clementine Plutonium Fast Reactor by reviewing archived information and data to conduct modern reactor analyses through the Nuclear Engineering & Nonproliferation Division (NEN-5). The Clementine reactor was modeled and simulated with ABAQUS.
2016 – 2020	**Undergraduate Research Assistant,** *Radiochemistry Program, UNLV* Primary Investigator: Frederic Poineau, Ph.D. Performed reflux reactions, recrystallization, and various methods for characterization while assisting faculty and graduate students with various projects.

Laboratory Techniques

Experimental	**Instrumental**
Electroanalytical Chemistry	Alpha, Gamma, & Ultraviolet-Visible Spectroscopy
Actinide Molten Salt Chemistry	Differential Scanning Calorimetry
FactSage Computational Methods	Inert Atmosphere Glovebox Experiments
Molten Salt Infrastructure Development	Potentiometry
Salt Synthesis & Purification	Radiation Monitoring & Analysis
Spectroelectrochemistry	Scanning Electron Microscopy
Synthesis & Analysis of Radioactive Materials	Thermogravimetric Analysis

Radionuclide Experience

^{99}**Tc** | $MTcO_4$ {M = Na,K}
^{237}**Np** | $Np(ClO)_X$, {X = 3,4,6}
^{238}**U** | UCl_3, UO_2, $UO_2(NO_3)_2$, $(NH_4)_4UF_8$, UF_4

Skills & Certifications

Abaqus Modeling Software - CAE
Cary & Ocean Optics Spectroscopy Software
Various Electrochemistry Software
IAEA Spent Fuel Management & Storage
Radiation Safety: Unsealed Sources
Radiation Detection
ACS Chemistry Advocacy Certification
Conflict Management & Resolution
Diversity & Inclusivity Training
Interpersonal Communication
Organizational Leadership
Small & Large Group Public Speaking

Research Education

2018 **Radiation Detection for Nuclear Security Summer School**, *PNNL*
Two-week course sponsored by the National Nuclear Security Administration that allowed students to learn about federal applications of nuclear sciences.

2018 **Nuclear Analytical Techniques Summer School**, *University of California, Davis*
One-week course sponsored by the Nuclear Science and Security Consortium discussing specific analytical techniques for work with radionuclides.

RESEARCH PUBLICATIONS & PRESENTATIONS

Peer-Reviewed Publications, Reports, & Conference Proceedings

Patenaude, H.K., Damjanovic, N., Rakos, J., Weber, D., Bryan, S., Lines, A., Heineman, W.R., Branch, S.D., Rusinek, C.A. (under review). "A Free-Standing Optically Transparent Boron-Doped Diamond Grid Electrode for Fundamental Spectroelectrochemistry," *Analytical Chemistry*.

Lhermitte, C.R., **Patenaude, H.K.**, Parker, S.S., Jackson, J.M., Monreal, M.J. (**2024**). "Electrochemical behavior and electromotive force measurements of molten U^{3+}/U^0 $MgCl_2$-NaCl," *Electrochimica Acta*, *487*, 144123. https://doi.org/10.1016/j.electacta.2024.144123

Patenaude, H.K. & Freibert, F.J. (**2023**). "Oh, My Darling Clementine: A Detailed History and Data Repository of the Los Alamos Plutonium Fast Reactor," *Nuclear Technology*, *209*(7), 963-1007. https://doi.org/10.1080/00295450.2023.2176686

Patenaude, H.K., Lhermitte, C.R., Czerwinski, K.R., Rusinek, C.A., Monreal, M.J. (**2023**, Nov). "Electrode Materials for Uranium Electroanalytical Chemistry in Molten

Chloride Salts," *Transactions of the American Nuclear Society*, *129*. Molten Salt Fuel Recycling. American Nuclear Society Winter Meeting and Technology Expo. Washington, DC. https://doi.org/10.13182/T129-42440

Patenaude, H.K. (**2022**). "Oh, My Darling Clementine: A History of the Los Alamos Plutonium Fast Reactor," *Actinide Research Quarterly*, *2*, 2-9. https://shorturl.at/vyKQ9

Patenaude, H.K. & Bloomfield, E.F. (**2022**). Topical analysis of nuclear experts' perceptions of publics, nuclear energy, and sustainable futures, *Frontiers in Communication, 7*, 762101. https://doi.org/10.3389/fcomm.2022.762101

Patenaude, H.K., Damjanovic, N., Rakos, J., Gonzalez, K., Branch, S.D., Rusinek, C.A. (**2022**, Nov). "Electrochemical Characterization of Europium(III/II) Chloride in Molten LiCl-KCl Using Boron-Doped Diamond," *Transactions of the American Nuclear Society, 127*, 466-469. Fuels and Materials for Molten Salt Reactors. American Nuclear Society Winter Meeting and Technology Expo. Phoenix, AZ. https://doi.org/10.13182/T127-39441

Patenaude, H.K., Damjanovic, N., Rakos, J., Gonzalez, K., Branch, S.D., Rusinek, C.A. (**2022**, Nov). "A Novel Optically Transparent Boron-doped Diamond Electrode Design for Spectroelectrochemistry," *Transactions of the American Nuclear Society, 127*, 130-133. Research by U.S. DOE NEUP Sponsored Students. American Nuclear Society Winter Meeting and Technology Expo. Phoenix, AZ. https://doi.org/10.13182/T127-39490

Patenaude, H.K. & Bloomfield, E.F. (**2022**, Nov). "Topical Analysis of Nuclear Experts' Perceptions of Publics, Nuclear Energy, and Sustainable Futures: A Publication Summary," *Transactions of the American Nuclear Society, 127*, 74-77. Innovations in Nuclear R&D Awards Oral Session. American Nuclear Society Winter Meeting and Technology Expo. Phoenix, AZ. https://doi.org/10.13182/T127-39440

Patenaude, H.K., Carlsen, B., Bloomfield, E.F. (**2020**, Nov). "INL Nuclear Communication Certification," *Transactions of the American Nuclear Society, 123*, 193-194. Cutting Edge Techniques in Education, Training, and Distance Education Panel. American Nuclear Society Winter Meeting and Technology Expo. Virtual. https://dx.doi.org/10.13182/T123-32946

Chamberlin, R.M., Tang, M., Nevarez, R.B., **Patenaude, H.K.**, Poineau, F., Montoya, D.P., Schappert, M.F. (**2019**, Oct). "Screening of Additional Candidate Low-Temperature Glasses for Technetium Recovered from Hanford Effluent Management Facility Evaporator Bottoms," Los Alamos, NM. Los Alamos National Laboratory. LA-UR-18-29730. https://doi.org/10.2172/1569723

Presentations & Posters

Chamberlain, J.L., **Patenaude, H.K.**, Musgrove, A., Batrice, R., Kardoulaki, E., Monreal, M.J., Coons, T. (**2024**, May). "Electrodeposition of Zirconium on Uranium Nitride on Molten Salts," Fission Surface Power/Nuclear Electric Propulsion Lightning Talk. Nuclear and Emerging Technologies for Space. Santa Fe, NM.

Patenaude, H.K. (**2024**, Mar). "Boron-Doped Diamond as a Resilient Electrode Materials in Molten Salts," Chemistry Colloquium. Chemistry Division, Los Alamos National Laboratory. Los Alamos, NM.

Patenaude, H.K., Mehta, V., Freibert, F.J. (**2024**, Feb). "Oh, My Darling Clementine: A Contemporary Investigation of the Los Alamos Plutonium Fast Reactor." Engineers Week Poster Session, Engineering Leadership Council. Los Alamos National Laboratory. Los Alamos, NM.

Patenaude, H.K., Lhermitte, C.R., Czerwinski, K.R., Rusinek, C.A., Monreal, M.J. (**2023**, Nov). "Electrochemical Investigation of Uranium Redox Behavior in Molten Chloride Salts Using Boron-Doped Diamond," Actinide Materials: Nuclear Fuels and Radwaste Matrices Oral Session. Nuclear Fuel Cycle (NFC3): A Chemistry Conference - Second Edition. Virtual.

Patenaude, H.K., Lhermitte, C.R., Czerwinski, K.R., Rusinek, C.A., Monreal, M.J. (**2023**, Nov). "Electrode Materials for f-Block Electroanalytical Chemistry in Molten Chloride Salts," Advanced Reactors and Fuel Cycle Options Oral Session. American Nuclear Society Winter Expo, Fuel Cycle & Waste Management Division. Washington, DC.

Patenaude, H.K. (*moderator*), Hagerott, V., Meyer, E., Piercy, C. (**2023**, Nov). "How to Talk to Policymakers," Young Members Group. American Nuclear Society Winter Expo. Washington, DC.

Patenaude, H.K. (*moderator*), Gonzalez, E., Houston, E., Iyengar, A., Piercy, C. (**2023**, Nov). "Nuclear Engineering Student Delegation Review," Human Capacity Building in Nuclear Nonproliferation Panel. Advances in Nuclear Nonproliferation Technology and Policy Conference. American Nuclear Society Winter Expo. Washington, DC.

Patenaude, H.K., Lhermitte, C.R., Czerwinski, K.R., Rusinek, C.A., Monreal, M.J. (**2023**, Oct). "Electrode Materials for f-Block Electroanalytical Chemistry in Molten Chloride Salts," Poster Session. Molten Salt Reactor Workshop, Oak Ridge National Laboratory. Oak Ridge, TN.

Patenaude, H.K., Lhermitte, C.R., Damjanovic, N., Rakos, J., Czerwinski, K.R., Rusinek, C.A., Monreal, M.J. (**2023**, Aug). "Electrochemical Investigation of Uranium Redox Behavior in Molten Chloride Salts Using Boron-Doped Diamond," Molten Salt Symposium Oral Session. American Chemical Society National Meeting. San Francisco, CA.

Patenaude, H.K., Lhermitte, C.R., Czerwinski, K.R., Rusinek, C.A., Monreal, M.J. (**2023**, Aug). "Electrochemical Investigation of Uranium Redox Behavior in Molten Chloride Salts Using Boron-Doped Diamond," Seaborg Institute Lecture Series. Los Alamos National Laboratory. Los Alamos, NM.

Patenaude, H.K., Lhermitte, C.R., Czerwinski, K.R., Rusinek, C.A., Monreal, M.J. (**2023**, Aug). "Electrode Materials for f-Block Electroanalytical Chemistry in Molten Chloride Salts," Student Poster Session. Los Alamos National Laboratory. Los Alamos, NM.

Patenaude, H.K., Lhermitte, C.R., Damjanovic, N., Rakos, J., Rusinek, C.A., Czerwinski, K.R., Monreal, M.J. (**2023**, May). "Electrochemical Characterization of

Molten Salt Fuel Systems with Boron-Doped Diamond," Actinide Separations Conference. Idaho National Laboratory. Idaho Falls, ID.

Patenaude, H.K., Lhermitte, C.R., Damjanovic, N., Rakos, J., Rusinek, C.A., Czerwinski, K.R., Monreal, M.J. (**2023**, May). "Electrochemical Characterization of Molten Salt Fuel Systems with Boron-Doped Diamond," Molten Salt Workshop. Los Alamos National Laboratory. Los Alamos, NM.

Bloomfield, E.F., Almanza, D., Estrada, E., Kelley, L., **Patenaude, H.K.** (**2023**, Apr). "(Im)Mobilizing Eco-Anxiety in Nevada," Environment, Justice, and the Politics of Emotion: A Virtual and In-Person Symposium. *Learning to Live With Climate Change*. Riverdale, CA.

Patenaude, H.K., Mehta V., Freibert, F.J. (**2023**, Apr). "Oh, My Darling Clementine: A Contemporary Investigation of the Los Alamos Plutonium Fast Reactor." Seaborg Institute Center for Advancing Actinide Science and Technology Laboratory Directed Research and Development Review. Los Alamos, NM.

Patenaude, H.K., Lhermitte, C.R., Damjanovic, N., Rakos, J., Monreal, M.J., Rusinek, C.A. (**2023**, Mar). "Electrochemical Characterization of Molten Salt Fuel Systems with Boron-Doped Diamond," Virtual Seminar Series. American Nuclear Society Materials Science and Technology Professional Division.

Patenaude, H.K., Lhermitte, C.R., Damjanovic, N., Rakos, J., Branch, S.D., Monreal, M.J., Rusinek, C.A. (**2023**, Mar). "Electrochemical Characterization of Molten Salt Fuel Systems with Boron-Doped Diamond," Materials and Chemistry for Molten Salt Systems Oral Session. 152nd Annual Minerals, Metals, and Materials Society Meeting and Exhibition. San Diego, CA.

Patenaude, H.K., Mehta V., Freibert, F.J. (**2023**, Mar). "Oh, My Darling Clementine: A Contemporary Investigation of the Los Alamos Plutonium Fast Reactor." Seaborg Institutes: Emerging Topics in Actinide Materials and Science Oral Session. 152nd Annual Minerals, Metals, and Materials Society Meeting and Exhibition. San Diego, CA.

Patenaude, H.K., Mehta V., Freibert, F.J. (**2023**, Feb). "Oh, My Darling Clementine: A Contemporary Investigation of the Los Alamos Plutonium Fast Reactor." Student Poster Session. 2nd International Workshop on Theory Frontiers in Actinide Science: Chemistry & Materials. Santa Fe, NM.

Patenaude, H.K., Damjanovic, N., Rakos, J., Gonzalez, K., Branch, S.D., Rusinek, C.A. (**2022**, Oct). "Electrochemical Characterization of Molten Salt Fuel Systems with Boron-Doped Diamond," Poster Session. Oak Ridge National Laboratory Molten Salt Reactor Workshop. Oak Ridge, TN.

Patenaude, H.K., Damjanovic, N., Rakos, J., Gonzalez, K., Branch, S.D., Rusinek, C.A. (**2022**, Oct). "Electrochemical characterization of molten salt fuel systems with boron-doped diamond," Inorganic and Materials Chemistry Oral Session. American Chemical Society Western Regional Meeting. Las Vegas, NV.

Damjanovic, N., **Patenaude, H.K.**, Rakos, J., Rusinek, C.A. (**2022**, Oct). "Free-standing optically transparent carbon electrodes for spectroelectrochemistry," Environmental

Chemistry, Energy Storage, Education Poster Session. American Chemical Society Western Regional Meeting. Las Vegas, NV.

Freibert, F.J., Johns, R.C. **Patenaude, H.K.** (**2022**, Sep). "A Contemporary Investigation of Clementine," Nuclear Fuel Cycle Oral Session. Plutonium Futures - The Science. Avignon, FR.

Patenaude, H.K., Rakos, J., Olney, R., Damjanovic, N., Branch, S.D., Rusinek, C.A. (**2022**, Apr). "Boron-doped diamond resilience in chloride and fluoride molten salt fuel systems." Salt Chemistry and Radiochemistry in Support of Molten Salt Reactors Oral Session. Twelfth International Conference on Methods and Applications of Radioanalytical Chemistry (MARC). Kona, HI.

Patenaude, H.K., Rakos, J., Olney, R., Damjanovic, N., Rusinek, C.A. (**2022**, Apr). "Electrochemical characterization of molten europium chloride with boron-doped diamond." Sciences Poster Session. Graduate & Professional Student Association Research Forum. University of Nevada, Las Vegas. Las Vegas, NV.

Patenaude, H.K. (**2022**, Apr). "The Rhetoric of Nuclear Power and Power of Nuclear Rhetoric." University of Nevada, Las Vegas Inspiration, Innovation, Impact Graduate Student Research Forum Series. Las Vegas, NV.

Patenaude, H.K., Rakos, J., Olney, R., Damjanovic, N., Branch, S.D., Rusinek, C.A. (**2022**, Mar). "Boron-doped diamond resistance in chloride and fluoride molten salt fuel systems." General Topics in Nuclear and Radiochemistry Oral Session. American Chemical Society National Meeting. San Diego, CA.

Patenaude, H.K., Rakos, J., Olney, R., Damjanovic, N., Branch, S.D., Rusinek, C.A. (**2022**, Mar). "Boron-doped diamond resistance in chloride and fluoride molten salt fuel systems." General Topics in Nuclear and Radiochemistry Sci-Mix Poster Session. American Chemical Society National Meeting. San Diego, CA.

Patenaude, H.K., Rakos, J., Damjanovic, N., Gelis, A.V., Rusinek, C.A. (**2021**, Dec). "Electrochemical characterization of molten uranium chloride fuel systems with boron-doped diamond." Virtual General Materials Poster Session. International Chemical Congress of Pacific Basin Societies.

Patenaude, H.K., Rakos, J., Olney, R., Damjanovic, N., Branch, S.D., Rusinek, C.A. (**2021**, Dec). "Boron-doped diamond resilience in molten LiCl-KCl." American Chemical Society Southern Nevada Section Student Poster Competition Exposition. Las Vegas, NV.

Patenaude, H.K. (**2021**, Apr). "Spectroelectrochemical Characterization of Uranium and Plutonium Chloride and Fluoride Molten Salt Fuel Systems." Pitch Your Generation IV Virtual Research Competition. Generation IV International Forum.

Patenaude, H.K. (**2021**, Apr). "Spectroelectrochemical Characterization of Uranium and Plutonium Chloride and Fluoride Molten Salt Fuel Systems." Pitch Your Ph.D. Oral Session. American Nuclear Society Student Conference. Virtual.

Patenaude, H.K., Carlsen, B., Bloomfield, E.F. (**2020**, Aug). "Nuclear Communication Certification." 2020 INL Summer Intern Virtual Poster Symposium.

Patenaude, H.K., Bloomfield, E.F. (**2020**, Feb). "Storytelling and Risk Communication in Nuclear Scientists' Perceptions of Publics, Nuclear Energy, and Sustainable

Futures." Nuclear Energy and Environmental In/Justice Panel. Western States Communication Association Convention: Communication, Agitation, & Justice. Denver, CO.

Patenaude, H.K., Nevarez, R.B., Poineau, F. (**2018**, Aug). "Selective Separation of Cesium Fission Product via β-diketones." Poster Session. UNLV Office of Undergraduate Research Symposium. Las Vegas, NV.

Patenaude, H.K., Nevarez, R.B., Poineau, F. (**2017**, Nov). "Selective Separation of Cesium Fission Products via β-diketones." Oral Presentation. UNLV Office of Undergraduate Research SLAM Lightning Talk Competition. Las Vegas, NV.

Professional Panels & Invited Talks

2023	**STEM Leadership Panel** Nevada Afterschool Network panel series exposing young students in Las Vegas to STEM careers.
2022	**Effectively Communicating your Research, Creative, & Scholarly Work Panelist** UNLV Graduate College Grad Academy Workshop Series discussing how students can best communicate and find opportunities to share their work in and outside of their specialty areas.
2021	**Outreach Webinar Panelist** U.S. WIN & Nuclear Matters Webinar, "Building Trust Online." Discussion regarding effective and empathetic nuclear science communication.
2021	**Women's History Month Panelist** UNLV Student Involvement & Activities WHM Panel: Supporting Women & Non-Binary Folks in Male-Dominated Fields. UNLV U.S. Women in Nuclear representative.
2020	**Medallion Ceremony Speaker** UNLV Honors College 2020 Graduate Medallion Ceremony keynote speaker.
2020	**Keynote Speaker** UNLV National Society of Collegiate Scholars Induction speech as Student Body President.
Summer 2019	**New Student Orientation Keynote Speaker** Speeches as Student Body President at the New Student Orientations for incoming students.
2019	**Scholar Achievement Panelist** UNLV Scholar Achievement Reception College of Sciences undergraduate panelist for high-achieving Las Vegas high school students.

2018	**Keynote Speaker** UNLV Honors & Research Symposium speech to high achieving high school seniors about the undergraduate experience in the Honors College, research, and campus involvement.
2017	**Undergraduate Research Conference Panelist** UNLV Undergraduate Research panelist regarding experience with undergraduate research.
2015	**Keynote Speaker** UNLV Honors Recruitment Banquet. Experience as a first-year, out-of-state student in the UNLV Honors College presented to high-achieving high school seniors.

GRANTS & AWARDS

Research Sponsorships

2023 – Present	*Harmonia Plutonium Science (PluS) Laboratory*, Nonproliferation Stewardship Program, National Nuclear Science Administration Office of Defense Nuclear Nonproliferation (NA-20)
2023 – Present	*Molten Salt Reactor Campaign*, Gateway for Innovation in Nuclear, U.S. Department of Energy
2023 – 2024	*Space Nuclear Propulsion Program*, National Aeronautics and Space Administration
2023	*Advanced Characterization to Enable Prediction of Actinide-Molten Salt Behavior*, LANL Laboratory Directed Research and Development Directed Research | **20210113DR**
2022 – 2024	*Glenn T. Seaborg Institute*, LANL Laboratory Directed Research and Development Centers Research | **20210527CR & 20240478CR**
2020 – 2024	*Nuclear Energy University Program*, U.S. Department of Energy | **20-19188**

Awards & Recognition

2021 – 2024	U.S. DOE Nuclear University Leadership Program Graduate Fellowship | **$161,000**
2024	LANL Chemistry Division SPOT Award | **$100**
2022	U.S. DOE Innovations in Nuclear Technology R&D Awards: 1st Place, Energy Policy | **$3,000**
2022	U.S. DOE Molten Salt Reactor Workshop Poster Session: 1st Place | **$500**
2022	ANS Methods in Analytical Radiochemistry Conference Oral Session: 1st Place | **$500**
2022	UNLV Graduate & Professional Student Association Research Poster Session: 1st Place | **$500**

2022	ACS Southern Nevada Graduate Student Travel Grant | **$300**
2021	ACS Southern Nevada Poster Session, 1st Place | **$400**
2021	Gen IV International Research Forum Pitch Your Ph.D. Finalist
2021 & 2020	U.S. Women in Nuclear Sponsored Student Program | **$200**
2020	Southwest Airline Research Travel Award | **$400**
2017	UNLV Undergraduate Research SLAM, 3rd Place | **$350**

Scholarships & Academic Achievements

2022	UNLV Nowak Notre Dame Scholarship | **$1,450**
2022	UNLV Gregg Calvird Scholarship | **$1,275**
2021	ANS Fuel Cycle & Waste Management Division John Randall Scholarship | **$5,000**
2019	U.S. DOE Nuclear Energy University Program Scholarship | **$7,500**
2019	UNLV Undergraduate NSHE Regents' Scholar Award | **$5,000**
2018 & 2019	UNLV Honors College Mentor Scholarship | **$5,000**
2018	UNLV Hall of Fame
2015 – 2019	Helping Hands Service Scholarship | **$20,000**
2015 – 2019	UNLV Rebel Challenge Scholarship | **$44,000**
2015 – 2019	UNLV Mary & John Hughes Provost Scholarship | **$20,000**
2015 – 2019	UNLV Provost Scholarship | **$13,000**
2015 – 2019	UNLV Top 10% Incentive Scholarship | **$4,000**
2015	UNLV Bennett Family Honors College Scholarship | **$2,000**
2015	Phoenix Education Burn Survivor Grant | **$1,000**

PROFESSIONAL EXPERIENCE

2020 – 2024	**Research Assistant**, *Public Communication Initiative, UNLV* Continuation of INL Internship project to construct a Nuclear Communication Certification for professionals within the nuclear technologies industry. Additional assistance in other PCI projects, including a climate change survey sponsored by the Nevada Governor's office.
2020	**Intern**, *Used Fuel Management, Idaho National Laboratory* Communication research-based internship at INL to create a Nuclear Communication Certification for nuclear experts to strengthen and practice their communication skills to build relationships and trust with their communities.
2017 – 2019	**Senior Editor**, *Spectra Undergraduate Research Journal* Created the foundation for *Spectra*, an undergraduate-operated, peer-reviewed research journal. Coordinated and composed biannual publication processes and mechanisms to spotlight research from high school to post-baccalaureate students, reviewed by graduate students and faculty.

2019	**Student Advocate**, *CSUN Student Government, UNLV* Legislative meetings in Carson City, NV regarding funding requests for student success at UNLV.
2019	**Undergraduate Teaching Assistant**, *College of Sciences, UNLV* Assisted the College of Sciences Dean in teaching SCI 102x, an introductory course for students entering STEM disciplines.
2016 – 2017	**Tutor**, *Asian American Native American Pacific Islander Serving Institution Program, UNLV* Undergraduate tutor for mathematics through calculus III and chemistry through organic chemistry.

PROFESSIONAL MEMBERSHIP

U.S. Women in Nuclear

2020 – Present	**Member**, *Communications Committee* Website coordinator (2022 - Present). Liaison to the Nuclear Executives of Tomorrow (NEXT) program (2021 - Present), including website construction for the program in collaboration with U.S. WIN and the Nuclear Energy Institute. Collected and published submissions for the national Outreach Library (2020 - 2021). Other general support of U.S. WIN communications, including publications and webinars.
2020 – 2022	**Founding President**, *UNLV Student Chapter* Aim to create an inclusive culture within the nuclear industry, provide opportunities for professional development and networking, and share the technology and impact of nuclear energy technology.

U.S. WIN Nuclear Executives of Tomorrow

2021 – Present	**U.S. WIN Liaison**, *Planning Committee* NEXT communications include the development of an encompassing communication strategy and coordinating NEXT updates through *The WINning Edge* newsletter, press releases, and website. Support for the general planning and logistics of NEXT.

American Nuclear Society

2023 – Present	**Member**, *Trinity Professional Section* Outreach events to local students and support for the section's website.
2022	**Student Program Co-Chair**, *Student Sections Committee, Winter Expo* Facilitated participation and coordinated volunteers for various components of the Winter Expo.

2022 **Alternate Chair**, **Advanced Reactors, Fuels, & Fuel Cycles**, *Winter Expo*
International High-Level Radioactive Waste Management Conference student chair.

2021 – 2023 **Student/Young Member Liaison**, *Fuel Cycle & Waste Management Division*
Connect and engage students with the FCWM Division's professional members and the division with the Student Sections Committee and Young Members Group. Help organize events and outreach for the division, including webinars about the fuel cycle.

2017 – 2024 **Member**, *UNLV Student Section*
Discussion of general topics related to the sphere of nuclear technology and sciences. Provide events for local youth to learn about nuclear sciences.

Nuclear Engineering Student Delegation

2023 **Co-Vice Chair**
Logistics, planning, and organizing for the 2023 delegation. Full participation in the delegation.

2022 **Nevada Representative**
First representative from Nevada to serve on NESD. Week-long lobbying trip in Washington, D.C., with nuclear science and engineering students from around the United States. Development of policy statements and in-person meetings with NV Senators and Congresspeople.

LEADERSHIP & SERVICE

Los Alamos Public Schools Science & Engineering Fair

2024 **Junior Chemistry Judge Captain**
Science fair judge for middle school chemistry projects.

Women Scientists: Force for Change

2022 **Graduate Student Mentor**
Leadership program for women enrolled in the UNLV College of Sciences. Mentoring, leadership training, and network building to support women in STEM.

Special Committees

2020 – 2021 **UNLV Graduate Student Advisory Board**
Advisory board to discuss the state of graduate student affairs within the Graduate College with the Dean and other University Administrators.

2019 – 2020 **NSHE Chancellor Search Committee**
Undergraduate student representative to advise the Nevada System of Higher Education Board of Regents on the Chancellor selection.

2019 – 2020 **UNLV President Search Committee**
Undergraduate student representative to advise the NSHE Board of Regents on the University President selection.

2019 – 2020 **UNLV President's Advisory Council**
Undergraduate student representative on issues affecting the campus. Advise the University President on matters related to undergraduate students.

Mentorship Co-Op, *UNLV*

2020 – 2021 **Graduate Student Mentor**
Mentored five students from pre-professional to engineering majors providing tips, tricks, referrals, guidance, and general support to help them reach their goals.

Consolidated Students of the University of Nevada

2019 – 2020 **Student Body President**, *Nevada Student Alliance*
Represented the 27,000+ undergraduate students at UNLV and legal head of CSUN. Constructed and managed the $1.2m annual operating budget. Managed and supervised the CSUN Executive Branch, including Executive Board, Cabinet, and Executive Departments (20+ students). Liaison between students and administration for both UNLV and NSHE. Established and secured communication with the student body. Established the CSUN President's Advisory Council.

2017 – 2019 **Senator**, *College of Sciences*
Represented 3,000+ students in the College of Sciences at UNLV. Assisted in managing the 1.2 million-dollar CSUN budget, assisted science organizations in securing resources, and general outreach to science constituents for feedback regarding safety, student resources, or any other concern. Participated in the College of Sciences administrative business.

2018 – 2019 **Senate President Pro Tempore**
Served as the head of the Legislative Branch of CSUN. Led and oversaw the Legislative Committee Chairs and the Legislative Internship Program. Parliamentarian of the Senate.

2017 – 2018 **Committee Chair**, *Ways & Means*
Chair of the finance committee, advised CSUN President in fiscal endeavors, including funding for student organizations, and crafting the annual operating budget.

Leadership Las Vegas: Education Day, *Leadership Foundation of Greater Las Vegas*

Jan 2019 **Invited Speaker**
Presentation to Las Vegas Community leaders about the UNLV student experience.

STEMpowerment Workshop, *500 Women Scientists*

Apr 2019 **Mentor**
Provided "speed mentoring" to women of all ages in five-minute intervals. Discussed the education, research, and infinite possibilities of STEM and careers to consider.